Pillared-Layer Metal-Organic Frameworks (MOFs) as Photocatalysts for Degradation of Dyes

Tesfaye Haile Habtemariam

A Thesis Submitted to
The Department of Chemistry

Presented in Fulfilment of the Requirements for the Degree of
Doctor of Philosophy (Inorganic Chemistry)

Addis Ababa University
Addis Ababa, Ethiopia
June, 2019

Pillared-Layer Metal-Organic Frameworks (MOFs) as Photocatalysts for Degradation of Dyes

Tesfaye Haile Habtemariam

A Thesis Submitted to
The Department of Chemistry

Presented in Fulfilment of the Requirements for the Degree of Doctor of Philosophy (Inorganic Chemistry)

Addis Ababa University
Addis Ababa, Ethiopia
June, 2019

Addis Ababa University

School of Graduate Studies

This is to certify that the thesis prepared by Tesfaye Haile Habtemariam entitled: "***Pillared-Layer Metal-Organic Frameworks (MOFs) as Photocatalysts for Degradation of Dyes***" and submitted in fulfilment of the requirement for the degree of Doctor of Philosophy (Inorganic Chemistry) complies with the regulations of the University and meets the accepted standards with respect to originality and quality.

Signed by the examining committee:

Examiner____________________________Signature______________Date ______________

Examiner____________________________Signature______________Date ______________

Examiner____________________________Signature______________Date ______________

Advisor_____________________________Signature______________ Date ______________

Advisor_____________________________Signature______________ Date ______________

____

Chair of Department or Graduate Programme Coordinator

Abstract

Pillared-Layer Metal-Organic Frameworks (MOFs) as Photocatalysts for Degradation of Dyes

Tesfaye Haile Habtemariam

Addis Ababa University, June 2019

Metal-Organic Frameworks (MOFs) are highly crystalline and porous materials. In this thesis, three sets of work have been undertaken. The first two involve the synthesis and characterization of pillared-layer MOFs and the third is a study of the photodegradation application of selected pillared-layer MOFs in the textile wastewater treatment sector.

In the first work, three pillared-layer Metal–Organic Frameworks (MOFs) were synthesized at room temperature in water/methanol mixed solvents and fully characterized. Fumaric acid was converted to its sodium fumarate salt and used as a linker to form MOFs in combination with the pillar, 4, 4'-bipyridine. The powder x-ray diffraction (PXRD) of two MOFs were found to be in good agreement with simulated diffractograms from single crystal data of related MOFs made at higher temperature using DMF as solvent. The study showed that room temperature synthesis (of such pillared-layer MOFs) could produce mesoporous MOFs in less toxic solvents. This could be an attractive approach to obtain MOFs in a greener way and will increase the applicability. Even though single crystals couldn't be obtained from all three newly prepared MOFs, quantitative amounts of MOFs could be obtained. Determination of the optical band gaps using Tauc plots revealed that $\{[Ni_2(Ox)_2(BPY)]\cdot 3.75H_2O\}_n$ is photo responsive in the visible region, whereas

$\{[Zn_2(Fu)_2(BPY)]\cdot 1.5H_2O\}_n$ and $\{[Cu_2(Fu)_2(BPY)]\cdot H_2O\}_n$ are responsive in the UV region.

Encouraged by the first set of the work, Zn (II) and Cu (II) based pillared-layer MOFs from sodium oxalate linker (and also 2-aminotherephtalate) and 4,4’-bipyridine pillar in water/methanol mixed solvents were synthesized at room temperature and characterized. Powdered MOFs were obtained and their crystallinity was studied using PXRD techniques. DICVOL06 in Expo2014 software was used to index PXRD patterns of the MOFs and it was possible to have crystal parameters. All the MOFs obtained have porosities in the mesoporous region. The optical band gap measurements showed that the $\{[Zn_2(ATA)_2(BPY)]\cdot H_2O\}_n$ is active in the visible region whereas $\{[Zn_2(Ox)_2(BPY)]\cdot 3.5H_2O\}_n$ and $\{[Cu_2(Ox)_2(BPY)]\cdot 0.5H_2O\}_n$ are active in the UV region. Magnetic property studies of the Cu and Ni-based MOFs revealed that there are long range cooperative spin exchange interactions between paramagnetic metal ions through diamagnetic units implying that the MOFs behaved as low dimensional magnetic materials.

In the last sets of the work, the photocatalytic performance of one of the pillared-layer MOF, $\{[Cu_2(Fu)_2(BPY)]\cdot H_2O\}_n$, has been studied in detail towards degradation of methyl orange as a model dye, which is toxic, nonbiodegradable, and discharged to the environment through wastewater by textile industries. The degradation of this model dye was investigated with UV radiation in the presence of the semiconducting MOF, $\{[Cu_2(Fu)_2(BPY)]\cdot H_2O\}_n$. The optimized conditions for the photodegradation efficiency of the MOF were achieved after considering the effect of pH, and MOF loading at a fixed dye concentration. 96 % of the 10-ppm methyl orange is photodegraded with 0.25 g/L

loading of the photocatalyst at pH 5.2 in 140 min of irradiation time. The photocatalyst was recycled five times with a 96 %, 88 %, 87 %, 80% and 53 % degradation efficiencies. The PXRD analysis of the recycled photocatalyst showed that the crystallinity of the MOF is maintained in the five runs.

Acknowledgments

Pursuing a PhD program is pains taking, but an enjoyable experience. There were a number of ups and downs in this exercise until appreciable results were obtained. The scientific experience acquired throughout the course of this work is really enjoyable and I hope will be the backbone for my future research career. I realize that research is not an independent activity and there are a number of people who generously leave their fingerprints on this work, for which I do not have enough words to express my gratitude.

Firstly, I would like to express my sincere gratitude to my supervisors Dr. Yonas Chebude and Prof. V.J.T Raju for their continuous support, patience, motivation, and immense knowledge. Their guidance helped me throughout the laboratory work and write up of this dissertation. I really do not forget the time Dr. Yonas spent to link up my PhD research visit to the University of Nottingham, UK, which played a profound role on the completion of this study. The friendly approach of the supervisors gave me great encouragement, freedom and confidence.

My sincere thanks also go to Professor Neil R. Champness of the University of Nottingham, UK, for hosting and supporting my visit and giving me an opportunity to work with his MOFs research group for three months. The scientific inspiration and enlightenment experienced through the MOF research was of great advantage to me. I am thankful to Nicholas Pearce, Joseph Ogar, and Charlotte Gidman to mention a few for their friendly approach and guidance in the laboratory.

I would like to express my gratitude and appreciation to the department of chemistry, Addis Ababa University for the financial support towards three months' research leave at the

University of Nottingham, UK. I thank my fellow lab mates at Addis Ababa University for the stimulating discussions, for the longer hours of working together in the laboratory, and for all the fun we have had in the last five years.

I would like to convey my heartfelt thanks to my home university, Wolaita Sodo University, Ethiopia for the sponsorship of my PhD at Addis Ababa University.

Last but not least, I am greatly indebted to my devoted wife Yemisrach Workneh. She is really keen in encouraging me to seriously focus on my PhD study while far away from me and taking care of our baby daughter, Hewan Tesfaye and baby boy, Bereket Tesfaye in my absence besides her career. I owe my every achievement to her.

Tesfaye Haile Habtemariam
Addis Ababa University, June 2019

Contents

List of Figures

List of Schemes

List of Tables

List of Abbreviations

ATA – 2-Aminotherephtalate

BET – Brunauer–Emmett–Teller

BPY – 4,4’-Bipyridyl

CIF – Crystallographic Information File

EDS – Energy-dispersive X-ray spectroscopy

FT-IR – Fourier-transform infrared spectroscopy

Fu – Fumarate

LAG Liquid Assisted Grinding

MO – Methyl Orange

MOFs – Metal-Organic Frameworks

MOFT-08-RT – $\{[Zn_2(Ox)_2(BPY)]\cdot 3.5H_2O\}_n$

MOFT-09-RT – $\{[Cu_2(Ox)_2(BPY)]\cdot 0.5H_2O\}_n$

MOFT-11-RT – $\{[Ni_2(Ox)_2(BPY)]\cdot 3.75H_2O\}_n$

MOFT-22-RT – $\{[Zn_2(Fu)_2(BPY)]\cdot 1.5H_2O\}_n$

MOFT-23-RT – $\{[Cu_2(Fu)_2(BPY)]\cdot H_2O\}_n$

MOFT-53-RT – $\{[Zn_2(ATA)_2(BPY)]\cdot H_2O\}_n$

Ox – Oxalate

PXRD – X-ray Powder Diffraction

PYTZ – 3,6-di(pyridin-4-yl)-1,2,4,5-tetrazine

SEM	–	Scanning Electron Microscopy
TGA	–	Thermogravimetric Analysis
UV	–	Ultraviolet

CHAPTER ONE

Introduction

Metal–organic frameworks (MOFs) represent a fascinating class of highly porous materials which were reported originally by Yaghi and co-workers in the 1990s.[13] Chemists have used porous materials, including clays and zeolites to trap and store gases for decades.[14, 15] The pores and channels in naturally occurring porous materials are of varying sizes. Therefore, researchers have sought to develop porous structures with uniform openings. In trying to construct such materials in the 1990s, Omar Yaghi at the University of California, Los Angeles, came up with a novel method for making frameworks with precisely controlled pore sizes. In 1998, Yaghi engineered the first MOF structure by mixing together two molecular building blocks, namely metal oxide and organic groups.[16]

The design and construction of metal–organic frameworks (MOFs) is currently of great interest in the fields of coordination chemistry and crystal engineering, because MOFs have an intriguing variety of topologies, fascinating structures, interesting properties and potential applications.[17] In general, the construction of MOFs depends on two primary components, namely the metal centres, including metal ions, metal clusters or secondary building units (SBUs), which act as connectors, and the organic ligands, which act as linkers. The most important characteristics of the connectors and linkers are the number and orientation of the interacting sites. Typical linkers are multidentate organic ligands with definite linking sites that determine the spatial arrangement of the connectors in the framework.[18]

During the past decade, MOFs have attracted extensive interest in the fields of chemistry, material science, medicine, and environmental science. However, most of the MOF applications, including gas separation, gas storage, chemical sensing, catalysis, drug delivery, and energy storage and conversion, were based on taking advantage of their porosity. Very recently, several studies have underscored the importance of the framework architecture itself, and especially the possibility to utilize the structural reinforcement of nitrogen-rich MOFs as energetic materials.[19]

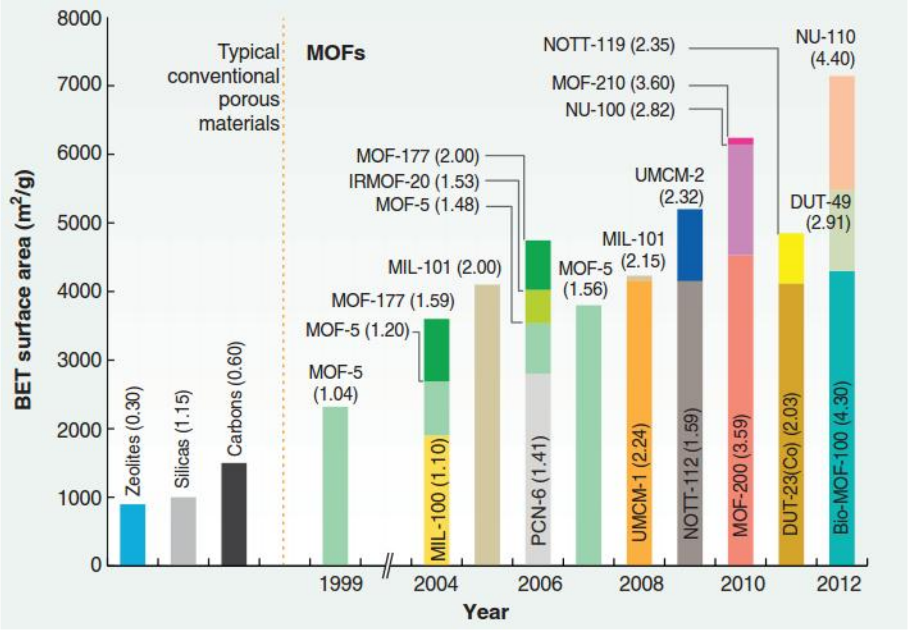

Figure 1 Progress in the synthesis of ultrahigh-porosity MOFs. BET surface areas of MOFs and typical conventional materials were estimated from gas adsorption measurements. The values in parentheses represent the pore volume (cm^3/g) of these materials.[6]

Based on the geometries of the organic linkers and coordination modes of the inorganic metal ions or clusters of metal ions, MOF structures can be designed according to targeted properties. Typical conventional porous materials like zeolites, silicas, and carbon nanotubes have smaller BET surface areas when compared to MOFs (Fig. 1). The figure also showed that a number of researches are being undergone to increase the surface area and pore volumes of MOFs. A key structural feature of MOFs is the ultrahigh porosity (up to 90% free volume) and incredibly high internal surface areas, extending beyond a Langmuir surface area of 10, 000 m^2g^{-1}, which play a crucial role in functional applications.[20]

A stable coordination network is achieved by considering the nature of the metal and ligand. From an industrial point of view, the stability of MOFs is a prerequisite for utilization. So far, numerous MOFs have been reported; however, very few possess high chemical stability, especially towards both acids and bases. For example, three typical MOFs, Cu-BTC, MOF-5, and MOF-74, which have been widely investigated, are unstable towards water. It has been a challenge to make chemically stable MOFs because of their susceptibility to link-displacement reactions when treated with solvents over extended periods of time (days). The first example of a MOF with exceptional chemical stability is zeolitic imidazolate framework–8 [ZIF-8, $Zn(MIm)_2$; MIm- = 2-methylimidazolate], which was reported in 2006. ZIF-8 is unaltered after immersion in boiling methanol, benzene, and water for up to 7 days, and in concentrated sodium hydroxide at 100°C for 24 hours. [6]

MOFs containing highly oxidized metals or a metal cluster tend to be more stable due to the stronger bonds. On the other hand, from the aspect of the ligand, introduction of hydrophobic or nonpolar groups can also enhance the water stability of MOFs.[21]

1.1 Synthesis of Metal Organic Frameworks (MOFs)

A summary of the various approaches for MOF preparation is illustrated in Fig. 2. Most MOF syntheses are liquid-phase syntheses, where separate metal salt and ligand solutions are mixed together or solvent is added to a mixture of solid salt and ligand in a reaction vial. Selection of a solvent for these liquid-phase reactions can be based on different aspects such as reactivity, solubility, redox potential, stability constant etc. Solvents also play an important role in determining the thermodynamics and activation energy for a particular reaction. Apart from liquid-phase synthesis, researchers have also attempted solid-phase syntheses of MOFs, because it is quicker and easier, but solid-state synthesis always faces difficulties in obtaining single crystals, and thereby determining product structure, which is otherwise quite easy in solution phase reactions. The slow evaporation method is a regular process of crystallization which has been applied for the last few decades to prepare MOF crystals. Although routine synthesis of MOFs involves solvothermal methods (Fig.3), other methods such as microwave-assisted synthesis,

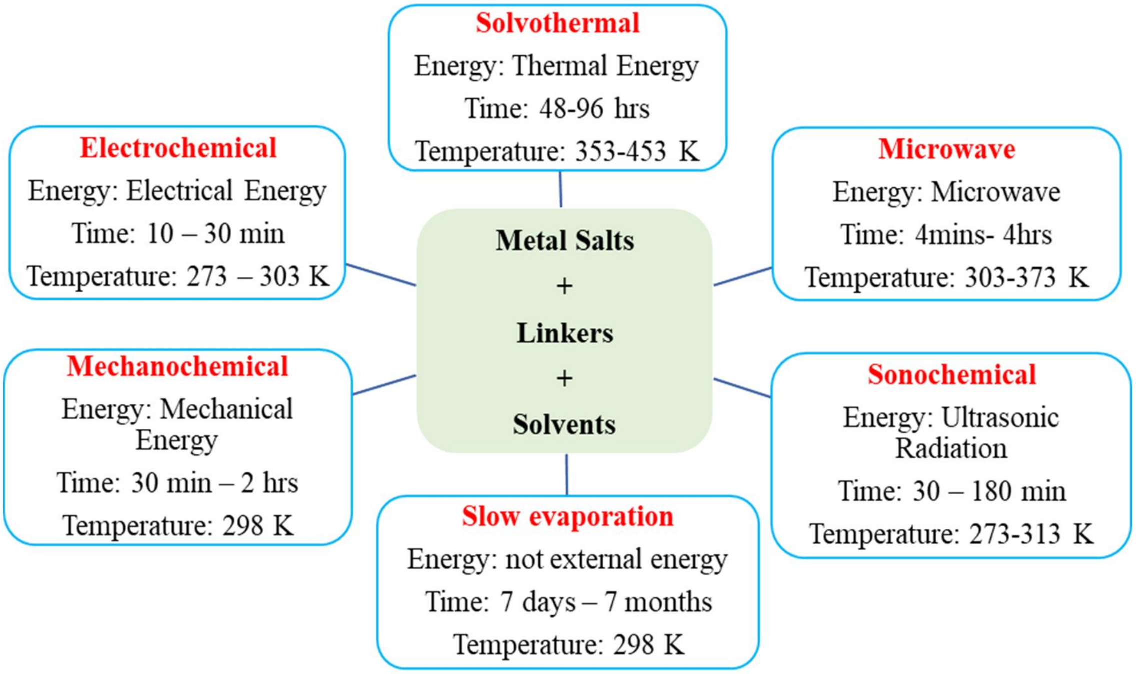

Figure 2 Conditions commonly used for MOF synthesis[8]

electrochemical synthesis, mechanochemical synthesis and sonochemical synthesis have been applied as alternatives for MOF synthesis.[8]

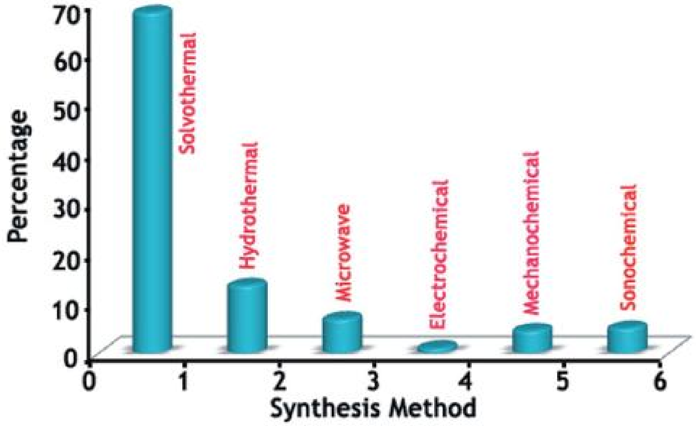

Figure 3 Indicative summary of the percentage of MOFs synthesized using the various preparation routes[8]

1.1.1 Solvothermal Synthesis

Solvothermal reactions (Fig. 4) are carried out in closed vessels under autogenous pressure above the boiling point of the solvent for the formation of new MOFs. Many starting materials can undergo quite unexpected chemical changes under solvothermal conditions, which are often accompanied by the formation of nanoscale morphologies that are not achievable by conventional methods. In most cases, high-boiling organic solvents have been used for solvothermal reactions. The most commonly used organic solvents are dimethylformamide, diethylformamide, acetonitrile, acetone, ethanol, and methanol. Mixtures of solvents have also been used to avoid problems of differing solubility for the different starting materials and products. Solvothermal reactions can be carried out in different temperature ranges, depending on the requirement of the reaction. Generally, glass vials are used for lower temperature reactions, while reactions performed at temperatures higher than ~400 K require Teflon-lined autoclaves.[22] The hydrothermal method (water as a solvent) has been used successfully for the synthesis of an enormous number of inorganic compounds and inorganic organic hybrid materials.[2, 8]

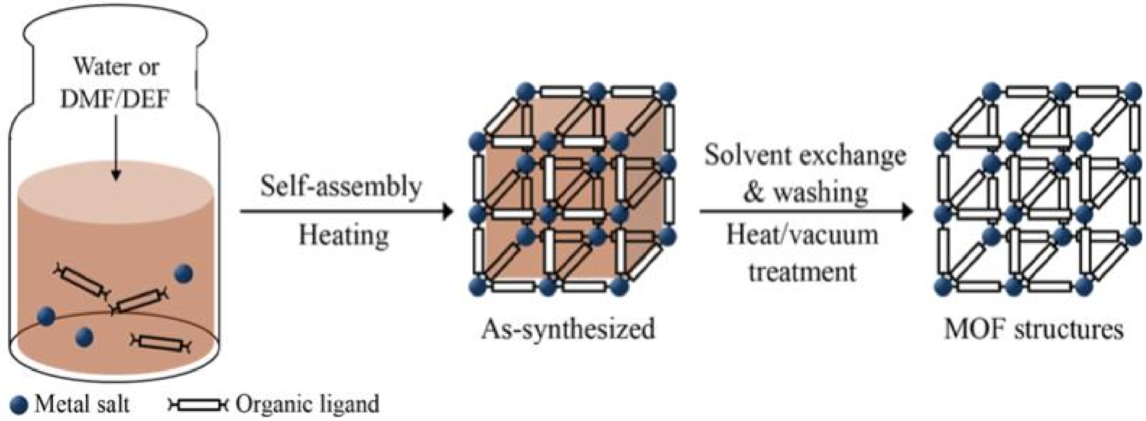

Figure 4 Conventional solvothermal synthesis of MOF structures[2]

1.1.2 Microwave-assisted Synthesis

Microwave synthesis techniques have been widely applied for rapid synthesis of nano porous materials under hydrothermal conditions. Besides fast crystallization, potential advantages of this technique include phase selectivity (selective synthesis of products with specific and distinctive crystal structure, les stable to hard, from the same reaction components), narrow particle size distribution (almost uniform crystal size), and facile morphology control.[23] Commercial microwave equipment provides adjustable power outputs and has a fiber optic temperature controller and pressure controller. In microwave synthesis, a substrate mixture in a suitable solvent is transferred to a Teflon vessel, sealed and placed in the microwave unit, and heated for the appropriate time at the set temperature (Fig. 5). The microwave approach, where an applied oscillating electric field is coupled with the permanent dipole moment of the molecules in the synthesis medium inducing molecular rotations results in rapid heating of the liquid phase.[2, 8] MW-assisted synthesis of MOFs has often been carried out at a temperature above 100°C with reaction times rarely exceeding one hour. Some reports describe the systematic variation of compositional and process parameters (solvent, irradiation time, reaction temperature, power level, molar ratio of the reactants, reactant concentration, etc.) in order to optimize the reaction conditions. In general, MW irradiation allows faster synthesis of smaller crystals compared to CE heating.[24]

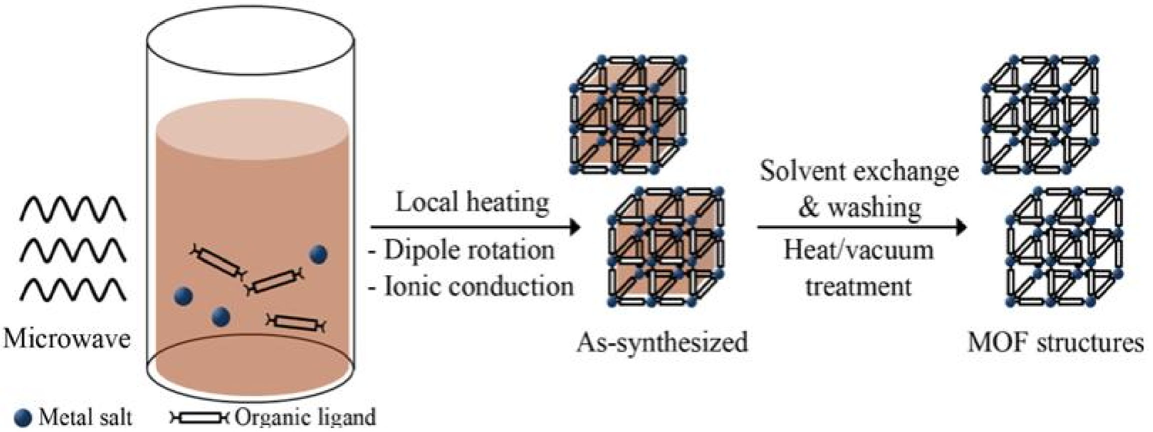

Figure 5 Microwave-assisted solvothermal synthesis of MOF structures[2]

1.1.3 Electrochemical Synthesis

The electrochemical synthesis of MOFs uses metal ions continuously supplied through anodic dissolution as a metal source instead of metal salts, which react with the dissolved linker molecules and a conducting salt in the reaction medium (Fig. 6). The metal deposition on the cathode is avoided by employing protic solvents, but in the process, hydrogen is generated. The electrochemical route is also possible to run a continuous process to obtain a higher solids content compared to normal batch reactions.[2, 8]

Researchers at BASF have performed the pioneering work and have established synthesis procedures for some Cu- and Zn-based MOFs. In their studies, various combinations of anode materials (Zn, Cu, Mg, Co) and linkers [1,3,5-H_3BTC, 1,2,3-H_3BTC, H_2BDC, and

H_2BDC- $(OH)_2$] as well as different experimental setups were reported, which also allowed the up-scaling of the syntheses. From these combinations, four Cu- or Zn-containing compounds with high porosity were obtained.[24] The HKUST-1 (HKUST= Hong Kong University of science and Technology) product was tested for its use in gas purification, i.e., removal of tetrahydrothiophene from natural gas, H_2 storage, and the separation of Kr-Xe mixtures.[25] This work was further extended to the chemistry of ZIFs.

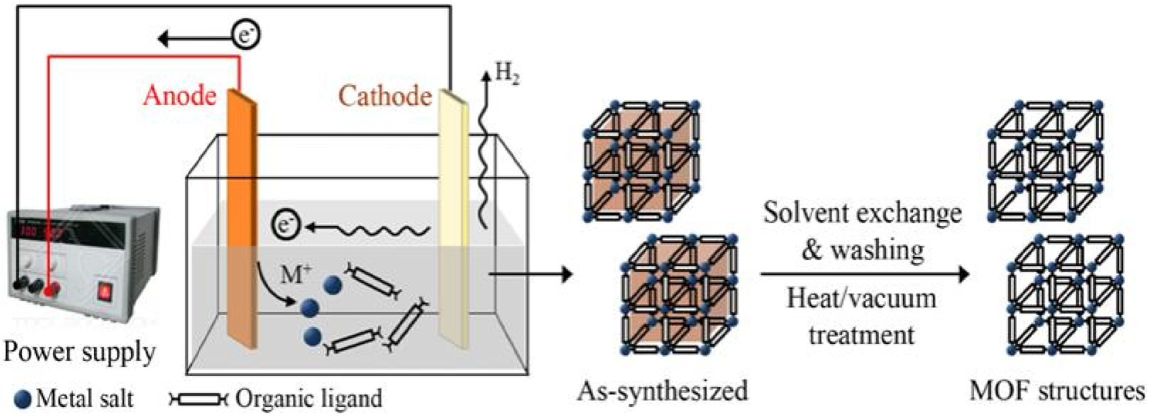

Figure 6 Electrochemical synthesis of MOF structures[2]

1.1.4 Mechanochemical Synthesis

Mechanical breakage of intramolecular bonds followed by a chemical transformation takes place in mechanochemical synthesis.[24] Mechanochemical reactions can occur at room temperature under solvent- free conditions, which is especially advantageous when organic solvents can be avoided. Quantitative yields of small MOF particles can be obtained in short reaction times, normally in the range of 10-60 min. In many occasions, metal oxides (Fig. 7 and 8) were found to be preferred over metal salts as starting materials, which result in water as the only side product. The critical contribution of moisture in mechanochemical synthesis of pillared type MOFs was recently reported by the Kitagawa group.[26]

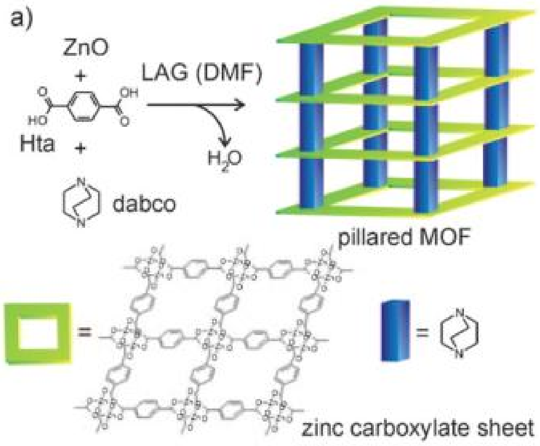

Figure 7 Ion- and liquid-assisted grinding (ILAG), in the construction of MOFs based on terephthalic acid (Hta)[12]

The addition of small amounts of solvents in liquid-assisted grinding (LAG) can lead to acceleration of mechanochemical reactions due to an increase of mobility of the reactants on a molecular level. The liquid can also work as a structure-directing agent. More recently, the extension of the method to ion- and liquid assisted grinding (ILAG) was reported to be highly efficient for the selective construction of pillared-layered MOFs.[12] However, mechanochemical synthesis is limited to specific MOF types only and large amounts of products is difficult to obtain.[2]

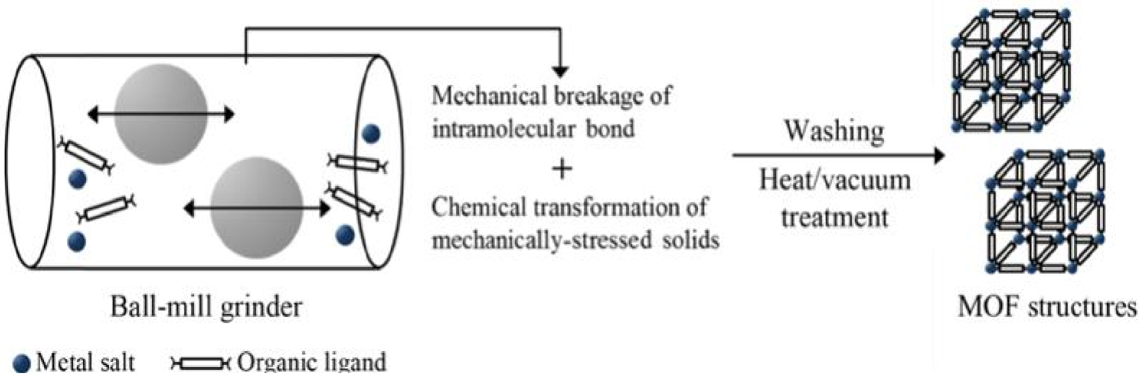

Figure 8 Mechanochemical synthesis of MOF structures[2]

1.1.5 Sonochemical Synthesis

Sonochemical methods via homogeneous and accelerated nucleation can also achieve a reduction in crystallization time than those by the conventional solvothermal synthesis. As shown in Fig. 9, a substrate solution mixture for a given MOF structure is introduced to a horn-type Pyrex reactor fitted to a sonicator bar with an adjustable power output without external cooling. Formation and collapse of bubbles formed in the solution after sonication (acoustic cavitation), produces very high local temperatures (~5,000 K) and pressures (~1,000 bar), and results in extremely fast heating and cooling rates (>1010K/s) producing fine crystallites. The primary goal of sonochemical synthesis in MOF science was to find a fast, energy-efficient, environmentally friendly, room temperature method that can be carried out easily. This is of special interest for their future application, since fast reactions could allow the scale up of MOFs. In addition, nanocrystalline particles, which are often obtained by sonochemical syntheses were also anticipated to be of advantage for their application. Systematic studies were carried out focusing on the role of reaction time and temperature, power level, and solvent. Short reaction times at ambient pressure were reported to lead to high yields of the desired product.[24, 27]

High-quality MOF-5 crystals in the 5-25 μm range were obtained within 30min by sonochemical synthesis using NMP (1-methyl-2-pyrrolidone) as the solvent. HKUST-1 was also prepared using DMF/EtOH/H_2O mixed-solution in an ultrasonic bath. The product formed after 5min as a nanocrystalline powder (10-40 nm), and increasing the reaction time led to larger crystals (50-200 nm) and higher yields, but further reaction resulted in their partial decomposition.[2]

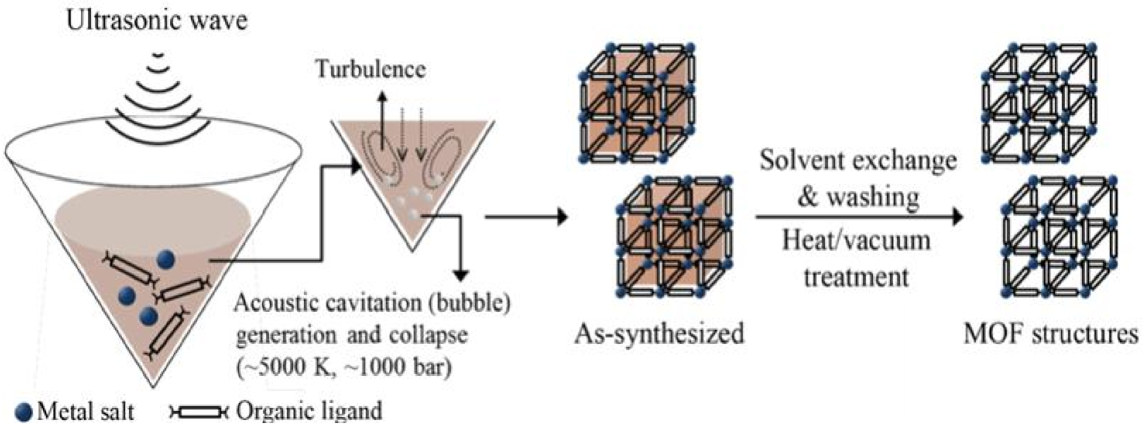

Figure 9 Sonochemical synthesis of MOFs structures[2]

1.1.6 Slow Evaporation Synthesis

The slow evaporation method is a conventional method to prepare MOFs, which mostly does not need any external energy supply. Although this method is sometimes preferred because it is a room-temperature process, its major disadvantage remains that it requires more time compared with other known conventional methods. In the slow evaporation method, a solution of the starting materials is concentrated by slow evaporation of the solvent at a fixed temperature, mostly at room temperature. Sometimes the process involves a mixture of solvents, which can increase the solubility of the reagents and can make the process faster by quicker evaporation of low-boiling solvents.[8, 28]

1.2 Applications of Metal-Organic Frameworks (MOFs)

1.2.1 Catalytic Transformations Within the Pores

The high surface areas, tunable pore metrics, and high density of active sites within the very open structures of MOFs offer many advantages in catalysis. MOFs can be used to support homogeneous catalysts, stabilize short-lived catalysts, perform size selectivity, and encapsulate catalysts within their pores.[29] The first example of catalysis in an extended framework, reported in 1994, involved the cyanosilylation of aldehydes in a Cd-based framework [$Cd(BPy)_2(NO_3)_2$; BPy = 4,4′-bipyridine] as a result of axial ligand removal.[30] This study also highlighted the benefits of MOFs as size-selective catalysts by excluding large substrates from the pores.

In 2006, it was shown that removal of solvent from HKUST-1 exposes open metal sites that may act as Lewis acid catalysts.[31] MIL-101 [$Cr_3X(H_2O)_2O(BDC)_3$; X= F, OH] and Mn-BTT have also been identified as Lewis acid catalysts in which the metal oxide unit functions as the catalytic site upon ligand removal. In addition, alkane and alkene oxidation, and oxidative coupling reactions have also been reported; they all rely on the metal sites within the SBUs for catalytic activity. The study of methane oxidation in vanadium-based MOF-48 is promising because the catalytic turnover and yield for this oxidation far exceed those of the analogous homogeneous catalysts. [32, 33]

One early example of the use of a MOF as a heterogeneous catalyst is PIZA-3, which contains a metalloporphyrin as part of the framework.[34] PIZA-3 is capable of hydroxylating alkanes and catalyzes the epoxidation of olefins. Schiff-base and binaphthyl metal complexes have also been incorporated into MOFs to achieve olefin epoxidation and diethyl zinc ($ZnEt_2$) additions to aromatic aldehydes, respectively. The incorporation of porphyrin units within the pores of MOFs can be accomplished during the synthesis (a “ship-in-a-bottle” approach that captures the units as the pores form), as illustrated for the zeolite-like MOF.[35] The pores of this framework accommodate high porphyrin loadings, and the pore aperture is small enough to prevent porphyrin from leaching out of the MOF.

The porphyrin metal sites were subsequently metallated and used for the oxidation of cyclohexane.

Integration of nanoparticles for catalysis by PSM (Post Synthetic Modification of Metal-Organic Frameworks) has been carried out to enhance particle stability or to produce uniform size distributions. Palladium nanoparticles were incorporated within MIL-101(Cr) for cross-coupling reactions. Most recently, a bifunctional catalytic MOF capable of water-splitting reactions was reported.[36] This MOF uses the organic linker and an encapsulated nanoparticle to transfer an electron to a proton in solution, leading to hydrogen evolution. A wide variety of MOFs have been designed with various transition metals as well as different poly-topic ligands and screened in heterogeneous catalysis of organic transformations but still there are hundreds of MOF materials that have not been explored for catalysis. Therefore, the use of MOFs in catalysis is extremely broad and increasing continuously.[37]

1.2.2 Photocatalysis

Photocatalysis is an environmentally-friendly technology to convert solar energy into chemical energy, such as photocatalytic splitting of water into H_2, photodegradation of organic molecules, and CO_2 photoreduction into solar fuels.[38] The application of MOFs in photocatalysis is emerging as an interesting topic. Compared with the traditional photocatalysts, the superiority of MOFs is based on their desirable topology and high surface area, which is beneficial for fast transport and good accommodation of guest molecules. Moreover, the band gap of MOFs is closely related to the HOMO–LUMO gap, which may be flexibly tuned through rational modification of the inorganic unit or the organic linker during synthetic procedures, thus the efficient light harvesting can be realized. [39] As per the Scopus database result in 2016, the number of published articles regarding MOFs is increasing very rapidly. The graphs in Fig. 10a and 10b reveal the number of papers published each year up to 2016.

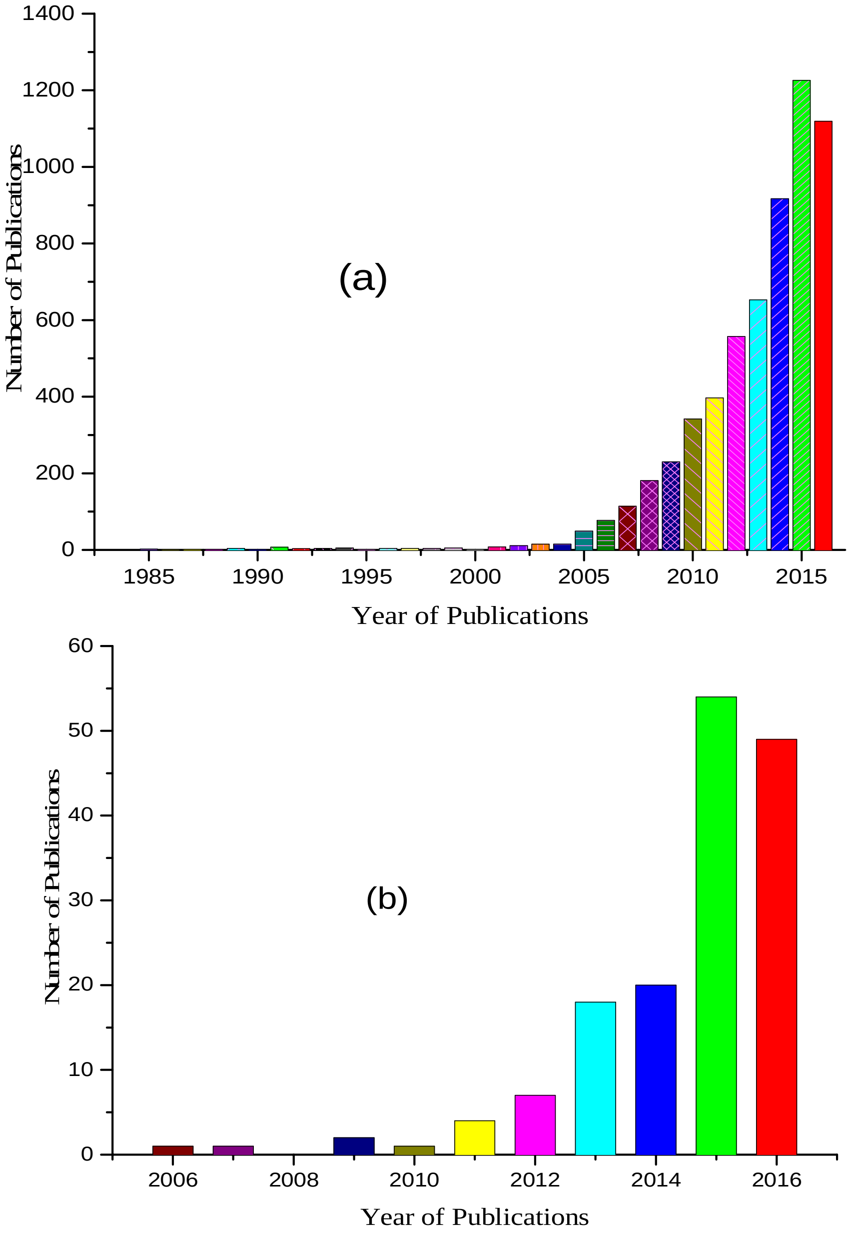

Figure 10 Number of publications regarding MOFs as a whole (a); MOFs papers published on Photocatalytic application only per year (b). https://www.scopus.com/results/results

In 2007, Alvaro *et al.* studied the photocatalytic properties of MOF-5 in the degradation of phenol in aqueous solution. Upon light excitation MOF-5 behaved as a semiconductor (Scheme 1) and passed through charge separation (electrons and holes) decaying in a microsecond time scale. The actual conduction band energy value was estimated to be 0.2 V versus NHE (Normal Hydrogen Electrode) with a band gap of 3.4 eV. Photoinduced electron transfer processes to viologen generates the corresponding viologen radical cation, while holes of MOF-5 oxidizes N,N,N',N'-tetramethyl-p-phenylenediamine.[10] Serre and Sanchez[9] synthesized the highly photon sensitive $Ti_8O_8(OH)_4(O_2C\text{-}C_6H_4\text{-}CO_2)_6$ (MIL-125(Ti)) in a solvent mixture of dimethylformamide (DMF) and methanol, and titanium tetraisopropoxide as a precursor in 2009. The results revealed that the reduction of Ti center and oxidation of adsorbed alcohol occur simultaneously over MIL-125(Ti) under UV-visible light irradiation, implying this MIL-125(Ti) is a potential stable photocatalyst (Scheme 2).

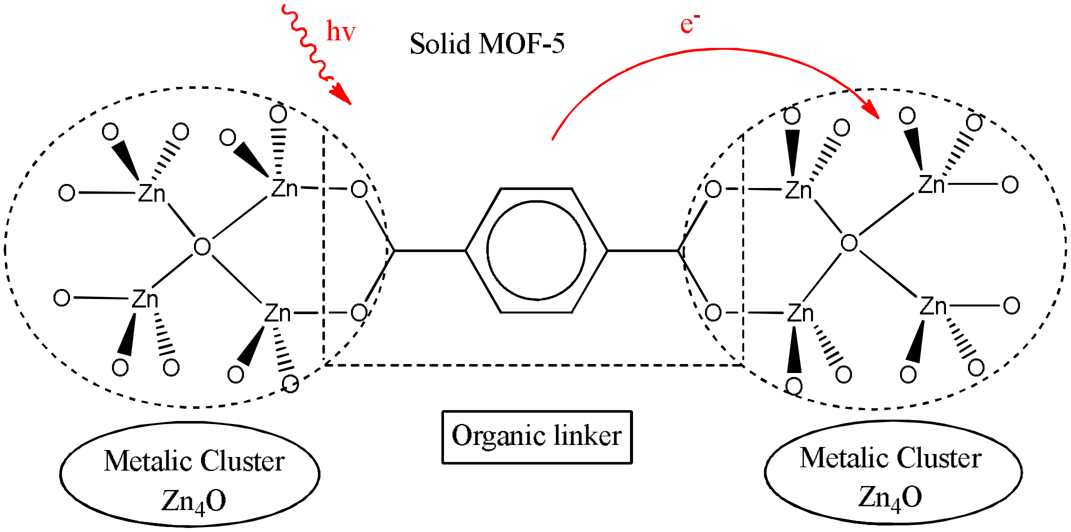

Scheme 1 Photophysical processes that occur after the irradiation of the MOF-5 solid material containing the terephthalate unit and Zn^{2+} [10]

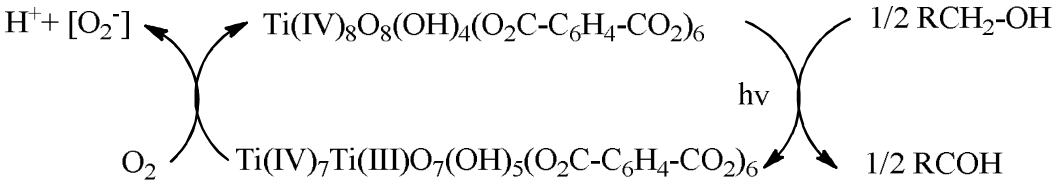

Scheme 2 Proposed mechanism for the reduction of MIL-125 in the presence of alcohols under UV radiation[9]

The iron(III)-based MOFs photocatalysts reported for the first time by Larurier *et al.* [40] could photodegrade Rhodamine 6G in aqueous solution under visible light irradiation in which the Fe-O cluster itself in the iron(III)-based MOFs (including MIL-101(Fe) and MIL-88(Fe)) could act as a semiconductor to absorb visible light and then induce the whole photocatalytic reaction, and the organic linkers facilitate the charge separation. Due to their superior framework topology and well-ordered porous structure in addition to the amenable organic linker/metal clusters, MOFs based photocatalysts are emerging as interesting materials.

A bifunctional photocatalyst-Fe-benzenedicarboxylate (MIL-53(Fe)) was synthesized successfully by Liang *et al.* [11] via a facile solvothermal method. The resulting MIL-53(Fe) photocatalyst exhibited an excellent visible light ($\lambda \geq 420$ nm) photocatalytic activity for the reduction of Cr(VI) to Cr(III) as shown in Scheme 3. The reduction rate has reached about 100% after 40 min of visible light irradiation, which has been more efficient than that of N-doped TiO_2 (85%) under identical experimental conditions.

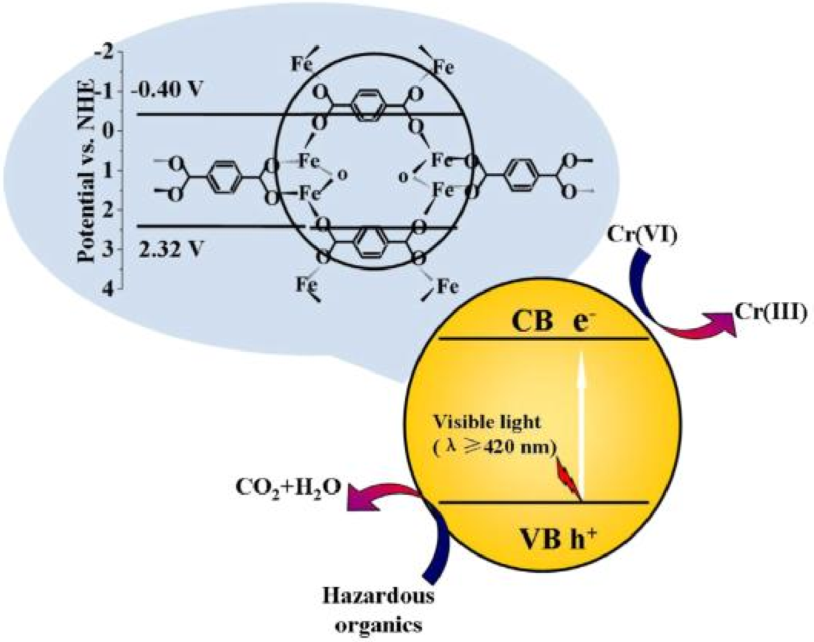

Scheme 3 A schematic illustration of simultaneous reduction of Cr (VI) and oxidation of dyes over MIL-53(Fe) under visible light irradiation.[11]

In 2016, Nasalevich *et al.*[41] focused on the electronic properties of NH_2-MIL-125(Ti), NH_2-UiO-66(Zr) and NH_2-UiO- 66(Hf) and their influence on the photocatalytic performance in hydrogen evolution reaction (HER). They also found out that LMCT (linker to metal charge transfer) excited state of NH_2-MIL-125(Ti) has a superior lifetime as compared to the organic-based states of the UiOs. The design of MOF for photocatalysis should focus on developing sufficiently long excited state lifetimes, thus improving catalytic activity.

Fe-based metal-organic frameworks (MOFs) including MIL-101(Fe), MIL-100(Fe), MIL-3(Fe), and MIL-88B(Fe) were prepared by Li. *et al.* via a facile solvothermal process and introduced as both adsorbents and catalysts to generate powerful radicals from persulfate for acid orange 7 (AO7) removal in aqueous solution.[42] The results showed that the ability of the materials in the combination of adsorption and degradation was in the order MIL-101(Fe) >MIL-100(Fe) > MIL-53(Fe) > MIL-88B(Fe), was closely related to the activity of metal ion in active site of the catalyst and the different cage dimension. The reactive species in MILs/persulfate system were identified as sulfate radicals and hydroxyl radicals.

The photocatalytic reduction of Cr(VI) was investigated by Shi. *et al.* over iron(III)-based metal–organic frameworks (MOFs) structured as MIL-88B. It is found that MIL-88B (Fe) MOFs, containing Fe_3-μ_3-oxo clusters, can be used as photocatalyst for the reduction of Cr(VI) under visible light irradiation, which is due to the direct excitation of Fe_3-μ_3-oxo clusters. The amine-functionalized MIL-88B(Fe) MOFs (denoted as NH_2–MIL-88B(Fe)) showed much higher efficiency for the photocatalytic Cr(VI) reduction under visible-light irradiation compared with MIL-88B (Fe). It was revealed that in addition to the direct excitation of Fe_3-μ_3-oxoclusters, the amine functionality in NH_2–MIL-88B(Fe) could be excited subsequent transfer of an electron to Fe_3-μ_3-oxo clusters, thus enhancing the photocatalytic activity for Cr(VI) reduction. The enhanced photocatalytic activity for Cr(VI) reduction is also achieved for two other amine-functionalized iron(III)-based MOFs (NH_2–MIL-53(Fe) and NH_2–MIL-101(Fe)).[43]

In 2013, Gao. *et al* reported a new Ti(IV)-based porous metal–organic framework (NTU-9), which displayed strong absorption in the visible region with a bandgap of 1.72 eV. The electronic structure and band gap were further investigated by DFT calculations. Photoelectrochemical studies indicated that NTU-9 was photoactive under visible light illumination (λ > 400 nm) and behaved as a p-type semiconductor. The results demonstrated that Ti(IV)-based MOFs could be promising visible-light photocatalysts for energy conversion and environmental remediation.[44]

1.2.3 Gas Adsorption for Alternative Fuels and Separations for Clean Air

1.2.3.4 Hydrogen adsorption

Much attention is being paid to increasing the storage of fuel gases such as hydrogen and methane under practical conditions. The first study of hydrogen adsorption was reported in 2003 for MOF-5.[45] This study confirmed the potential of MOFs for application to hydrogen adsorption, which has led to the reporting of hydrogen adsorption data for hundreds of MOFs.[46] In general, the functionality of organic linkers has little influence on hydrogen adsorption[47], whereas increasing the pore volume and surface area of MOFs markedly enhances the gravimetric hydrogen uptake at 77 K and high pressure, as exemplified by the low-density materials: NU-100 and MOF-210 exhibit hydrogen adsorption as high as 7.9 to 9.0 weight percent (wt%) at 56 bar for both MOFs and 15wt% at 80 bar for MOF-210.[48, 49]However, increasing the surface area is not always an effective tool for increasing the volumetric hydrogen adsorption, which can be accomplished by increasing the adsorption enthalpy of hydrogen (Q_{st}).[50]

1.2.3.5 Methane adsorption

An alternative high-density fuel source to hydrogen and gasoline is natural gas (methane). The first study of high-pressure methane adsorption in an extended metal-organic structure was reported in 2000 for $CuSiF_6(BPy)_2$,[51] which demonstrated an uptake capacity of 104 mg/g at 36 atm and 298 K. As is the case for hydrogen adsorption, the total gravimetric methane uptake capacity is generally proportional to the pore volume of MOFs. The calculated total uptake values for MOF-177, MOF-200, and MOF-210 are 345 mg/g, 446 mg/g, and 476 mg/g, respectively, at 80 bar and 298 K. These values are much greater than those of any other MOF. The amount of methane stored in a vessel filled with one of these MOFs is at least double the amount that could be stored in an empty vessel at room temperature and pressures up to 80 bar.[48] This technology is now being commercialized by BASF for automobile fueling.

1.2.3.6 Carbon dioxide adsorption

MOFs also offer reversible carbon dioxide adsorption and are promising materials for the selective capture of carbon dioxide from the atmosphere and flue gas. Carbon dioxide adsorption in MOFs was first reported in 1998 for MOF-2 [Zn(BDC)].[52] As expected, the best carbon dioxide uptake reported to date was observed in a MOF with ultrahigh porosity, MOF-200 (2437 mg/g at 50 bar and 298 K).[48] In practical terms, a gas tank filled with MOF-177 or MOF-200 would store 9 times or 17 times as much carbon dioxide at 35 bar, respectively, as the corresponding pressurized tank without MOF. On the other hand, many carbon dioxide capture applications will operate at low pressure so that the Henry's law constant (i.e., initial slope of the isotherm) can be used as an indicator of the carbon dioxide selectivity. MOFs with open metal sites were found to have desirable high initial Q_{st} values of 62 kJ/mol and 47 kJ/mol for MIL-101(Cr) and Mg-MOF-74, respectively[53, 54], thereby offering enhanced carbon dioxide uptake and selectivity at low pressures. Basic nitrogen centers have also been post synthetically added to MOFs with open metal sites by using N,N′-dimethylethylenediamine (DMEN), where the highest initial Q_{st} for $H_3[(Cu_4Cl)_3(BTTri)_8(DMEN)_{12}]$ [$BTTri^{3-}$= 4,4′,4″-(benzene- 1,3,5-triyl)tris(1,2,3-triazol-1-ide)] is estimated to be 96 kJ/mol.[55] An ideal material for carbon dioxide capture from fuel and combustion gases requires high selectivity in the presence of water, it is useful to target MOFs in which the competition between carbon dioxide and water for adsorption is minimized. In this respect, chemical binding of carbon dioxide in a recent MOF synthesized to make organic carbonates reversibly is a promising approach.[56]

1.2.3.7 Gas Separation

Gas storage experiments on MOFs have also been extended to the separation of hydrocarbons, toxic molecules (e.g., ammonia and chlorine), and water. For instance, $Cu_2(PZDC)_2(Pyz)$ (PZDC = pyrazine-2,3-dicarboxylate; Pyz = pyrazine) selectively takes up acetylene over carbon dioxide through hydrogen bonding between acetylene and oxygen atoms on the MOF internal surface.[57] Ammonia was previously considered to be too reactive for MOFs; however, chemically stable Zr-MOFs, such as UiO-66-NH_2 $[Zr_6O_4(OH)_4(BDC\text{-}NH_2)_6]$ and other derivatives, maintain their structures after the process of ammonia adsorption and desorption.[58] Gas separation processes in MOFs generally rely on both the size of the pores and the affinity of MOFs for the targeted gases.

1.2.4 Magnetic properties of MOFs

The magnetic properties such as ferromagnetism, antiferromagnetism, and ferrimagnetism of poly-metallic systems derive from the cooperative exchange interactions between the paramagnetic metal ions or organic radicals through diamagnetic bridging entities. Therefore, their magnetic behaviors depend on the intrinsic nature of both the metal and the organic ligand as well as the particular level of organization created by the metal–ligand coordination interaction. As a result, in pursuing the magnetism of MOFs, the ligand design is crucial both to organize the paramagnetic metal ions in a desired topology and to efficiently transmit exchange interactions between the metal ions in a controlled manner. The formation of a bulk material with non- zero spin requires a framework that allows for parallel coupling of the spins of neighboring paramagnetic spin carriers or antiparallel coupling of unequal spins. Canted spin orientations may also result. It should be pointed out that there is always a tendency for antiparallel coupling of spins because the state of low-spin multiplicity is often more stable than the state of high-spin multiplicity. [59, 60] Magnetic studies of MOFs are embedded in the area of molecular magnets and the design of low-dimensional magnetic materials, magnetic sensors, and multifunctional materials. Indeed, closed-shell organic ligands that are typically used in MOFs mostly give rise to only weak magnetic interactions. In order to achieve a strong coupling between the metal centers, short oxo, cyano, or azido bridges are needed. [61]

1.2.5 Luminescence and Sensors in MOFs

Luminescence MOFs (LMOFs) have been widely explored in many sensory applications due to their unique ability to selectively capture analyte molecules. Their permanent porosity often serves as a powerful platform for the reversible adsorption and release of these molecules. Therefore, LMOF based sensors can be highly recyclable and economically effective. LMOFs have been proven to be successful in the detection of volatile organic compounds, small molecules, and ionic species. The thermochromic properties of some LMOFs have led to the discovery of luminescent thermometers. In addition, the versatile functionalities of LMOFs make them extremely useful in the biological realm, exemplified by bio-sensing and bio-imaging. Another sphere of luminescence-based sensing application is the detection of energetic materials, such as explosives and explosive-like molecules. [62-64]

1.2.6 Drug Storage and Delivery in MOFs

One of the most important challenges in drug delivery research is the efficient delivery of drugs in the body using nontoxic nanocarriers. Some of the requirements for an efficient therapy with nanocarriers are to (1) control the release and avoid the "burst effect", (2) control matrix degradation and engineer its surface, (3) be detectable by various imaging techniques, (4) efficiently entrap drugs with high loading capacity. In addition to these requirements, toxicity and biocompatibility are the two other important criteria related to the material considered as a potential novel drug carrier. For example, some metals are known to be highly toxic, yet they still exist in appreciable amounts in the body.[65]

MOFs can be regarded as optimal drug delivery materials (Scheme 4) due to the possibility of adjusting the framework's functional groups and tuning of the pore size. Even though the major interest in MOFs has been in the area of high-density gas storage for potential use in separations, fuel cells, and other energy-related applications, recent reports suggest that MOFs may have a significant role in drug delivery. The ability to engineer controlled localized delivery of drugs might both contribute to the efficiency of the treatment and reduce side effects.[4]

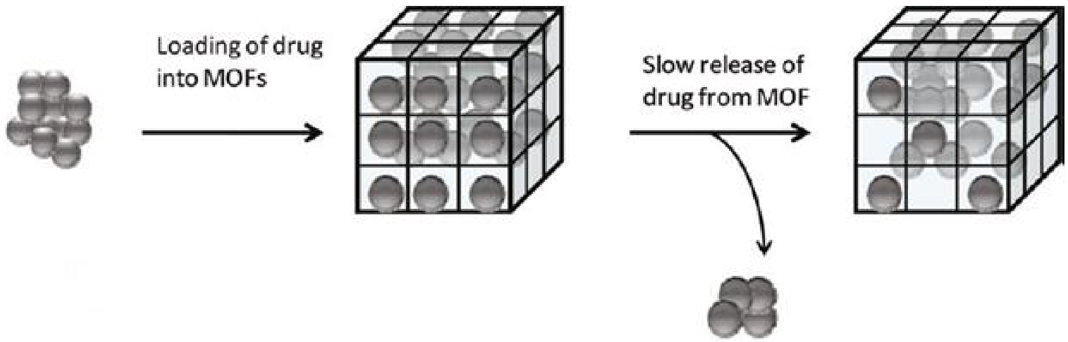

Scheme 4 Generalized scheme for the use of MOFs as drug delivery vehicles.[4]

1.3 Formulation of Research Gaps

Majority of the MOFs being synthesized nowadays are in a solvothermal approach using high boiling solvents like DMF and DEF which are also more toxic in nature. The reaction takes about 96 h at a minimum temperature of 120 ^{o}C. This approach is time taking and power consuming. High temperatures over long period of time is actually promote the decomposition of DMF into basic products which could deprotonate the carboxylic acids functions and bind the metal centers. The guest solvents (DMF: bp= 156 ^{o}C) do not easily evacuate from the MOFs structure after the end of the reaction at low temperature. Endeavor to evacuate the solvents at higher temperature might sometime lead to collapse of the framework.

In the present investigation salt form a dicarboxylic acid linker (instead of the acid form) in aqueous medium coupled with a linear nitrogen containing bipyridine pillar in methanol and a metal center were included in designing pillared-layer MOFs. The dicarboxylate linker is fast to bind to the metal center when compared to the dicarboxylic acid at room temperature. The solvents, water and methanol, are less toxic compared to DMF and can easily be evacuated from the framework structure at lower temperature. The incorporation of nitrogen containing pillar in the MOFs structure increases the water stability of the MOFs as the N-containing units have higher pKa value than water.

Polluted water out flows from textile industries are responsible for the hazardous situations, challenging the safety of human, animal and plant population. Literature survey revealed, this could be due to release of different dyes during coloring of fabrics. Dyes whose concentrations are higher than 1 ppm are toxic when degraded to aromatic amine.

Evaluation of the photocatalytic performance of MOFs towards the degradation of these is a relevant exercise. Researchers are synthesizing and studying the crystal structures of a large number of MOFs, but are not adequately focusing attention on worthwhile applications such as photocatalytic performance. The current study aims to fill this gap by making some selective and systematic photocatalytic studies on the new MOF material.

1.4 Significance of the Study

The emission of effluents from textile industries has been a major concern of the modern world, due to the great pollution that these effluents promote on the water resources.[66] Textile wastewater is an amalgam of pollutants but mainly it is characterized by high levels of Chemical Oxygen Demand (COD), Biological Oxygen Demand (BOD), dissolved solids and colors. During the dyeing operation a significant amount of dyes remain unfixed on the fabric and they are directly discharged into the water bodies.[67]

Dye concentrations higher than 1 mg/L caused by the direct discharges of textile effluents, give color to the water body and are easily visualized by naked eye. High concentrations of textile dyes in water bodies stop the reoxygenation capacity of the receiving water and cutoff sunlight, thereby upsetting biological activity in aquatic life and also the photosynthesis process of aquatic plants or algae.[68]

Due to their synthetic nature and aromatic structure, most dyes are non-biodegradable, having carcinogenic action or causing allergies, dermatitis, skin irritation or different tissular changes. Various azo dyes show both acute and chronic toxicity, causing high potential health risk due to their adsorption and breakdown toxic amines through the gastrointestinal tract, skin, lungs. They also form hemoglobin adducts and disturb blood formation. LD_{50} values reported for aromatic azo dyes range between 100 and 2000 mg/kg body weight.

Typical conventional porous materials such as zeolites, silica and carbon have low BET surface areas and low capacity to adsorb large amount of dyes at once. Being a highly porous material with Langmuir surface area approaching 10,000 m^2g^{-1}, metal–organic frameworks (MOFs) having semiconducting can adsorb and degrade organic textile effluent dyes in to less toxic substances when exposed to light of appropriate frequency. Literature survey reveals that exploration, innovations and applications in this field of research need more attention.

In this PhD research project, it is aimed to investigate photocatalytic MOFs for wastewater treatment in the textile industrial effluent. The motivation in this regard is the observation of colored/ polluted wastewater near most textile industries in Ethiopia, which is hazardous situation. This relates to discharged organic dyes in the effluents.

Thus, finding a facile way to design and synthesize novel MOFs with excellent stability and application may make great contribution towards the development of efficient effluent treatment methodology while catering to the needs of a healthy community.

Therefore, in this research project, it is aimed to design and synthesize stable MOFs and study their properties as possible applicants to adsorb and degrade textile effluent dyes into harmless substances so that the people in the vicinity of textile industries will not suffer a lot from the effluents when the catalyst is produced in large scale.

1.5Aims and Objectives of the Study

1.5.1 General Objectives

- To synthesize and characterize pillared-layer metal-organic frameworks (MOFs)
- To investigate their possible application in the adsorption and photocatalytic degradation of dyes in textile wastewater effluents.

1.5.2 Specific Objectives

- To synthesize MOFs using transition metal salts, mixed N-heterocyclic and di-carboxylic linkers
- To characterize the MOFs using elemental analysis, N_2 adsorption-desorption, XRD, SEM and TGA studies; and FT-IR and UV-Vis spectroscopy.
- To carry out band gap measurement of MOFs for selective application in photocatalysis.
- To apply the MOFs in photocatalytic degradation of toxic organic dyes in textile wastewater effluents using UV and Visible light photoreactors.
- To evaluate the crystallin stability of the MOFs used in the degradation of dyes

CHAPTER TWO

MOFs Characterization Techniques

The characterization techniques used in the present study are briefly discussed. They are X-ray diffraction (XRD), Fourier Transform Infrared Spectroscopy (FT-IR), Thermogravimetric Analysis (TGA), N_2-Sorption, Scanning Electron Microscopy (SEM), and Diffuse Reflectance UV-Vis Spectroscopy.

2.1 X-Ray Diffraction (XRD)

XRD analysis has a wide range of applications in material science, chemistry, geology, environmental science, forensic science, and the pharmaceutical industry for characterizing materials. Amorphous materials are readily recognized by the absence of peaks in an XRD pattern. The technique is also used for studying particles in liquid suspensions or polycrystalline solids (bulk or thin film materials). Other applications of XRD analysis include determination of phase transitions in a given substance, semi-quantitative determination of phases present in a sample, measurement of crystallite size particularly in nano materials, analysis of stress and crystal structure analysis by Rietveld refinement.

The three-dimensional structure of crystalline materials is defined by regular, repeating planes of atoms that form a crystal lattice. When a focused X-ray beam interacts with these planes of atoms, part of the beam is transmitted, part is absorbed by the sample, part is refracted and scattered, and part is diffracted. Diffraction of an X-ray beam by a crystalline solid is analogous to diffraction of light by droplets of water, producing the familiar rainbow. X-rays are diffracted by each mineral differently, depending on what atoms make up the crystal lattice and how these atoms are arranged. When an X-ray beam hits a sample and is diffracted, we can measure the distances between the planes of the atoms that constitute the sample by applying Bragg's Law (Fig. 11), named after William Lawrence Bragg, who first proposed it in 1921. Bragg's Law is: ***$n\lambda = 2d \sin\theta$***, where the integer *n* is the order of the diffracted beam, λ is the wavelength of the incident X-ray beam, *d* is the distance between adjacent planes of atoms (the *d*-spacings), and *θ* is the angle of incidence of the X-ray beam. Since we know and we can measure λ, we can calculate the *d*-spacings. The geometry of an XRD unit is designed to accommodate this measurement. The characteristic set of *d*-spacings generated in a typical X-ray scan provides a unique "fingerprint" of the mineral or minerals present in the sample. When properly interpreted, by comparison with standard reference patterns and measurements, this "fingerprint" allows for identification of the material.

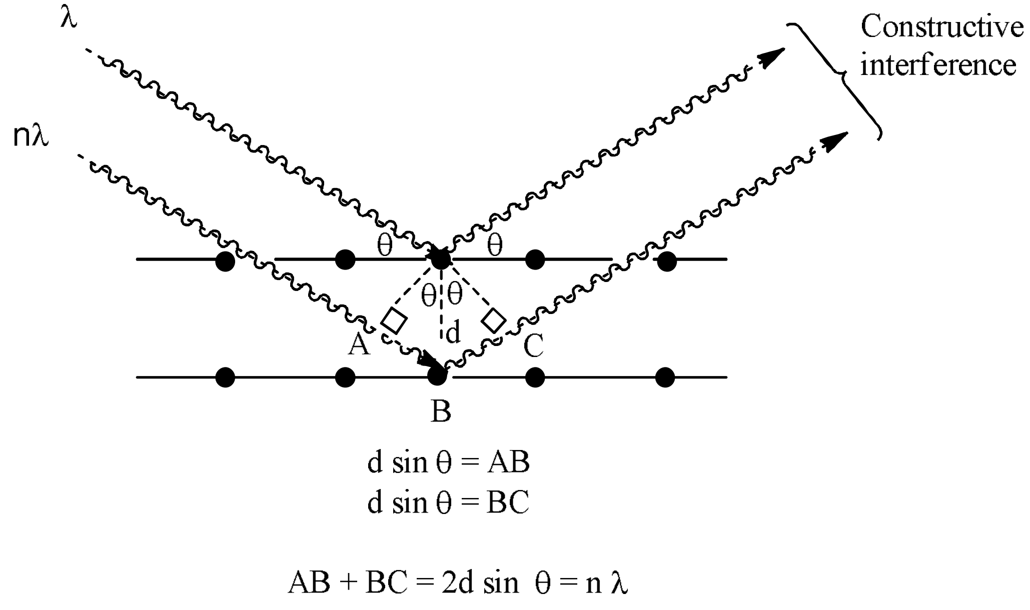

Figure 11 Bragg's Law, which governs the conditions required for the constructive interference of waves[1]

In X-ray powder diffractometry, X-rays are generated within a sealed tube that is under vacuum. A current is applied that heats a filament within the tube; the higher the current the greater the number of electrons emitted from the filament. This generation of electrons is analogous to the production of electrons in a television picture tube. A high voltage, typically 15-60 kilovolts, is applied within the tube. This high voltage accelerates the electrons, which then hit a target, commonly made of copper. When these electrons hit the target, X-rays are produced. The wavelength of these X-rays is characteristic of that target. These X-rays are collimated and directed onto the sample, which has been ground to a fine powder (typically to produce particle sizes of less than 10 microns). A detector detects the X-ray signal; the signal is then processed either by a microprocessor or electronically, converting the signal to a count rate. Changing the angle between the X-ray source, the sample, and the detector at a controlled rate between preset limits is an X-ray scan. The detector records the angles at which the families of lattice planes scatter (diffract) the x-ray beams and the intensities of the diffracted x-ray beams. The detector is scanned around the sample along a circle, in order to collect all the diffracted X-ray beams. The angular positions (2θ) and intensities of the diffracted peaks of radiation (*reflections or peaks*) produce a two-dimensional pattern. Each reflection represents the x-ray beam diffracted by a family of lattice planes (*hkl)*. This pattern is characteristic of the material analyzed (fingerprint).[1] The crystallinity of MOFs were characterized by PXRD (PANalytical X'pert MPD) with Cu K_α radiation (λ= 1.54178 Å) at a scanning rate of 0.001557 $^{o}sec^{-1}$.

2.2 Thermogravimetric Analysis (TGA)

In thermogravimetric analysis (TGA), the change in mass of a sample is monitored as the sample is heated. More generally, TGA is used to investigate the thermal degradation of inorganic compounds or polymers or the gas uptake of a solid. TGA instrument is able to simultaneously heat (at a constant rate) and record the mass of a sample. Samples are usually heated in air or N_2, or in an atmosphere of a reactive gas (e.g. H_2) for studying the uptake of a particular gas.[69] Thermogravimetric measurements of the MOFs under study were carried out using TGA Q500 (TA Instruments) with Ar flow rate of 10 mL min^{-1}.

2.3 N_2-Sorption

Gas adsorption is of major importance for the characterization of a wide range of porous materials. Of all the gases and vapors, which are readily available and could be used for the adsorption studies, nitrogen has remained universally pre-eminent. With the aid of user-friendly commercial equipment and on-line data processing, it is now possible to use nitrogen adsorption at 77 K for both routine quality control and the investigation of new materials.[70]

An Adsorption isotherm is obtained by measuring the amount of gas adsorbed across a wide range of relative pressures at a constant temperature (typically liquid N_2, 77K). Conversely desorption isotherms are achieved by measuring gas removed as pressure is reduced. The majority of physisorption isotherms could be grouped into the six types as per the 1985 IUPAC recommendations. In 2015, IUPAC has refined the original classifications of physisorption isotherms in to eight types (Fig. 12) and associated hysteresis loops.[3] A more gradual curvature (i.e., a less distinctive point B) in type II isotherm is an indication of a significant amount of overlap of monolayer coverage and the onset of multilayer adsorption in non-porous or macroporous adsorbents.

Adsorption isotherms are classified as based on the strength of the interaction between the

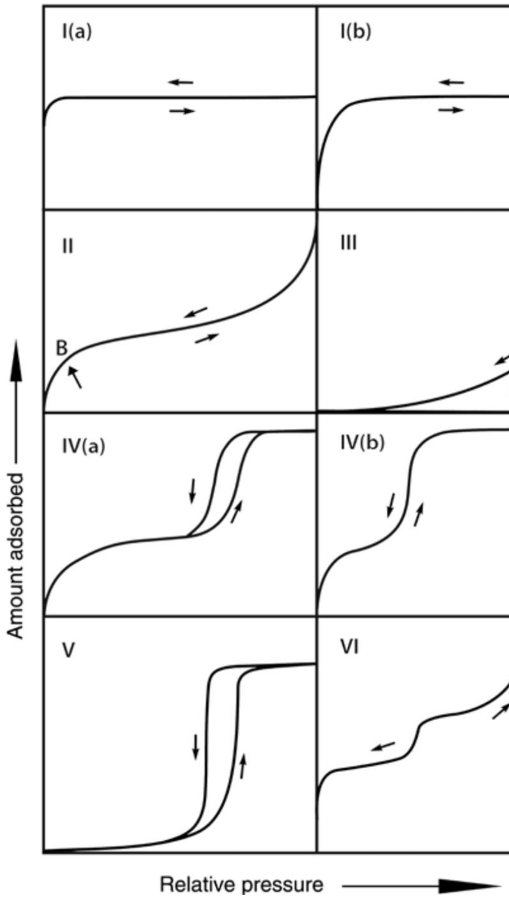

Figure 12 Classification of physisorption isotherms[3]

sample surface and adsorptive, and the existence or absence of pores (Table 1). However, some adsorption measurements do not fit into any of the adsorption isotherm types I to IV. These may be classified as mixed types of adsorption isotherms. For example, nitrogen adsorption for a porous sample with large external surface area may generate a compound isotherm resembling types I and II, or types I and IV. To analyze an adsorption isotherm, one has to assume certain sample features, such as the pores from the shape of the isotherm and analyze them using an appropriate analysis method such as determination of the pore diameter from porosity distribution curve using NLDFT (Non- Local Density Functional Theory). The IUPAC classification of pore diameter for a micropore, mesopore, and macropore materials are up to 2 nm, 2 to 50 nm, and 50 nm or up, respectively.

Table 1 features of adsorption isotherms

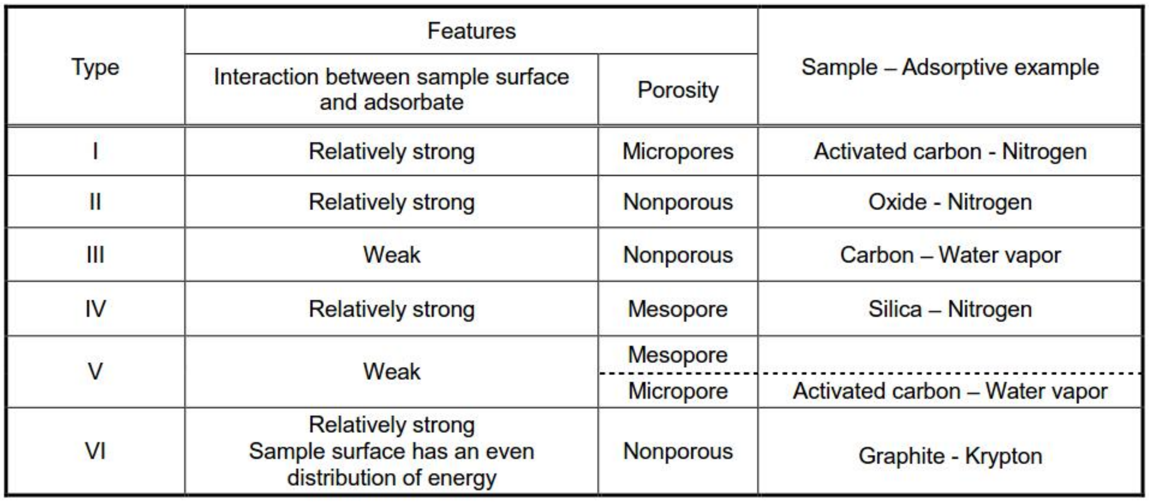

Type	Features		Sample – Adsorptive example
	Interaction between sample surface and adsorbate	Porosity	
I	Relatively strong	Micropores	Activated carbon - Nitrogen
II	Relatively strong	Nonporous	Oxide - Nitrogen
III	Weak	Nonporous	Carbon – Water vapor
IV	Relatively strong	Mesopore	Silica – Nitrogen
V	Weak	Mesopore	
		Micropore	Activated carbon – Water vapor
VI	Relatively strong Sample surface has an even distribution of energy	Nonporous	Graphite - Krypton

Nitrogen adsorption-desorption isotherms in this study were measured using Micromeritics-Smart Vac Prep System with Micromeritics 3Flex Surface Characterization Analyzer. The instrument gives information about the pore size, pore volume and surface area of the material.

2.4 Scanning Electron Microscopy (SEM)

Scanning Electron Microscopy (SEM) provides high-resolution and long-depth-of-field images of the sample near the surface. SEM is one of the most widely used analytical tools, due to the extremely detailed images it can quickly provide. Coupled to an auxiliary Energy Dispersive X-ray Spectroscopy (EDS) detector, SEM also offers elemental identification of nearly the entire periodic table. Applications include failure analysis, dimensional analysis, process characterization, reverse engineering, and particle identification.[1] The morphologies and EDS of the MOFs in this study were characterized by FEI Quanta 650 ESEM equipped with Oxford Instruments X-Max 150 mm^2 EDS detector with AZtec software at 20kV, spot 3-4, using low vacuum x-ray cone accessory at 80Pa.

2.5 UV-Vis Diffuse Reflectance Spectroscopy

Diffuse reflectance measurement gives a spectrum in percent reflectance vs wavelength plot for powders. The reflectance spectrum is obtained by collection and analysis of surface-reflected electromagnetic radiation from a so-called mat or dull surfaces textured like powders. The reflectance data obtained from the instrument can be processed to give a Tauc plot which is characterized by having Kubelka-Munk function in the y-axis and energy (eV) in the X-axis. The optical edges or gaps can be inferred by linear extrapolation of the absorbance from the high slope region of the Tauc plot or Kubelka-Munk function ($(\alpha h\nu)^n$) versus $h\nu$ plot.[71] Where: α = absorptive coefficient usually expressed as $(1-R_\infty)^2/2R_\infty$, h = planks constant, R_∞ = diffuse reflectance, and ν = frequency. The determination of band gaps in materials is important to obtain the basic solid-state physics. Band gap indicates the difference in energy between the top of the valence band filled with electrons and the bottom of the conduction band devoid of electrons. The band gap is related to the electric conductivity of the materials. There is generally no band gap in metals, but the band gap value in insulators is known to be large, and that in semiconductors is typically intermediate between these two. UV-visible diffuse reflectance spectra for the band gap determination in this research were run using Cary 5000 UV-Vis-NIR spectrometer.

2.6 Magnetic Susceptibility Measurements

MSB Auto, Sherwood scientific instrument generates gram susceptibility, χ_g, data for a given paramagnetic substance. The following calculations were made to arrive at the magnetic moments, μ_{eff}.

a) $\chi_M = \chi_g \times M$

b) $\chi'_M = \chi_M - \chi^{dia}$

c) $\mu_{eff}\,(magnetic \quad moment) = \sqrt{8 \times \chi'_m \times T} \;\; = \sqrt{n(n+2)}$

Where: χ_M = molar magnetic susceptibility

χ_g = gram magnetic susceptibility

M = molecular weight of the MOFs

χ'_M = corrected molar magnetic susceptibility

χ^{dia} = diamagnetic corrections for the ligand atoms and the inner core electrons of the metal

μ_{eff} = effective (spin only) magnetic moment

T = temperature in Kelvin

n = number of unpaired electrons

2.7 Summary of Instruments Used in this Study

The crystallinity of MOFs was characterized by PXRD (PANalytical X'pert MPD) with Cu K_α radiation (λ= 1.54178 Å) at a scanning rate of $0.001557^o sec^{-1}$. The morphologies and EDX were characterized by FEI Quanta 650 ESEM equipped with Oxford Instruments X-Max 150 mm^2 EDS detector with AZtec software at 20kV, spot 3-4, using low vacuum x-ray cone accessory at 80Pa. Nitrogen adsorption-desorption isotherms were measured using Micromeritics-Smart Vac Prep System with Micromeritics 3Flex Surface Characterization Analyzer. The FT-IR spectra were recorded using a PerkinElmer Spectrum 65 FT-IR Spectrometer. Thermogravimetric measurements were carried out using TGA Q500 (TA Instruments) with an Ar flow rate of 10 ml min^{-1}. Micro elemental analysis measurement of the MOFs samples was carried out by EA 1112 Flash CHNS/O-analyser (carrier gas flow rate of 120 ml/min, reference flow rate 100 ml/min, oxygen flow rate 250 ml/min; furnace temperature of 900 °C and oven temperature of 75 °C). UV-visible diffuse reflectance spectra for the band gap determination were run using Cary 5000 UV-Vis-NIR spectrometer. The photocatalytic degradation study was done in a laboratory-UV-reactor system with 150 W UV-immersion lamp of model TQ 150. The residual absorbance of the photodegraded dye solution was recorded using T60 UV-Visible spectrometer. The PXRD of recycled MOFs used in the photodegradation experiment were studied using Rigaku MiniFlex600- Benchtop XRD instrument. The magnetic properties of the MOFs were studied using MSB AUTO (Sherwood Scientific) instrument.

2.8 Reagents used in the study

The main reagents used in this dissertation are listed as follows: Copper nitrate trihydrate, nickel nitrate hexahydrate, zinc nitrate hexahydrate, 4,4’-bipyridyl hydrate, sodium oxalate, fumaric acid, methanol, DMF; all of which are used as received from Sigma Aldrich. The pillar 3,6-di(pyridin-4-yl)-1,2,4,5-tetrazine (PYTZ) has been synthesized and characterized by NMR spectroscopy (Appendix G).

Initially, the research work was based on the synthesis of MOFs from a dicarboxylate linker, a metal salt, and a pillar in 1:1:1 mole ratio, respectively. Nearly forty products were synthesized, but the elemental analysis of almost all of those products couldn’t suggest the well-known empirical formulae (of the form M_2L_2P) for pillared-layer type of MOFs. Where M=Metal, L= linker, and P=pillar. In the attempt, we used dicarboxylic linkers such as fumaric acid, sodium oxalate, 1,4-benzene dicarboxylic acid both in the acid and salt form. The pillars used were 4,4’-bipyridine and pyrazine. The linkers and pillars were allowed to react with either of the metal ions Ni(II), Co(II), Cu(II), Zn(II) and Fe(III) at room temperature for 24 h (Appendix I). As this approach couldn’t give pillared-layer MOFs a modified approach was made by changing the molar ratio to 1:1:0.5 for the linker, metal, and pillars, respectively.

This PhD research is categorized in to five sections as it is depicted in the **scheme 5**. The first three sets of the work involve the room temperature synthesis and characterization of pillared-layer MOFs (molar ratio for the linker, metal, and pillar is 1:1:0.5). The fourth work involves an attempted solvothermal synthesis of MOFs using longer pillar called PYTZ. The intended pillared-layer MOFs were not formed as per the elemental analysis data. The synthetic scheme for the pillar PYTZ and an attempt for the synthesis of pillared-layer MOFs in this case are shown in Appendix F and H. The last work involves evaluation of photocatalytic performance of selected MOFs.

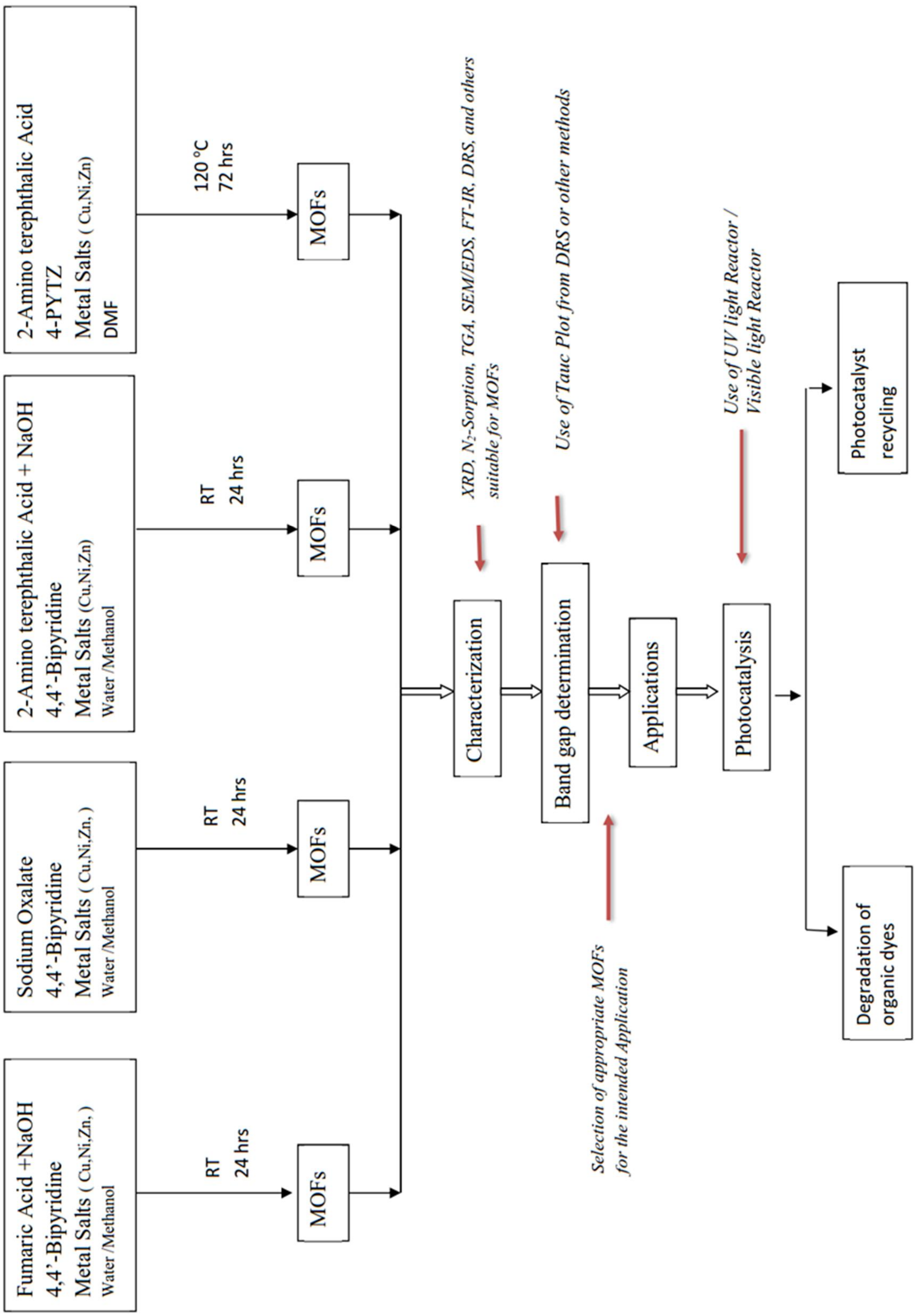

Scheme 5 Generalized research outline

CHAPTER THREE

Room Temperature Synthesis of MOFs Pillared by 4,4’-bipyridine

3.1Introduction

Pillared-layer MOFs are constructed from infinite layers pillared by linear bidentate linkers through dative bonds or supramolecular interactions. Such a topology has greatly advanced in recent years due to the combined use of bipyridine and polycarboxylate.[72] In 2009, Tomislav and László reported the mechanochemical construction of metal–organic polymers (Fig.13a) from a metal oxide, achieved via a LAG approach and obtained pillared-layer MOFs.[26, 73]

Anne and Claudio[74] reported synthesis of pillared MOFs using 4,4’-bipyridine as a pillar and the structure consists of a di-metal paddle wheel unit (Fig. 13b). The report by Bao *et al*[75] shows the reaction of $Zn(NO_3)_2\cdot 6H_2O$, various dicarboxylic acids, and either 4,4′-bipyridine or N,N′-di(4-pyridyl)-1,4,5,8-naphthalenetetracarboxydiimide in DMF solvent

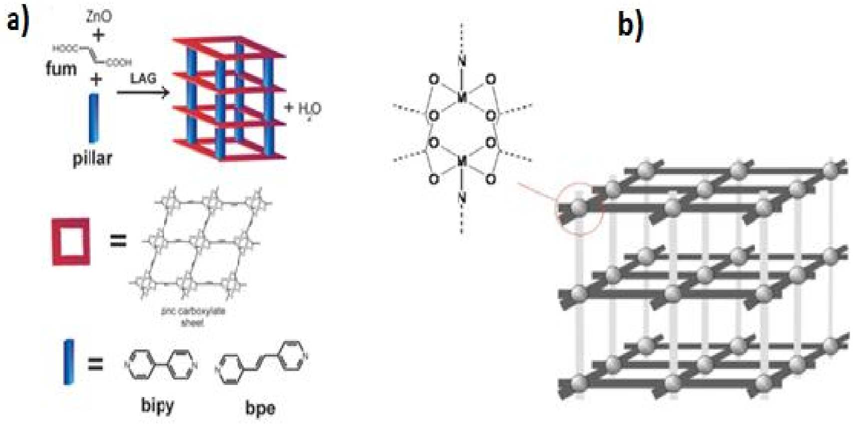

Figure 13 (a) Construction of pillared MOFs by three-component neutralization and coordination-driven mechanochemical assembly. (b) Paddle wheel unit of the MOFs reported by Anne[10]

and higher temperature produced a family of anisotropic, mixed-ligand, open-framework compounds featuring paddle-wheel-type coordination of Zn(II) pairs in two dimensions and pyridyl ligand pillaring in the third. The structure obtained from the CIF of this work shows a bi metal paddle wheel unit of the MOF (Fig**.** 14a, 14a').

Another research group, Fujii *et al.* [76] in the UK synthesized pillared MOFs in a mechanochemical process using ball and mill only and arrived at similar MOFs structure that some other research groups had synthesized before in DMF and at higher temperature. This research group got powdered pillared MOFs and compared their powder XRD patterns with the XRD pattern of the single crystal MOFs made in DMF and at higher temperature obtained from the CCDC 280541 for Zn pillared MOFs.

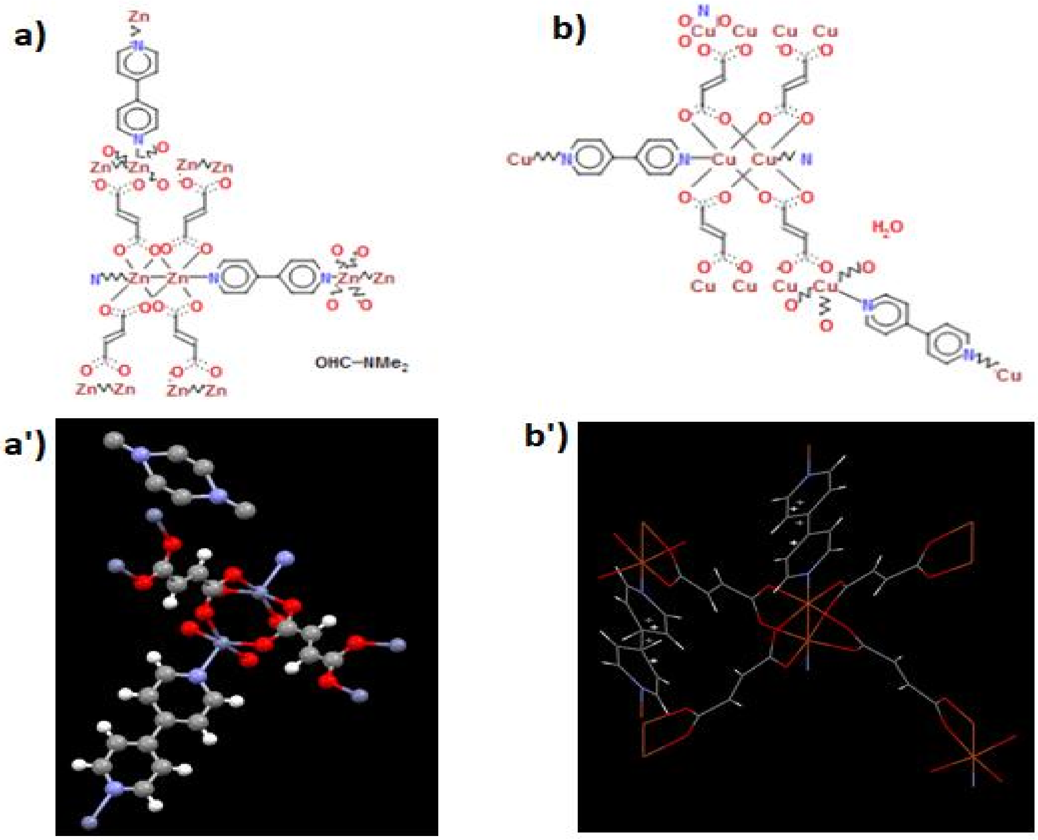

Figure 14 (a, a') Connectivity of the Zn paddle-wheel MOF archived from the CIF of CCDC-280541. (b, b') Connectivity of the Cu paddle-wheel MOF archived from the CIF file of CCDC-616535.

This work describes the synthesis and characterization of Zn and Cu pillared MOFs from zinc(II) and copper(II) nitrate, 4,4'-bipyiridine pillar and sodium salt of fumaric acid linker in a mixture of water and methanol solvent. The merit of this method lies in dispensing with the use of more toxic solvents such as DMF (Scheme 6). The PXRD of these MOFs were compared with the PXRD patterns calculated from CCDC 280541 for Zn paddle-wheel MOFs and CCDC 616535 for Cu paddle-wheel MOFs from CIF of the similar MOFs made in DMF at a higher temperature. Encouraged by the results, a new Ni-based MOF was prepared under similar synthetic conditions from nickel (II) nitrate, 4,4'-bipyridine pillar and sodium oxalate linker and included in this report. An attempt to synthesize crystalline Ni-fumarate-BPY analogue was not successful as the PXRD result showed a highly amorphous pattern. This might be due to the interpenetration that would exist in most MOFs when using longer linkers like fumarate and BPY compared to oxalates. This could disorder the framework when using Ni. Short linkers are usually employed when working with Ni-pillared MOFs.[77]

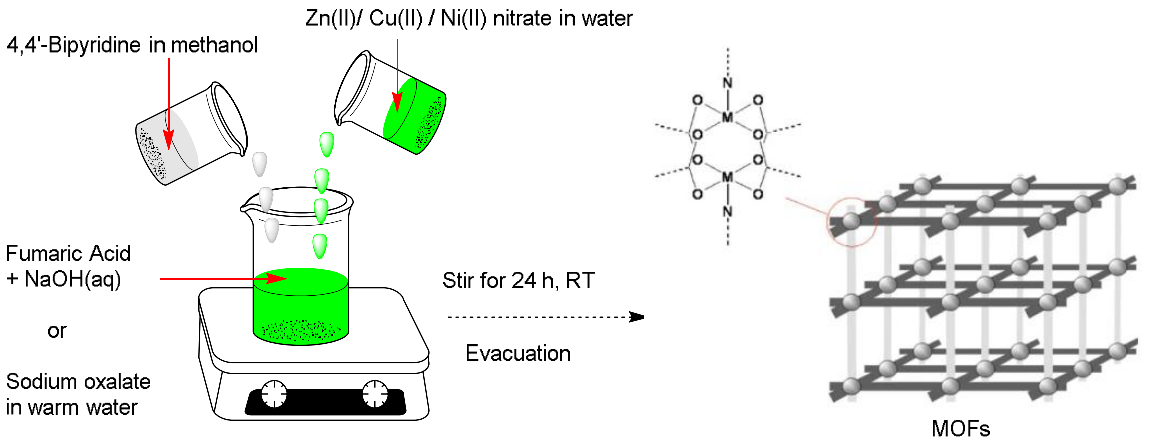

Scheme 6 Schematic representation of synthesis of MOFs in the current work

Based on the PXRD, CHN analysis, FT-IR, TGA and other characterization techniques and comparison with similar MOFs made earlier at higher temperature and DMF, the formation of MOFs with paddle-wheel structures (Fig. 15 or 16) are concluded.

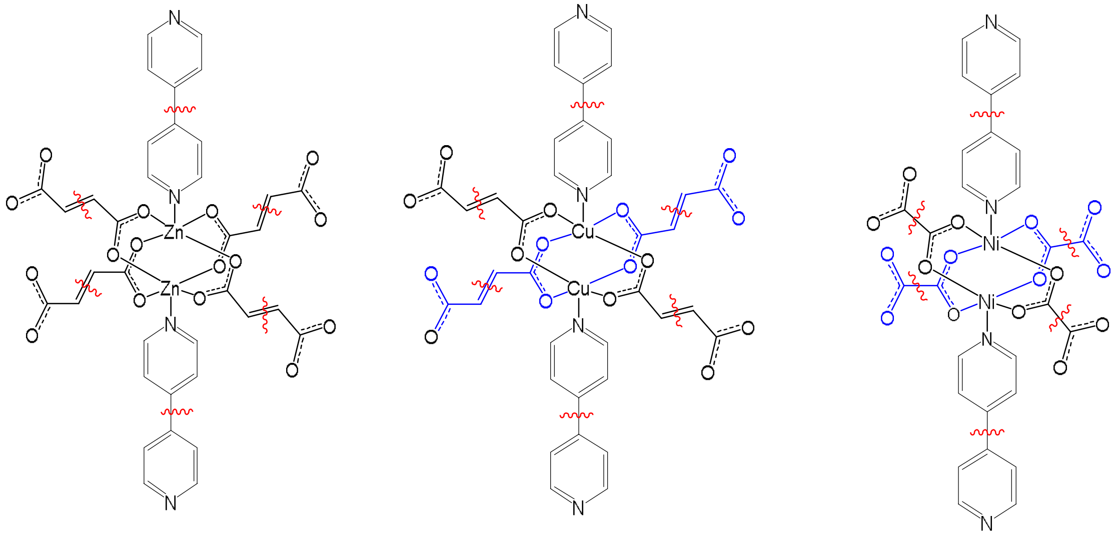

MOFT-22-RT
$\{[Zn_2(Fu)_2(BPY)]\cdot 1.5H_2O\}_n$

MOFT-23-RT
$\{[Cu_2(Fu)_2(BPY)]\cdot H_2O\}_n$

MOFT-11-RT
$\{[Ni_2(Ox)_2(BPY)].3.75H_2O\}_n$

Figure 15 Connectivity of the paddle wheel units in the current report or MOFT-22-RT= $\{[Zn_2(Fu)_2(BPY)]\cdot 1.5H_2O\}_n$; MOFT-23-RT = $\{[Cu_2(Fu)_2(BPY)]\cdot H_2O\}_n$; MOFT-11-RT = $\{[Ni_2(Ox)_2(BPY)]\cdot 3.75H_2O\}_n$. Guest solvent molecules are excluded in the structure.

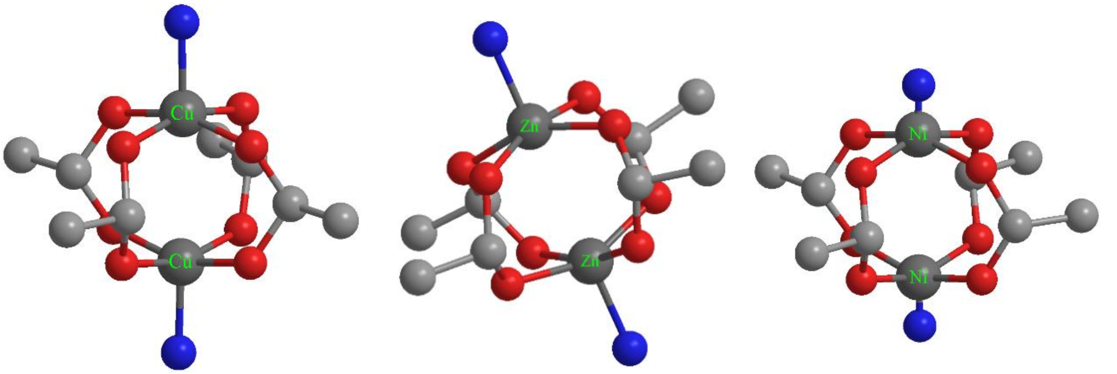

MOFT-23-RT MOFT-22-RT MOFT-11-RT

Figure 16 3D version of the paddle-wheel SBUs for MOFT-23-RT, MOFT-22-RT, and MOFT-11-RT

3.2Experimental

Synthesis of MOFT-23-RT ($\{[Cu_2(Fu)_2(BPY)]\cdot H_2O\}_n$)

This compound was synthesized by modification of the procedure previously reported.[74, 77, 78] A clear solution of Na_2Fu was prepared by dissolving 8 mmol (0.32 g) of NaOH in 15 mL deionized water and adding 4 mmol (0.4432 g) of fumaric acid while stirring at room temperature. To the above solution, 40 mL of a methanolic solution of BPY (2 mmol, 0.348 g) (BPY= 4,4'-bipyridyl hydrate) was added. The combined solution was stirred for 30 min and $Cu(NO_3)_2\cdot 3H_2O$ (4 mmol, 0.9664 g) in water (5 mL) was added forming a cyan-colored suspension. The mixture was stirred at room temperature for 24 hours. The resulting cyan color product was filtered under suction, washed with 3 x 5 mL of deionized water followed by 3 x 5 mL of methanol and then dried in vacuum oven at 80 ^{o}C for 5 h, yielding 0.95 g (ca. 90 % based on BPY) of a cyan color solid $\{[Cu_2(Fu)_2(BPY)]\cdot H_2O\}_n$. Elemental analyses: Calcd. (found) % for $C_{18}H_{14}N_2O_9Cu_2$: C, 40.80; H, 2.64; N, 5.28%.: (C, 40.70); (H, 2.39); (N, 5.04).

Synthesis of MOFT-22-RT ($\{[Zn_2(Fu)_2(BPY)]\cdot 1.5H_2O\}_n$)

Procedure for the synthesis of this compound was similar to that of $\{[Cu_2(Fu)_2(BPY)]\cdot H_2O\}_n$ except that $Cu(NO_3)_2\cdot 3H_2O$ was replaced by $Zn(NO_3)_2\cdot 6H_2O$. The reaction yielded 0.66 g (ca. 61 % based on BPY) of $\{[Zn_2(Fu)_2(BPY)]\cdot 1.5H_2O\}_n$ in the form of white solid (Fu=Fumarate). Elemental analyses: Calcd. (found) % for $C_{18}H_{15}N_2O_{9.5}Zn_2$: C, 39.84; H, 2.76; N, 5.16%. (C, 39.73); (H, 2.97); (N, 4.89).

Synthesis of MOFT-11-RT ($\{[Ni_2(Ox)_2(BPY)]\cdot3.75H_2O\}_n$)

This compound was synthesized by simple modification of the procedure previously reported.[74, 78] In this synthesis, Na_2Ox (4 mmol, 0.540 g) was dissolved in warm deionized water (20 mL). To this solution 40 mL methanolic solution of $BPY\cdot H_2O$ (2 mmol ,0.348 g) was added. The mixture was stirred for 30 min and $Ni(NO_3)_2\cdot6H_2O$ (4 mmol, 1.1632 g) was added. The pH of the solution was found to be between 5 and 6. The resulting mixture was stirred at room temperature for 24 hours. A light blue product was formed. The resulting product was filtered under suction, washed with 3 x 5ml of deionized water and then with 3 x 5 mL of methanol and evacuated in a vacuum oven at 80 ^{o}C for 5 h, yielding 0.94 g (ca. 91 % based on BPY) of $\{[Ni_2(Ox)_2(BPY)]\cdot3.75H_2O\}_n$ in the form of light blue solid (Ox=Oxalate). Elemental analyses: Calcd. (found) % for $C_{14}H_{15.5}N_2Ni_2O_{11.75}$: C, 32.55; H, 2.99; N, 5.41%. (C, 32.49); (H, 2.71); (N, 5.13).

3.3Results and Discussion

PXRD: The three MOFs were studied by PXRD and it was found that the patterns of the MOFs prepared at room temperature are in good agreement with the corresponding patterns of the same MOFs prepared in DMF at higher temperature (Fig. 17). For

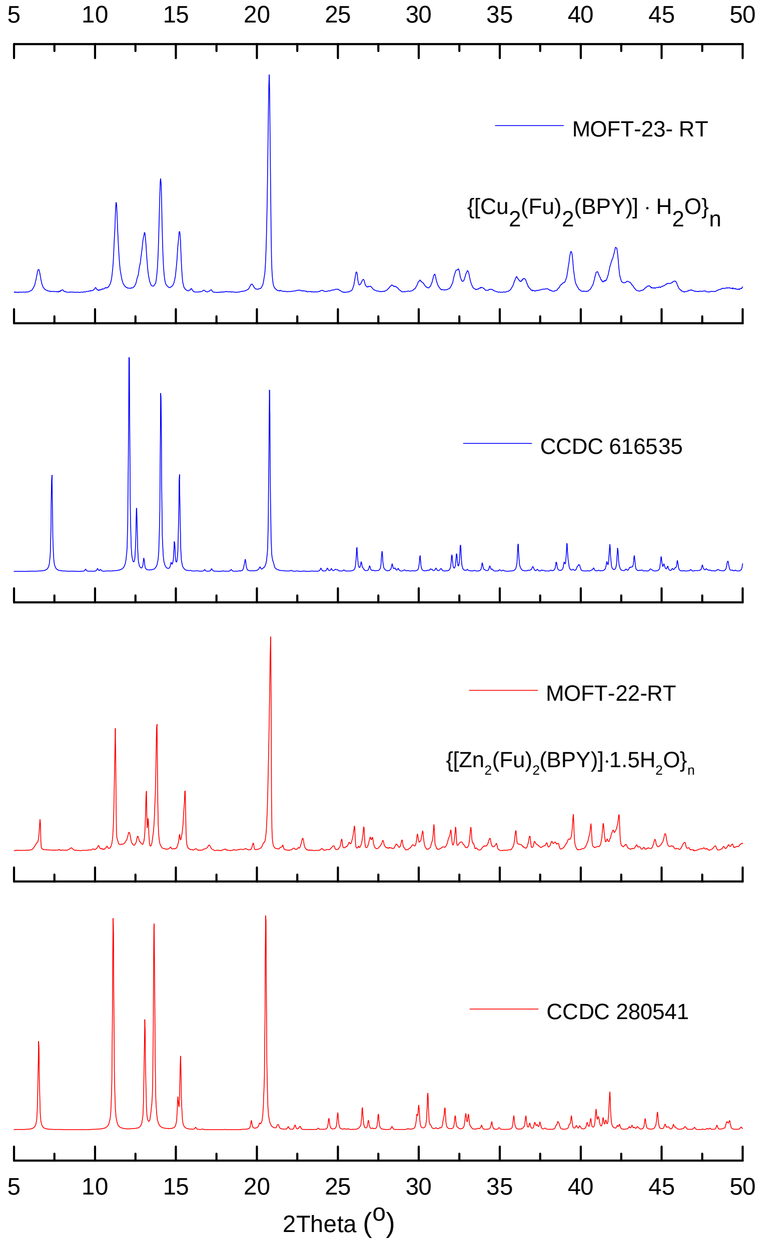

Figure 17 PXRD patterns of MOFT-22-RT and MOFT-23-RT with their simulated PXRD patterns from SXRD of pillared MOFs, CCDC 280541 and CCDC 616535, respectively that were originally made in DMF at higher temperature.

$\{[Zn_2(Fu)_2(BPY)]\cdot 1.5H_2O\}_n$, comparison of the PXRD pattern is made with that of simulated PXRD pattern from the single crystal originally prepared in DMF at higher temperature.[75] Both PXRD patterns have similar peaks at 2θ = 6.5, 11.12, 13.07, 13.73, 15.36, and 20.72. The existence of low intensity peaks at 2θ= 12.19 and 12.85 in $\{[Zn_2(Fu)_2(BPY)]\cdot 1.5H_2O\}_n$ that are not seen in the pattern calculated from the CIF (CCDC 280541) might be attributed to the presence of water in the MOF structure replacing DMF in the previously reported system. Similarly, comparison of the PXRD for $\{[Cu_2(Fu)_2(BPY)]\cdot H_2O\}_n$ was made with that simulated from the previously reported CIF (CCDC 616535) of the single crystal of the corresponding pillared MOF prepared in DMF at higher temperature.[15] Both MOFs show similar peak position at 2θ = 20.85, 15.29, 14.04. The peak position that are observed at 12.56, 12.12, and 7.3 in the simulation pattern are seen at 11.03, 11.38 and 6.5, respectively in the $\{[Cu_2(Fu)_2(BPY)]\cdot H_2O\}_n$. Some broadening is observed for these three characteristic peaks, indicating smaller particle size of the powder obtained using room temperature synthesis. Overall, comparison of PXRD of $\{[Zn_2(Fu)_2(BPY)]\cdot 1.5H_2O\}_n$ and $\{[Cu_2(Fu)_2(BPY)]\cdot H_2O\}_n$ to literature counterparts confirm that it is possible to prepare MOFs at room temperature, replacing DMF with water and methanol as solvent. Fig. 18 shows the PXRD pattern of a crystalline MOF $\{[Ni_2(Ox)_2(BPY)]\cdot 3.75H_2O\}_n$, which was synthesized in a similar fashion to $\{[Zn_2(Fu)_2(BPY)]\cdot 1.5H_2O\}_n$ and $\{[Cu_2(Fu)_2(BPY)]\cdot H_2O\}_n$ in water and methanol, but by replacing the fumarate linker with oxalate and by using $Ni(NO_3)_2\cdot 6H_2O$ as the source of the metal node. An attempt to synthesize crystalline Ni-Fumarate-BPY analogue was not successful with the PXRD revealing the formation of a highly amorphous product.

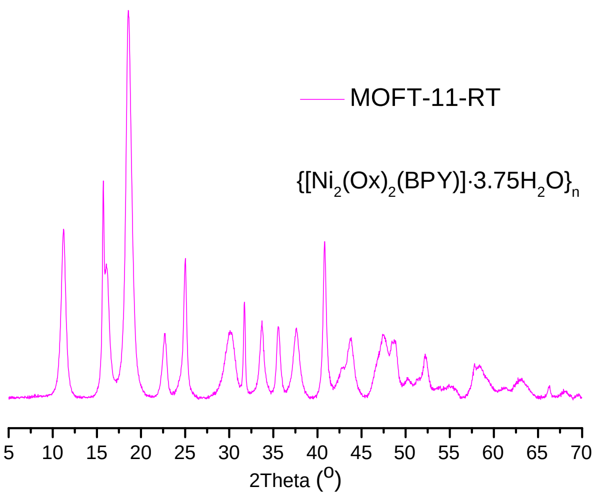

Figure 18 PXRD of MOFT-11-RT

The MOFs in this study are all obtained as powders and crystal parameters were determined using DICVOL06 found in Expo2014 software.[76, 79, 80] The PXRD patterns of {[Zn_2(Fu)$_2$(BPY)]·1.5H_2O}$_n$ and {[Cu_2(Fu)$_2$(BPY)]·H_2O}$_n$ were indexed and a Rietveld refinement used to confirm that both MOFs crystalize in the triclinic *P*-1 space group. In contrast, indexing of the PXRD pattern of {[Ni_2(Ox)$_2$(BPY)}·3.75H_2O}$_n$ showed that this MOF crystalizes in the monoclinic space group P2/m (Table 2). The unit cell volumes for

Table 2 Crystal data and structural refinement parameters indexed by DICVOL06

	MOFT-22-RT	**MOFT-23-RT**	**MOFT-11-RT**
Empirical formula	$C_{18}H_{15}N_2O_{9.5}Zn_2$	$C_{18}H_{14}N_2O_9Cu_2$	$C_{14}H_{15.5}N_2Ni_2O_{11.5}$
Formula weight	542.08	527.93	517.17
Crystal system	Triclinic	Triclinic	Monoclinic
Space group	P-1	P-1	P2/m
a(Å)	8.877(5)	6.9084	21.8354
b(Å)	15.143(3)	9.0654	9.7326
c (Å)	15.168(5)	13.7042	13.6908
α (°)	115.85(2)	95.93	90.00
β (°)	93.29(2)	94.42	102.12
γ(°)	97.51(2)	100.60	90.00
V(Å^3)	1804.0(13)	835.04	2844.69
Z	3	1.5	5
ρ_{calc} (g cm^{-3})	1.57	1.66	1.53
Counts	2475	2475	2475
λ(nm)	1.540598	1.540598	1.540598

the MOFs indicate that each system is potentially porous, taking into account the volume occupied by the framework components. The crystallite sizes of the MOFs products are estimated using the Scherrer formula (K=0.94) and calculated as 69333.2 Å (Rp(%)=18.1), 1958.6 Å (Rp(%)=11.4), and 771.9 Å (Rp(%)=16.6) for $\{[Zn_2(Fu)_2(BPY)]\cdot1.5H_2O\}_n$, $\{[Cu_2(Fu)_2(BPY)]\cdot H_2O\}_n$, and $\{[Ni_2(Ox)_2(BPY)]\cdot3.75H_2O\}_n$, respectively. The software automatically selected the peaks in the PXRD patterns that are appropriate for crystallite size estimation between 2θ= 30-50°.

FT-IR: The three MOFs **{**$[Zn_2(Fu)_2(BPY)]\cdot1.5H_2O\}_n$, $\{[Cu_2(Fu)_2(BPY)]\cdot H_2O\}_n$ and $\{[Ni_2(Ox)_2(BPY)]\cdot3.75H_2O\}_n$ were studied by FT-IR. Fig. 19a, 19b (and full size in Appendix D) show the FT-IR spectra of those MOFs, linkers and the pillars from which

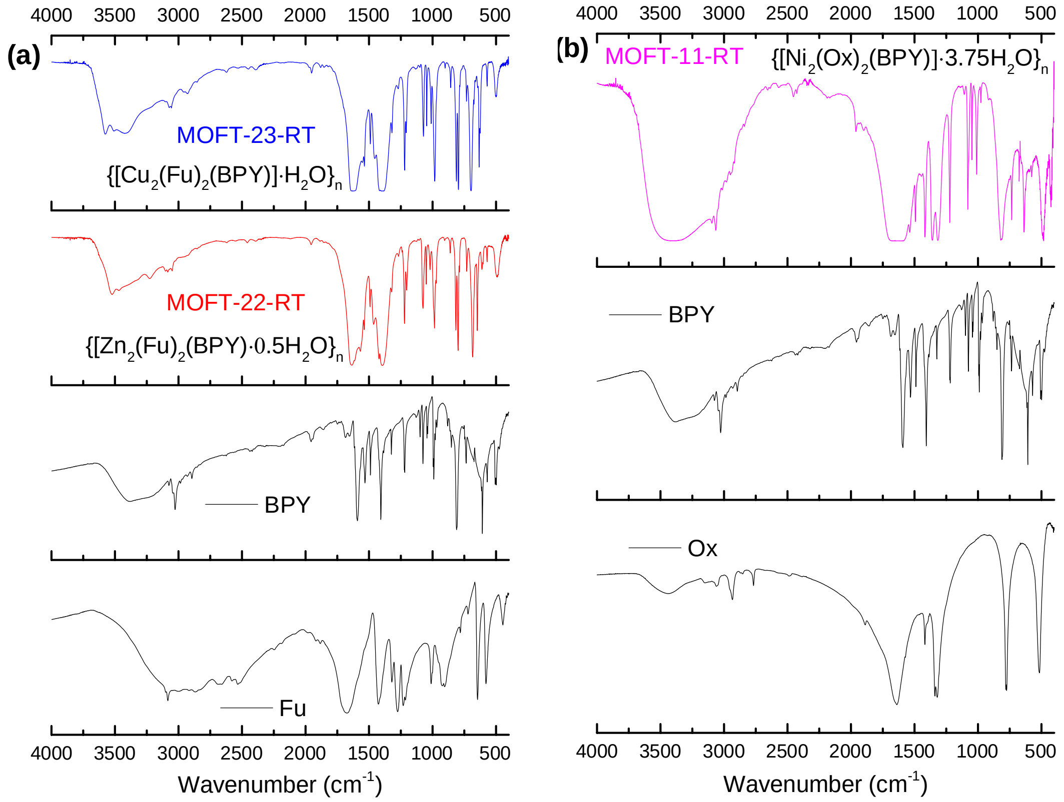

Figure 19 (a) FT-IR spectra of MOFT-22-RT, MOFT-23-RT, 4,4'-bipyridyl hydrate and fumaric acid. (b) FT-IR spectra of MOFT-11-RT, 4,4'-bipyridyl hydrate and sodium oxalate.

the MOFs are derived. In Fig 19a the C=O stretching frequency of fumaric acid appears at 1678 cm^{-1}. This peak is shifted to the lower frequency region (1618 cm^{-1}) after coordination to Zn(II) in $\{[Zn_2(Fu)_2(BPY)]\cdot 1.5H_2O\}_n$ and Cu(II) in $\{[Cu_2(Fu)_2(BPY)]\cdot H_2O\}_n$. Similarly, in Fig. 19b the C=O stretching frequency of oxalate is seen at 1642 cm^{-1}, but the C=O stretching frequency in the resulting $\{[Ni_2(Ox)_2(BPY)]\cdot 3.75H_2O\}_n$ shifted to a broader band centered at 1630 cm^{-1} after coordination to Ni. The ring breathing mode observed in BPY in the region between 735-571 cm^{-1} and 1038-966 cm^{-1} are seen in the resulting three MOFs after coordination with the metals with some change in the peak intensity and position. The narrow ring breathing at 1405 cm^{-1} in BPY becomes more intense and wider in $\{[Zn_2(Fu)_2(BPY)]\cdot 1.5H_2O\}_n$ and $\{[Cu_2(Fu)_2(BPY)]\cdot H_2O\}_n$ after coordination but less intense in $\{[Ni_2(Ox)_2(BPY)]\cdot 3.75H_2O\}_n$. The C-C and C-N stretching frequency of the pillar BPY is observed at 1583 cm^{-1}. This peak is merged to the C=O stretching frequency centered at 1618 cm^{-1} for all three MOFs. These frequency shifts as well as change in intensity are ascribed to coordination of nitrogen to the metals in the MOFs under study. The symmetric and asymmetric vibrations of the carboxylate (COO^-) group coordinated to Zn (II) and Cu (II) in $\{[Zn_2(Fu)_2(BPY)]\cdot 1.5H_2O\}_n$ and $\{[Cu_2(Fu)_2(BPY)]\cdot H_2O\}_n$, are seen at 1618 cm^{-1} and 1380 cm^{-1} respectively but merge with the C-N and ring breathing bands of the pyridyl group. This made the peaks wider and intense. The same phenomenon is observed for peaks at 1630 cm^{-1} and 1333 cm^{-1} in $\{[Ni_2(Ox)_2(BPY)]\cdot 3.75H_2O\}_n$. Generally, the shift in FT-IR between the unreacted and reacted linkers and pillar show coordination of oxygen and nitrogen to the metal cations in each MOF.[16,17]

Thermal Analysis

The thermal stabilities of $\{[Ni_2(Ox)_2(BPY)]\cdot 3.75H_2O\}_n$, $\{[Zn_2(Fu)_2(BPY)]\cdot 1.5H_2O\}_n$, and $\{[Cu_2(Fu)_2(BPY)]\cdot H_2O\}_n$ were examined by TGA under argon atmosphere from room temperature to 700 °C using heating rate of 10 °C min^{-1} and the differential curves associated with the TGA curve show sharp mass losses at different temperature as depicted in Fig. 20, 21, and 22.

MOFT-11-RT. The TGA curve of $\{[Ni_2(Ox)_2(BPY)]\cdot 3.75H_2O\}_n$ in Fig.20 indicates that the water loss is observed as two steps of 7.2 % (calcd.7.5%) up to 190 °C, corresponding to 2.15 water molecules followed by 5.9 % (calcd. 5.6 %) assigned to loss of 1.6 water molecules bellow 345 °C that are deeply adsorbed in the pores. A significant mass loss of

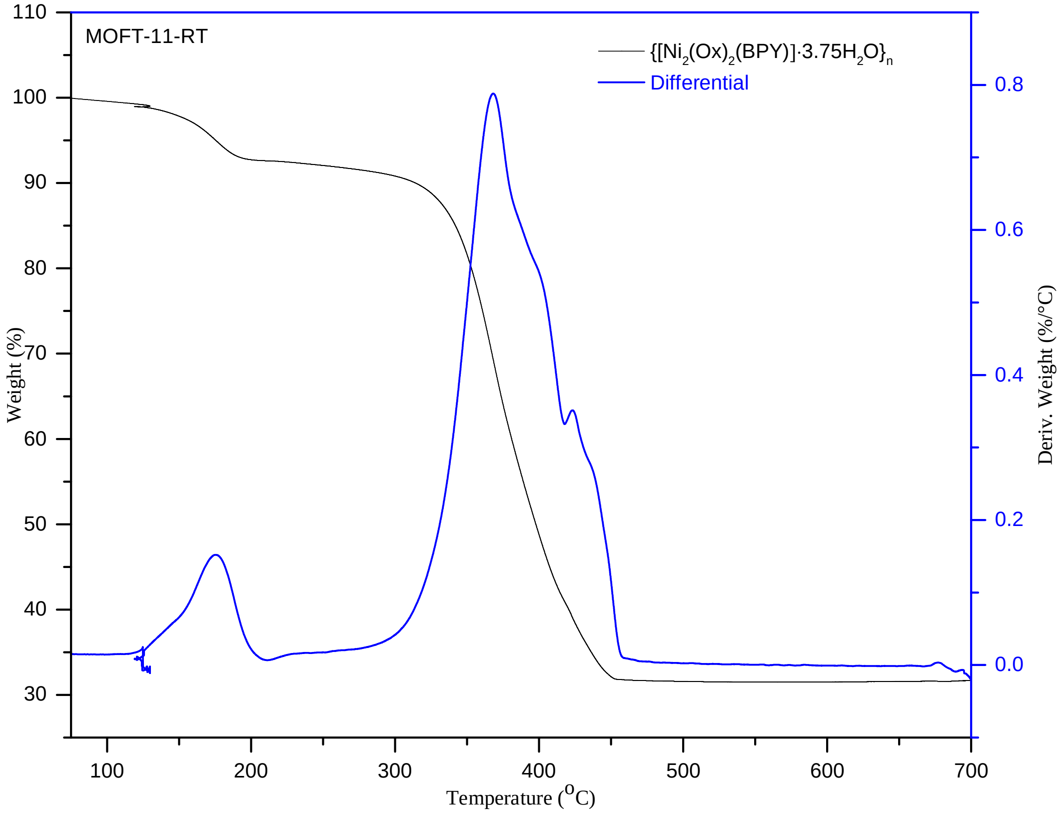

Figure 20 TGA of MOFT-11-RT

57.7 % (calcd. 58 %) in the temperature ranges 345 - 453 °C of MOFT-11-RT corresponds to synchronous mass losses of one mole equivalent of 4,4'-pyridine, 2CO and $2CO_2$. The final 31 % (calcd. 29 %) residue in the TGA curve of MOFT-11-RT matches satisfactorily with the formation of 2NiO. The final oxide residue also confirms the presence of two Ni in the empirical formula of this MOF in the paddle wheel.

MOFT-22-RT. Fig. 21 shows the TGA curve of $\{[Zn_2(Fu)_2(BPY)]\cdot1.5H_2O\}_n$. The first 5.12 % mass loss bellow 333 °C showed removal of 1.5 water molecules (calcd.4.98 %). A sharp mass loss occurred starting between 333 °C - 455 °C indicates collapse of the frameworks and removal of the organic matter. The 32.7 % residue above 455 °C in this TGA profile corresponds to two ZnO left at the end (calcd. 30.03 %). The formation of two

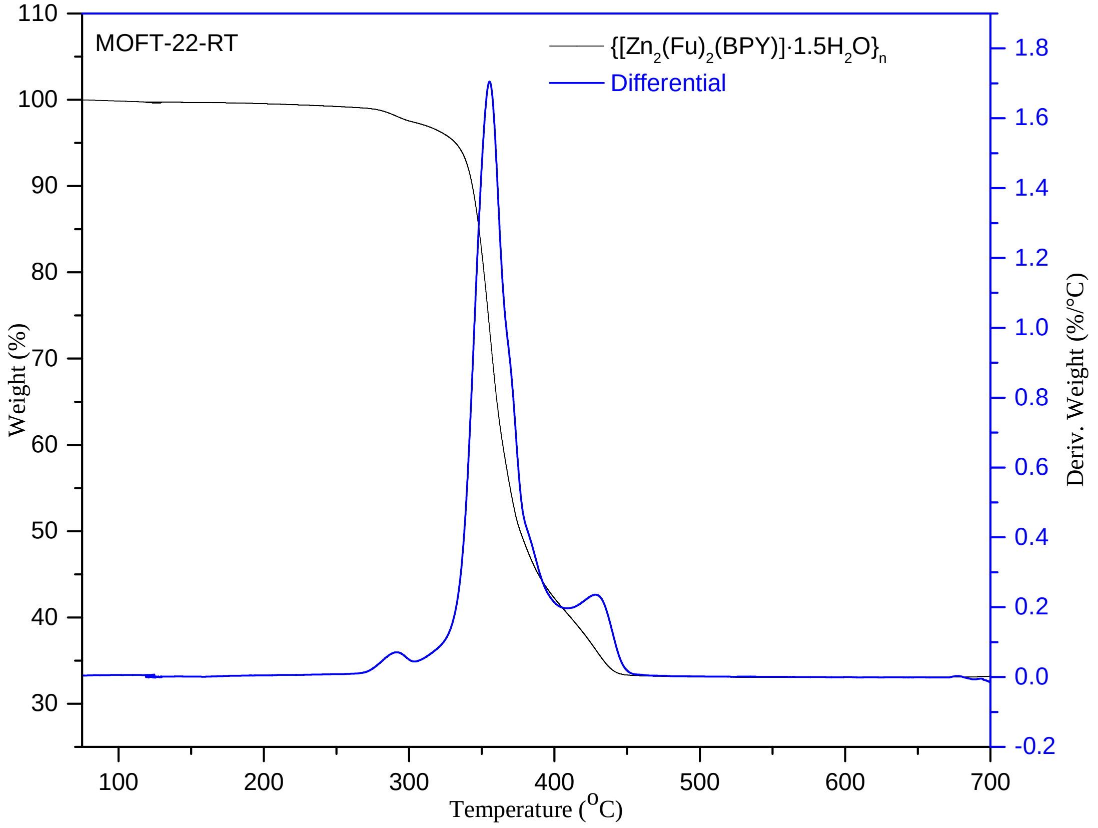

Figure 21 TGA of MOFT-22-RT

ZnO as a residue also imply the presence of two Zn in the empirical formula of this Zn-MOF in the paddle wheel.

MOFT-23-RT. In the case of $\{[Cu_2(Fu)_2(BPY)]\cdot H_2O\}_n$ a weight loss (Fig. 22) in the range of 90-240 °C (calcd. 3.4%) is attributed to the removal of one water molecule from the framework. The second weight loss is observed in the range of 240-360 °C, corresponding to decomposition of the framework. The final 30.9 % residual weight for MOFT-23-RT corresponds to two weight equivalents of CuO (calcd. 30.05 %). This confirms that MOFT-23-RT contains two Cu in its empirical formula in the paddle wheel.

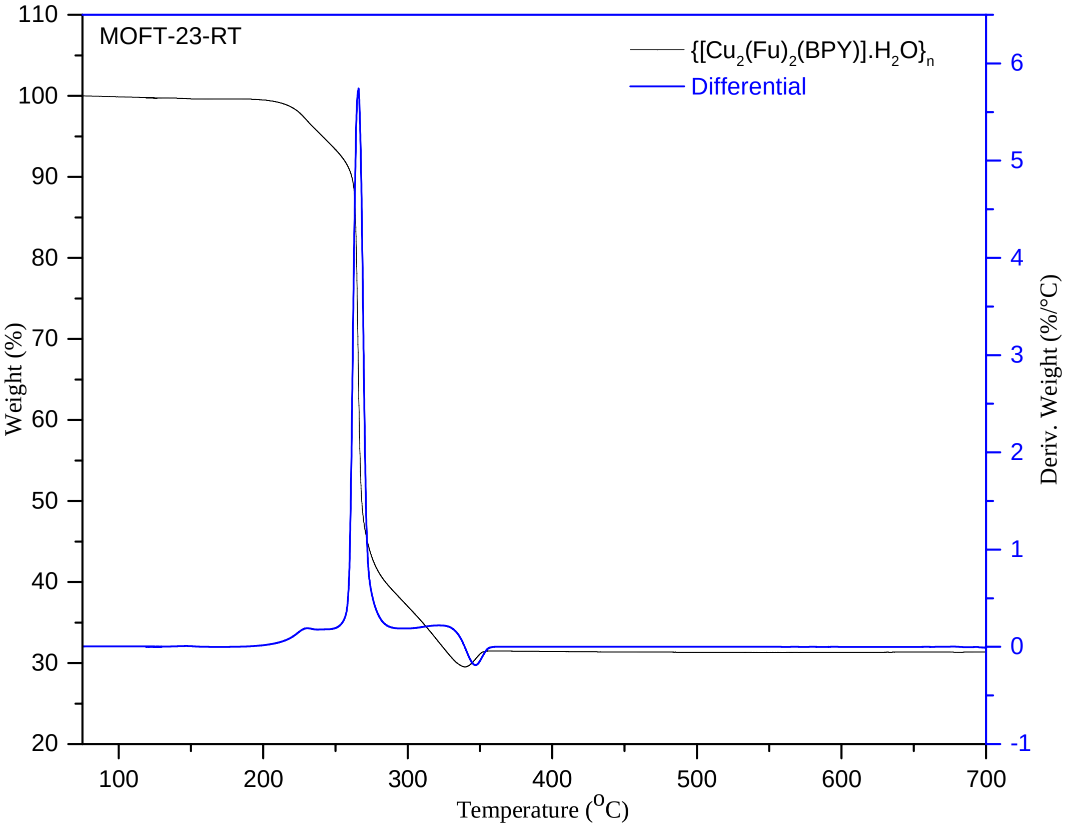

Figure 22 TGA of MOFT-23-RT

Determination of Surface Area, Pore Volume and Pore Size

The Brunauer-Emmet-Teller (BET) surface areas of the samples were calculated using N_2 adsorption data at 77 K. Pore diameter, BJH pore volume and BET surface area are given in Table 3. It is known that samples of $Zn_2(Fu)_2(BPY)$ prepared from DMF does not exhibit any uptake of N_2[75] and similarly the structure of $Cu_2(Fu)_2(BPY)$[81] has small pores, ca. 3.6 Å in diameter, both probably as a result of doubly interpenetrated arrangements. It is likely that $Ni_2(Ox)_2BPY$ also has small pores as a result of the shorter linker (oxalate) in comparison to fumarate. The similar pore diameters of over 3 nm observed in each case suggests that the interpenetration or the network effect might be resolved to some extent when the MOFs are prepared in water/methanol mixed solvents than in DMF. The shape of the isotherms shown in this study could be ascribed to the fact that dynamic/ flexible pillared-layer MOFs can reversibly change their channels by a large magnitude while retaining similar topologies, corresponding to expansion (lp phase) and contraction (np phase) up on the guest N_2 adsorption and desorption.[82] The structural transformation has an effect[83] on the shape of the isotherm or hysteresis (Fig. 23a,b,and c) and could not exactly fit to the models reported by IUPAC.[3] This is expected for most real samples and the models work best for rigid MOFs that do not show flexibility. The pore widths from

Table 3 N_2-sorption data for MOFT-11-RT, MOFT-22-RT and MOFT-23-RT

MOFs	Pore diameter [nm]	BJH Pore Volume [cm^3g^{-1}]	BET Surface area [m^2g^{-1}]
MOFT-11-RT	3.27	1.180	981.74
MOFT-22-RT	3.27	1.407	1,604.44
MOFT-23-RT	3.03	0.995	775.16

NLDFT fit or dV/dW vs pore size distribution plot obtained from the instrument are shown in Fig. 23a', b', and c' for $\{[Ni_2(Ox)_2(BPY)]\cdot 3.75H_2O\}_n$, $\{[Zn_2(Fu)_2(BPY)]\cdot 1.5H_2O\}_n$, and $\{[Cu_2(Fu)_2(BPY)]\cdot H_2O\}_n$, respectively depicting that the MOFs have pore sizes in lower mesoporous region. It is also evident from Table 3 that $\{[Zn_2(Fu)_2(BPY)]\cdot 1.5H_2O\}_n$ has the largest BET surface area of the three MOFs in this study.

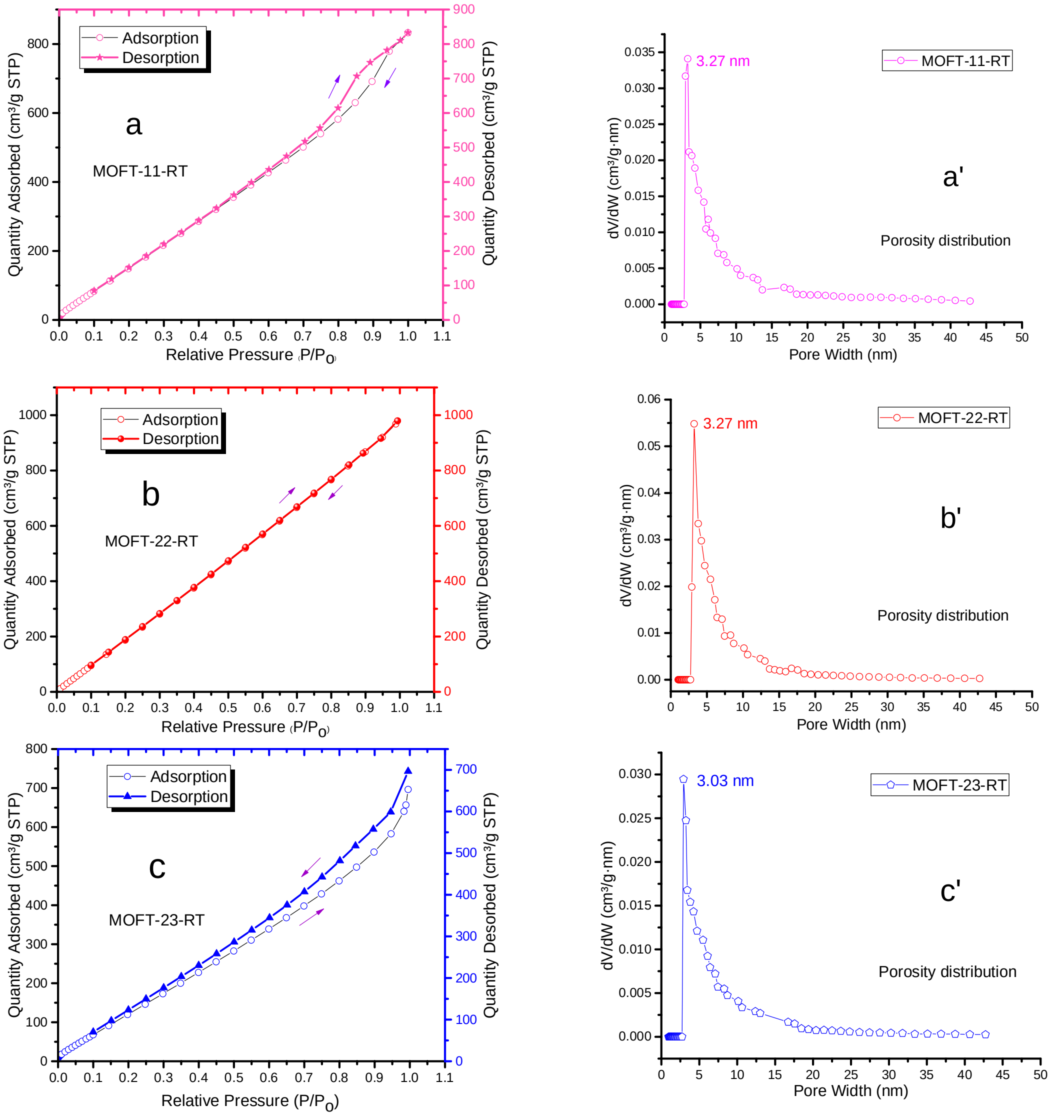

Figure 23 Porosity properties of MOFT-11-RT, MOFT-22-RT and MOFT-23-RT determined by N_2 adsorption–desorption method. (a, b, c) N_2 adsorption–desorption isotherms of MOFT-11-RT, MOFT-22-RT and MOFT-23-RT, respectively. (a', b', c') The pore size distribution curves for the corresponding MOFT-11-RT, MOFT-22-RT and MOFT-23-RT, respectively synthesized under the same conditions.

Morphological Characterization

SEM micrographs and X-ray microanalysis (SEM/EDX) were recorded by using FEI Quanta 650 ESEM instrument equipped with Oxford Instruments X-Max 150mm^2 EDS detector with AZtec software at 20kV spot 3-4, using low vacuum x-ray cone accessory at 80Pa. SEM images of the three MOFs are shown in Figure 24. Both $\{[Ni_2(Ox)_2(BPY)\cdot 3.75H_2O\}_n$ and $\{[Zn_2(Fu)_2(BPY)]\cdot 1.5H_2O\}_n$ show crystals with parallelepiped-like morphologies whereas $\{[Cu_2(Fu)_2(BPY)]\cdot H_2O\}_n$ contains much smaller crystallites giving a cotton-like appearance. SEM/EDX analysis gives information about the sample surfaces with high depth of field and lateral resolutions of around 1-20nm,[84, 85] indicating that EDX only provides microanalysis for the surface of particles (Figure 25-27). This means that the EDS cannot show the bulk micro analysis and is only the surface analysis. SEM/EDS analysis of $\{[Ni_2(Ox)_2(BPY)]\cdot 3.75H_2O\}_n$ (O: 63.0%; C: 22.1%; Ni: 14.8%), $\{[Zn_2(Fu)_2(BPY)]\cdot 1.5H_2O\}_n$ (O: 63.4%; C: 22.5%; Zn: 13.5%) and $\{[Cu_2(Fu)_2(BPY)]\cdot H_2O\}_n$ (O: 64.0%; C: 22.8%; Ni: 13.2%). Importantly it is noteworthy that the SEM/EDX microanalysis confirms the absence of sodium in the MOF materials.

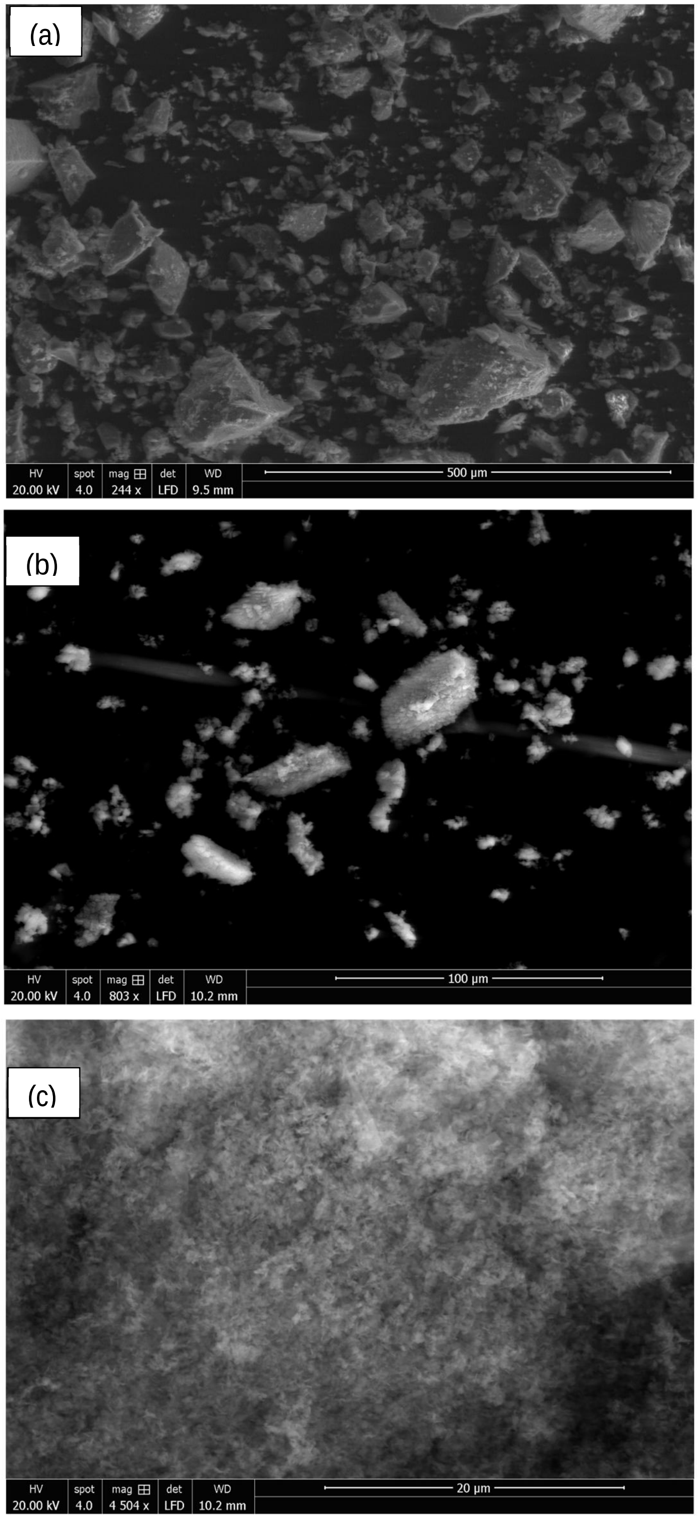

Figure 24 SEM images of MOFT-11-RT (a), MOFT-22-RT (b) and MOFT-23-RT (c)

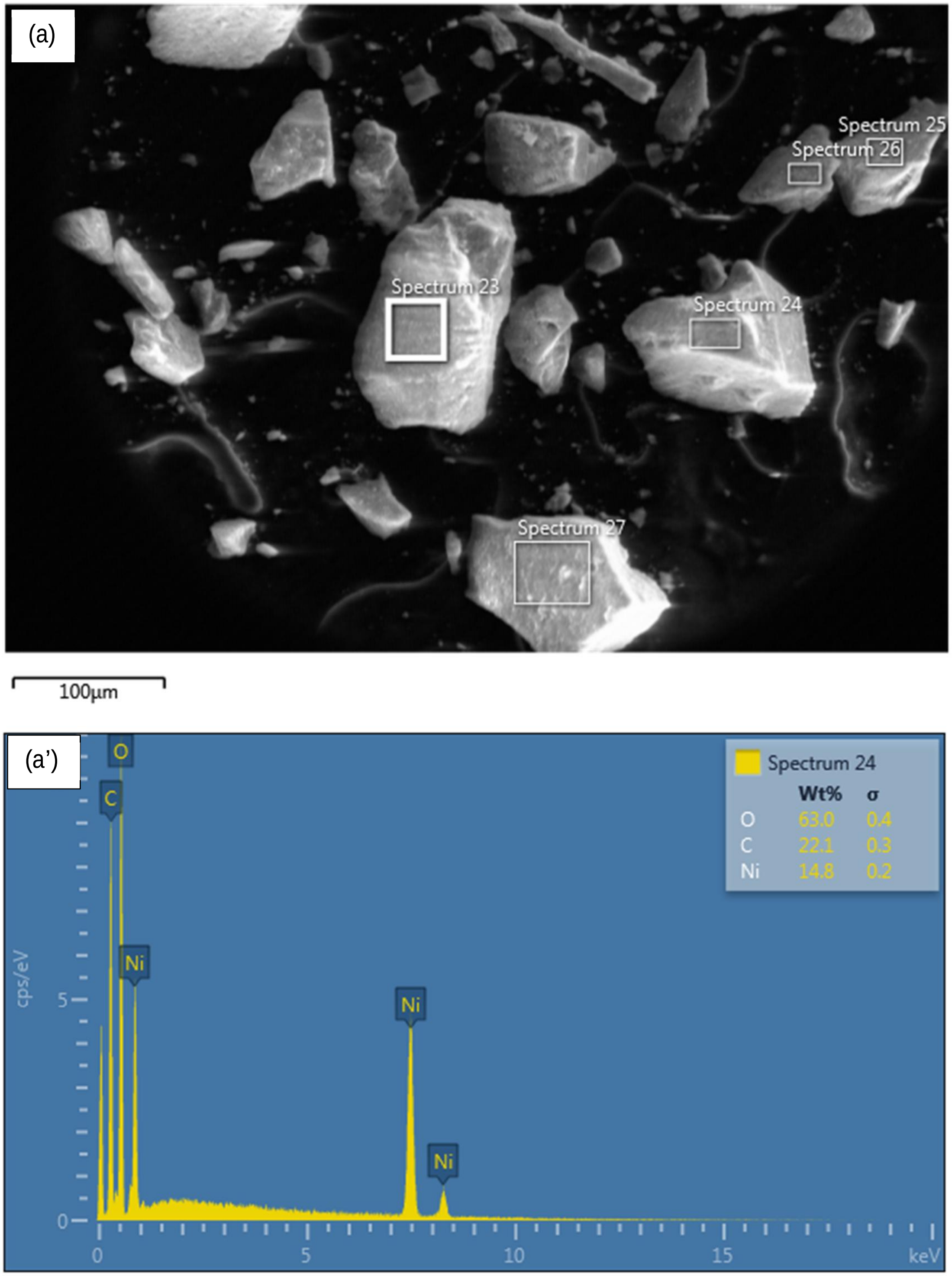

Figure 25 SEM (a) and EDS (a’) of MOFT-11-RT

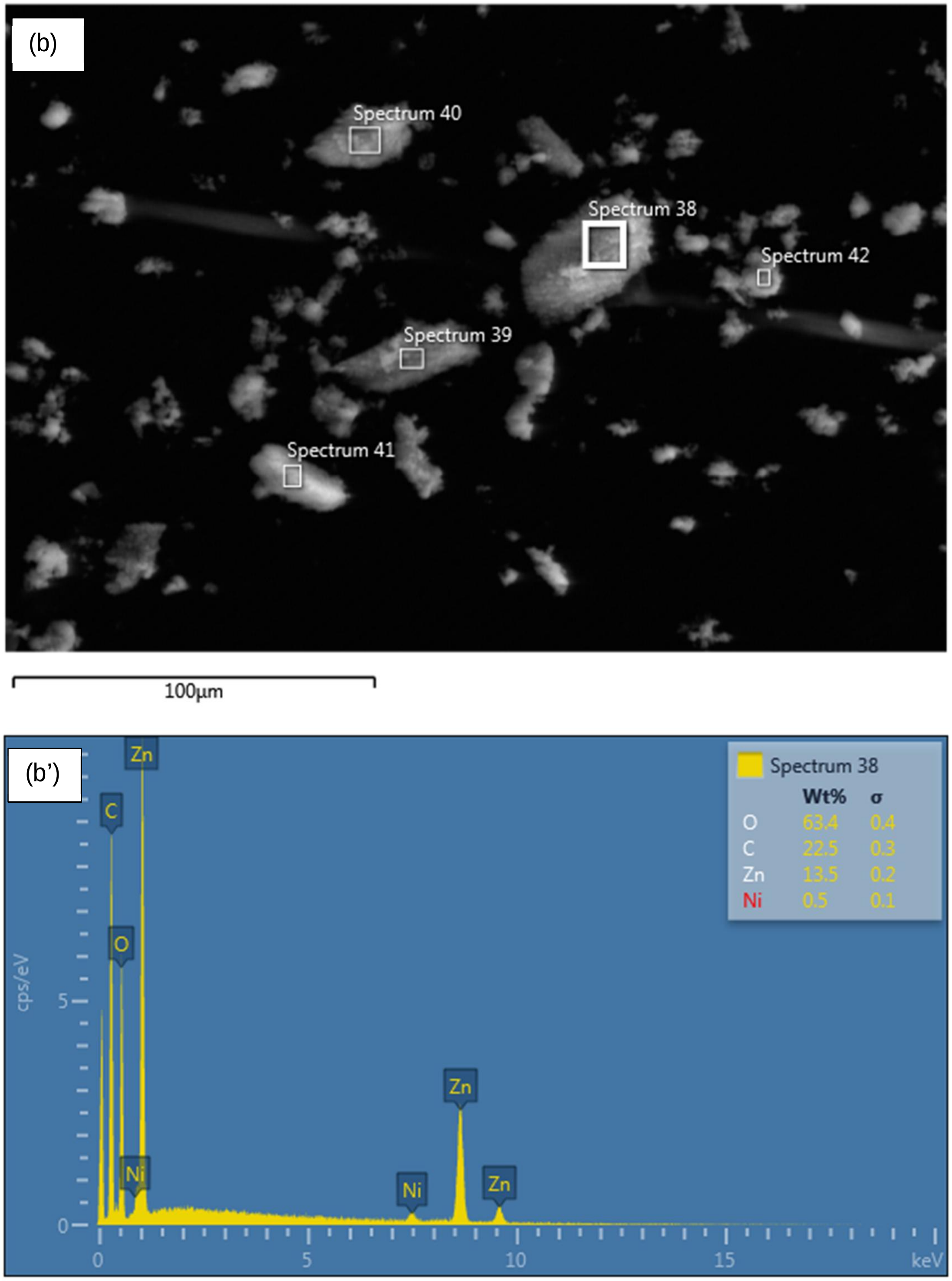

Figure 26 SEM (b) and EDS (b') of MOFT-22-RT

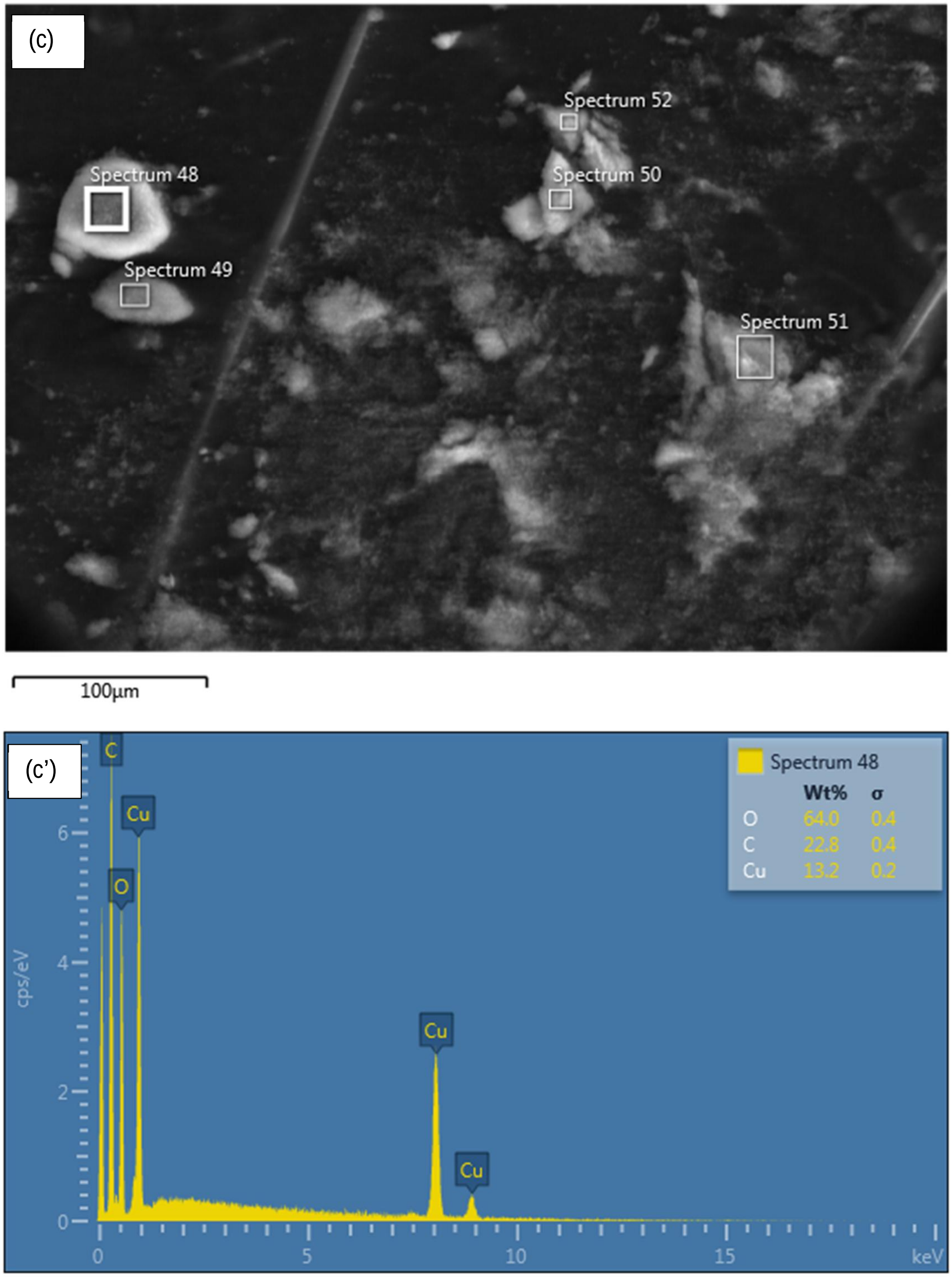

Figure 27 SEM (a) and EDS (b) of MOFT-23-RT

Solid State UV-Vis Study

The solid state UV-Vis spectra shown in Fig. 28 for the powdered microcrystaline $\{[Ni_2(Ox)_2(BPY)]\cdot 3.75H_2O\}_n$, $\{[Zn_2(Fu)_2(BPY)]\cdot 1.5H_2O\}_n$, and $\{[Cu_2(Fu)_2(BPY)]\cdot H_2O\}_n$ depict the electronic transitions with in the linkers. The absorption coeficients (F(R) or α) at 225nm, 230nm, and 240nm for $\{[Cu_2(Fu)_2(BPY)]\cdot H_2O\}_n$, $\{[Zn_2(Fu)_2(BPY)]\cdot 1.5H_2O\}_n$, and $\{[Ni_2(Ox)_2(BPY)]\cdot 3.75H_2O\}_n$, respectively are ascribed to the $n \rightarrow \sigma^*$ electronic transitions with in the linkers and pillars in the framework. The absorptions at 280 nm, 275 nm and 350 nm are also assigned to the $\pi \rightarrow \pi^*$ electronic transitions in the pillar aswell as the linkers in the framework. The weak absorption broad band centered at 735 nm for $\{[Cu_2(Fu)_2(BPY)]\cdot H_2O\}_n$ confirms the $^2T_2 \leftarrow {}^2E$ electronic transition in the SBU and Cu^{2+} is in its d^9 state. The distorted octahedral geometry around Cu^{2+} is expected to show three absorptions in this region. The broad band appearing in the spectrum is attributed to be a combination of them. The Ni-based $\{[Ni_2(Ox)_2(BPY)]\cdot 3.75H_2O\}_n$ showed a weaker broad band centered at 630 nm corresponding to the d-d transition of $Ni^{2+}(d^8)$ in the paddle-wheel unit. The bands at 275 nm, 350 nm, and 630 nm as shown in Fig. 28 are ascribed to the electronic transitions $^3T_1(P) \leftarrow {}^3A_2$, $^3T_1(F) \leftarrow {}^3A_2$, and $^3T_2(F) \leftarrow {}^3A_{2,}$ respectively. The white Zn-based $\{[Zn_2(Fu)_2(BPY)]\cdot 1.5H_2O\}_n$ did not show any absorptions in the visible region, consistent with its d^{10} configuration.

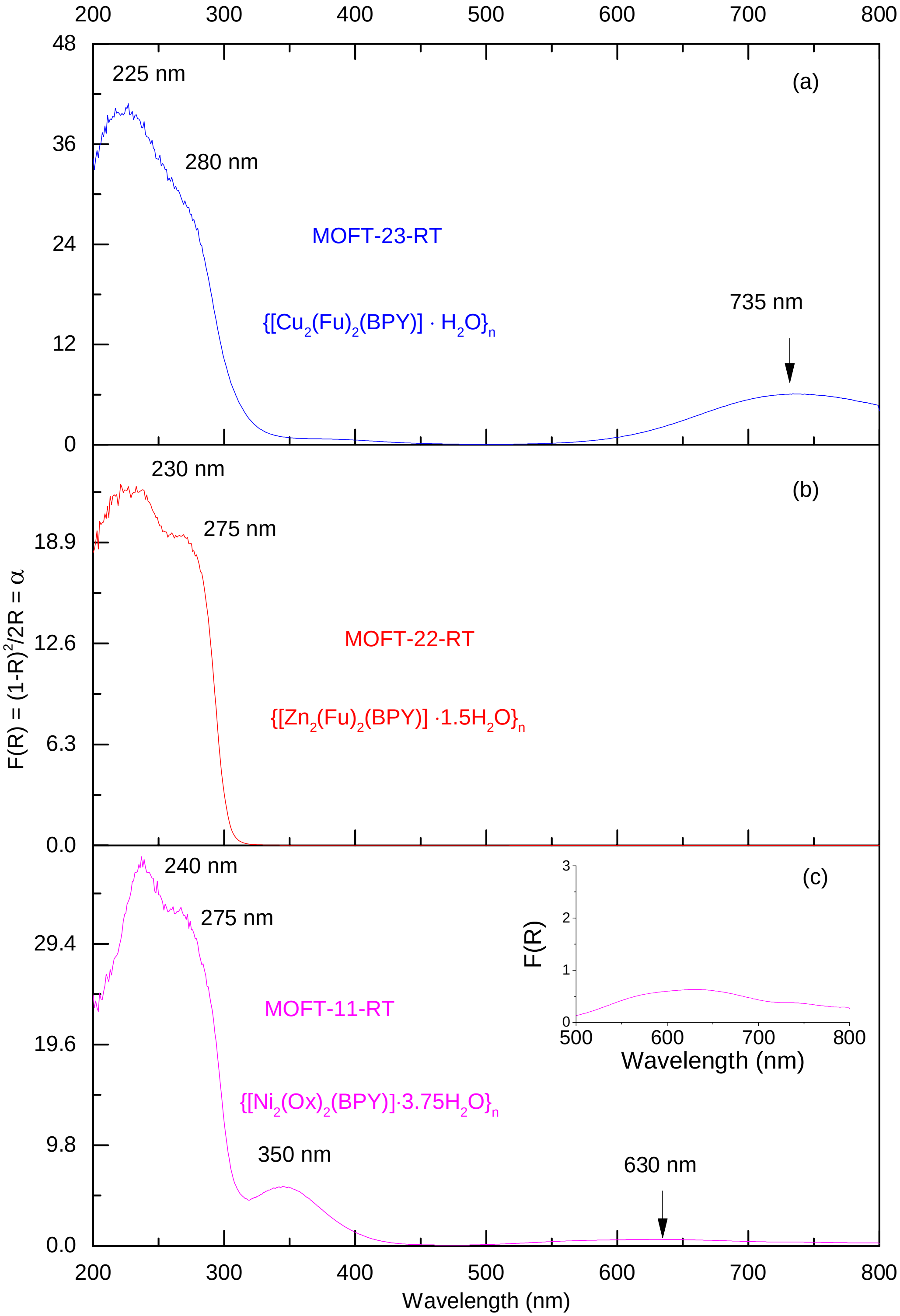

Figure 28 Solid state absorption coefficient Vs wavelength spectra for MOFT-11-RT, MOFT-22-RT, and MOFT-23-RT

Band Gap Determination

The electronic band gaps of the MOFs were determined (Fig. 29) from the plots of $(\alpha h\nu)^{1/2}$ versus photon energy (hν).[71] Where α or (F(R∞) is the absorption coefficient and hν is photon energy. Data for these plots were calculated and obtained from the diffuse reflectance versus wavelength spectral data run using Cary 5000 UV-Vis-NIR spectrometer. The optical edges or gaps were inferred by linear extrapolation of the absorbance from the high slope region obtained from the modified Kubelka-Munk ($(\alpha h\nu)^{1/2}$) versus hν plot (Fig. 29). This results in a band gap of 2.67eV and 3.76 eV for

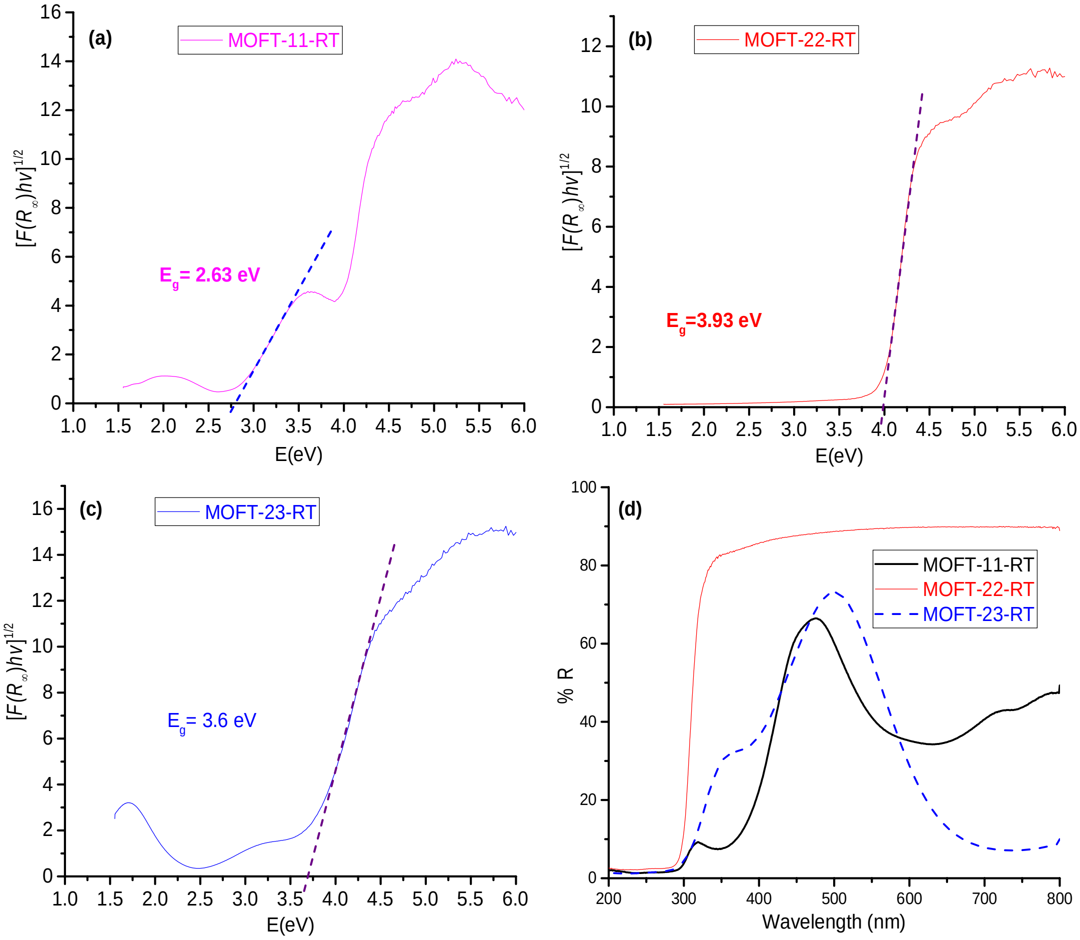

Figure 29 The optical band gaps of MOFT-11-RT (a), MOFT-22-RT (b), MOFT-23-RT (c) and UV-vis reflectance of the three MOFs from which the optical band gaps are determined (d).

$\{[Ni_2(Ox)_2(BPY)]\cdot 3.75H_2O\}_n$ which is ascribed to particles with varying size or the presence of some kind of defect, 3.93 eV for $\{[Zn_2(Fu)_2(BPY)]\cdot 1.5H_2O\}_n$ and 3.6 eV for $\{[Cu_2(Fu)_2(BPY)]\cdot H_2O\}_n$. We can generalize that $\{[Ni_2(Ox)_2(BPY)]\cdot 3.75H_2O\}_n$ is active both in the visible region and UV region, whereas $\{[Zn_2(Fu)_2(BPY)]\cdot 1.5H_2O\}_n$ and $\{[Cu_2(Fu)_2(BPY)]\cdot H_2O\}_n$ only in the UV region for application purposes.

3.4 Summary

In summary, three pillared-layer MOFs were synthesized at room temperature in low toxicity solvents. The PXRD of two of the MOFs were compared to calculated PXRD patterns from literature CIFs of the analogous MOFs prepared in DMF at higher temperatures, giving close agreement. Determination of the optical band gaps revealed that $\{[Ni_2(Ox)_2(BPY)]\cdot 3.75H_2O\}_n$ is active in the visible region, whereas $\{[Zn_2(Fu)_2(BPY)]\cdot 1.5H_2O\}_n$ and $\{[Cu_2(Fu)_2(BPY)]\cdot H_2O\}_n$ are active in the UV region. Even though single crystals could not be obtained from each MOFs, it is apparent that we are able to prepare quantitative amounts of MOFs (compared to the conventional synthesis of MOFs in a solvothermal approach using scintillation vials) under simple conditions in a beaker in benign water and methanol solvents. Our approach offers promise for preparing MOFs under sustainable conditions and potentially on large scale.

CHAPTER FOUR

4,4’-Bipyridyl Pillared MOFs: Oxalate And 2-Aminoterephthalate Salts as Source of Linkers at Room Temperature

4.1Introduction

Metal–Organic Frameworks (MOFs) are new class of porous crystalline materials consisting of metal ions or clusters and organic linkers. MOFs are prepared by assembly of metal cations/metal clusters and organic ligands.[19] As of the Scopus database result over 9,060 MOFs papers are published (Fig. 30a) from 1985 to May 2018. Of those MOFs 165 publications (Fig. 30b) are on Pillared-layer MOFs. This shows that researchers are intensively working and publishing articles on Metal-Organic Frameworks. This is due to the fact that MOFs have fascinating applications on gas storage,[86-89] gas separation,[18, 90-92] chemical sensing,[62, 93, 94] catalysis,[72, 95, 96] drug delivery[97-99] and energy storage. [100-103]

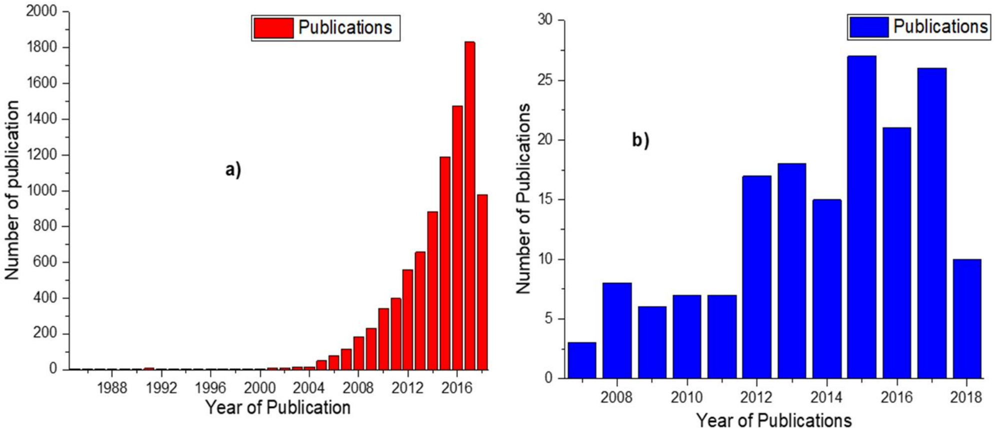

Figure 30 (a) Number of MOFs articles published per year, (b) Number of Pillared-Layer MOFs articles published per year.

MOFs are now a days classified in to four generations (Fig. 31) based on their interaction with guest species and active sites:[5] 1st generation MOFs collapse on guest removal, 2nd generation. MOFs have permanent porosity against guest removal, 3rd generation MOFs show flexible and dynamic properties, and 4th generation MOFs can sustain post-processing (modifiable positions: (1) metal/cluster sites, (2) organic linkers, and (3) vacant space).[5]

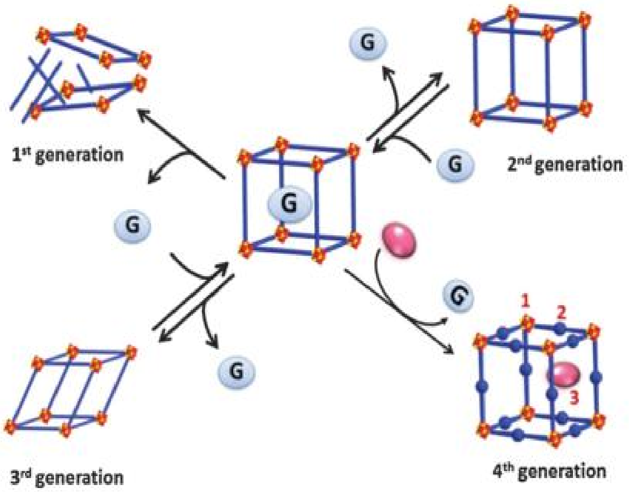

Figure 31 Classification of MOFs based on host-guest interaction[5]

Pillared-layer MOFs are amongst the third generation flexible MOFs which can undergo framework flexibility and dynamics in the solid state and may bring new applications to heterogeneous catalysis by enforcing physical, chemical and environmental stimuli responses, and utilizes the guest-host responses to accomplish transition state recognition and regulation reminiscent of the allosteric nature of enzymes.[104] Room temperature synthesis of MOFs has an advantage in that it prevents the thermally sensitive organic linkers from decomposing before they form the MOFs.[105]

Pillared-layer MOFs are constructed from infinite layers pillared by linear bidentate linkers through dative bonds or supramolecular interactions. Such a topology has greatly advanced in recent years due to the combined use of bipyridine and polycarboxylate (Scheme 7).[72, 74, 106, 107]

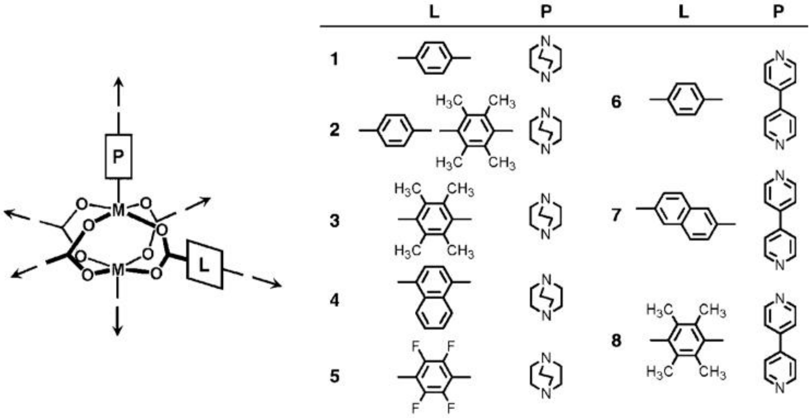

Scheme 7 Linkers (**L**) and Pillars (**P**) in paddle-wheel based nets **1-8** reported by Chun[109]

Most MOFs prepared only from dicarboxylate linkers and metal salts are unstable when exposed to water or humid as the water displaces the coordinated carboxylate oxygen. This is due to the fact that water has a higher pKa value in comparison to carboxylates. The stability of MOFs in water is increased by incorporation of nitrogen donor pillars having higher pKa value than water. The other option is to use the metal center with higher oxidation state or linkers functionalized with non-polar group.[101, 108-110]

This work is an extension of the study in Chapter Three, where we synthesized and characterized the $M_2(Fu)_2BPY$ MOFs at room temperature in a mixture of water and methanol solvents. In the work, we were able to compare the PXRD of the room temperature synthesized MOFs with that of the previously prepared same MOFs in DMF solvent and at a higher temperature. We also remind that the $\{[Ni_2(Ox)_2(BPY)]\cdot 3.75H_2O\}_n$ was synthesized and characterized. This encouraged us to extend the synthesis and characterization to zinc and copper-based pillared MOFs from Zn (II) and Cu (II) nitrate, 4,4’-bipyridine pillar and sodium oxalate as a source of a linker in a mixture of water and less toxic methanol solvents than DMF (Scheme 8).

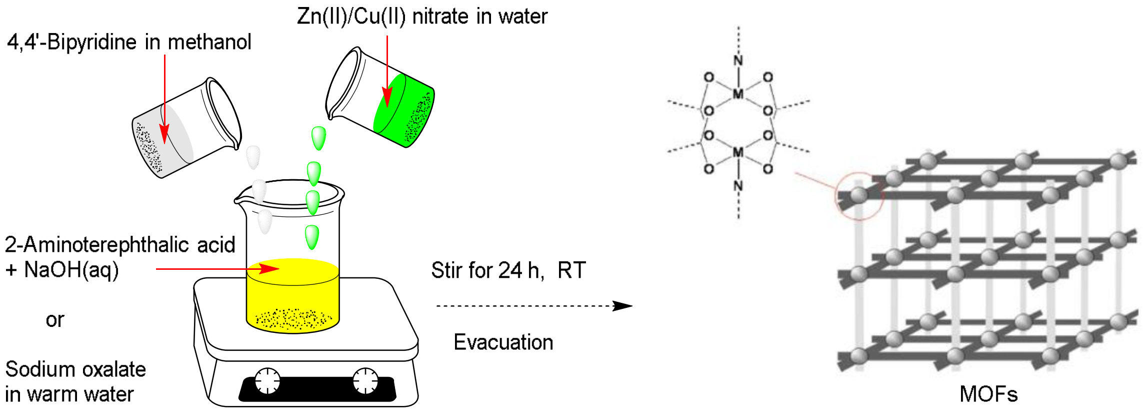

Scheme 8 Schematic representation of MOFs synthesis in the current work

Another attention was given to conversion of 2-aminoterephthalic acid into its sodium salt by reacting two equivalents of NaOH with one equivalent of 2-aminoterephthalic acid before the actual MOFs synthesis. An aqueous solution of zinc (II) nitrate, a methanolic solution of 4,4’-bipyridine and sodium salt of 2-aminoterephthalic acid could form MOFs. A salt form of the linker could easily and quickly form MOFs. This enabled the reaction to proceed at room temperature in water and methanol solvents. Researchers have been using toxic DMF solvent just to deprotonate the acidic protons of the poly-carboxylate linkers at high temperature for long period of reaction time. The current work could address this limitation and adopts a greener approach of MOFs synthesis. Analysis of PXRD, CHN, FT-IR, TGA results in the current report showed that a bi-metallic paddle-wheel is formed as the basic unit of the crystal system in each MOFs (Fig. 32 or 33). In 1973, Kanda *et al.*[111] published an article on the dithiooxamide copper coordination polymer. It was a two-dimensional polymer consisted of a bi-metallic unit without a pillar. The dithiooxamide group has similar connectivity to bi-copper unit as oxalate does in this report.

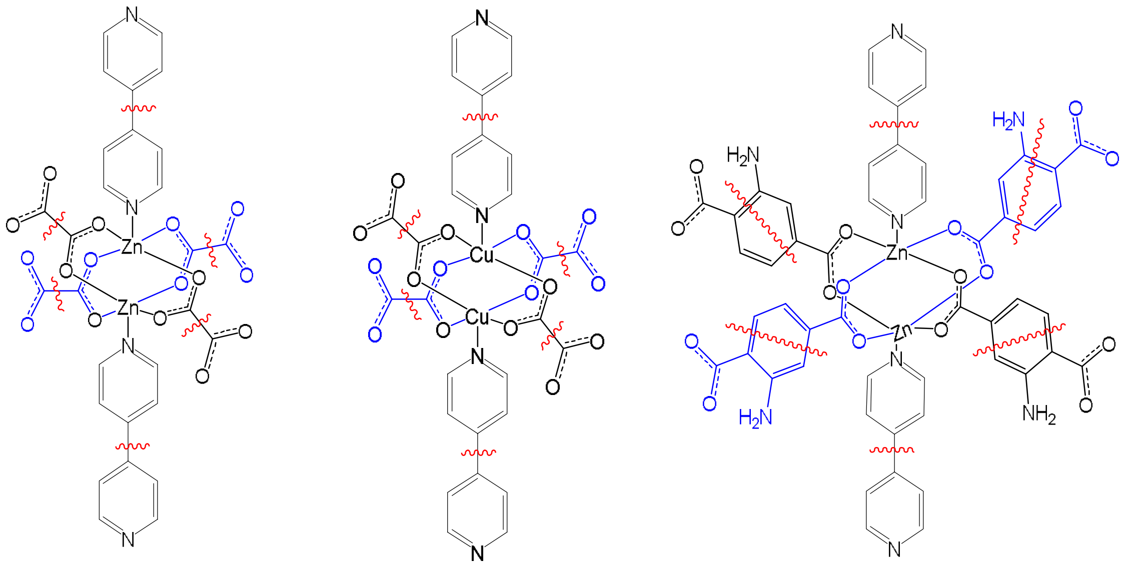

MOFT-08-RT
{[$Zn_2(Ox)_2(BPY)$]·$3.5H_2O$}$_n$

MOFT-09-RT
{[$Cu_2(Ox)_2(BPY)$]·$0.5H_2O$}$_n$

MOFT-53-RT
{[$Zn_2(ATA)_2(BPY)$]·$1.8H_2O$}$_n$

Figure 32 Paddle-wheel units in the current report: MOFT-08-RT= {[$Zn_2(Ox)_2(BPY)$]·$3.5H_2O$}$_n$; MOFT-09-RT={[$Cu_2(Ox)_2(BPY)$]·$0.5H_2O$}$_n$; and MOFT-53-RT={[$Zn_2(ATA)_2(BPY)$]·$1.8H_2O$}$_n$. Note that guest solvent molecules are excluded from the paddle- wheel units.

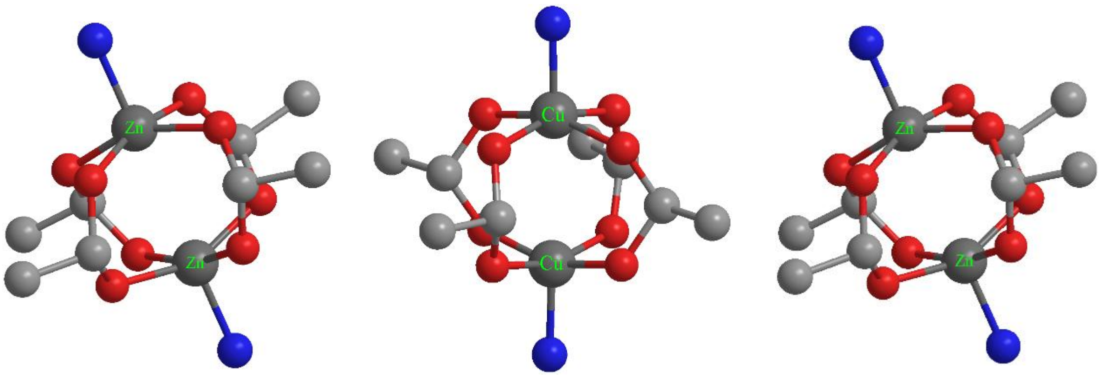

MOFT-08-RT

MOFT-09-RT

MOFT-53-RT

Figure 33 3D version of the paddle-wheel units for MOFT-08-RT, MOFT-09-RT, and MOFT-53-RT

4.2Experimental

Synthesis of MOFT-08-RT ({$[Zn_2(Ox)_2(BPY)]\cdot3.5H_2O$}$_n$)

{$[Zn_2(Ox)_2(BPY)]\cdot3.5H_2O$}$_n$ was synthesized by a simple modification of the procedure previously reported.[74, 78] In this synthesis, Na_2Ox (4 mmol, 0.540 g) was dissolved in warm deionized water (20 mL). To this solution 40 mL methanolic solution of $BPY\cdot H_2O$ (2 mmol, 0.348 g) was added. The combined mixture was stirred for 30 min and $Zn(NO_3)_2\cdot6H_2O$ (4 mmol, 1.189 g) was added. pH of the solution was monitored and found to be about 6. The overall mixture was stirred at room temperature for 24 hours. A white colored product was observed. It was filtered under suction, washed with 3 x 5 mL of deionized water and then with 3 x 5 mL of methanol and dried in a vacuum oven at 80 ^oC for 5 h, yielding 0.95 g (ca. 91 % based on BPY) of $[Zn_2(Ox)_2(BPY)]\cdot3.5H_2O$}$_n$ in the form of white solid. Elemental analyses: Calcd. (found) % for $C_{14}H_{14.5}N_2O_{11.25}Zn_2$: C, 32.24; H, 2.80; N, 5.32 %. (C, 32.36); (H, 2.58); (N, 5.13).

Synthesis of MOFT-09-RT ({$[Cu_2(Ox)_2(BPY)]\cdot0.5H_2O$}$_n$)

{$[Cu_2(Ox)_2(BPY)]\cdot0.5H_2O$}$_n$ was synthesized by the simple modification of the procedure previously reported.[74, 78] In this synthesis, Na_2Ox (1 mmol, 0.134 g) was dissolved in warm deionized water (10 mL). To this solution 30 mL methanolic solution of $BPY\cdot H_2O$ (0.5 mmol, 0.087 g) was added. The combined mixture was stirred for 30 min and $Cu(NO_3)_2\cdot3H_2O$ (1 mmol, 0.242 g) was added. The overall mixture was stirred at room temperature for 24 hours. The resulting product was filtered under suction, washed with 3 x 5 mL of deionized water and then with 3 x 5 mL of methanol and evacuated in a vacuum oven at 80 ^oC for 5 h, yielding 0.198 g (ca. 84% based on BPY) of

$\{[Cu_2(Ox)_2(BPY)]\cdot 0.5H_2O\}_n$ in the form of light blue solid (Ox=Oxalate). Elemental analyses: Calcd. (found) % for $C_{14}H_9N_2Cu_2O_{8.5}$: C, 35.9; H, 1.94; N, 5.98%. (C, 35.83); (H, 1.73); (N, 5.97).

Synthesis of MOFT-53NT-RT ($\{[Zn_2(ATA)_2(BPY)]\cdot H_2O\}_n$)

$\{[Zn_2(ATA)_2(BPY)]\cdot H_2O\}_n$ was synthesized by a simple modification of the procedure previously reported.[74, 77, 78] A clear solution of $Na_2(ATA)$ was prepared by dissolving 8 mmol (0.32 g) of NaOH in 45 mL Milli-Q water and adding 4 mmol (0.7243 g) of 2-aminoterephthalic acid while stirring at room temperature. To the above solution, 50 mL of a methanolic solution of BPY (2 mmol, 0.348 g) (BPY= 4,4'-bipyridyl hydrate) was added. The combined solution was stirred for 30 min and $Zn(NO_3)_2\cdot 6H_2O$ (4 mmol, 1.189 g) in water (5 mL) was added forming a yellowish-colored suspension. The overall mixture was stirred at room temperature for 24 hours. The resulting product was filtered under suction, washed with 3 x 5 mL of Milli-Q water followed by 3 x 5 mL of methanol and then dried in an evacuated vacuum oven at 80 ^{o}C for 12 h, yielding 1.057 g (ca. 79% based on BPY) of a yellowish colour solid $\{[Zn_2(ATA)_2(BPY)]\cdot H_2O\}_n$. Elemental analyses: Calcd. (found) % for $C_{26}H_{20}N_4O_9Zn_2$: C, 47.08; H, 3.04; N, 8.45%. (C, 47.43); (H, 2.97); (N, 8.49).

4.3 Results and Discussion

PXRD: The crystallinity of the MOF products was determined by powder x-ray diffraction (PXRD) technique. As shown in Fig. 34, the well-defined diffraction pattern revealed the

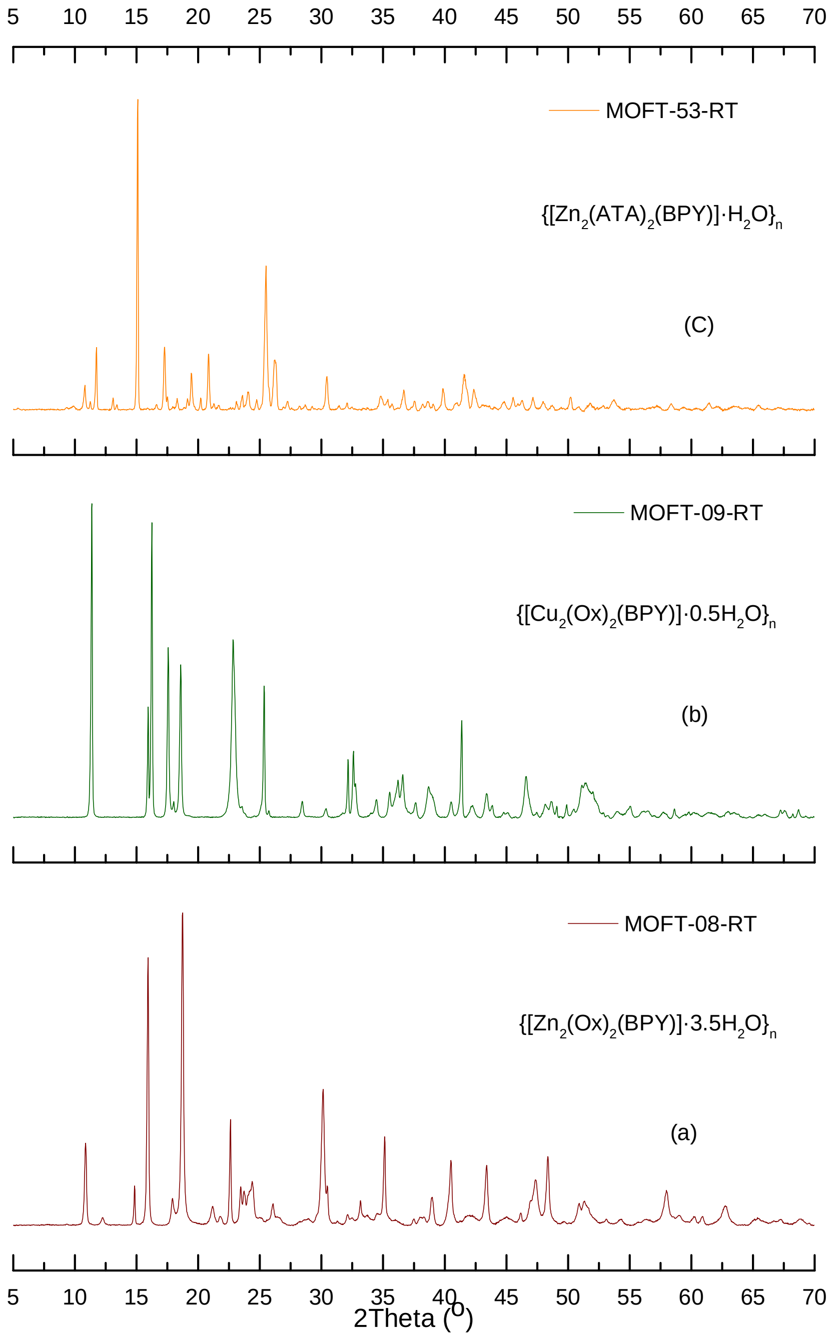

Figure 34 PXRD patterns for (a) MOFT-08-RT, (b) MOFT-09-RT and (c) MOFT-53-RT

high crystallinity of the MOFs products. Sharp and high-intensity diffraction peaks in the range of 2θ= 10 – 25 were observed in common to $\{[Zn_2(Ox)_2(BPY)]\cdot 3.5H_2O\}_n$, $\{[Cu_2(Ox)_2(BPY)]\cdot 0.5H_2O\}_n$, and $\{[Zn_2(ATA)_2(BPY)]\cdot H_2O\}_n$. The Zn (II) based MOFT-08-RT (Fig. 34a) showed sharp diffraction peaks at 2θ= 10.9, 14.8, 16.1, 18.6, 22.7. The PXRD patterns of the MOFs were indexed and Rietveld refined with DICVOL06 in Expo2014 software.[79] This resulted in MOFT-08-RT (Table 4) crystallized with monoclinic crystal system and space group: P2/m, cell parameters: *a* 16.3668Å *b* 15.5878Å *c* 8.1424Å, α 90.00 β 93.79 γ 90.00 and ρ (g/cm^3) 2.13. Similarly, the Cu (II) based MOFT-09-RT (Fig. 34b) showed sharp and high-intensity diffraction peaks at 2θ= 11.3, 16.2, 17.7, 18.6, 22.85, and 25.2. Indexation with DICVOL06 and Rietveld refinement revealed that MOFT-09-RT (Table 4) crystallized with a monoclinic crystal system and space group: P2/m, cell parameters: *a* 10.9529Å *b* 11.1327Å *c* 5.5095Å, α 90.00 β 94.01 γ 90.00 and ρ(g/cm^3) 1.18. These two MOFs products differ only in the metal center and have the same linker (oxalate) and the same pillar (4,4'bipyridine). The third and the Zn(II) based MOFT-53-RT (Fig. 34c) is shown with diffraction peaks at 2θ= 10.8, 11.8, 14.8, 17.0, 19.4, 21.7, and 25.4. This MOFs product has the same pillar and metal center as MOFT-08-RT but differs in its linker (2-aminoterephthalic acid). DICVOL06 indexation and Rietveld refinement of the PXRD pattern by Expo2014 showed that MOFT-53-RT (Table 4) has a triclinic crystal system with space group: P-1, cell parameters: *a* 9.650(3)Å *b* 10.920(2)Å *c* 13.382(3)Å, α 98.988(12) β 91.49(2) γ 106.301(11) and ρ*(g/cm^3)* 1.82. The MOFs products were obtained as powder and were not soluble in most solvents. Therefore, recrystallization and crystal growth experiment to find crystals suitable for single crystal x-ray diffraction (SXRD) study was not done for all the MOFs. In the case when powdered

MOFs are obtained by synthesis, Expo2014 software is a good tool of kits for phasing crystal structures directly from powder data.[79]

The crystallite sizes estimated by the Scherrer formula (K= 0.94) using the match! 3 software are 482.6 Å, 2521.0 Å, and 2381.6 Å for MOFT-08-RT, MOFT-09-RT, and MOFT-53-RT, respectively. The peaks in the XRD patterns between 2θ= 30-50 that are appropriate for crystallite size estimation were automatically selected by the software.

Table 4 Crystal data and structural refinement parameters

	MOFT-08-RT	**MOFT-09-RT**	**MOFT-53-RT**
Empirical formula	$C_{14}H_{14.5}N_2Zn_2O_{11.25}$	$C_{14}H_9N_2Cu_2O_{8.5}$	$C_{26}H_{20}N_4O_9Zn_2$
Formula weight	521.53	468.32	663.22
Crystal system	Monoclinic	Monoclinic	Triclinic
Space group	P2/m	P2/m	P-1
a(Å)	16.3668	10.9529	9.650(3)
b(Å)	15.5878	11.1327	10.920(2)
c (Å)	8.1424	5.5095	13.382(3)
α (°)	90.00	90.00	98.988(12)
β (°)	93.79	94.01	91.49(2)
γ (°)	90.00	90.00	106.301(11)
V(Å^3)	2072.78	670.15	1333.3(6)
Z	4	1.5	2
ρ_{calc} (g cm^{-3})	2.13	1.18	1.82
Counts	2475	2347	2475
λ(nm)	1.540598	1.540598	1.540598

FT-IR: The IR spectra of $\{[Zn_2(Ox)_2(BPY)]\cdot 3.5H_2O\}_n$, $\{[Cu_2(Ox)_2(BPY)]\cdot 0.5H_2O\}_n$, and $\{[Zn_2(ATA)_2(BPY)]\cdot H_2O\}_n$ are shown in Fig. 35 and Appendix D. The asymmetric and symmetric NH_2 stretching vibrations observed at 3507 and 3390 cm^{-1} for 2-aminoterephthalic acid (2ATA) in Fig. 35d are shifted to 3401 and 3322 cm^{-1} in the resulting MOFT-53-RT (Fig. 35c). The broad band merging to the NH_2 vibrations signifies that there is water molecule in this MOFs. The peaks at 1610 and 1500 cm^{-1} in Fig. 35d might represent N-H bending band and NH_2 wagging and twisting band, respectively. The C=O stretching frequency observed in 2ATA at 1678 cm^{-1} is shifted to 1564 cm^{-1} in the IR spectrum of MOFT-53-RT (Fig. 35c). Similarly, in Fig. 35f the C=O stretching frequency of oxalate is observed at 1642 cm^{-1}, and the C=O stretching frequency (strong) in the resulting MOFT-08-RT and MOFT-09-RT are observed at 1618 cm^{-1} after coordination to

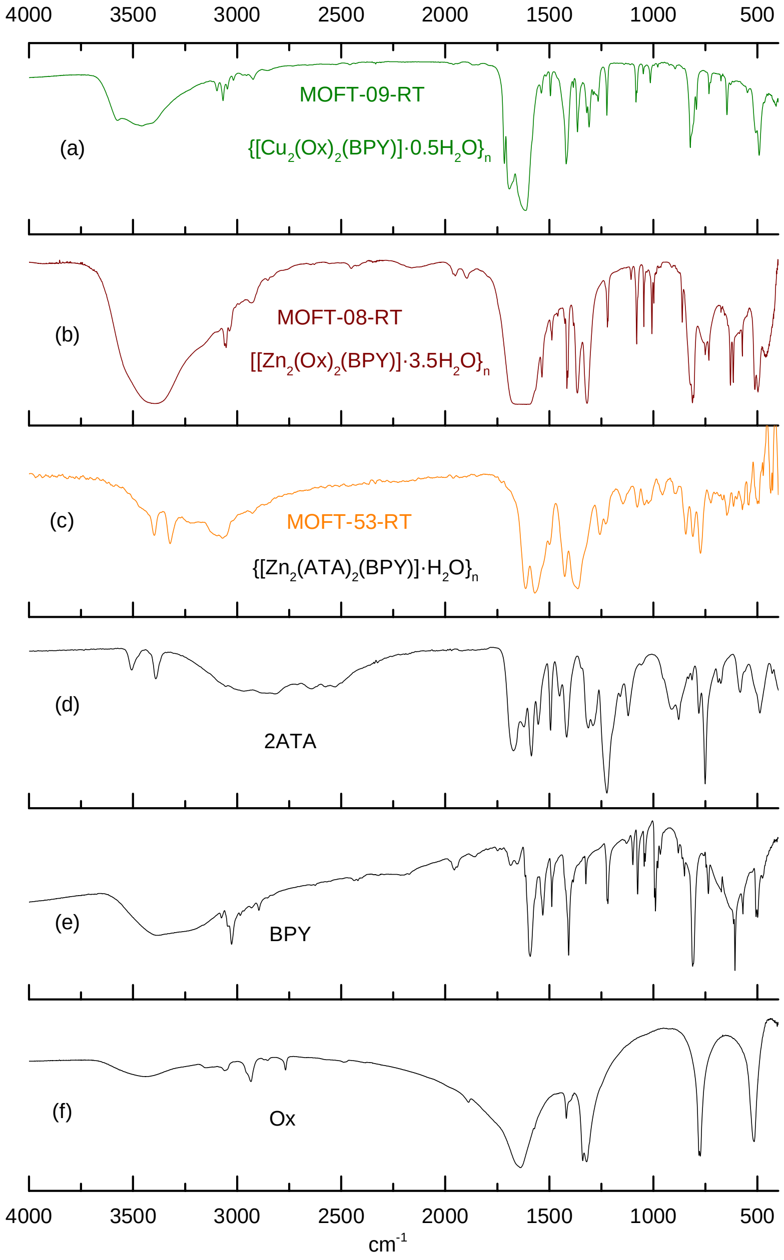

Figure 35 FT-IR Spectra of (a) MOFT-09-RT, (b) MOFT-08-RT, (c) MOFT-53-RT, (d) 2-Aminoterephthalat (e) 4,4’-bipyridine, (f) Sodium oxalate

Zn(II) and Cu(II), respectively. The C-N stretching frequency of the pillar (4,4'-BPY) is observed at 1583 cm^{-1} (Fig. 35e). This peak is shifted and coincident with the C=O stretching frequency of MOFT-08-RT, MOFT-09-RT, and MOFT-53-RT. The peaks at 407 cm^{-1} in Fig. 35a, c and 454 cm^{-1} in Fig. 35b are ascribed to the coordination of nitrogen to the corresponding metal center.[112, 113] The broad bands centered at about 3400 cm^{-1} are ascribed to presence of water in all the MOFs. Generally, the shift in the vibrational frequency in the FT-IR spectra show coordination of oxygen and nitrogen to the Zn(II) in MOFT-08-RT and MOFT-53-RT, Cu(II) in MOFT-09-RT.[114-117]

Thermal Analysis

The thermal stabilities of $\{[Zn_2(Ox)_2(BPY)]\cdot 3.5H_2O\}_n$ and $\{[Cu_2(Ox)_2(BPY)]\cdot 0.5H_2O\}_n$ were examined by TGA under an argon atmosphere and that of $\{[Zn_2(ATA)_2(BPY)]\cdot H_2O\}_n$ in air from room temperature to 700 ^oC using heating rate of 10 ^oC min^{-1} and the differential curves associated with the TGA curve shows the sharp weight losses at a different temperature as depicted in Fig. 36-38.

MOFT-08-RT: The TGA curve of $\{[Zn_2(Ox)_2(BPY)]\cdot 3.5H_2O\}_n$ in Fig.36 shows a first sharp differential weight loss of 5.7 % (calcd.5.46 %) at 94.3 ^oC implying a loss of 1.6 adsorbed water molecules from the moisture. The next 7.4 % differential weight loss (calcd.7.31 %) at 186.9 ^oC is assigned to loss of two guest water molecules from the MOF structure. The massive and sharp differential weight losses at 327 ^oC and 352 ^oC show collapse of the framework and losses of the organic matter. The final 32 % (calcd. 31 %) residue in the TGA curve of MOFT-08-RT is attributed to the formation of two ZnO. The final oxide residue also confirms the presence of two Zn (II) in the empirical formula of $\{[Zn_2(Ox)_2(BPY)]\cdot3.5H_2O\}_n$ in the paddle wheel unit.

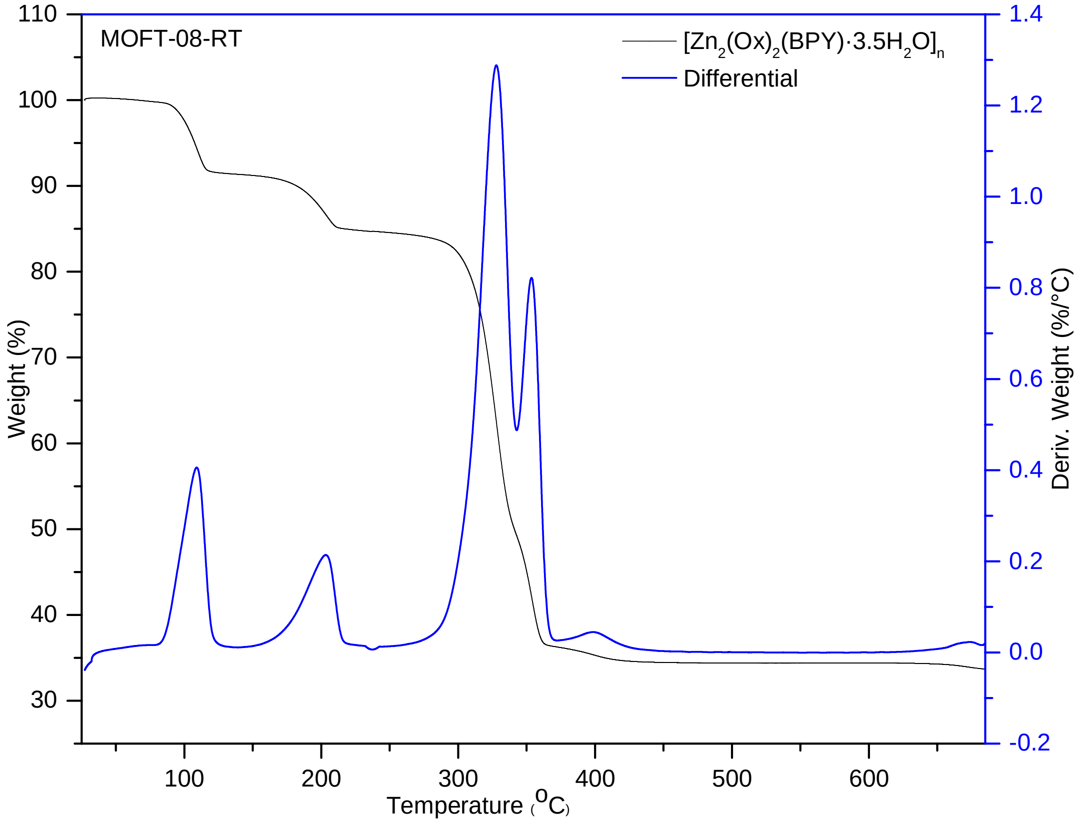

Figure 36 TGA of MOFT-08-RT

MOFT-09-RT: In Fig.37, a thermogravimetric analysis shows $\{[Cu_2(Ox)_2(BPY)]\cdot0.5H_2O\}_n$ lost 1.7 % of its weight (calc. 1.9 %) as 0.5 H_2O up to 227 °C. The next massive and sharp weight loss shown by the differential curve centered at 247 °C is ascribed to collapse of the MOFs framework and removal of the organic matter. The plateau in the TGA curve above 300 °C corresponding to 33. 57 % weight residue matched very well with two CuO (calc. 33.97 %). The weight percent of 2CuO residue gave information about the weight percent of Cu in the MOFs. This corresponds to two Cu(II) in the empirical formula of $\{[Cu_2(Ox)_2(BPY)]\cdot 0.5H_2O\}_n$.

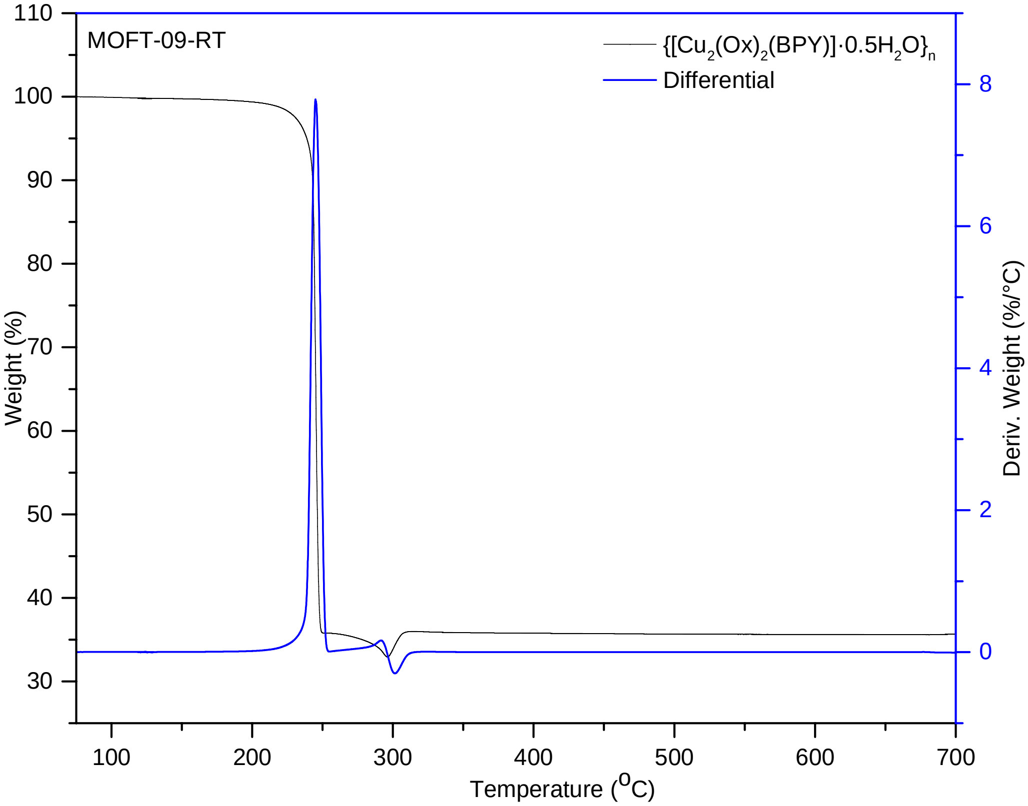

Figure 37 TGA of MOFT-09-RT

MOFT-53-RT. The TGA curve in Fig. 38 depicts $\{[Zn_2(ATA)_2(BPY)]\cdot H_2O\}_n$ has good thermal stability up to nearly 400 °C. The first 3.11 % (calc. 2.72 %) weight loss until 225 °C is assigned to losses of one guest water molecules from the MOFs structure. The huge and sharp differential weight loss shown and centered at 425 °C depicts the collapse of the framework by losing the organic matter. This is the point where the MOFs loses its stability. The 24.0 % weight residue (calc. 24.54 %) shown in the plateau above 470 °C in the TGA curve corresponds to the two equivalents of residual ZnO. This residue also confirms two Zn (II) in the empirical formula of $\{[Zn_2(ATA)_2(BPY)]\cdot H_2O\}_n$ in the paddle-wheel.

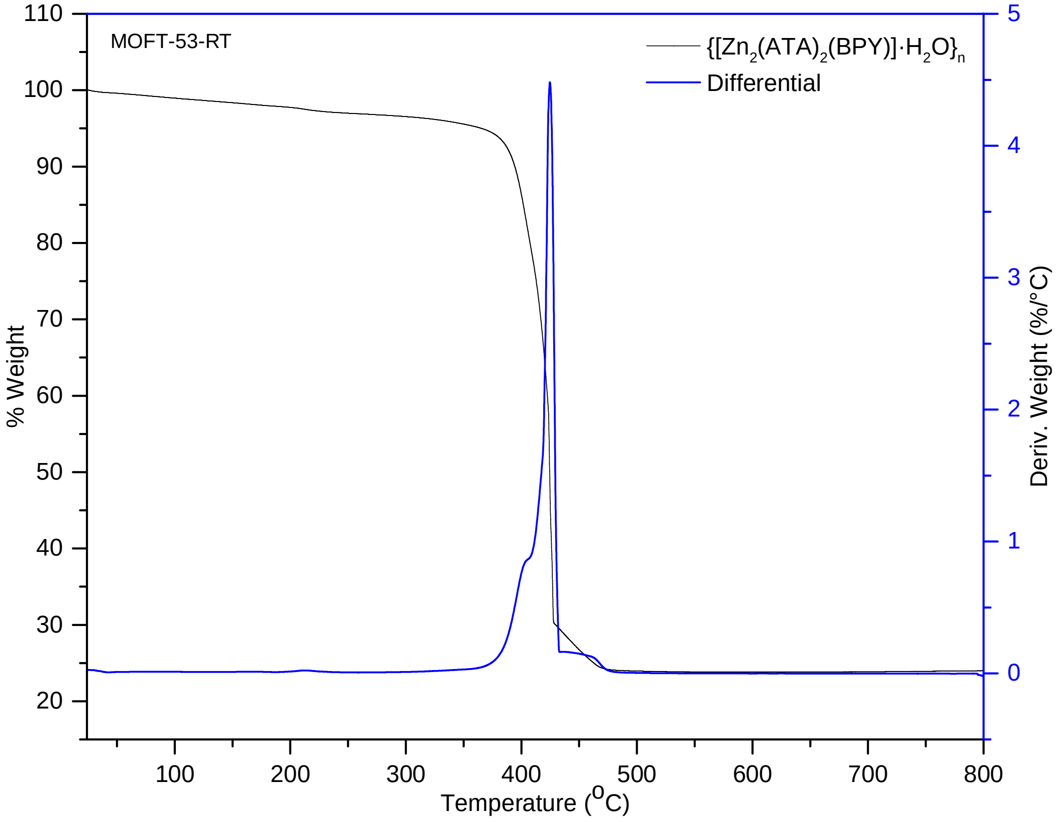

Figure 38 TGA of MOFT-53-RT

Determination of Surface Area, Pore Volume and Pore Size

The Brunauer-Emmet-Teller (BET) surface areas of MOFs were determined as follows: About 40 mg MOF samples were degassed under vacuum at 180 ^{0}C for 3 h to remove moisture from the pores of the MOFs. The MOF samples were then placed in an automatic Surface Area Analyzer (Micromeritics 3Flex Surface Characterization Analyzer), which measures adsorption/ desorption of nitrogen gas at 77 K. The BET surface areas of the samples were calculated using N_2 adsorption data at 77 K. Fig. 39 and Table 5 show the

N_2-gas adsorption/ desorption isotherms, porosity distribution curves and summary of the BET surface areas, respectively. The pore diameter of MOFT-08-RT is calculated and

Table 5 N_2-sorption data for MOFT-08-RT, MOFT-09-RT, and MOFT-53-RT

MOFs	Pore diameter [nm]	BJH Pore Volume [cm^3g^{-1}]	Surface area [m^2g^{-1}]
			BET
MOFT-08-RT	3.27	0.67	711.6
MOFT-09-RT	3.17	0.93	988.6
MOFT-53-RT	3.27	0.41	454.3

determined from porosity distribution curve as 3.27 nm with a BJH pore volume of 0.67 cm^3g^{-1} and a BET surface area of 711.6 m^2g^{-1}. MOFT-09-RT showed a pore diameter of 3.17 nm and a BJH pore volume of 0.93 cm^3g^{-1} with a BET surface area of 988.6 m^2g^{-1}. MOFT-53-RT is different from the above two MOFs in its linker. It was prepared by replacing the oxalate linker with 2-aminoterephitalate keeping the pillar 4,4'-bipyridine the same and using Zn (II) metal source. The average pore diameter for MOFT-53-RT is 3.27 nm and BET surface area of 454.3 m^2g^{-1}. Of the three MOFs reported in here, MOFT-53-RT has the least BET surface area. This is ascribed to the amino functionality takes space and decreases the BET Surface area in the MOFs. The adsorption and desorption of N_2 gas in the hysteresis overlapped one over the other (Fig. 39a, b, c). Room temperature synthesized powdered MOF-5 by Yaghi and co-workers[105] shows similar isotherm to the current work. The isotherms are somewhat different from the models explained in report given in 2015 by IUPAC.[3] This is attributed to the flexibility that exist in most pillared-layer MOFs as the pore size differ during the host-guest interaction up on adsorption and desorption process.[118] Information about the pore widths was obtained from the mesopore size distribution curves of the three MOFs in this study as shown in Fig. 39a’, b’, and c’ for MOFT-08-RT, MOFT- 09-RT and MOFT-53-RT, respectively.

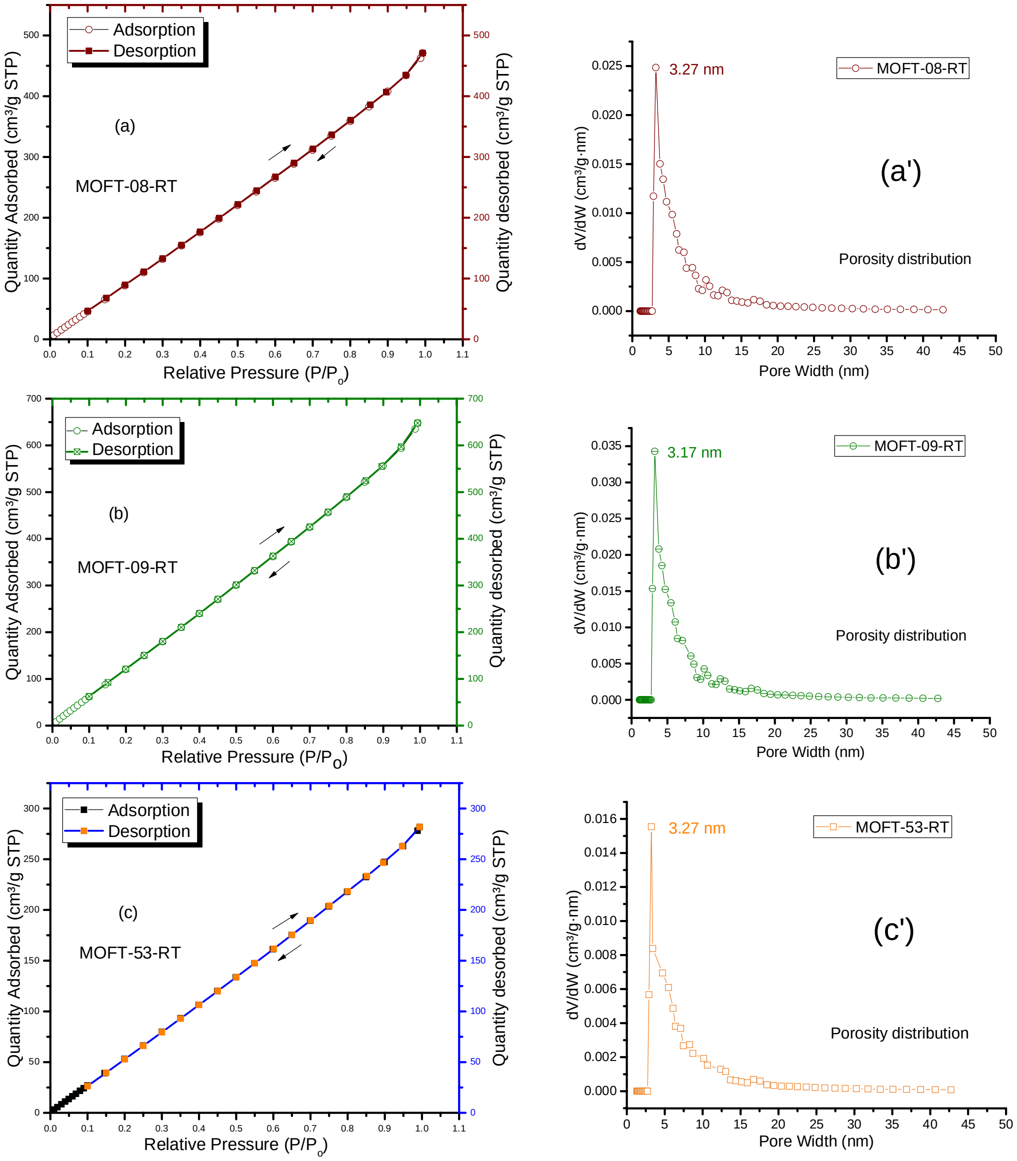

Figure 39 N_2 adsorption-desorption isotherms for MOFT-08-RT (a), MOFT-09-RT (b) and MOFT-53-RT (c): porosity distribution for MOFT-08-RT (a’), MOFT-09-RT (b’) and MOFT-53-RT (c’)

Morphological Characterization

SEM micrographs and X-ray microanalysis (SEM/EDS) were recorded by using FEI Quanta 650 ESEM instrument equipped with Oxford Instruments X-Max 150 mm^2 EDS detector with AZtec software at 20kV, spot 3-4, using low vacuum x-ray cone accessory at 80Pa. Fig. 40a shows that MOFT-08-RT crystals have very tiny cubic like morphology. In comparison, MOFT-09-RT crystals (Fig. 40b) were rod-shaped. SEM image of MOFT-53-RT (Fig. 40c) shows needle-shaped morphology forming a sphere like cluster. The SEM/EDS analysis gives information about the sample surfaces with high depth of field and lateral resolutions of around 1-20 nm.[84, 85] This means that the EDS microanalysis cannot show the bulk micro analysis and is only the surface analysis. SEM/EDS analysis of MOFT-08-RT in some portion of the surface (Fig. 41a') shows 67.2 % oxygen, 24.4 % carbon and 8 % Zinc by weight. Similar analysis of MOFT-09-RT in some portion of the surface (Fig. 42b') shows 64.3 % oxygen, 22.9 % carbon, 12.5 % copper by weight. SEM/EDS micro analysis of MOFT-53-RT also gave information about the surface (Fig. 43c') as 68.5 % oxygen, 25.1 % carbon, and 6.1 % zinc. The SEM/EDS micro analysis depicted the major species that constitute the MOFs framework near the surface.

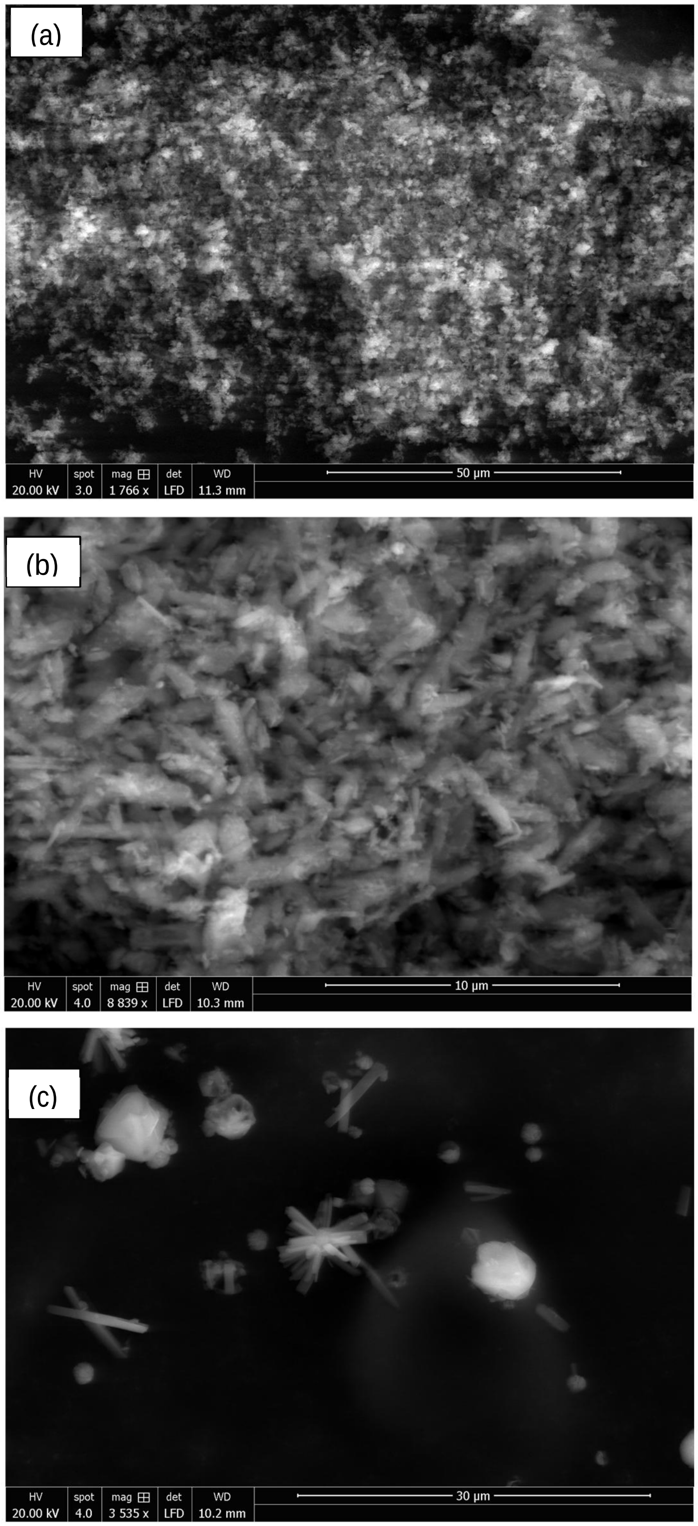

Figure 40 SEM images of MOFT-08-RT (a), MOFT-09-RT (b) and MOFT-53 (c)

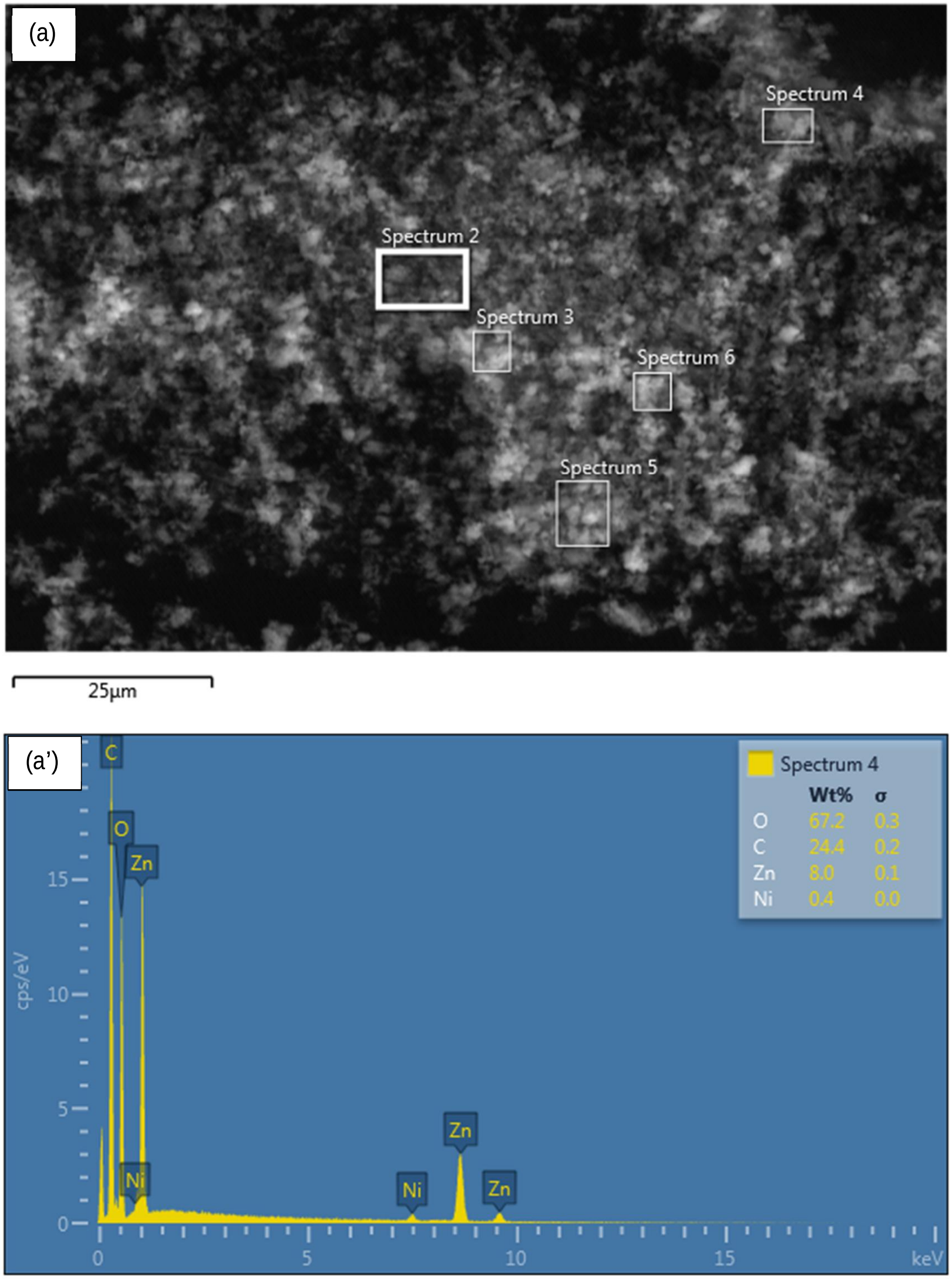

Figure 41 SEM image (a) and EDS (a') of MOFT-08-RT

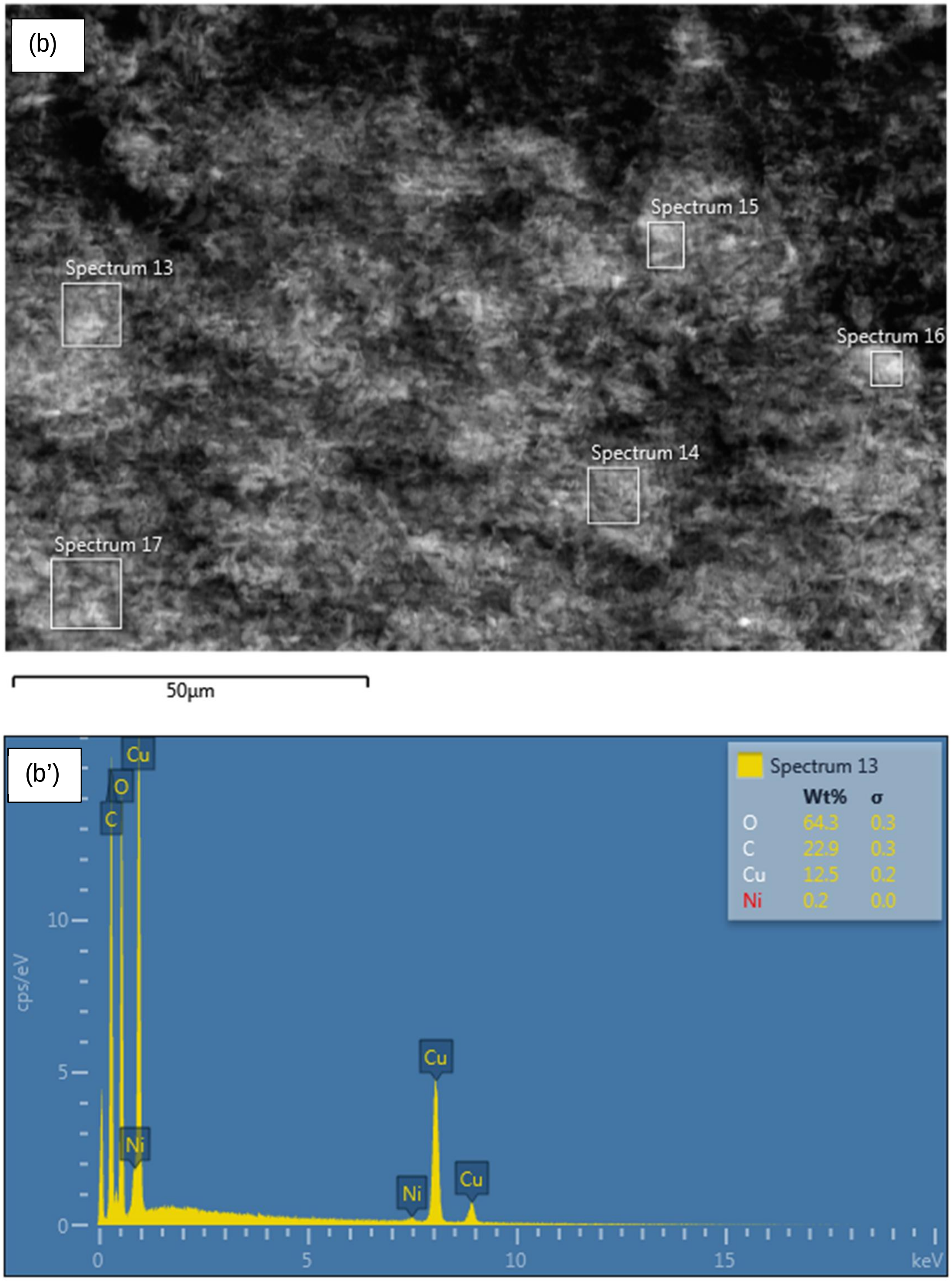

Figure 42 SEM image (b) and EDS (b') of MOFT-09-RT

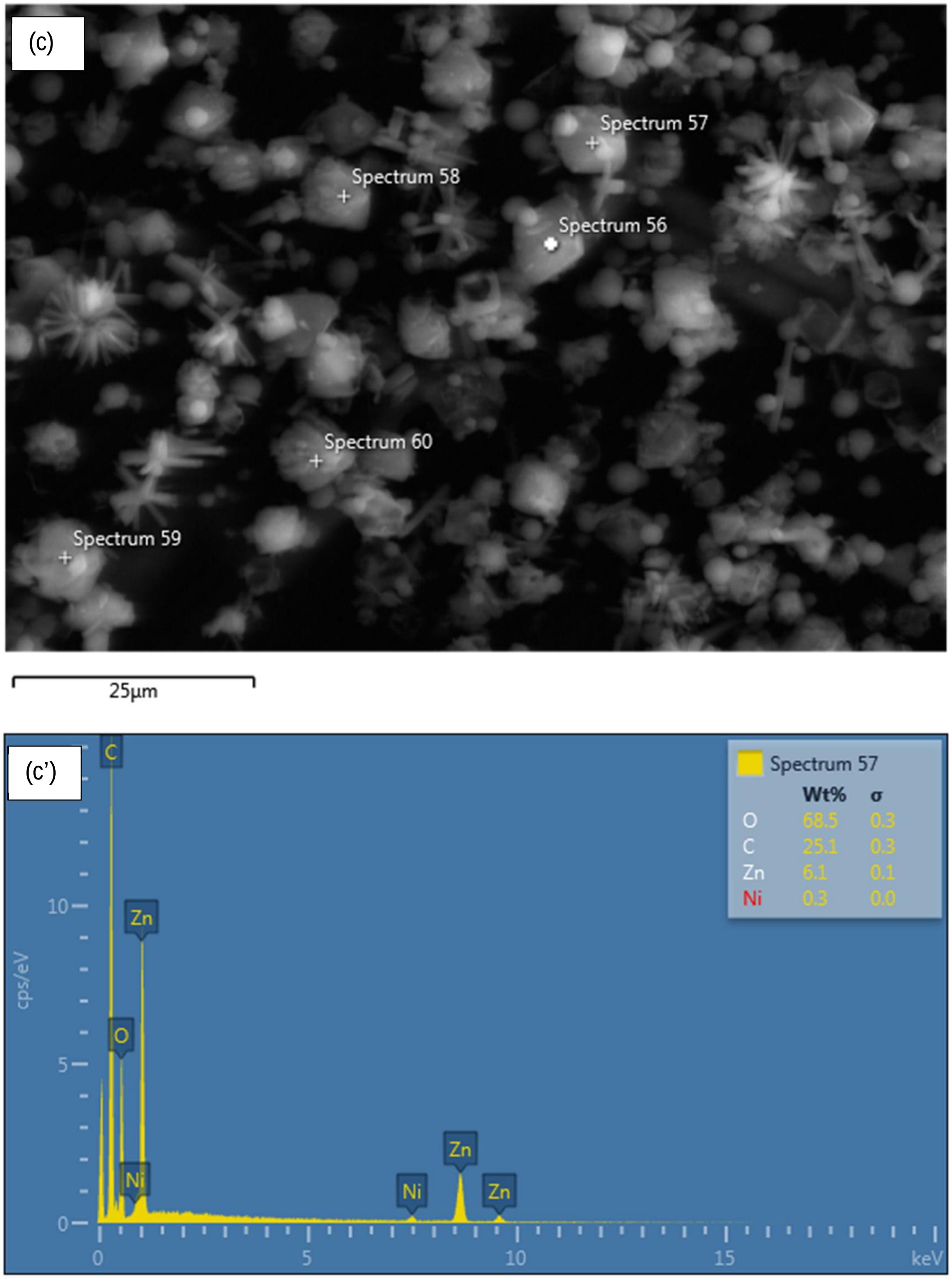

Figure 43 SEM image (c) and EDS (c') of MOFT-53-RT

Solid State UV-Vis Study

The solid state uv-vis spectra of MOFT-08-RT, MOFT-09-RT, and MOFT-53-RT are shown in Fig. 44. The spectra are plotted as the absorption coefficient α or F(R) which is known as the Kubelka-Munk function vs wavelength of the uv-vis light absorbed by microcrystalline powdered MOFs. The Cu- based MOFT-09-RT in Fig. 44b was recorded

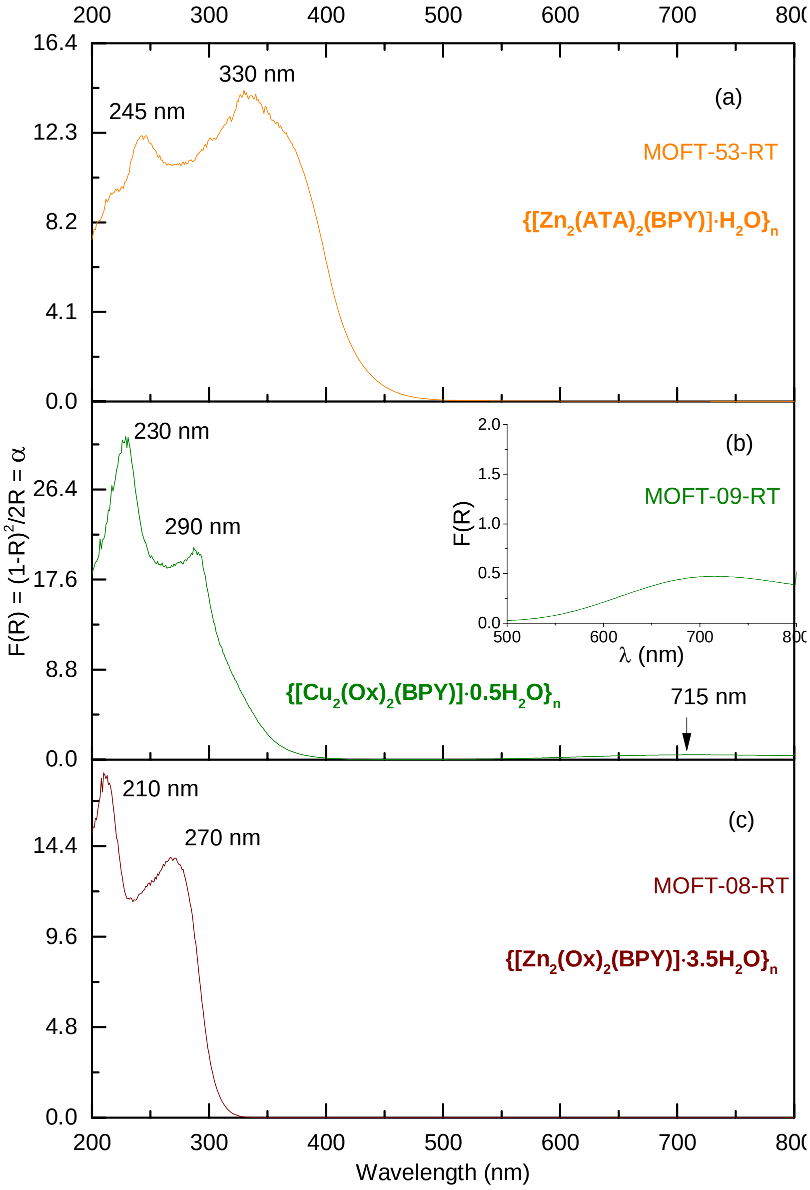

Figure 44 Solid state Uv-Vis spectra of MOFT-53-RT, MOFT-09-RT, and MOFT-08-RT

as having a week absorptive coefficient broadband centered at 715 nm corresponding to the $^2T_{2g} \leftarrow {}^2E_g$. This shows that the paddle wheel unit consists of Cu^{2+} species in d^9 state. The Zn-based MOFT-08-RT (Fig. 44c) and MOFT-53-RT (Fig. 44a) do not show such a week intensity broad band at higher wevelengths. This is ascribed to the presence of Zn^{2+} in the paddle wheel with filled d^{10} orbitals. The most intense bands bellow 400 nm in all the MOFs at 245 nm, 230 nm, and 210 nm are assigned to the $n \rightarrow \sigma^*$ electronic transitions in with in the linkers and pillars in the framework as showen in Fig 44. The band assignments at 330 nm 290 nm, and 270 nm are asscribed to the $\pi \rightarrow \pi^*$ electronic transiotions with in the linkers and pillars in the respective MOFs.

Band gap determination

The band gaps of the MOFs were determined (Fig. 45) from the plots of $(\alpha h\nu)^{1/2}$ versus photon energy ($h\nu$).[71] Where α or ($F(R_\infty)$) is the absorption coefficient and $h\nu$ is photon energy. Data for these plots were calculated and obtained from the diffuse reflectance versus wavelength spectral data run using Cary 5000 UV-Vis-NIR spectrometer. The optical edges or gaps were inferred by linear extrapolation of the absorbance from the high slope region obtained from the modified Kubelka-Munk ($(\alpha h\nu)^{1/2}$) versus $h\nu$ plot. This results in a band gap of 3.86 eV for MOFT-08-RT (photo active in the UV region), 3.18 eV for MOFT-09-RT (photo active in the UV region) and 2.63 eV for MOFT-53-RT (photo active in the visible region).

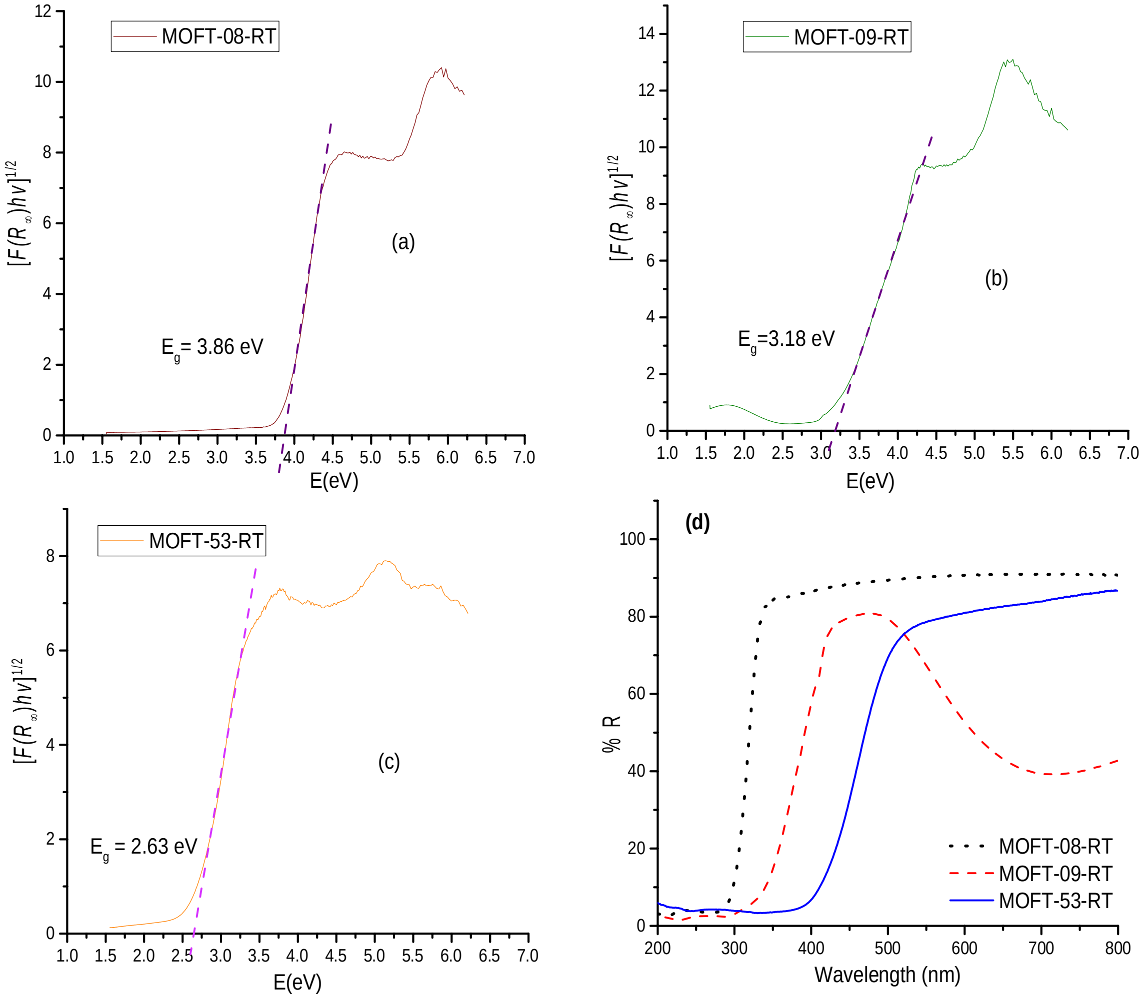

Figure 45 Optical band gaps of MOFT-08-RT (a), MOFT-09-RT (b), MOFT-53-RT (c) and DRS of the respective MOFs from which the energy gaps are determined.

Magnetic Properties

The magnetic properties of the three MOFs, $\{[Cu_2(Ox)_2(BPY)]\cdot0.5H_2O\}_n$, $\{[Ni_2(Ox)_2(BPY)]\cdot3.75H_2O\}_n$, and $\{[Cu_2(Fu)_2(BPY)]\cdot H_2O\}_n$ are measured at 294 K using the MSB AUTO (Sherwood Scientific) and shown in Table 6. Magnetic susceptibility measurement of MOFT-23-RT ($\{[Cu_2(Fu)_2(BPY)]\cdot H_2O\}_n$) by the inverse Gouy method shows that the gram susceptibility or $\chi_g = 3.379 \times 10^{-6}$ for which the effective magnetic moment, μ_{eff}, after calculating the diamagnetic correction is 2.1 BM. This value corresponds to the presence of 1.37 unpaired electrons (n) in this bimetallic system. This is less than the two unpaired electrons expected in the two Cu(II) centers (one for each, $(d_{z^2})^1$ or $(d_{x^2-y^2})^1$) in the paddle wheel. The decrease in the number of unpaired electrons observed is ascribed to the presence of metal to metal magnetic communication (Scheme 9) through the diamagnetic pillar (BPY) and /or linker (fumarate). If the single unpaired electron occupies (d_{z^2}) or ($d_{x^2-y^2}$) orbital of the first Cu(II) center, it interacts magnetically with another unpaired electron in the (d_{z^2}) or ($d_{x^2-y^2}$) orbital of the next Cu(II) center through the diamagnetic (D) unit. The interaction might also extend directly between the two metals. This could result in significant magnetic coupling between the two spins through the conjugated bridges.[119, 120] A similar explanation of metal to metal magnetic communication (Scheme 10) can also be applied for MOFT-09-RT ($\{[Cu_2(Ox)_2(BPY)]\cdot 0.5H_2O\}_n$) with the magnetic moment of 2.3 BM and an unpaired electrons (n) of 1.5. Note that the longer fumarate linker in MOFT-23-RT is replaced by the shorter oxalate linker in MOFT-09-RT. A canted antiferromagnetism[121, 122] is observed in MOFT-11-RT ($\{[Ni_2(Ox)_2(BPY)]\cdot 3.75H_2O\}_n$). The observed spin-only magnetic moment indicates that there are only 0.083 unpaired electrons (n) in the paddle wheel system as a result of magnetic coupling. The two unpaired electrons per Ni(II) are $(d_{z^2})^1$ and $(d_{x^2-y^2})^1$. The supper exchange through the diamagnetic unit (Scheme 11) may act to cant the spins and could make MOFT-11-RT antiferromagnetic.

Table 6 Magnetic susceptibility data of the MOFT-23-RT ($\{[Cu_2(Fu)_2(BPY)]\cdot H_2O\}_n$), MOFT-11-RT ($\{[Ni_2(Ox)_2(BPY)]\cdot 3.75H_2O\}_n$), and MOFT-09-RT ($\{[Cu_2(Ox)_2(BPY)]\cdot 0.5H_2O\}_n$ at 294 K.

MOF	M (g/mol)	χ_g (294K)	$\chi_M = \chi_g * M$	χ^{dia}	$\chi'_M = \chi_M - \chi^{dia}$	$\mu_{eff} = \sqrt{8 * \chi'_M * T}$ (BM)	n
MOFT-23-RT	527.93	3.379×10^{-6}	1.78×10^{-3}	-1.84×10^{-4}	1.96×10^{-3}	2.1	1.37
MOFT-11-RT	517.17	1.385×10^{-5}	7.16×10^{-3}	-2.29×10^{-4}	7.394×10^{-5}	0.4	0.083
MOFT-09-RT	468.32	4.473×10^{-6}	2.09×10^{-3}	-1.87×10^{-4}	2.28×10^{-3}	2.3	1.5

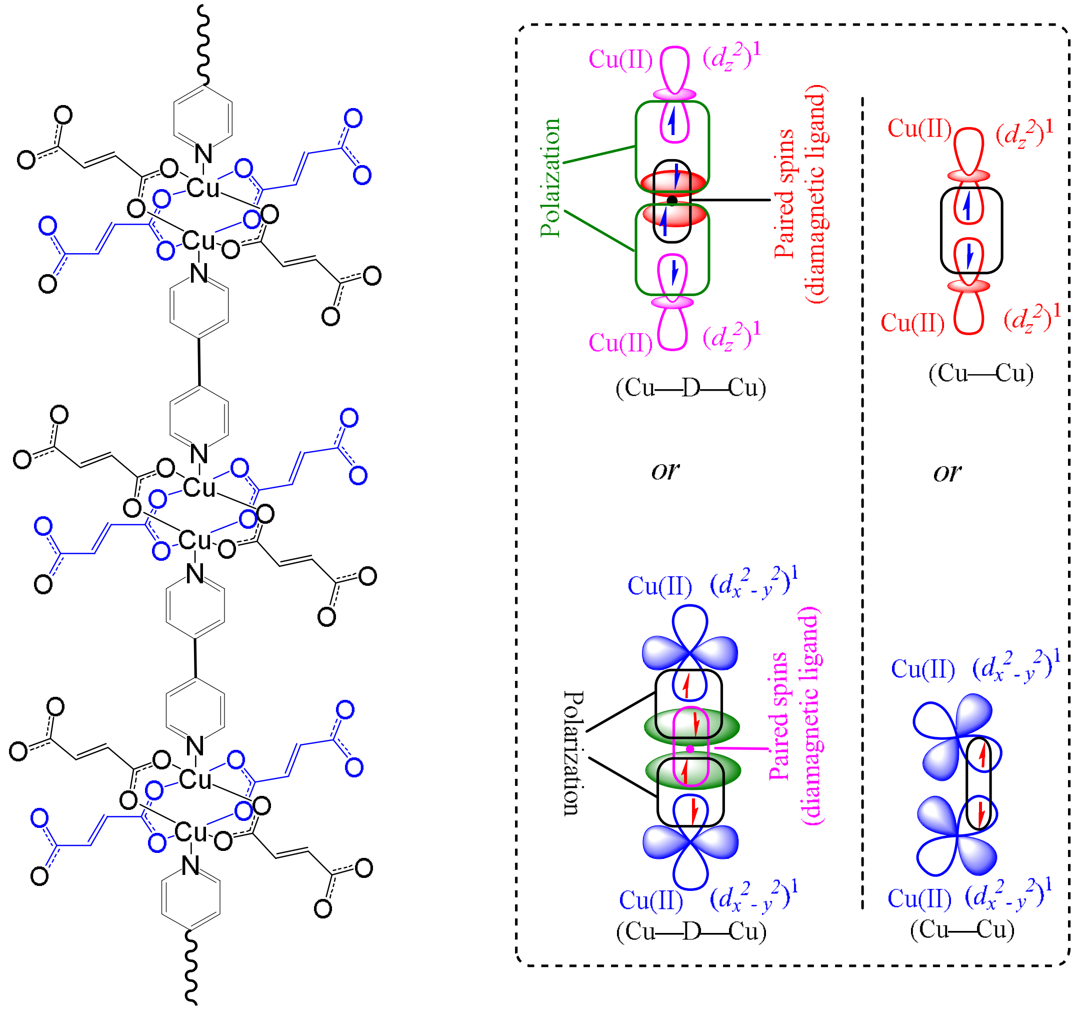

Scheme 9 Schematic representation of magnetic exchange between Cu(II) centres through diamagnetic bridge in MOFT-23-RT ($\{[Cu_2(Fu)_2(BPY)]\cdot H_2O\}_n$). Note that “D” is a diamagnetic unit (Fumarate or BPY).

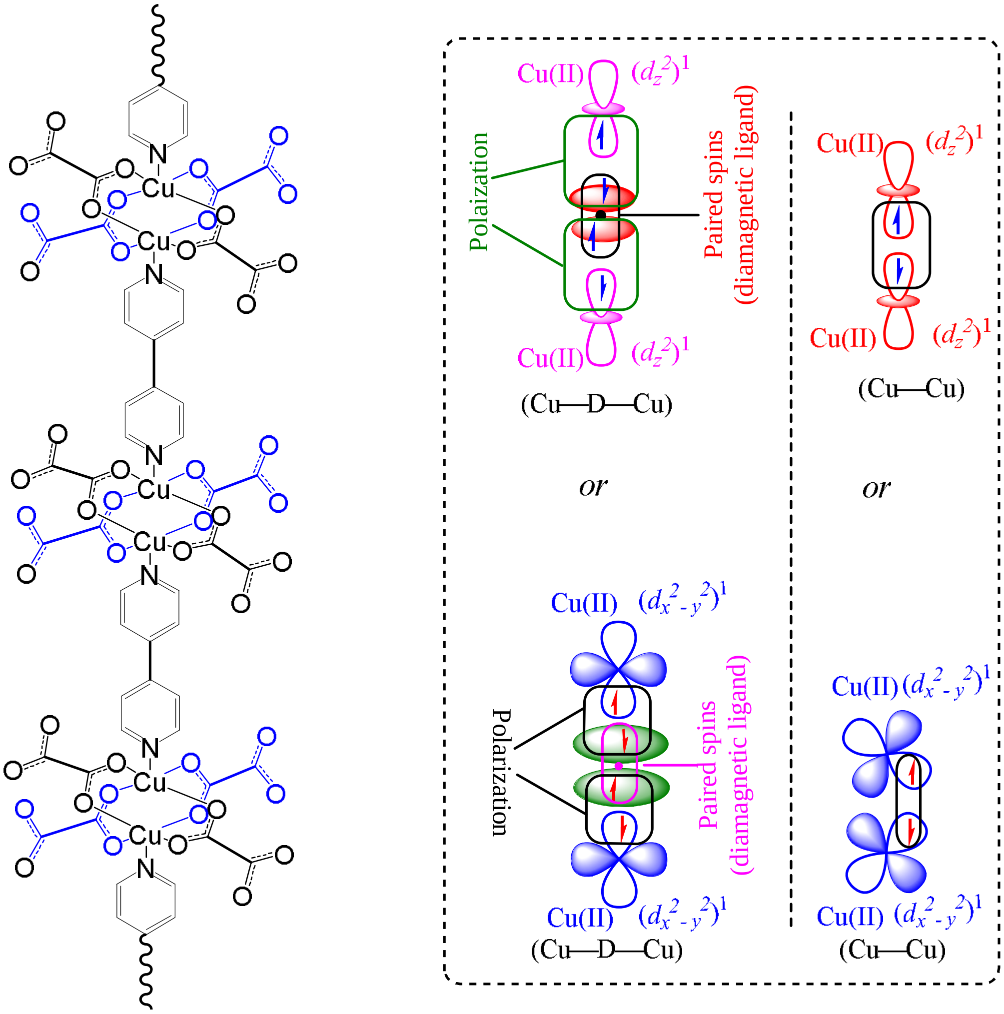

Scheme 10 Schematic representation of magnetic exchange between Cu(II) centres through diamagnetic bridge in MOFT-09-RT ({[Cu$_2$(Ox)$_2$(BPY)]·0.5H$_2$O}$_n$) Note that "D" is a diamagnetic unit (oxalate or BPY).

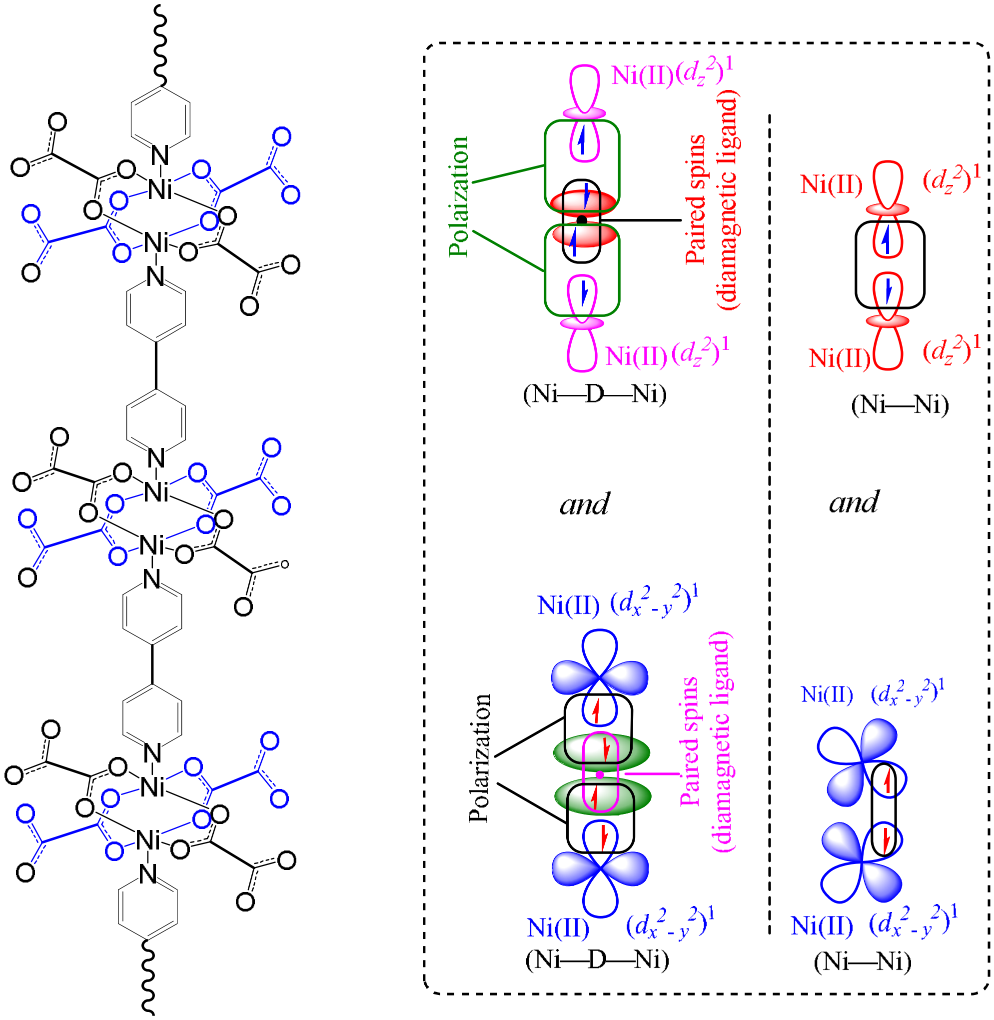

Scheme 11 Schematic representation of magnetic exchange between Ni(II) centres through diamagnetic bridge in MOFT-11-RT ($\{[Ni_2(Ox)_2(BPY)]\cdot 3.75H_2O\}_n$). Note that “D” is a diamagnetic unit (oxalate or BPY).

4.4 Summary

In summary, we have synthesized and characterized Zn (II) and Cu (II) based pillared-layer MOFs from sodium salt of oxalate linker (and also 2-aminotherephtalate) and 4,4'-bipyridine pillar in water/methanol mixed solvents to address problems of solubility at room temperature. Powdered MOFs were obtained and their crystallinity was studied using PXRD techniques. DICVOL06 in Expo2014 software was used to index PXRD patterns of the MOFs and to obtain their crystal parameters. All the three MOFs obtained have porosity in the mesoporous region. The optical band gap measurement showed the Zn (II) based MOFT-53-RT is active in the visible region, whereas the Zn (II) based MOFT-08-RT and Cu (II) based MOFT-09-RT are active in the UV region. The magnetic studies of the MOFs, $\{[Cu_2(Fu)_2(BPY)]\cdot H_2O\}_n$ and $\{[Ni_2(Ox)_2(BPY)]\cdot 3.75H_2O\}_n$ (Synthes shown Chapter 3) and $\{[Cu_2(Ox)_2(BPY)]\cdot 0.5H_2O\}_n$ (synthesis shown in this chapter) indicate that there are metal to metal magnetic communication of the spins through the diamagnetic bridge in all the three dimension of the framework.

CHAPTER FIVE

Investigation of Photocatalytic Performance of MOFT-23-RT Towards Toxic Dye Degradation in Wastewater Effluents

5.1 Introduction

Textile wastewater consists of different types of contaminants. Dyes which remain unfixed to clothing are usually the main environmental contaminants discharged into water bodies by textile industries. In addition to textile industries, the leather processing industry, paper industry, food industry, hair colorings also contribute towards the presence of dyes in wastewater. Over 10,000 types of dyes are being manufactured with a total annual production of more than 7 x 10^5 tones.[123] About 10 % of the dyes used in industries are discharged to the ecosystem which is very harmful.[124] Most dyes, especially the azo dyes are highly toxic and are carcinogenic in nature which should be treated before their discharge to the environment.[125] Water bodies polluted with dyes are easily seen as colored even at low concentration and they block sunlight from reaching the bulk of the affected water, thereby disturbing the photosynthetic activity. They also reduce the level of dissolved oxygen required by organisms in water streams. The biological oxygen demand (BOD) and chemical oxygen demand (COD) in water body will therefore be high.[126]

There are different ways to remove dyes from the affected wastewater; adsorption,[127] flocculation-coagulation,[128] membrane filtration and biological treatment.[129] However, most of these processes simply transfer the pollutants from one to another medium, causing secondary pollution. Oxidation of dyes through photocatalysis, using semiconductors can effectively remove dyes by converting them in to water and carbon dioxide. Photocatalytic degradation of organic dyes is advantageous over adsorption in that no further treatment is required to eliminate the organics.[130]

The photocatalytic reaction proceeds through an electron promotion process involving the highest occupied molecular orbital (HOMO, the VB) and the lowest unoccupied molecular orbital (LUMO, the CB).[131, 132] Under light of sufficient frequency of irradiation, the electrons (e^-) in the VB excite to the vacant CB leaving the holes (h^+) behind in the VB. The adsorbed oxygen can accept e^- to form oxygen radicals ($^{\bullet}O_2^-$) ($O_2 + e^- \rightarrow$ ($^{\bullet}O_2^-$)), and it further transforms in to active $^{\bullet}OH$ ($^{\bullet}O_2^- + 2H^+ \rightarrow {}^{\bullet}OH + OH^-$). Meanwhile, the h^+ in the VB can interact with OH^-, forming the $^{\bullet}OH$ active species for dye degradation.[133, 134]

Metal-Organic Frameworks (MOFs) are highly crystalline structures composed of metal clusters bound via coordination to organic ligands. The structures are highly porous and tunable.[6] The optical property of MOFs coupled to their ability to host other more photo-sensitive molecules play a great role in the degradation of toxic organic dyes.[135, 136] Most MOFs including MOF-5 are unstable in water and hence the synthesis of water stable MOFs should be systematically designed so as to use them in the photodegradation of an aqueous solution of azo dyes. A span of publication results on the Scopus database in the last four years shows that the utilization of MOFs for photodegradation of dyes is increasing nowadays (Fig. 46). Photocatalytic dye degradation is affected by several operational conditions like, the initial concentration of the dye, the pH of the medium, and the effect of the catalytic dosage or loading.[137] Optimum condition for a dye degradation is investigated after working on the above parameters. Adsorption of the dye molecules occurs on the surface of the MOFs before photocatalytic degradation and it proceeds through a number of different mechanisms such as electrostatic interactions, hydrogen bonding, π-π stacking/interactions, and hydrophobic interactions.[138]

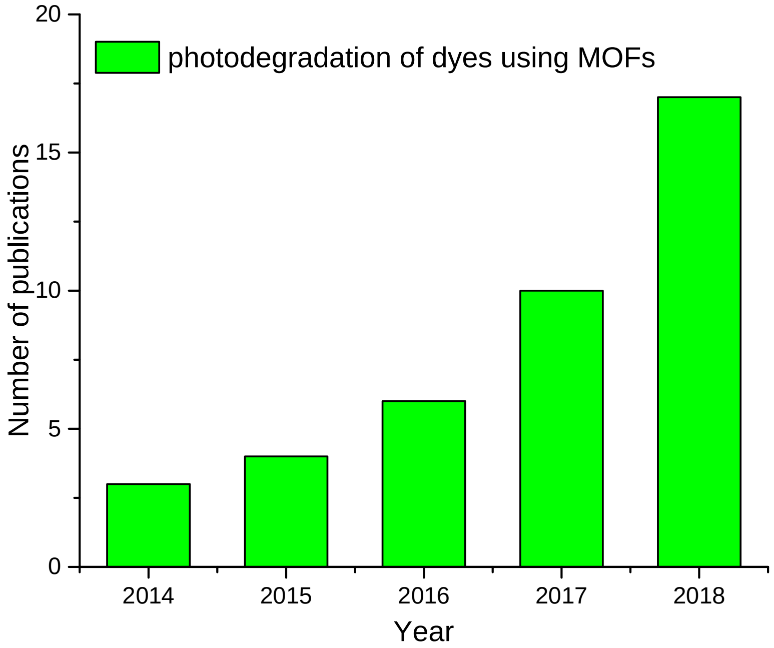

Figure 46 Number of papers published in the last 4 years spanned on Scopus database from 2014 to 2018 using key words "dye photodegradation using MOFs"

In this study, the photocatalytic performance of one of the water stable pillared-layer MOFs synthesized and characterized fully in Chapter Three (MOFT-23-RT = $\{[Cu_2(Fu)_2(BPY)]\cdot H_2O\}_n$) is evaluated towards the degradation of methyl orange which is mostly released to the environment as textile wastewater effluent. Methyl orange (MO) is one of the most stable azo dyes which are extensively used in the textile industry and resistant to biodegradation. Degradation of such a dye molecules into some simpler molecules can reduce the environmental pollution caused by them.[139] Methyl orange having a chemical formula of $C_{14}H_{14}N_3NaO_3S$ and molecular weight of 327.33 g/mol has an absorption maximum at 464 nm when subjected to UV-visible light in aqueous form. A photoreactor system with a UV lamp and MO having λ_{max} at 464 nm are shown in Fig. 47. This absorption maximum decreases as a function of increasing light irradiation time if the catalyst has a semiconducting nature and appropriate band gap. The optical band gap of MOFT-23-RT (E_g = 3.6 eV) was determined using the data obtained from diffuse reflectance spectroscopy (see Chapter Three). This shows that the MOFs under study is active in the UV region, and the photocatalytic performance of MOFT-23-RT is evaluated by degradation of MO under laboratory-UV-reactor system with 150 W UV-immersion lamp of model TQ 150 at room temperature.

The photocatalytic evaluation of $\{[Cu_2(Fu)_2(BPY)]\cdot H_2O\}_n$ is highly based on its stability in aqueous medium for prolonged hours of time. The Zn-based MOFs $\{[Zn_2(Fu)_2(BPY)]\cdot 1.5H_2O\}_n$ and $\{[Zn_2(Ox)_2(BPY)]\cdot 3.5H_2O\}_n$ are also evaluated but the MOF-dye suspension became opaque on stirring and it was not possible to recover the MOF. $\{[Ni_2(Ox)_2(BPY)]\cdot 3.75H_2O\}_n$ and $\{[Zn_2(ATA)_2(BPY)]\cdot H_2O\}_n$ are active in the visible region and we could not evaluate their photocatalytic activity using a vis-LED

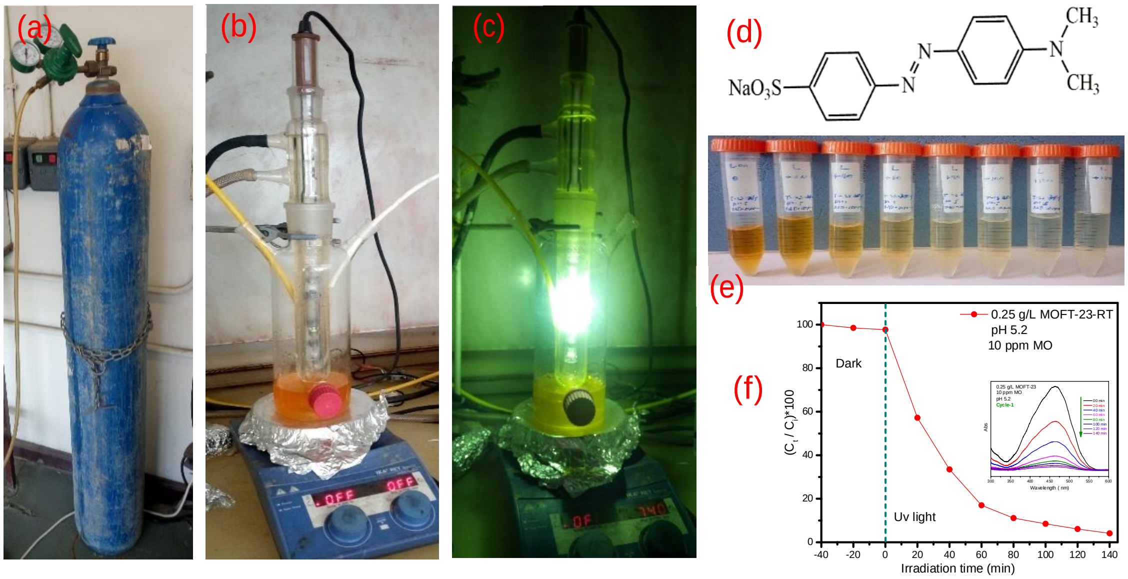

Figure 47 a) oxygen gas for purging in to the dye suspension; b) laboratory-UV-reactor system with 150 W UV-immersion lamp of model TQ 150 containing 10 ppm MO stirring in dark; c) UV light on MO/ MOFT-23-RT suspension for 140 min; d) Methyl orange (MO); e) 20 min interval withdrawn samples of photodegraded MO for 140 min; f) percentage degradation efficiency of MOFT-23-RT in the first run.

photoreactor in our lab. Therefore, the focus of the research is on $\{[Cu_2(Fu)_2(BPY)]\cdot H_2O\}_n$ (MOFT-23-RT).

5.2 Experimental

5.2.1 Photocatalytic dye degradation experiment

The photocatalytic performance of MOFT-23-RT ($\{[Cu_2(Fu)_2(BPY)]\cdot H_2O\}_n$) was evaluated by photodegradation of methyl orange (MO) under laboratory-UV-reactor system with 150 W UV-immersion lamp of model TQ 150 at room temperature (25 ^oC). The immersion lamp is equipped with outside quartz glass jacket through which water flows continuously to prevent over heating of the system. A 0.25 g/L or 0.5 g/L of MOFT-23-RT was placed in to 100 mL of MO aqueous solution having an initial concentration of 10 ppm in a quartz reactor. Prior to UV light irradiation, the suspension was magnetically stirred in dark for 40 min to ensure establishment of an adsorption-desorption equilibrium. During photodegradation reaction, stirring was maintained to keep the mixture in suspension, and oxygen gas was purged continuously as a primary oxidant to produce radicals. About 5 mL of the sample was extracted at every 20-minute time interval using a syringe fitted with a needle and centrifuged for 5 min. The change in the intensity of absorption maxima of MO (i.e. at 464 nm fixed wavelength) was recorded to determine the residual concentration of the dye in solution using T60 UV-Visible spectrometer. The percentage degradation of the dye molecules was calculated using the equation 1.

$$\text{Dye degradation efficiency (\%)} = (C_t / C_o) \times 100 \quad \ldots\ldots\ldots\ldots\ldots\ldots\ldots\ldots\ldots \text{(1)}$$

where C_o is the initial dye concentration and C_t is the concentration at any time t.

The degradation kinetics study was carried out by varying the MOFs dosage from 0.25 g/L to 0.5 g/L and also at pH 5.2 and 8.3. The pseudo first order kinetic model is followed for all the conditions by fixing the initial dye concentration the same as represented by the Langmuir–Hinshelwood equation (equation 2).

$$\ln (C_t / C_o) = -Kt \quad \ldots\ldots\ldots\ldots\ldots\ldots\ldots\ldots\ldots\ldots\ldots\ldots\ldots\ldots\ldots \quad (2)$$

where, C_o represents the initial concentration of the dye before irradiation and C_t, the residual dye concentration, after irradiation at time t. *K* is the rate constant (min^{-1}) which is determined by executing linear regression.

5.3 Results and Discussion

5.3.1 Evaluation of Photocatalytic Activity of MOFT-23-RT Towards MO Degradation

The photocatalytic activity of MOFT-23-RT was studied using methyl orange (MO) as a model dye molecule under UV irradiation based on the band gap of the MOFs catalyst. Before UV light irradiation and O_2 purging, the MOF/dye suspension was first stirred in the dark for ca. 40 min, to ensure establishment of adsorption/desorption equilibrium. Within 40 min stirring in dark, MOFT-23-RT was able to adsorb and remove below 3 % of the dye at pH 5.2 with initial dye concentration of 10 ppm and MOF loading of 0.25 g/L. The photocatalytic degradation of 10 ppm MO dye solution was studied by considering parameters like the effect of MOFs loading, pH of the media, and degradation kinetics. The catalytic performance of the MOFs was also evaluated for five cycles at pH 5.2.

5.3.2 Effect of MOFs Loading

The effect of MOFs loading on the MO degradation was studied at a fixed dye concentration and pH of the medium under UV light irradiation. 0.25 g/L and 0.5 g/L of the MOFs catalyst were used to degrade 10 ppm of the dye solution in the presence of UV light in quartz reactor by keeping the pH conditions the same both in less acidic (pH 5.2) and basic (pH 8.3) medium. The result of MOFs loading on MO degradation (Fig. 48c) shows that a 0.25 g/L MOFs loading would degrade MO to a greater extent (96 %) when

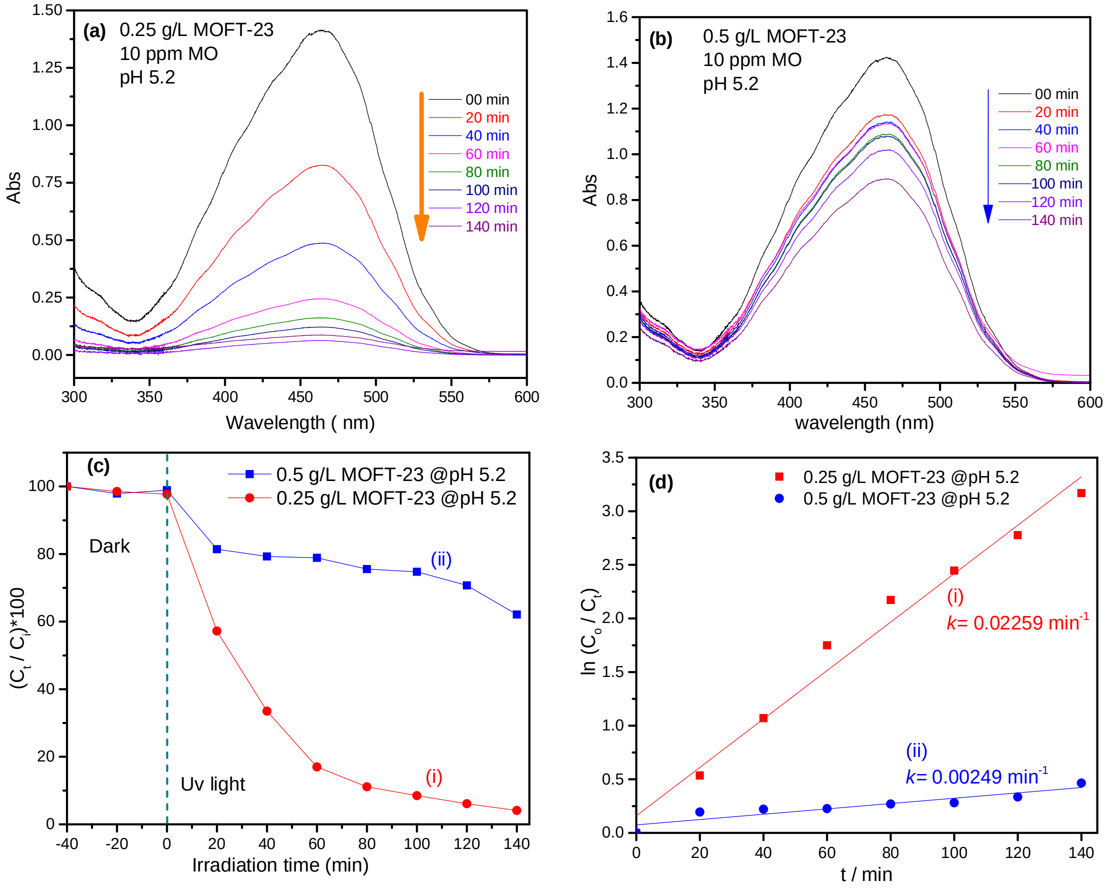

Figure 48 a decrease in the absorption maxima (λ ≈ 464 nm) of MO with UV-light irradiation time at pH 5 in the pressence of (a) 0.25g /L MOFT-23Hf-RT, (b) 0.5g/L MOFT-23Hf-RT. (c) Photocatalytic MO degradation efficiency (%) in the presence of (i) 0.25 g/L and (ii) 0.5g/L of MOFT-23Hf-RT under UV-light irradiation at pH 5. (d) Fitting of pseudo-first-order kinetics lines for the photodegradation of 10ppm MO in the presence of (i) 0.25 g/L, and (ii) 0.5g/L MOFT-23Hf-RT at pH 5, respectively.

compared to a 0.5 g/L loading (38 %) at pH 5.2 for the same 10 ppm MO initial concentration after 140 min UV light irradiation. The photodegradation reaction catalyzed by a 0.25g/L MOFT-23-RT proceed by a pseudo-first order kinetics (Fig. 48d(i)) and has a higher rate constant (k=0.02259 min^{-1}) when compared to the one catalyzed by a 0.5 g/L MOFs, k= 0.00249 min^{-1} (Fig. 48d(ii). This is ascribed to the fact that an excess use of a photocatalyst particles may increase the opacity of the suspension which may retard the MO degradation rate.[140] Another possible reason could be the fact that as the amount of MOFs loading increases, an aggregation of the MOFs might occur and cannot evenly disperse in to the dye solution, and hence the amount of dye degraded decreases. An excessive amount of a photocatalyst might also block light penetration which can then decrease the rate constant.[141, 142] A 96 % MO degradation (with comparatively higher rate constant) achieved after a dosage of 0.25 g/L MOFT-23-RT shows that the MOF has more active sites at this dosage and could absorb large number of photons.[143]

5.3.3 Effect of pH of the media

The pH of the suspension plays an important role in the degradation of most dyes. The photocatalytic degradation of MO is investigated at pH 2, 5.2, and 8.3 at a fixed dye concentration and MOFs dosage. MOFT-23-RT was found to be unstable in the suspension at pH 2. Most textile wastewater effluents are released to the environment having pH range from 5 to 8 and the study focused mainly on pH 5.2 and 8.3 (Fig. 49 & 50). It is observed from the fig. 49c that the maximum degradation efficiency (96 %) is achieved at pH 5.2 whereas 45 % of the MO is photodegraded at pH 8.3 after 140 min UV light irradiation at a 0.25 g/L MOFs loading. For a 0.5 g/L MOFs loading, 38% of the MO was photodegraded at pH 5.2, but only 7 % at pH 8.3 for the 140 min UV light irradiation time (Fig. 50c). This shows that in either MOFs loading, it is at pH 5.2 that the maximum amount of the dye molecules are photodegraded and removed. This is attributed to the fact that lower pH value is able to increase the positive surface charges of MOFT-23-RT and hence it could adsorb through electrostatic interaction and assist photodegradation of anionic methyl orange up on UV light irradiation.[137, 144, 145] For a 0.25 g/L loading, the reaction kinetics has fitted the pseudo first order model with rate constants of k= 0.02259 min^{-1} at pH 5.2,

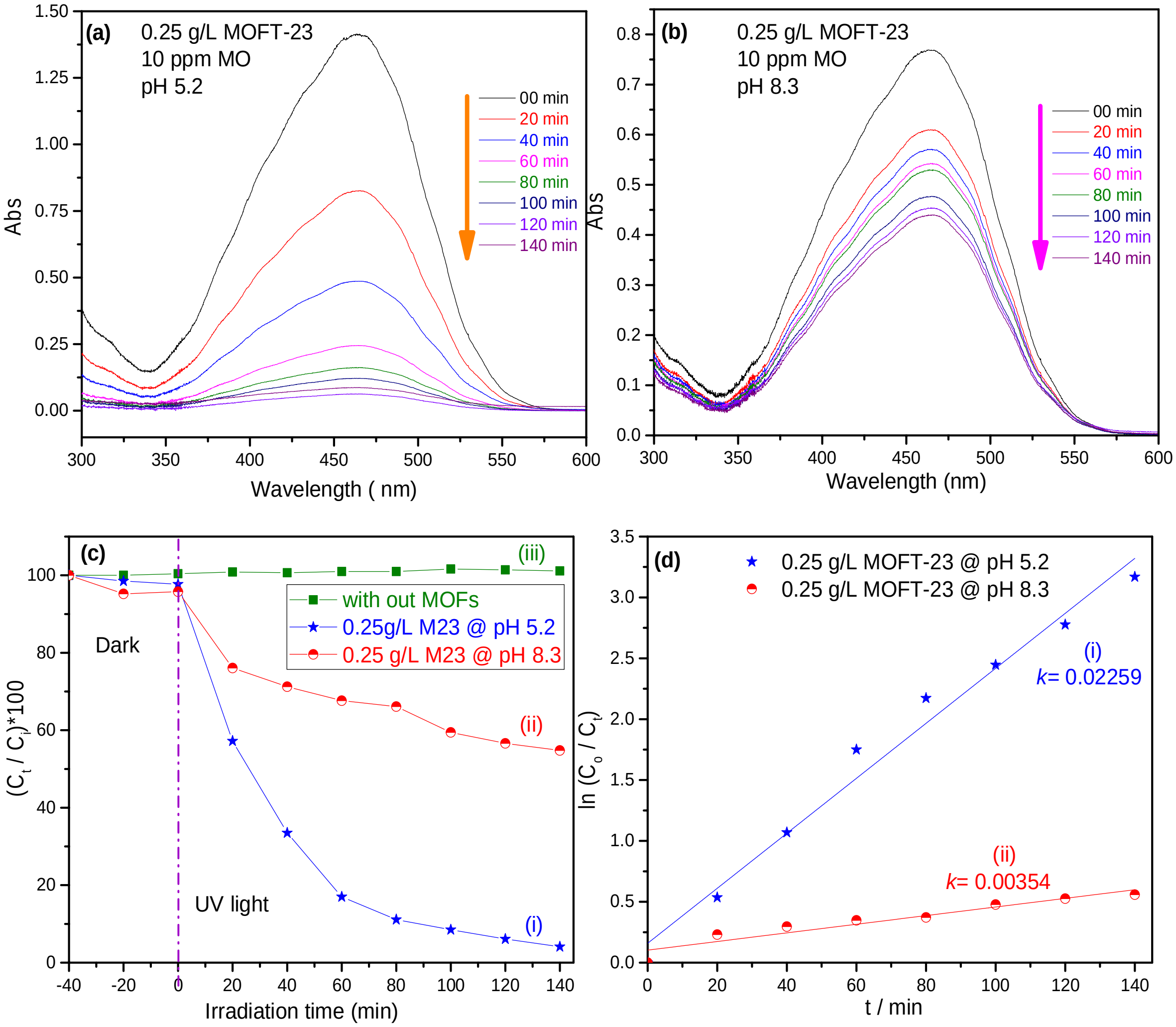

Figure 49 a decrease in the absorption maxima (λ ≈ 464 nm) of MO with UV-light irradiation time at (a) pH 5.2 and (b) pH 8.3 in the presence of 0.25g /L MOFT-23-RT. (c) Photocatalytic MO degradation efficiency (%) in the presence of 0.25 g/L of MOFT-23-RT under UV-light irradiation at (i) pH 5.2, and (ii) pH 8.3. Reaction rate constant (k) of the pseudo-first-order kinetic model for photodegradation of 10ppm MO in the presence of (d) 0.25 g/L and MOFT-23-RT at (i) pH 5.2, and (ii) pH 8.3

and *k*= 0.00354 min^{-1} at pH 8.3 (Fig. 49d). When the MOFs loading was doubled in to 0.5 g/L, the pseudo first order kinetic model could result in lower rate constants of *k*= 0.00249 min^{-1} at pH 5.2, and *k*= 0.000324 min^{-1} (Fig. 50d’). This shows that fast photodegradation of MO is observed at pH 5.2 for a 0.25 g/L MOFT-23-RT dosage.

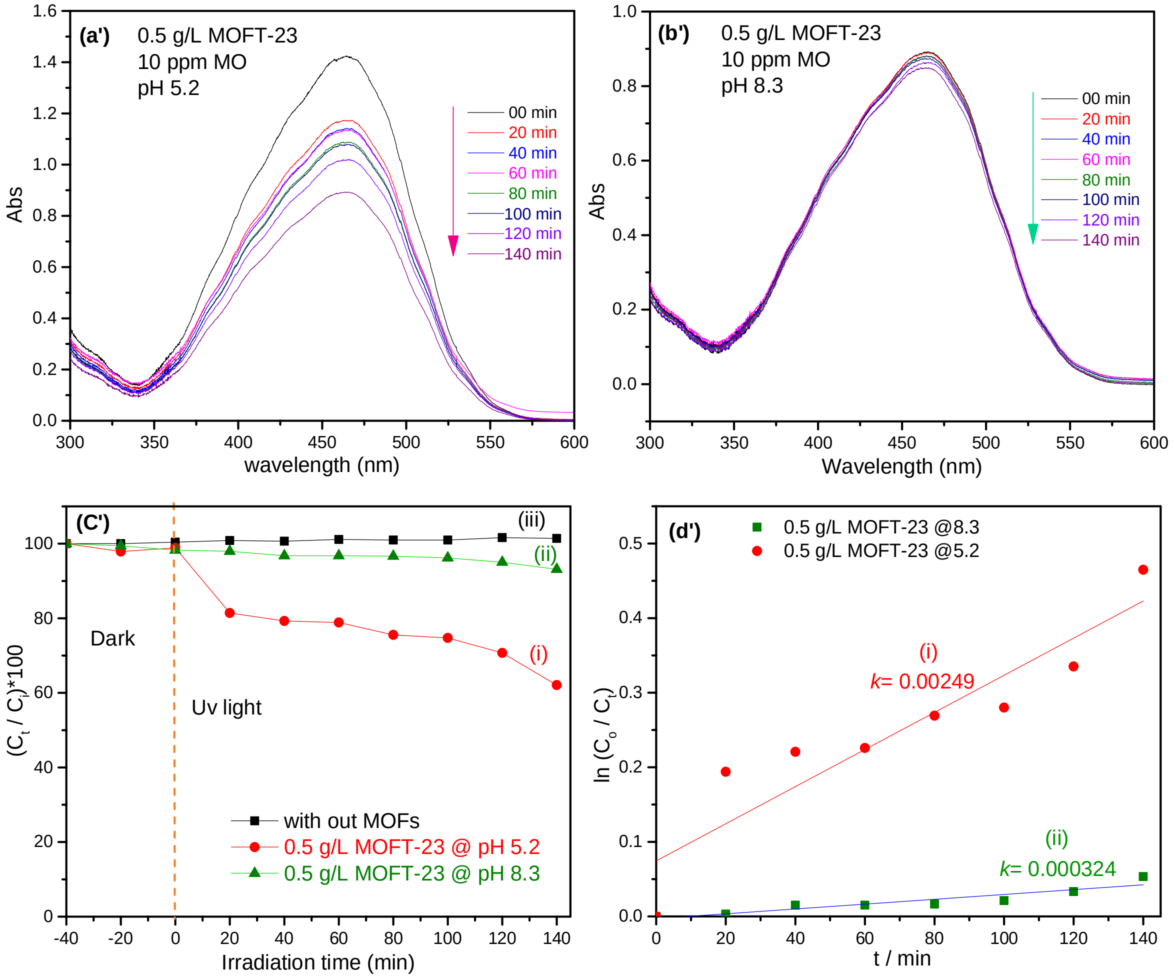

Figure 50 a decrease in the absorption maxima (λ ≈ 464 nm) of MO with UV-light irradiation time at (a’) pH 5.2 and (b’) PH 8.3 in the pressence of 0.5g /L MOFT-23-RT. (c’) Photocatalytic MO degradation efficiency (%) in the presence of 0.5 g/L of MOFT-23-RT under UV-light irradiation at (i) pH 5.2, and (ii) pH 8.3. Reaction rate constant (k) of the pseudo-first-order kinetic model for photodegradation of 10ppm MO in the presence of (d) 0.25 g/L and (d’) 0.5 g/L MOFT-23-RT at (i) pH 5.2, and (ii) pH 8.3

Reusability of MOFT-23-RT Photocatalyst

As shown in the previous sections, the optimized conditions for the photodegradation of 10 ppm MO is loading of 0.25 g/L MOFT-23-RT at pH 5.2. This could result in a 96 % photodegradation efficiency of the MOF. The reusability of the MOF under study was tested over five cycles (Fig. 51 and 52). The recycled catalyst was washed with deionized water several times and then kept in vacuum oven at 80 ^{o}C for 3 h. The first, second, third, and the fourth runs showed a photodegradation efficiency of 96 %, 88 %, 87%, and 80 %, respectively. 53% of the dye is photodegraded by the photocatalyst in the fifth cycle. A remarkable decrease in the photodegradation efficiency is observed in using the catalyst for the fifth cycle. The pseudo first order kinetic (Fig. 52b and Table 7) resulted in rate constants k= 0.02259, k=0.01463, k=0.01422, k=0.01303, and k=0.00458 min^{-1} for the first, second, third, fourth, and fifth cycles, respectively. The results showed that the performance of MOFT-23-RT towards photodegradation of MO did not decrease significantly over the first three cycles and the photodegradation was very rapid as witnessed by the rate constants.

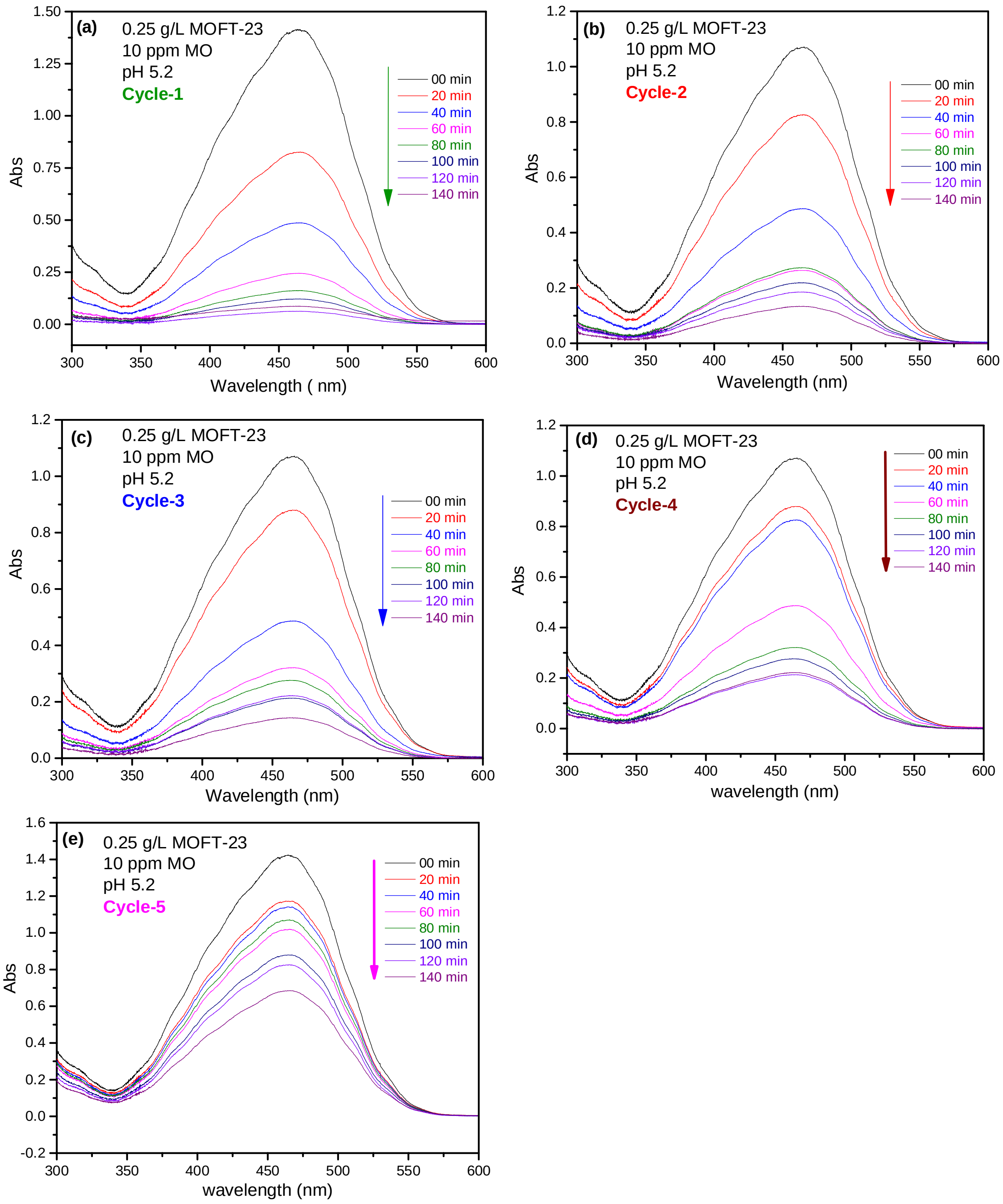

Figure 51 a decrease in the absorption maxima (λ ≈ 464 nm) of MO with UV-light irradiation time at pH 5 in the pressence of 0.25g /L MOFT-23-RT for the (a) first cycle, (b) second cycle, and (c) third cycle. (d) fourt cycle, and and fivth cycles

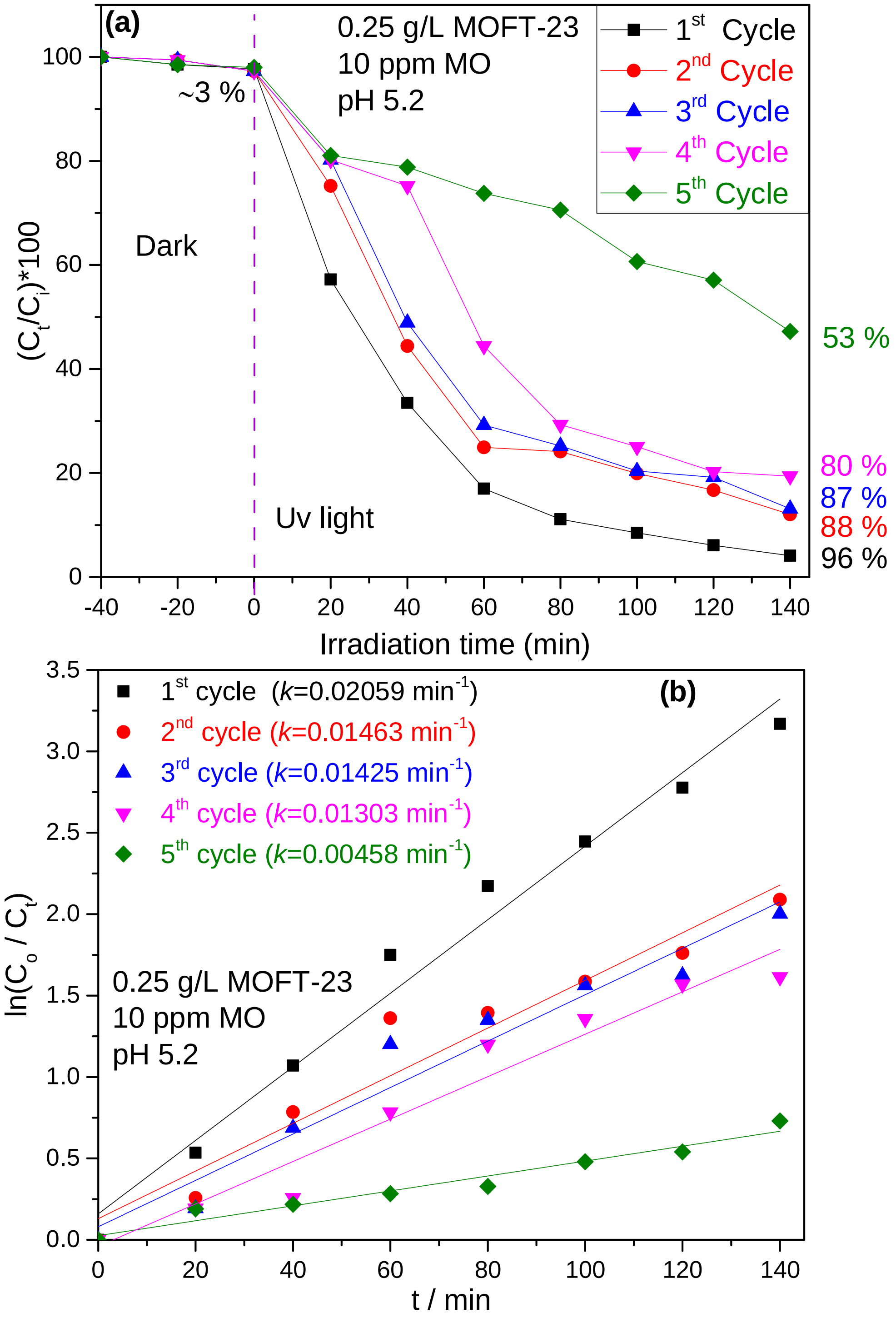

Figure 52 (a) Photocatalytic MO degradation efficiency (%) in the presence of 0.25 g/L of MOFT-23-RT under UV-light irradiation at pH 5.2 for the five consequtive cycles. (b) Reaction rate constant (k) of the pseudo-first-order kinetic model for photodegradation of 10ppm MO in the presence of 0.25 g/L MOFT-23-RT at pH 5.2 for five conseqitive cycles.

Table 7 Parameters of pseudo-first order kinetics model for the degradation of methyl orange (MO) under UV light irradiation (R^2 = correlation coefficient).

Cycles	MOFs loading (g/L)	pH	C_o (ppm)	Degradation (%)	k (min^{-1})	R^2
Cycle-1	0.25	5.2	10	96	0.02259	0.98147
	0.5	5.2	10	38	0.00249	0.8547
	0.25	8.3	10	45	0.00354	0.91445
	0.5	8.3	10	7	0.000324	0.86542
Cycle-2	0.25	5.2	10	88	0.01463	0.9459
Cycle-3	0.25	5.2	10	87	0.01425	0.95469
Cycle-4	0.25	5.2	10	80	0.01303	0.95536
Cycle-5	0.25	5.2	10	53	0.00458	0.95756

5.3.4 XRD Analysis of The Recycled MOFs

It was observed in the previous section that the reused catalyst showed a degradation efficiency of 96 %, 88 %, 87 %, 80 %, and 53 % for the photodegradation of 10 ppm MO

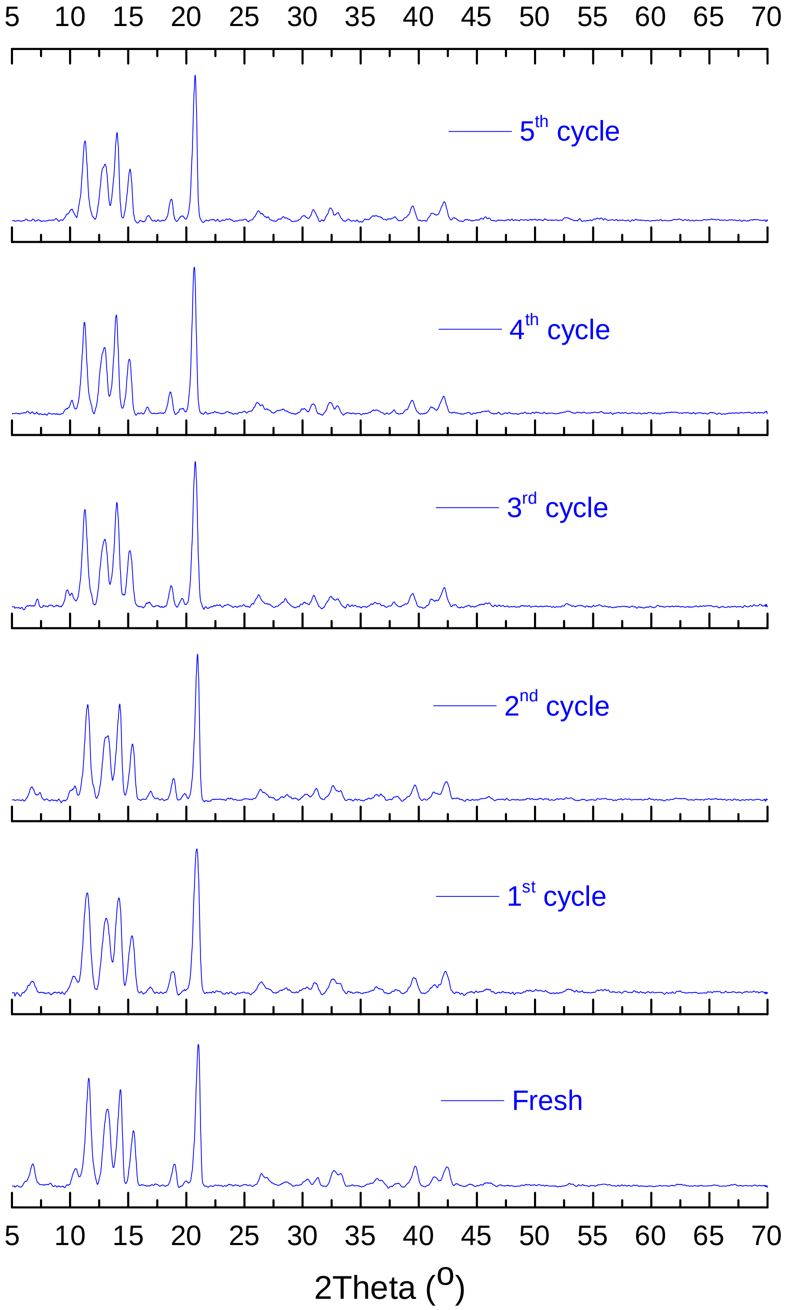

Figure 53 The PXRD patterns of MOFT-23-RT before and after the five consecutive photocatalytic degradation cycles towards 10 ppm methyl orange (recorded using Rigaku MiniFlex 600 XRD instrument)

at pH 5.2 during the first, second, third, fourth, and fifth cycles, respectively under UV light irradiation in the presence of oxygen purging. It was also indicated that the reused MOF was filtered, washed and then dried after each experiment. In order to make sure that the dye degradation over the MOFT-23-RT is a catalytic process and also prove that it is stable, the PXRD of the fresh MOFs was compared with the ones used for the five cycles in the dye degradation study (Fig. 53). This shows that PXRD patterns have close similarities with each other except for minor reduction in the intensity of the peak at $2\theta = 6.6$ after the third cycle. The result demonstrated that MOFT-23-RT is stable to dye photodegradation and may be recycled for the catalytic degradation of methyl orange and wastewater effluents of textile industry.

5.3.5 Mechanism for The Photodegradation of MO by MOFT-23-RT

An aqueous solution of model azo dye (10 ppm methyl orange) was subjected to UV light irradiation in the presence of MOFT-23-RT having a band gap of 3.6 eV for an irradiation time of 140 min. The color was changing from orange towards colorless as a function of increasing irradiation time. The concentration of the dye molecules in aqueous solution has been decreased to a greater extent as witnessed by the UV-Vis instrument and shown in the previous sections. The photocatalyst was also recycled over three runs and showed no obvious decay in its catalytic efficiency towards degradation of methyl orange. The PXRD patterns of the recycled MOFs have close similarity to the unused MOFs indicating no significant adsorption of the MO on the surface of the photocatalyst after use and wash up.

The photocatalytic performance is ascribed to the high surface area, value of band gap, and crystallinity of the photocatalyst.[146] The general mechanism for MO photodegradation by MOFT-23-RT are proposed and shown in Fig. 54. Upon sufficient UV light irradiation, electrons from the 2p orbitals of O, C, and N of the linker and pillar (valence band (VB)) jump to conduction band (CB) of the metal cluster (Cu^{2+}).[136, 147] This leaves holes (h^+) behind in the VB and electrons (e^-) in the CB. The electrons and holes migrate to the surface of MOFT-23-RT. The holes (h^+) oxidize hydroxyl (H_2O) to highly reactive hydroxyl radicals ($^\bullet OH$). The electron in the CB are scavenged by molecular oxygen on the photocatalyst forming superoxide radicals ($^\bullet O_2^-$) which finally transform in to hydroxyl radicals ($^\bullet OH$). Hydroxyl radicals generated by the electrons and holes have the ability to

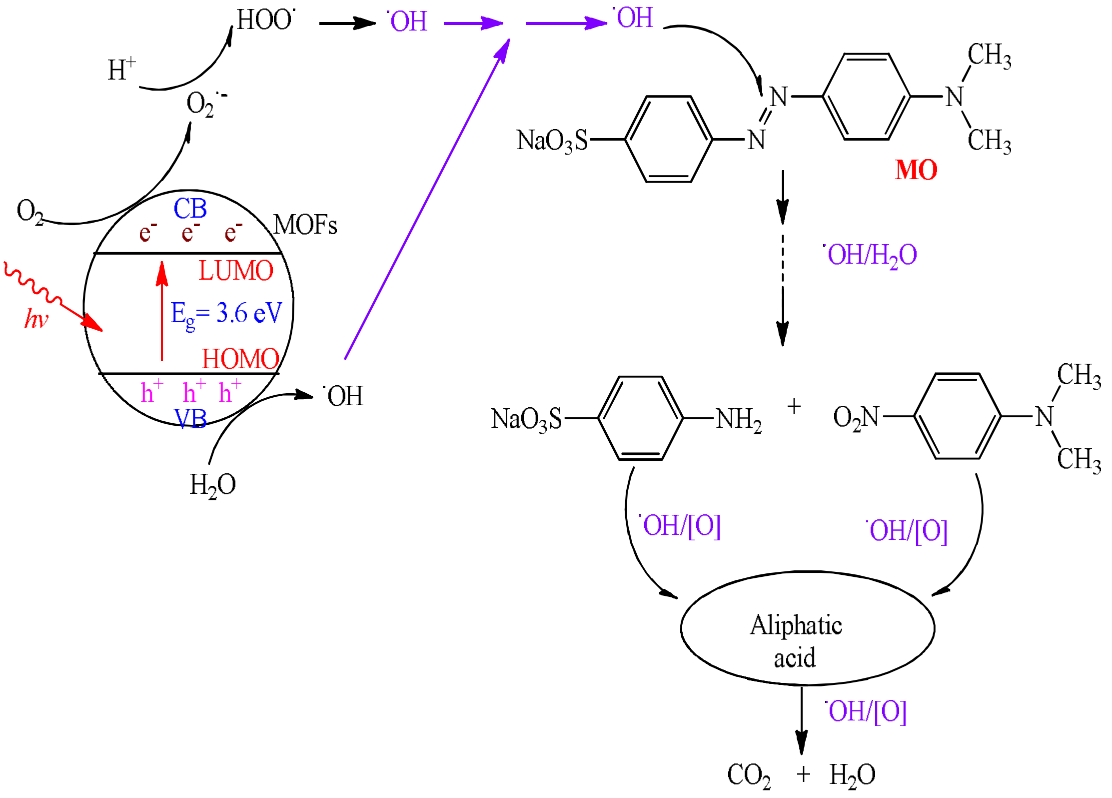

Figure 54 Main pathways proposed for methyl orange photodegraded by MOFT-23-RT under UV light irradiation. Adapted from reference. [7]

decompose the non-biodegradable methyl orange into carbon dioxide, water and some other simpler products.[139, 146]

5.2 Summary

In this chapter, the photocatalytic performance of one of the pillared-layer MOFs, $\{[Cu_2(Fu)_2(BPY)]\cdot H_2O\}_n$, has been studied in detail towards degradation of methyl orange which is toxic, nonbiodegradable, and discharged to the environment as a wastewater by textile industries. This model dye is degraded in the laboratory in the presence of UV light and $\{[Cu_2(Fu)_2(BPY)]\cdot H_2O\}_n$. The optimized conditions for the photodegradation efficiency of the MOF were achieved after considering the effect of pH, and MOF loading at a fixed dye concentration. 96 % of the 10-ppm methyl orange is photodegraded after loading of 0.25 g/L of the photocatalyst in to 100 mL of an aqueous solution of the dye at pH 5.2 for 140 min UV light irradiation time. The photocatalyst is recycled for five times and we were able to achieve a 96 %, 88 %, 87 %, 80 %, and 53 % degradation efficiencies in the first, second, third, fourth, and fifth cycles, respectively. The PXRD analysis of the used photocatalyst showed that the crystallinity of the MOF is maintained in the five runs. Thus $\{[Cu_2(Fu)_2(BPY)]\cdot H_2O\}_n$ can be applied for the degradation of methyl orange in the real textile wastewater.

CONCLUSIONS

In this dissertation, the synthesis and characterization of six MOFs has been included. The MOFs differ in their metal centers and length of the linkers keeping the pillar the same. The synthesis avoids use of toxic organic solvents and is at room temperature. The photocatalytic evaluation of $\{[Cu_2(Fu)_2(BPY)]\cdot H_2O\}_n$ is studied in detail based on its stability in aqueous medium for prolonged hours of time using UV irradiation in the presence of oxygen towards degradation of one of the toxic azo dyes called methyl orange. $\{[Ni_2(Ox)_2(BPY)]\cdot 3.75H_2O\}_n$ and $\{[Zn_2(ATA)_2(BPY)]\cdot H_2O\}_n$ are active in the visible region. Those MOFs are strongly recommended for the degradation of dyes in visible light reactor system. Overall, sustainable approach of MOFs synthesis was employed for environmental remediation.

REFERENCES

1. L. E. Smart and E. A. Moore, *Solid State Chemistry: An Introduction, Third Edition,* Taylor & Francis, 2005.
2. J. K. Yu-Ri Lee, and Wha-Seung Ahn, Synthesis of metal-organic frameworks: A mini review, *Korean J. Chem. Eng.*, 2103, **39**, 1667-1680.
3. M. Thommes, Physisorption of gases, with special reference to the evaluation of surface area and pore size distribution (IUPAC Technical Report). *Journal*, 2016, **38**, 25.
4. S. Keskin and S. Kızılel, Biomedical Applications of Metal Organic Frameworks, *Industrial & Engineering Chemistry Research*, 2011, **50**, 1799-1812.
5. J. Liu, L. Chen, H. Cui, J. Zhang, L. Zhang and C.-Y. Su, Applications of metal-organic frameworks in heterogeneous supramolecular catalysis, *Chemical Society Reviews*, 2014, **43**, 6011-6061.
6. H. Furukawa, K. E. Cordova, M. O'Keeffe and O. M. Yaghi, The Chemistry and Applications of Metal-Organic Frameworks, *Science*, 2013, **341**.
7. C.-C. Wang, J.-R. Li, X.-L. Lv, Y.-Q. Zhang and G. Guo, Photocatalytic organic pollutants degradation in metal–organic frameworks, *Energy & Environmental Science,* 2014, **7**, 2831-2867.
8. C. Dey, T. Kundu, B. P. Biswal, A. Mallick and R. Banerjee, Crystalline metal-organic frameworks (MOFs): synthesis, structure and function, *Acta Crystallographica Section B*, 2014, **70**, 3-10.

9. M. Dan-Hardi, C. Serre, T. Frot, L. Rozes, G. Maurin, C. Sanchez and G. Férey, A New Photoactive Crystalline Highly Porous Titanium(IV) Dicarboxylate, *Journal of the American Chemical Society*, 2009, **131**, 10857-10859.

10. M. Alvaro, E. Carbonell, B. Ferrer, F. X. Llabrés i Xamena and H. Garcia, Semiconductor Behavior of a Metal-Organic Framework (MOF), *Chemistry – A European Journal*, 2007, **13**, 5106-5112.

11. R. Liang, F. Jing, L. Shen, N. Qin and L. Wu, MIL-53(Fe) as a highly efficient bifunctional photocatalyst for the simultaneous reduction of Cr(VI) and oxidation of dyes, *Journal of Hazardous Materials*, 2015, **287**, 364-372.

12. T. Friščić, D. G. Reid, I. Halasz, R. S. Stein, R. E. Dinnebier and M. J. Duer, Ion- and Liquid-Assisted Grinding: Improved Mechanochemical Synthesis of Metal–Organic Frameworks Reveals Salt Inclusion and Anion Templating, *Angewandte Chemie International Edition*, 2010, **49**, 712-715.

13. O. M. Yaghi and H. Li, Hydrothermal Synthesis of a Metal-Organic Framework Containing Large Rectangular Channels, *Journal of the American Chemical Society*, 1995, **117**, 10401-10402.

14. L. Michels, J. O. Fossum, Z. Rozynek, H. Hemmen, K. Rustenberg, P. A. Sobas, G. N. Kalantzopoulos, K. D. Knudsen, M. Janek, T. S. Plivelic and G. J. da Silva, Intercalation and Retention of Carbon Dioxide in a Smectite Clay promoted by Interlayer Cations, *Scientific Reports*, 2015, **5**, 8775.

15. L. P. Cavalcanti, G. N. Kalantzopoulos, J. Eckert, K. D. Knudsen and J. O. Fossum, A nano-silicate material with exceptional capacity for CO_2 capture and storage at room temperature, *Scientific Reports*, 2018, **8**, 11827.

16. K. Sanderson, Materials chemistry: Space invaders, *Nature*, 2007, **448**, 746-748.

17. Y. He, B. Li, M. O'Keeffe and B. Chen, Multifunctional metal-organic frameworks constructed from meta-benzenedicarboxylate units, *Chemical Society Reviews*, 2014, **43**, 5618-5656.

18. F. A. Almeida Paz, J. Klinowski, S. M. F. Vilela, J. P. C. Tome, J. A. S. Cavaleiro and J. Rocha, Ligand design for functional metal-organic frameworks, *Chemical Society Reviews*, 2012, **41**, 1088-1110.

19. J. Zhang and J. n. M. Shreeve, 3D Nitrogen-rich metal-organic frameworks: opportunities for safer energetics, *Dalton Transactions*, 2016, DOI: 10.1039/C5DT04456A.

20. Q.-L. Zhu and Q. Xu, Metal-organic framework composites, *Chemical Society Reviews*, 2014, **43**, 5468-5512.

21. K. Wang, H. Huang, W. Xue, D. Liu, X. Zhao, Y. Xiao, Z. Li, Q. Yang, L. Wang and C. Zhong, An ultrastable Zr metal-organic framework with a thiophene-type ligand containing methyl groups, *CrystEngComm*, 2015, **17**, 3586-3590.

22. C.-C. Wang and J. Y. Ying, Sol−Gel Synthesis and Hydrothermal Processing of Anatase and Rutile Titania Nanocrystals, *Chemistry of Materials*, 1999, **11**, 3113-3120.

23. N. A. Khan and S. H. Jhung, Synthesis of metal-organic frameworks (MOFs) with microwave or ultrasound: Rapid reaction, phase-selectivity, and size reduction, *Coordination Chemistry Reviews*, 2015, **285**, 11-23.

24. N. Stock and S. Biswas, Synthesis of Metal-Organic Frameworks (MOFs): Routes to Various MOF Topologies, Morphologies, and Composites, *Chemical Reviews*, 2012, **112**, 933-969.

25. U. Mueller, M. Schubert, F. Teich, H. Puetter, K. Schierle-Arndt and J. Pastre, Metal-organic frameworks-prospective industrial applications, *Journal of Materials Chemistry*, 2006, **16**, 626-636.

26. H. Sakamoto, R. Matsuda and S. Kitagawa, Systematic mechanochemical preparation of a series of coordination pillared layer frameworks, *Dalton Transactions*, 2012, **41**, 3956-3961.

27. A. Gedanken, Using sonochemistry for the fabrication of nanomaterials, *Ultrasonics Sonochemistry*, 2004, **11**, 47-55.

28. Y. Yoo, V. Varela-Guerrero and H.-K. Jeong, Isoreticular Metal−Organic Frameworks and Their Membranes with Enhanced Crack Resistance and Moisture Stability by Surfactant-Assisted Drying, *Langmuir*, 2011, **27**, 2652-2657.

29. J. Lee, O. K. Farha, J. Roberts, K. A. Scheidt, S. T. Nguyen and J. T. Hupp, Metal-organic framework materials as catalysts, *Chemical Society Reviews*, 2009, **38**, 1450-1459.

30. M. Fujita, Y. J. Kwon, S. Washizu and K. Ogura, Preparation, Clathration Ability, and Catalysis of a Two-Dimensional Square Network Material Composed of Cadmium(II) and 4,4'-Bipyridine, *Journal of the American Chemical Society*, 1994, **116**, 1151-1152.

31. L. Alaerts, E. Séguin, H. Poelman, F. Thibault-Starzyk, P. A. Jacobs and D. E. De Vos, Probing the Lewis Acidity and Catalytic Activity of the Metal–Organic

Framework [$Cu_3(btc)_2$] (BTC=Benzene-1,3,5-tricarboxylate), *Chemistry – A European Journal*, 2006, **12**, 7353-7363.

32. B. Xiao, H. Hou and Y. Fan, Catalytic applications of CuII-containing MOFs based on N-heterocyclic ligand in the oxidative coupling of 2,6-dimethylphenol, *Journal of Organometallic Chemistry*, 2007, **692**, 2014-2020.

33. A. Phan, A. U. Czaja, F. Gándara, C. B. Knobler and O. M. Yaghi, Metal–Organic Frameworks of Vanadium as Catalysts for Conversion of Methane to Acetic Acid, *Inorganic Chemistry*, 2011, **50**, 7388-7390.

34. K. S. Suslick, P. Bhyrappa, J. H. Chou, M. E. Kosal, S. Nakagaki, D. W. Smithenry and S. R. Wilson, Microporous Porphyrin Solids, *Accounts of Chemical Research*, 2005, **38**, 283-291.

35. M. H. Alkordi, Y. Liu, R. W. Larsen, J. F. Eubank and M. Eddaoudi, Zeolite-like Metal−Organic Frameworks as Platforms for Applications: On Metalloporphyrin-Based Catalysts, *Journal of the American Chemical Society*, 2008, **130**, 12639-12641.

36. C. Wang, K. E. deKrafft and W. Lin, Pt Nanoparticles@Photoactive Metal–Organic Frameworks: Efficient Hydrogen Evolution via Synergistic Photoexcitation and Electron Injection, *Journal of the American Chemical Society*, 2012, **134**, 7211-7214.

37. A. H. Chughtai, N. Ahmad, H. A. Younus, A. Laypkov and F. Verpoort, Metal-organic frameworks: versatile heterogeneous catalysts for efficient catalytic organic transformations, *Chemical Society Reviews*, 2015, **44**, 6804-6849.

38. Y. Li, H. Xu, S. Ouyang and J. Ye, Metal-organic frameworks for photocatalysis, *Physical Chemistry Chemical Physics*, 2016, **18**, 7563-7572.

39. L. Shen, S. Liang, W. Wu, R. Liang and L. Wu, Multifunctional NH_2-mediated zirconium metal-organic framework as an efficient visible-light-driven photocatalyst for selective oxidation of alcohols and reduction of aqueous Cr(VI), *Dalton Transactions*, 2013, **42**, 13649-13657.

40. K. G. M. Laurier, F. Vermoortele, R. Ameloot, D. E. De Vos, J. Hofkens and M. B. J. Roeffaers, Iron(III)-Based Metal–Organic Frameworks As Visible Light Photocatalysts, *Journal of the American Chemical Society*, 2013, **135**, 14488-14491.

41. M. A. Nasalevich, M. van der Veen, F. Kapteijn and J. Gascon, Metal-organic frameworks as heterogeneous photocatalysts: advantages and challenges, *CrystEngComm*, 2014, **16**, 4919-4926.

42. X. Li, W. Guo, Z. Liu, R. Wang and H. Liu, Fe-based MOFs for efficient adsorption and degradation of acid orange 7 in aqueous solution via persulfate activation, *Applied Surface Science*, 2016, **369**, 130-136.

43. L. Shi, T. Wang, H. Zhang, K. Chang, X. Meng, H. Liu and J. Ye, An Amine-Functionalized Iron(III) Metal–Organic Framework as Efficient Visible-Light Photocatalyst for Cr(VI) Reduction, *Advanced Science*, 2015, **2**, n/a-n/a.

44. J. Gao, J. Miao, P.-Z. Li, W. Y. Teng, L. Yang, Y. Zhao, B. Liu and Q. Zhang, A p-type Ti(iv)-based metal-organic framework with visible-light photo-response, *Chemical Communications*, 2014, **50**, 3786-3788.

45. N. L. Rosi, J. Eckert, M. Eddaoudi, D. T. Vodak, J. Kim, M. O'Keeffe and O. M. Yaghi, Hydrogen Storage in Microporous Metal-Organic Frameworks, *Science*, 2003, **300**, 1127-1129.

46. M. P. Suh, H. J. Park, T. K. Prasad and D.-W. Lim, Hydrogen Storage in Metal–Organic Frameworks, *Chemical Reviews*, 2012, **112**, 782-835.

47. J. L. C. Rowsell and O. M. Yaghi, Effects of Functionalization, Catenation, and Variation of the Metal Oxide and Organic Linking Units on the Low-Pressure Hydrogen Adsorption Properties of Metal−Organic Frameworks, *Journal of the American Chemical Society*, 2006, **128**, 1304-1315.

48. H. Furukawa, N. Ko, Y. B. Go, N. Aratani, S. B. Choi, E. Choi, A. Ö. Yazaydin, R. Q. Snurr, M. O'Keeffe, J. Kim and O. M. Yaghi, Ultrahigh Porosity in Metal-Organic Frameworks, *Science*, 2010, **329**, 424-428.

49. O. K. Farha, A. Özgür Yazaydın, I. Eryazici, C. D. Malliakas, B. G. Hauser, M. G. Kanatzidis, S. T. Nguyen, R. Q. Snurr and J. T. Hupp, De novo synthesis of a metal–organic framework material featuring ultrahigh surface area and gas storage capacities, *Nat Chem*, 2010, **2**, 944-948.

50. A. G. Wong-Foy, A. J. Matzger and O. M. Yaghi, Exceptional H_2 Saturation Uptake in Microporous Metal−Organic Frameworks, *Journal of the American Chemical Society*, 2006, **128**, 3494-3495.

51. S.-i. Noro, S. Kitagawa, M. Kondo and K. Seki, A New, Methane Adsorbent, Porous Coordination Polymer $[\{CuSiF_6(4,4'\text{-bipyridine})_2\}_n]$, *Angewandte Chemie International Edition*, 2000, **39**, 2081-2084.

52. H. Li, M. Eddaoudi, T. L. Groy and O. M. Yaghi, Establishing Microporosity in Open Metal−Organic Frameworks: Gas Sorption Isotherms for Zn(BDC) (BDC = 1,4-Benzenedicarboxylate), *Journal of the American Chemical Society*, 1998, **120**, 8571-8572.

53. P. L. Llewellyn, S. Bourrelly, C. Serre, A. Vimont, M. Daturi, L. Hamon, G. De Weireld, J.-S. Chang, D.-Y. Hong, Y. Kyu Hwang, S. Hwa Jhung and G. Férey, High Uptakes of CO_2 and CH_4 in Mesoporous Metal-Organic Frameworks MIL-100 and MIL-101, *Langmuir*, 2008, **24**, 7245-7250.

54. S. R. Caskey, A. G. Wong-Foy and A. J. Matzger, Dramatic Tuning of Carbon Dioxide Uptake via Metal Substitution in a Coordination Polymer with Cylindrical Pores, *Journal of the American Chemical Society*, 2008, **130**, 10870-10871.

55. T. M. McDonald, D. M. D'Alessandro, R. Krishna and J. R. Long, Enhanced carbon dioxide capture upon incorporation of N,N[prime or minute]-dimethylethylenediamine in the metal-organic framework CuBTTri, *Chemical Science*, 2011, **2**, 2022-2028.

56. J. J. Gassensmith, H. Furukawa, R. A. Smaldone, R. S. Forgan, Y. Y. Botros, O. M. Yaghi and J. F. Stoddart, Strong and Reversible Binding of Carbon Dioxide in a Green Metal–Organic Framework, *Journal of the American Chemical Society*, 2011, **133**, 15312-15315.

57. R. Matsuda, R. Kitaura, S. Kitagawa, Y. Kubota, R. V. Belosludov, T. C. Kobayashi, H. Sakamoto, T. Chiba, M. Takata, Y. Kawazoe and Y. Mita, Highly controlled acetylene accommodation in a metal-organic microporous material, *Nature*, 2005, **436**, 238-241.

58. W. Morris, C. J. Doonan and O. M. Yaghi, Postsynthetic Modification of a Metal–Organic Framework for Stabilization of a Hemiaminal and Ammonia Uptake, *Inorganic Chemistry*, 2011, **50**, 6853-6855.

59. M. Kurmoo, Magnetic metal-organic frameworks, *Chemical Society Reviews*, 2009, **38**, 1353-1379.

60. P. D. Southon, L. Liu, E. A. Fellows, D. J. Price, G. J. Halder, K. W. Chapman, B. Moubaraki, K. S. Murray, J.-F. Létard and C. J. Kepert, Dynamic Interplay between Spin-Crossover and Host−Guest Function in a Nanoporous Metal−Organic Framework Material, *Journal of the American Chemical Society*, 2009, **131**, 10998-11009.

61. R. J. Kuppler, D. J. Timmons, Q.-R. Fang, J.-R. Li, T. A. Makal, M. D. Young, D. Yuan, D. Zhao, W. Zhuang and H.-C. Zhou, Potential applications of metal-organic frameworks, *Coordination Chemistry Reviews*, 2009, **253**, 3042-3066.

62. Z. Hu, B. J. Deibert and J. Li, Luminescent metal-organic frameworks for chemical sensing and explosive detection, *Chemical Society Reviews*, 2014, **43**, 5815-5840.

63. M. D. Allendorf, C. A. Bauer, R. K. Bhakta and R. J. T. Houk, Luminescent metal-organic frameworks, *Chemical Society Reviews*, 2009, **38**, 1330-1352.

64. Y. Cui, Y. Yue, G. Qian and B. Chen, Luminescent Functional Metal–Organic Frameworks, *Chemical Reviews*, 2012, **112**, 1126-1162.

65. D. Peer, J. M. Karp, S. Hong, O. C. Farokhzad, R. Margalit and R. Langer, Nanocarriers as an emerging platform for cancer therapy, *Nat Nano*, 2007, **2**, 751-760.

66. Bruna de Campos Ventura-Camargo and M. A. Marin-Morales, Azo Dyes: Characterization and Toxicity– A Review, *Textiles and Light Industrial Science and Technology (TLIST)*, 2013, **2**, 85-103.
67. A. Wasti and M. Ali Awan, Adsorption of textile dye onto modified immobilized activated alumina, *Journal of the Association of Arab Universities for Basic and Applied Sciences*, 2016, **20**, 26-31.
68. C. Zaharia, D. Suteu, A. Muresan, R. Muresan and A. Popescu, Textile wastewater treatment by homogeneous oxidation with hydrogen peroxide, *Environmental Engineering and Management Journal*, 2009, **8**, 1359-1369.
69. Q. Yao, J. Su, O. Cheung, Q. Liu, N. Hedin and X. Zou, Interpenetrated metal–organic frameworks and their uptake of CO_2 at relatively low pressures, *Journal of Materials Chemistry*, 2012, **22**, 10345-10351.
70. K. Sing, The use of nitrogen adsorption for the characterisation of porous materials, *Colloids and Surfaces A: Physicochemical and Engineering Aspects*, 2001, **187–188**, 3-9.
71. R. López and R. Gómez, Band-gap energy estimation from diffuse reflectance measurements on sol–gel and commercial TiO_2: a comparative study, *Journal of Sol-Gel Science and Technology*, 2012, **61**, 1-7.
72. Z. Yin, Y.-L. Zhou, M.-H. Zeng and M. Kurmoo, The concept of mixed organic ligands in metal-organic frameworks: design, tuning and functions, *Dalton Transactions*, 2015, **44**, 5258-5275.

73. T. Friscic and L. Fabian, Mechanochemical conversion of a metal oxide into coordination polymers and porous frameworks using liquid-assisted grinding (LAG), *CrystEngComm*, 2009, **11**, 743-745.

74. A. Pichon, C. M. Fierro, M. Nieuwenhuyzen and S. L. James, A pillared-grid MOF with large pores based on the $Cu_2(O_2CR)_4$ paddle-wheel, *CrystEngComm*, 2007, **9**, 449-451.

75. B.-Q. Ma, K. L. Mulfort and J. T. Hupp, Microporous Pillared Paddle-Wheel Frameworks Based on Mixed-Ligand Coordination of Zinc Ions, *Inorganic Chemistry*, 2005, **44**, 4912-4914.

76. K. Fujii, A. L. Garay, J. Hill, E. Sbircea, Z. Pan, M. Xu, D. C. Apperley, S. L. James and K. D. M. Harris, Direct structure elucidation by powder X-ray diffraction of a metal-organic framework material prepared by solvent-free grinding, *Chemical Communications*, 2010, **46**, 7572-7574.

77. A. C. Tella and S. O. Owalude, A green route approach to the synthesis of Ni(II) and Zn(II) templated metal–organic frameworks, *Journal of Materials Science*, 2014, **49**, 5635-5639.

78. N. T. S. Phan, T. T. Nguyen and P. H. L. Vu, A Copper Metal–Organic Framework as an Efficient and Recyclable Catalyst for the Oxidative Cross-Dehydrogenative Coupling of Phenols and Formamides, *ChemCatChem*, 2013, **5**, 3068-3077.

79. A. Altomare, C. Cuocci, C. Giacovazzo, A. Moliterni, R. Rizzi, N. Corriero and A. Falcicchio, EXPO2013: a kit of tools for phasing crystal structures from powder data, *Journal of Applied Crystallography*, 2013, **46**, 1231-1235.

80. A. Boultif and D. Louer, Powder pattern indexing with the dichotomy method, *Journal of Applied Crystallography*, 2004, **37**, 724-731.

81. B. Chen, S. Ma, F. Zapata, F. R. Fronczek, E. B. Lobkovsky and H.-C. Zhou, Rationally Designed Micropores within a Metal−Organic Framework for Selective Sorption of Gas Molecules, *Inorganic Chemistry*, 2007, **46**, 1233-1236.

82. Z.-J. Lin, J. Lu, M. Hong and R. Cao, Metal-organic frameworks based on flexible ligands (FL-MOFs): structures and applications, *Chemical Society Reviews*, 2014, **43**, 5867-5895.

83. I. Senkovska and S. Kaskel, Ultrahigh porosity in mesoporous MOFs: promises and limitations, *Chemical Communications*, 2014, **50**, 7089-7098.

84. P. D. Brown, H. K. Edwards and M. W. Fay, Microscopy at the life sciences / physical sciences interface, *Journal of Physics: Conference Series*, 2010, **241**, 012019.

85. H. K. Edwards, M. W. Fay, S. I. Anderson, C. A. Scotchford, D. M. Grant and P. D. Brown, An appraisal of ultramicrotomy, FIBSEM and cryogenic FIBSEM techniques for the sectioning of biological cells on titanium substrates for TEM investigation, *Journal of Microscopy*, 2009, **234**, 16-25.

86. H. Furukawa, N. Ko, Y. B. Go, N. Aratani, S. B. Choi, E. Choi, A. Ö. Yazaydin, R. Q. Snurr, M. O'Keeffe, J. Kim and O. M. Yaghi, Ultrahigh Porosity in Metal-Organic Frameworks, *Science*, 2010, **329**, 424.

87. J. Zha and X. Zhang, Room-Temperature Synthesis of Two-Dimensional Metal–Organic Frameworks with Controllable Size and Functionality for Enhanced CO_2 Sorption, *Crystal Growth & Design*, 2018, **18**, 3209-3214.

88. B. Chen, S. Xiang and G. Qian, Metal−Organic Frameworks with Functional Pores for Recognition of Small Molecules, *Accounts of Chemical Research*, 2010, **43**, 1115-1124.

89. S. K. Elsaidi, M. H. Mohamed, C. M. Simon, E. Braun, T. Pham, K. A. Forrest, W. Xu, D. Banerjee, B. Space, M. J. Zaworotko and P. K. Thallapally, Effect of ring rotation upon gas adsorption in SIFSIX-3-M (M = Fe, Ni) pillared square grid networks, *Chemical Science*, 2017, **8**, 2373-2380.

90. J.-R. Li, Y. Ma, M. C. McCarthy, J. Sculley, J. Yu, H.-K. Jeong, P. B. Balbuena and H.-C. Zhou, Carbon dioxide capture-related gas adsorption and separation in metal-organic frameworks, *Coordination Chemistry Reviews*, 2011, **255**, 1791-1823.

91. Y. S. Bae and R. Q. Snurr, Development and evaluation of porous materials for carbon dioxide separation and capture, *Angewandte Chemie - International Edition*, 2011, **50**, 11586-11596.

92. T. Rodenas, I. Luz, G. Prieto, B. Seoane, H. Miro, A. Corma, F. Kapteijn, F. X. Llabrés I Xamena and J. Gascon, Metal-organic framework nanosheets in polymer composite materials for gas separation, *Nature Materials*, 2015, **14**, 48-55.

93. B. Wang, Q. Yang, C. Guo, Y. Sun, L.-H. Xie and J.-R. Li, Stable Zr(IV)-Based Metal–Organic Frameworks with Predesigned Functionalized Ligands for Highly Selective Detection of Fe(III) Ions in Water, *ACS Applied Materials & Interfaces*, 2017, **9**, 10286-10295.

94. M.-Q. Wang, Y. Zhang, S.-J. Bao, Y.-N. Yu and C. Ye, Ni(II)-Based Metal-Organic Framework Anchored on Carbon Nanotubes for Highly Sensitive Non-Enzymatic Hydrogen Peroxide Sensing, *Electrochimica Acta*, 2016, **190**, 365-370.

95. J. Huang, Y. Li, R. K. Huang, C. T. He, L. Gong, Q. Hu, L. Wang, Y. T. Xu, X. Y. Tian, S. Y. Liu, Z. M. Ye, F. Wang, D. D. Zhou, W. X. Zhang and J. P. Zhang, Electrochemical Exfoliation of Pillared-Layer Metal–Organic Framework to Boost the Oxygen Evolution Reaction, *Angewandte Chemie - International Edition*, 2018, **57**, 4632-4636.

96. H. Zhao, Q. Xia, H. Xing, D. Chen and H. Wang, Construction of Pillared-Layer MOF as Efficient Visible-Light Photocatalysts for Aqueous Cr(VI) Reduction and Dye Degradation, *ACS Sustainable Chemistry & Engineering*, 2017, **5**, 4449-4456.

97. H. Zheng, Y. Zhang, L. Liu, W. Wan, P. Guo, A. M. Nyström and X. Zou, One-pot Synthesis of Metal–Organic Frameworks with Encapsulated Target Molecules and Their Applications for Controlled Drug Delivery, *Journal of the American Chemical Society*, 2016, **138**, 962-968.

98. H.-X. Zhao, Q. Zou, S.-K. Sun, C. Yu, X. Zhang, R.-J. Li and Y.-Y. Fu, Theranostic metal-organic framework core-shell composites for magnetic resonance imaging and drug delivery, *Chemical Science*, 2016, **7**, 5294-5301.

99. W. Lin, Q. Hu, K. Jiang, Y. Yang, Y. Yang, Y. Cui and G. Qian, A porphyrin-based metal–organic framework as a pH-responsive drug carrier, *Journal of Solid State Chemistry*, 2016, **237**, 307-312.

100. D. Sheberla, J. C. Bachman, J. S. Elias, C.-J. Sun, Y. Shao-Horn and M. Dincă, Conductive MOF electrodes for stable supercapacitors with high areal capacitance, *Nature Materials*, 2016, **16**, 220.

101. C. Qu, Y. Jiao, B. Zhao, D. Chen, R. Zou, K. S. Walton and M. Liu, Nickel-based pillared MOFs for high-performance supercapacitors: Design, synthesis and stability study, *Nano Energy*, 2016, **26**, 66-73.

102. M. Liu, F. Zhao, D. Zhu, H. Duan, Y. Lv, L. Li and L. Gan, Ultramicroporous carbon nanoparticles derived from metal–organic framework nanoparticles for high-performance supercapacitors, *Materials Chemistry and Physics*, 2018, **211**, 234-241.

103. J. Linnemann, L. Taudien, M. Klose and L. Giebeler, Electrodeposited films to MOF-derived electrochemical energy storage electrodes: a concept of simplified additive-free electrode processing for self-standing, ready-to-use materials, *Journal of Materials Chemistry A*, 2017, **5**, 18420-18428.

104. D. Bradshaw, J. B. Claridge, E. J. Cussen, T. J. Prior and M. J. Rosseinsky, Design, Chirality, and Flexibility in Nanoporous Molecule-Based Materials, *Accounts of Chemical Research*, 2005, **38**, 273-282.

105. D. J. Tranchemontagne, J. R. Hunt and O. M. Yaghi, Room temperature synthesis of metal-organic frameworks: MOF-5, MOF-74, MOF-177, MOF-199, and IRMOF-0, *Tetrahedron*, 2008, **64**, 8553-8557.

106. D. Tanaka, A. Henke, K. Albrecht, M. Moeller, K. Nakagawa, S. Kitagawa and J. Groll, Rapid preparation of flexible porous coordination polymer nanocrystals with accelerated guest adsorption kinetics, *Nat Chem*, 2010, **2**, 410-416.

107. H. Chun, D. N. Dybtsev, H. Kim and K. Kim, Synthesis, X-ray Crystal Structures, and Gas Sorption Properties of Pillared Square Grid Nets Based on Paddle-Wheel Motifs: Implications for Hydrogen Storage in Porous Materials, *Chemistry – A European Journal*, 2005, **11**, 3521-3529.

108. Z.-P. Qi, J.-M. Yang, Y.-S. Kang, F. Guo and W.-Y. Sun, Facile water-stability evaluation of metal-organic frameworks and the property of selective removal of dyes from aqueous solution, *Dalton Transactions*, 2016, **45**, 8753-8759.

109. H. Jasuja, Y. Jiao, N. C. Burtch, Y.-G. Huang and K. S. Walton, Synthesis of Cobalt-, Nickel-, Copper-, and Zinc-Based, Water-Stable, Pillared Metal–Organic Frameworks, *Langmuir*, 2014, **30**, 14300-14307.

110. J. B. DeCoste, G. W. Peterson, H. Jasuja, T. G. Glover, Y.-G. Huang and K. S. Walton, Stability and degradation mechanisms of metal-organic frameworks containing the $Zr_6O_4(OH)_4$ secondary building unit, *Journal of Materials Chemistry A*, 2013, **1**, 5642-5650.

111. S. Kanda, A. Suzuki and K. Ohkawa, Syntheses of Nonstereospecific and Stereospecific Lamellar Coordination Polymers. N,N -Disubstituted Dithiooxamides Copper Coordination Polymers, *Product R&D*, 1973, **12**, 88-96.

112. J. R. Durig and D. W. Wertz, Spectroscopic Review of the Normal Vibrations of Metal Complexes with Nitrogen-Containing Ligands, *Applied Spectroscopy*, 1968, **22**, 627-633.

113. D. C. Bradley and M. H. Gitlitz, Metal–Nitrogen Infrared Stretching Frequencies in Dialkylamido-transition Metal Compounds, *Nature*, 1968, **218**, 353-354.

114. X.-M. Shi, W. Hai-Yan, L. Yan-Bing, Y. Jing-Xiu, C. Lei, H. Ge, W.-Q. Xu and B. Zhao, *Spectroscopic studies on Co(II), Ni(II), Zn(II) complexes with 4,4′-bipyridine*, 2010.

115. K. Nakamoto, *Infrared and Raman Spectra of Inorganic and Coordination Compounds, Part B: Applications in Coordination, Organometallic, and Bioinorganic Chemistry*, Wiley, 2009.

116. M. Karabacak, M. Cinar, Z. Unal and M. Kurt, FT-IR, UV spectroscopic and DFT quantum chemical study on the molecular conformation, vibrational and electronic transitions of 2-aminoterephthalic acid, *Journal of Molecular Structure*, 2010, **982**, 22-27.

117. X. Li, L. Zheng, L. Huang, O. Zheng, Z. Lin, L. Guo, B. Qiu and G. Chen, Adsorption removal of crystal violet from aqueous solution using a metal-organic frameworks material, copper coordination polymer with dithiooxamide, *Journal of Applied Polymer Science*, 2013, **129**, 2857-2864.

118. A. Schneemann, V. Bon, I. Schwedler, I. Senkovska, S. Kaskel and R. A. Fischer, Flexible metal-organic frameworks, *Chemical Society Reviews*, 2014, **43**, 6062-6096.

119. G. Mínguez Espallargas and E. Coronado, Magnetic functionalities in MOFs: from the framework to the pore, *Chemical Society Reviews*, 2018, **47**, 533-557.

120. J. L. Manson, J. A. Schlueter, K. E. Garrett, P. A. Goddard, T. Lancaster, J. S. Möller, S. J. Blundell, A. J. Steele, I. Franke, F. L. Pratt, J. Singleton, J. Bendix, S. H. Lapidus, M. Uhlarz, O. Ayala-Valenzuela, R. D. McDonald, M. Gurak and C. Baines, Bimetallic MOFs $(H_3O)x[Cu(MF_6)(pyrazine)_2]\cdot(4 - x)H_2O$ (M = V^{4+}, x =

0; M = Ga^{3+}, x = 1): co-existence of ordered and disordered quantum spins in the V^{4+} system, *Chemical Communications*, 2016, **52**, 12653-12656.

121. X.-Y. Wang, Z.-M. Wang and S. Gao, Constructing magnetic molecular solids by employing three-atom ligands as bridges, *Chemical Communications*, 2008, DOI: 10.1039/B708122G, 281-294.

122. W. Wang, L. Q. Yan, J. Z. Cong, Y. L. Zhao, F. Wang, S. P. Shen, T. Zou, D. Zhang, S. G. Wang, X. F. Han and Y. Sun, Magnetoelectric coupling in the paramagnetic state of a metal-organic framework, *Scientific Reports*, 2013, **3**, 2024.

123. G. Moussavi and M. Mahmoudi, Removal of azo and anthraquinone reactive dyes from industrial wastewaters using MgO nanoparticles, *Journal of Hazardous Materials*, 2009, **168**, 806-812.

124. I. Bazin, A. Ibn Hadj Hassine, Y. Haj Hamouda, W. Mnif, A. Bartegi, M. Lopez-Ferber, M. De Waard and C. Gonzalez, Estrogenic and anti-estrogenic activity of 23 commercial textile dyes, *Ecotoxicology and Environmental Safety*, 2012, **85**, 131-136.

125. N. O. San, A. Celebioglu, Y. Tümtaş, T. Uyar and T. Tekinay, Reusable bacteria immobilized electrospun nanofibrous webs for decolorization of methylene blue dye in wastewater treatment, *RSC Advances*, 2014, **4**, 32249-32255.

126. H. Liu, N. Gao, M. Liao and X. Fang, Hexagonal-like Nb_2O_5 Nanoplates-Based Photodetectors and Photocatalyst with High Performances, *Scientific Reports*, 2015, **5**, 7716.

127. R. Kumar, J. Rashid and M. A. Barakat, Synthesis and characterization of a starch–AlOOH–FeS_2 nanocomposite for the adsorption of congo red dye from aqueous solution, *RSC Advances*, 2014, **4**, 38334-38340.

128. K. E. Lee, N. Morad, T. T. Teng and B. T. Poh, Reactive Dye Removal Using Inorganic–Organic Composite Material: Kinetics, Mechanism, and Optimization, *Journal of Dispersion Science and Technology*, 2014, **35**, 1557-1570.

129. A. Paz, J. Carballo, M. J. Pérez and J. M. Domínguez, Biological treatment of model dyes and textile wastewaters, *Chemosphere*, 2017, **181**, 168-177.

130. P. K. Boruah, P. Borthakur, G. Darabdhara, C. K. Kamaja, I. Karbhal, M. V. Shelke, P. Phukan, D. Saikia and M. R. Das, Sunlight assisted degradation of dye molecules and reduction of toxic Cr(VI) in aqueous medium using magnetically recoverable Fe_3O_4/reduced graphene oxide nanocomposite, *RSC Advances*, 2016, **6**, 11049-11063.

131. M. A. Nasalevich, C. H. Hendon, J. G. Santaclara, K. Svane, B. van der Linden, S. L. Veber, M. V. Fedin, A. J. Houtepen, M. A. van der Veen, F. Kapteijn, A. Walsh and J. Gascon, Electronic origins of photocatalytic activity in d^0 metal organic frameworks, *Scientific Reports*, 2016, **6**, 23676.

132. X. Li, L. Yang, C. Qin, F.-H. Liu, L. Zhao, K.-Z. Shao and Z.-M. Su, POM-based inorganic–organic hybrid compounds: synthesis, structures, highly-connected topologies and photodegradation of organic dyes, *RSC Advances*, 2015, **5**, 59093-59098.

133. R. Ghosh, A. K. S, S. M. Pratik, A. Datta, R. Nath and S. Mandal, Synthesis, structure, photocatalytic and magnetic properties of an oxo-bridged copper dimer, *RSC Advances*, 2014, **4**, 21195-21200.

134. Z. Wu, X. Yuan, J. Zhang, H. Wang, L. Jiang and G. Zeng, Photocatalytic Decontamination of Wastewater Containing Organic Dyes by Metal–Organic Frameworks and their Derivatives, *ChemCatChem*, 2017, **9**, 41-64.

135. M. A. Nasalevich, M. van der Veen, F. Kapteijn and J. Gascon, Metal–organic frameworks as heterogeneous photocatalysts: advantages and challenges, *CrystEngComm*, 2014, **16**, 4919-4926.

136. S. Wang and X. Wang, Multifunctional Metal–Organic Frameworks for Photocatalysis, *Small*, 2015, **11**, 3097-3112.

137. N. M. Mahmoodi, J. Abdi, M. Oveisi, M. Alinia Asli and M. Vossoughi, Metal-organic framework (MIL-100 (Fe)): Synthesis, detailed photocatalytic dye degradation ability in colored textile wastewater and recycling, *Materials Research Bulletin*, 2018, **100**, 357-366.

138. Z. Hasan and S. H. Jhung, Removal of hazardous organics from water using metal-organic frameworks (MOFs): Plausible mechanisms for selective adsorptions, *Journal of Hazardous Materials*, 2015, **283**, 329-339.

139. M. C. Das, H. Xu, Z. Wang, G. Srinivas, W. Zhou, Y.-F. Yue, V. N. Nesterov, G. Qian and B. Chen, A Zn_4O-containing doubly interpenetrated porous metal–organic framework for photocatalytic decomposition of methyl orange, *Chemical Communications*, 2011, **47**, 11715-11717.

140. R. W. Matthews, Photooxidative degradation of coloured organics in water using supported catalysts. TiO_2 on sand, *Water Research*, 1991, **25**, 1169-1176.

141. M. Saquib, M. Abu Tariq, M. M. Haque and M. Muneer, Photocatalytic degradation of disperse blue 1 using UV/TiO_2/H_2O_2 process, *Journal of Environmental Management*, 2008, **88**, 300-306.

142. A. Ajmal, I. Majeed, R. N. Malik, H. Idriss and M. A. Nadeem, Principles and mechanisms of photocatalytic dye degradation on TiO_2 based photocatalysts: a comparative overview, *RSC Advances*, 2014, **4**, 37003-37026.

143. H. Zhu, R. Jiang, Y. Fu, Y. Guan, J. Yao, L. Xiao and G. Zeng, Effective photocatalytic decolorization of methyl orange utilizing TiO_2/ZnO/chitosan nanocomposite films under simulated solar irradiation, *Desalination*, 2012, **286**, 41-48.

144. H.-P. Jing, C.-C. Wang, Y.-W. Zhang, P. Wang and R. Li, Photocatalytic degradation of methylene blue in ZIF-8, *RSC Advances*, 2014, **4**, 54454-54462.

145. S.-H. Huo and X.-P. Yan, Metal–organic framework MIL-100(Fe) for the adsorption of malachite green from aqueous solution, *Journal of Materials Chemistry*, 2012, **22**, 7449-7455.

146. M. Y. Masoomi, M. Bagheri and A. Morsali, High efficiency of mechanosynthesized Zn-based metal-organic frameworks in photodegradation of congo red under UV and visible light, *RSC Advances*, 2016, **6**, 13272-13277.

147. M. Gutierrez, B. Cohen, F. Sánchez and A. Douhal, Photochemistry of Zr-based MOFs: ligand-to-cluster charge transfer, energy transfer and excimer formation, what else is there?, *Physical Chemistry Chemical Physics*, 2016, **18**, 27761-27774.

APPENDIX A: Extended frameworks

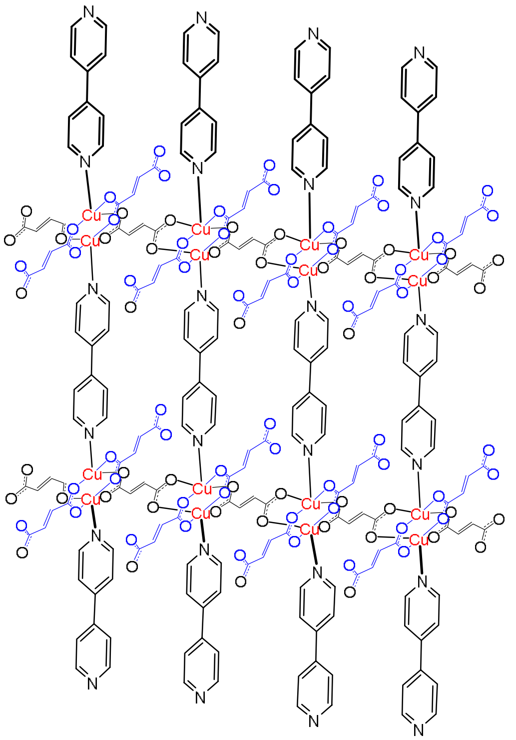

MOFT-23-RT ({[$Cu_2(Fu)_2(BPY)$]·H_2O}$_n$)

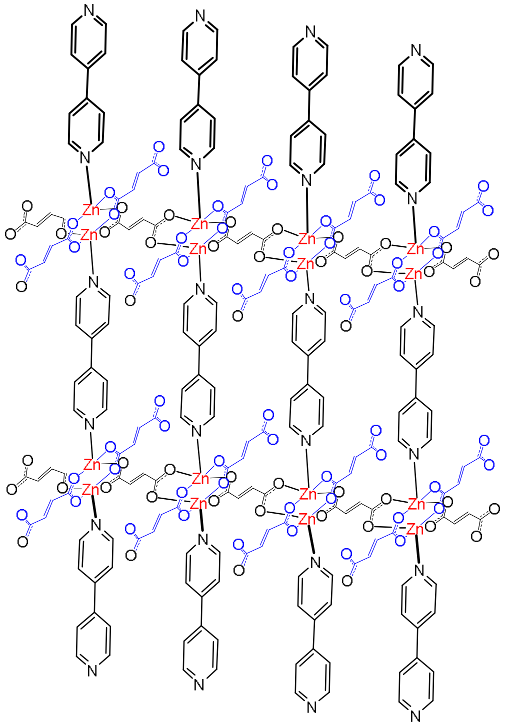

MOFT-22-RT ({[$Zn_2(Fu)_2(BPY)$]·1.5H_2O}$_n$)

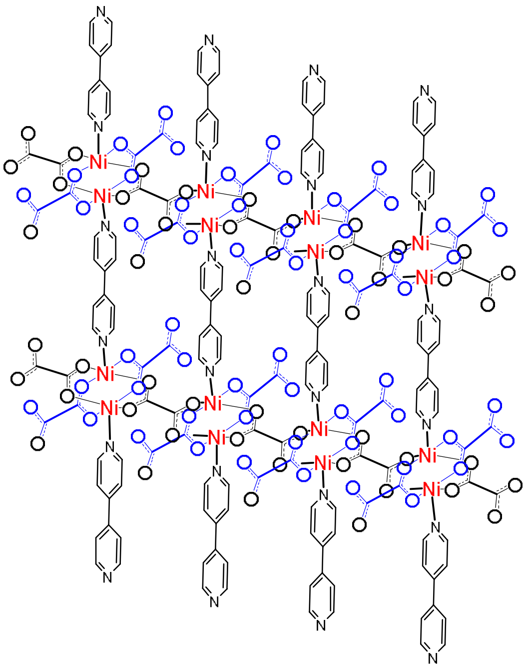

MOFT-11-RT ({[$Ni_2(Ox)_2(BPY)$]·3.75H_2O}$_n$)

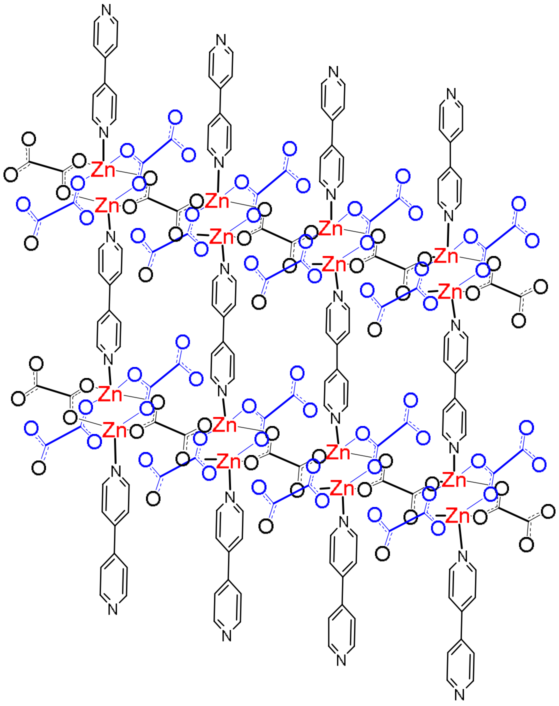

MOFT-08-RT ($\{[Zn_2(Ox)_2(BPY)]\cdot 3.5H_2O\}_n$)

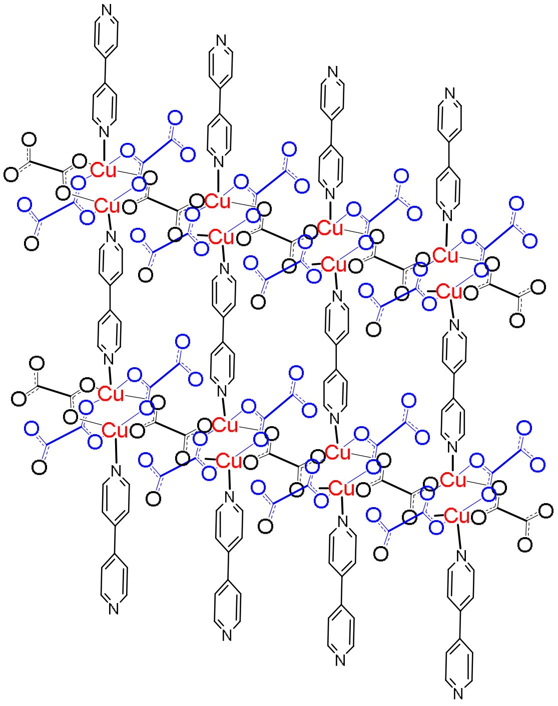

MOFT-09-RT ($\{[Cu_2(Ox)_2(BPY)]\cdot 0.5H_2O\}_n$)

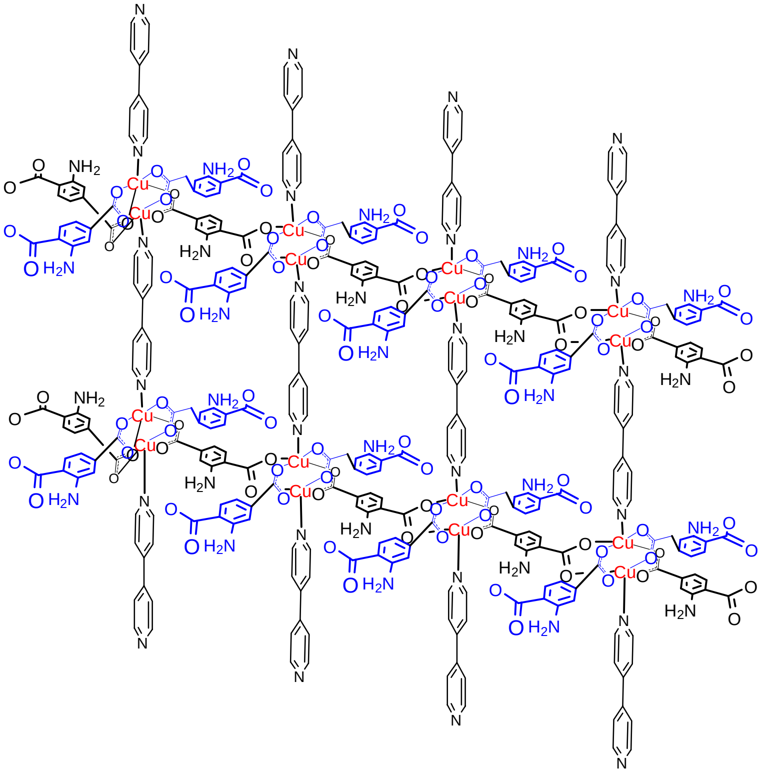

MOFT-53-RT ($\{[Zn_2(ATA)_2(BPY)]\cdot H_2O\}_n$)

APPENDIX B: MOFs Synthetic Schemes

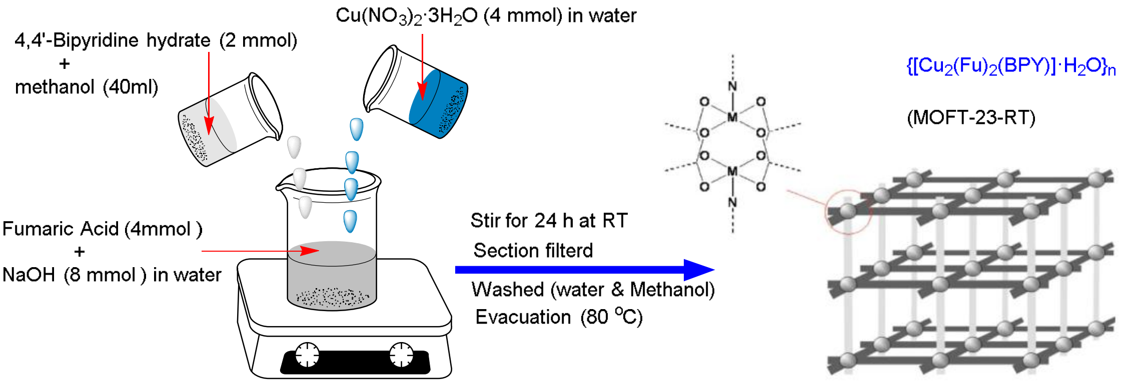

Synthetic scheme for {[Cu$_2$(Fu)$_2$(BPY)]·H$_2$O}$_n$

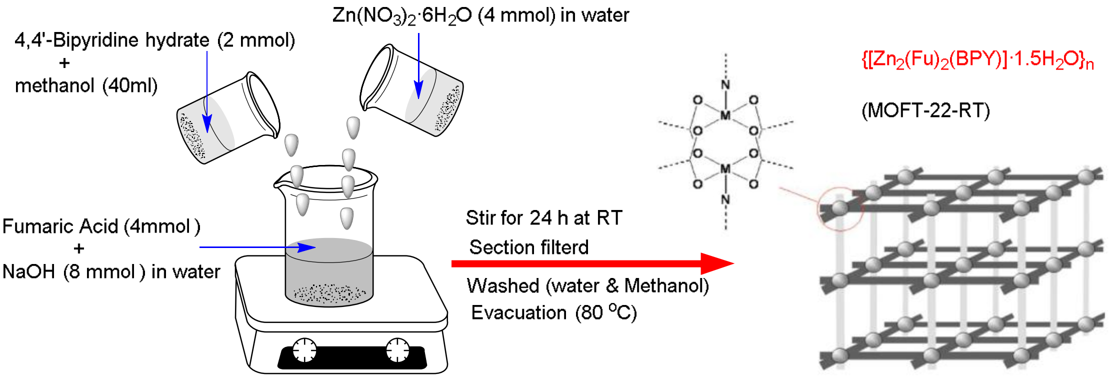

Synthetic scheme for {[Zn$_2$(Fu)$_2$(BPY)]·1.5H$_2$O}$_n$

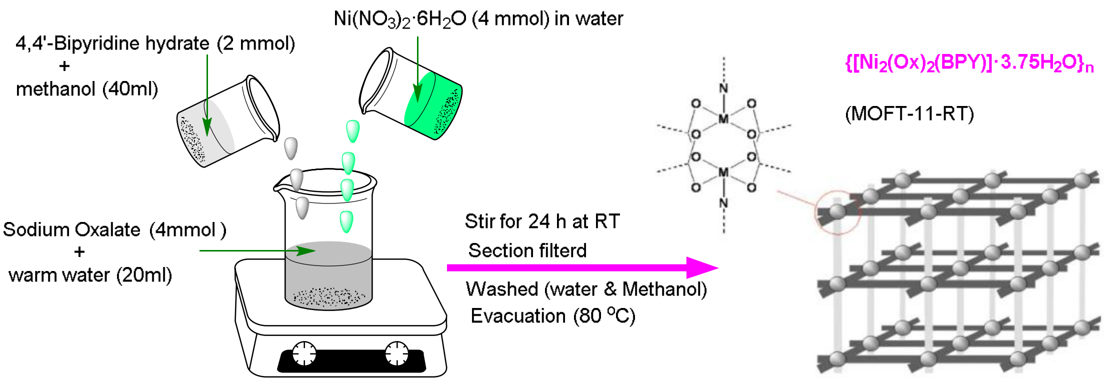

Synthetic scheme for $\{[Ni_2(Ox)_2(BPY)]\cdot 3.75H_2O\}_n$

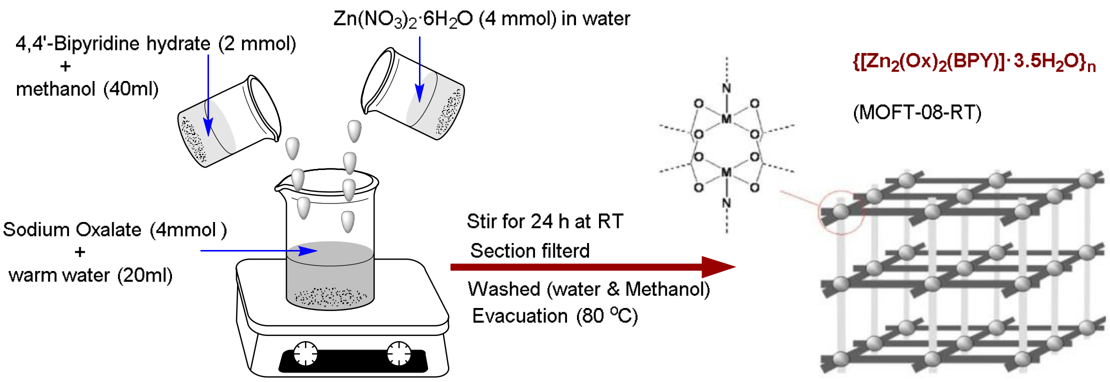

Synthetic scheme for $\{[Zn_2(Ox)_2(BPY)]\cdot 3.5H_2O\}_n$

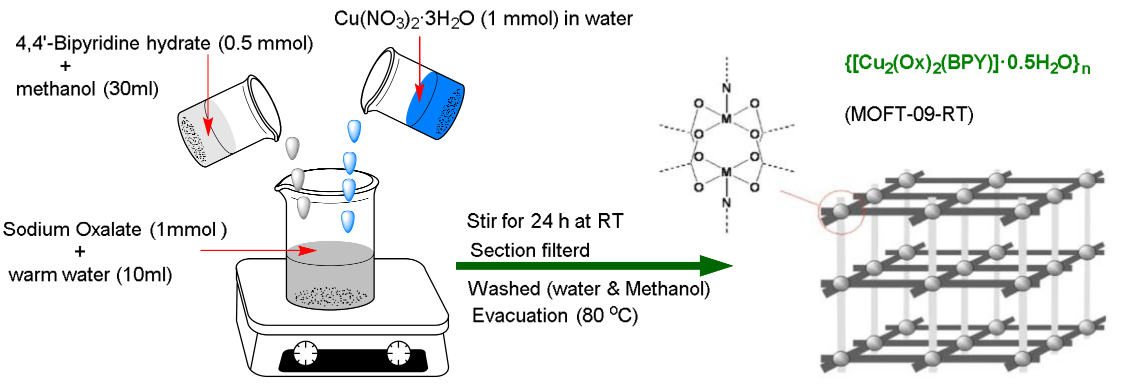

Synthetic scheme for {[Cu$_2$(Ox)$_2$(BPY)]·0.5H$_2$O}$_n$

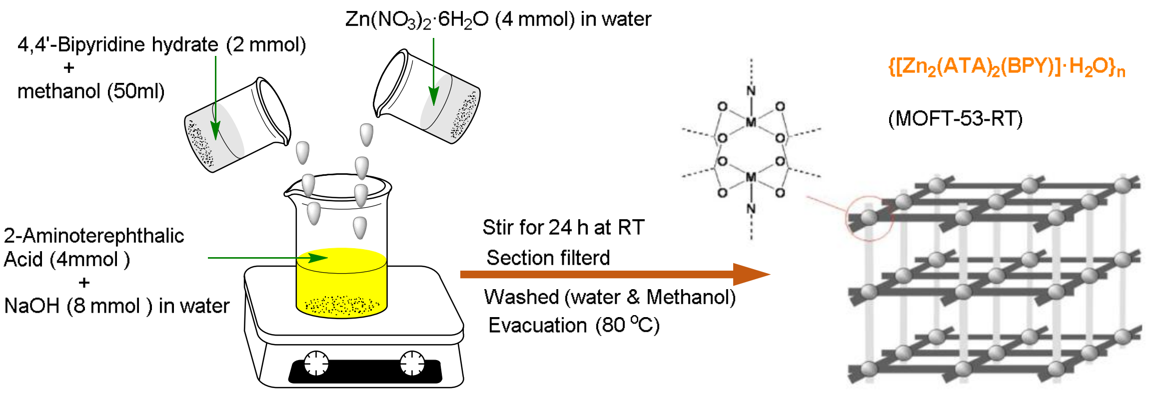

Synthetic scheme for {[Zn$_2$(ATA)$_2$(BPY)]·H$_2$O}$_n$

APPENDIX C: PXRD patterns of MOFs

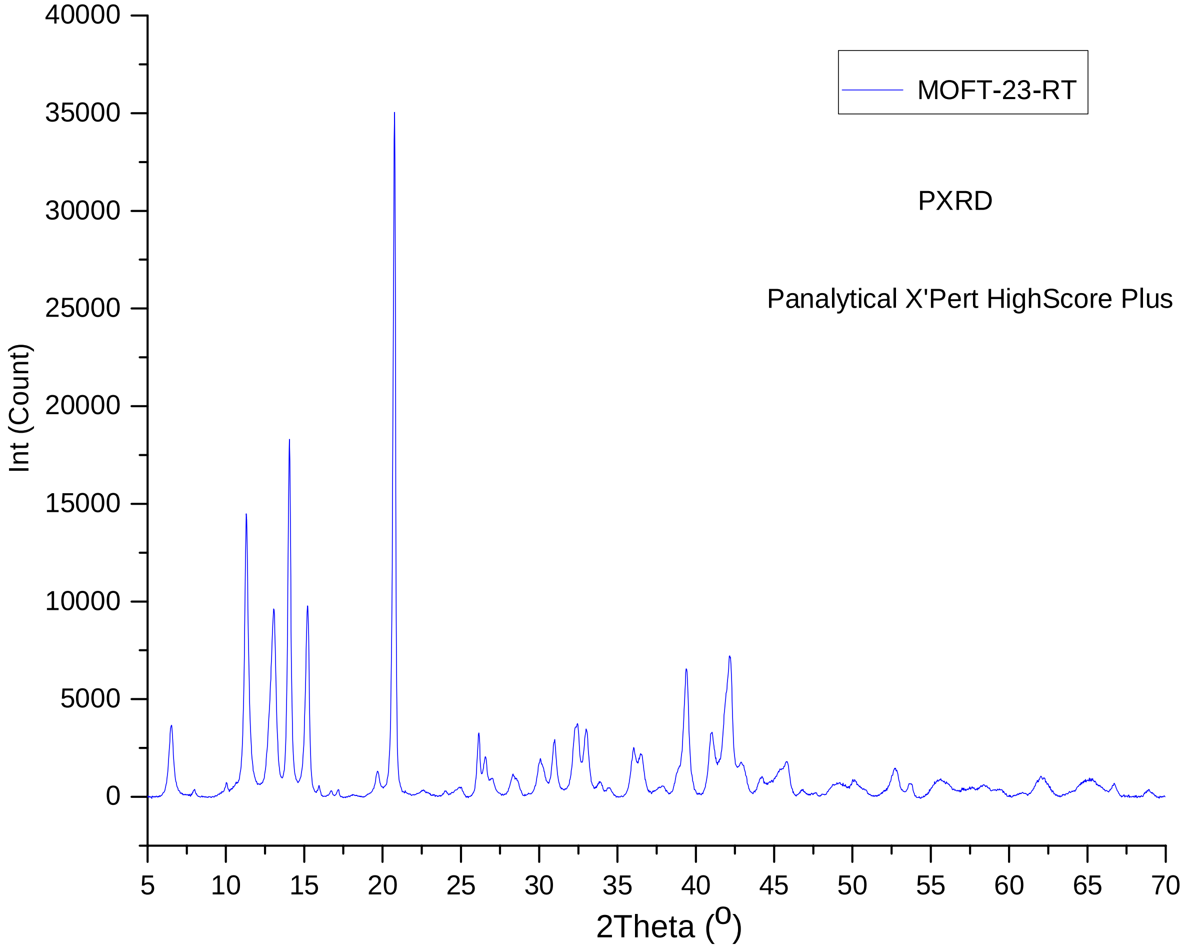

PXRD pattern of $\{[Cu_2(Fu)_2(BPY)]\cdot H_2O\}_n$

………PXRD patterns of MOFs

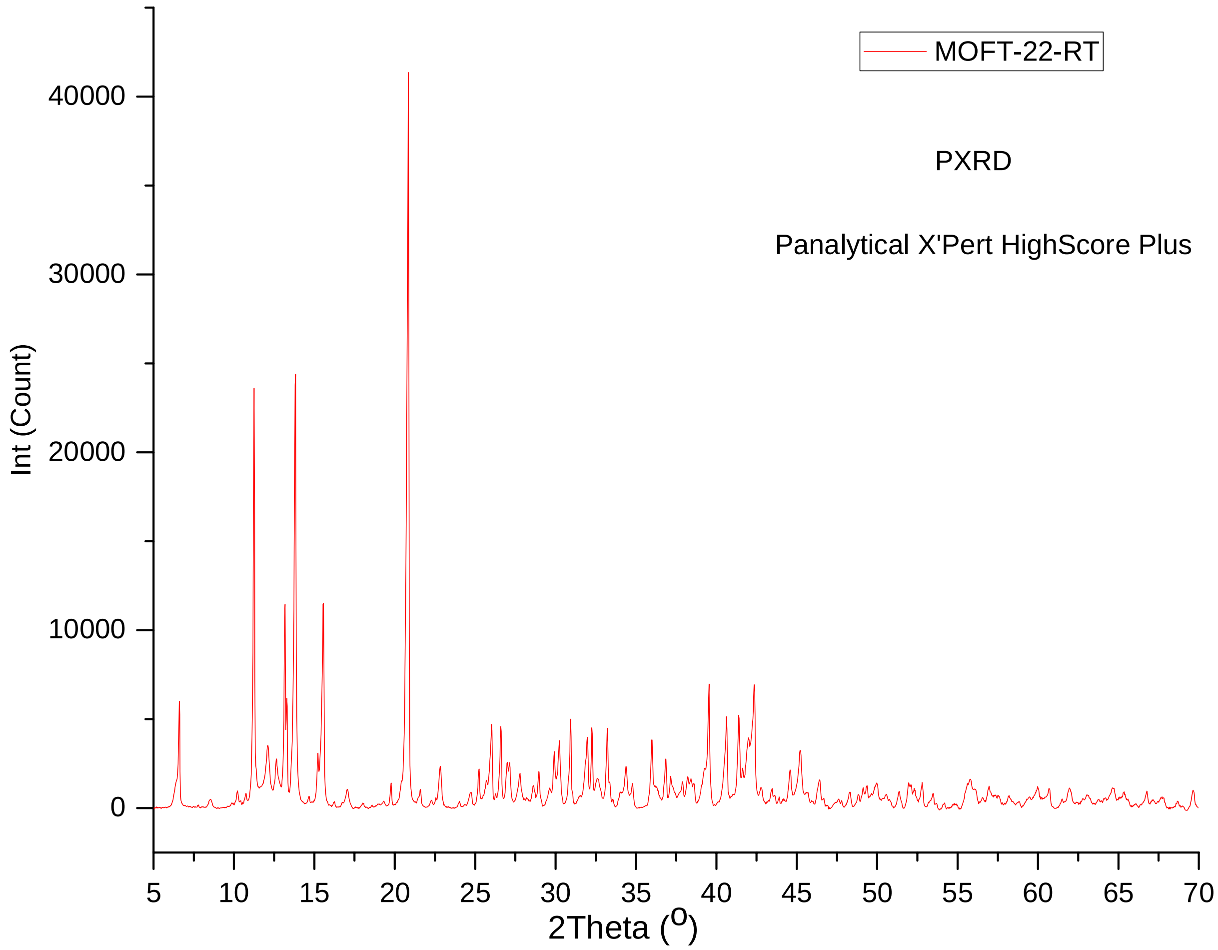

PXRD pattern of $\{[Zn_2(Fu)_2(BPY)]\cdot1.5H_2O\}_n$

……...PXRD patterns of MOFs

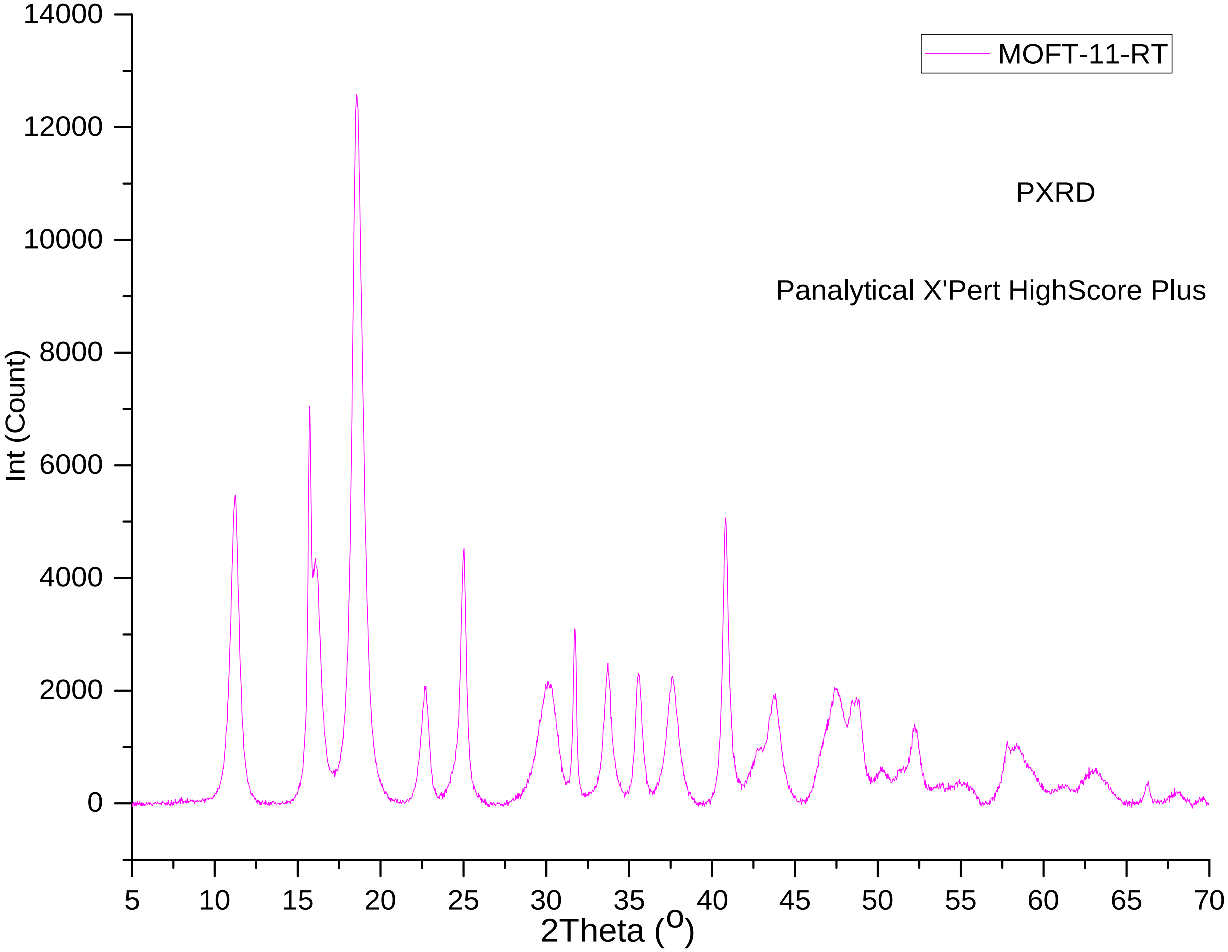

PXRD pattern of {[$Ni_2(Ox)_2(BPY)$]·3.75H_2O}$_n$

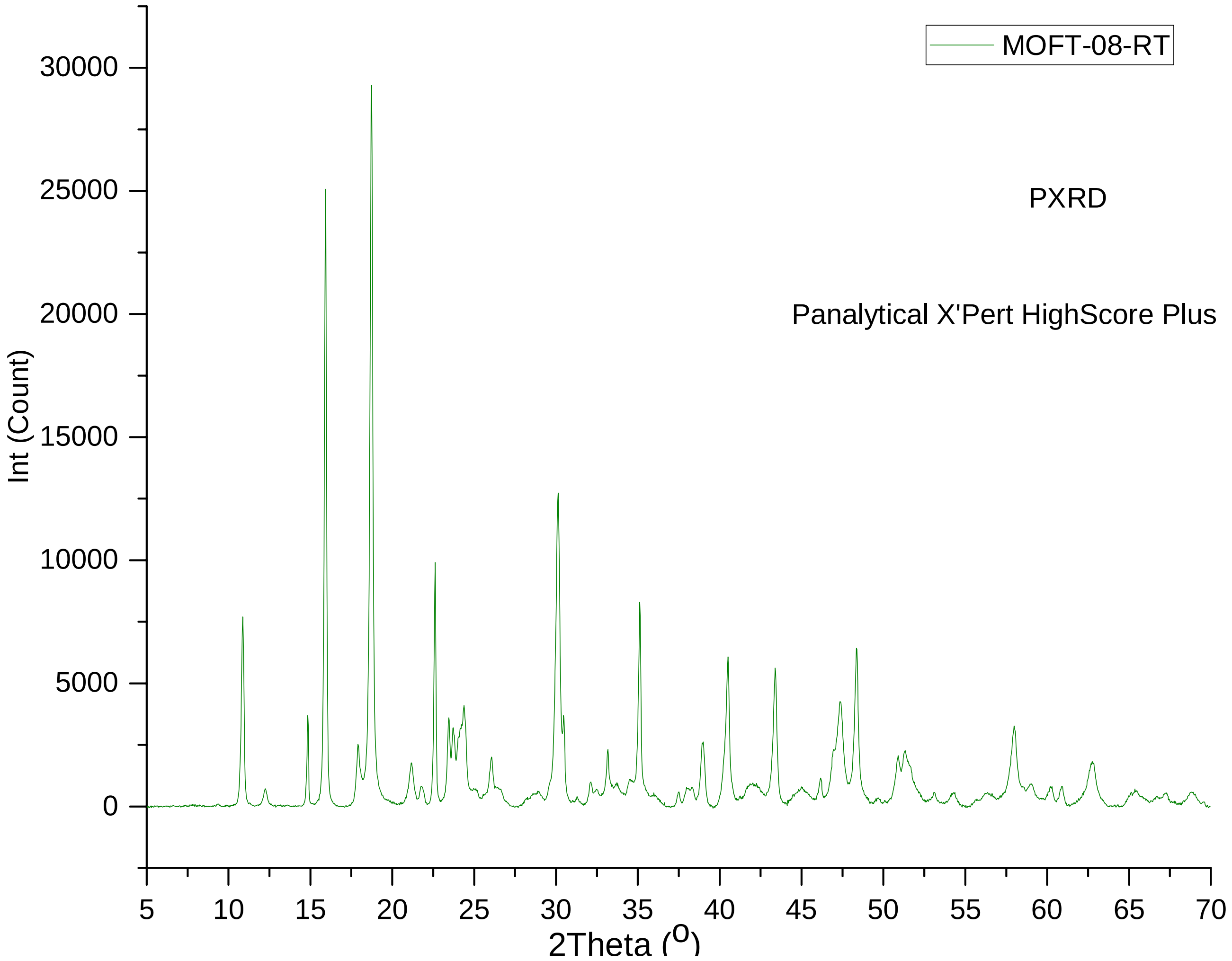

PXRD pattern of $\{[Zn_2(Ox)_2(BPY)]\cdot 3.5H_2O\}_n$

…….PXRD patterns of MOFs

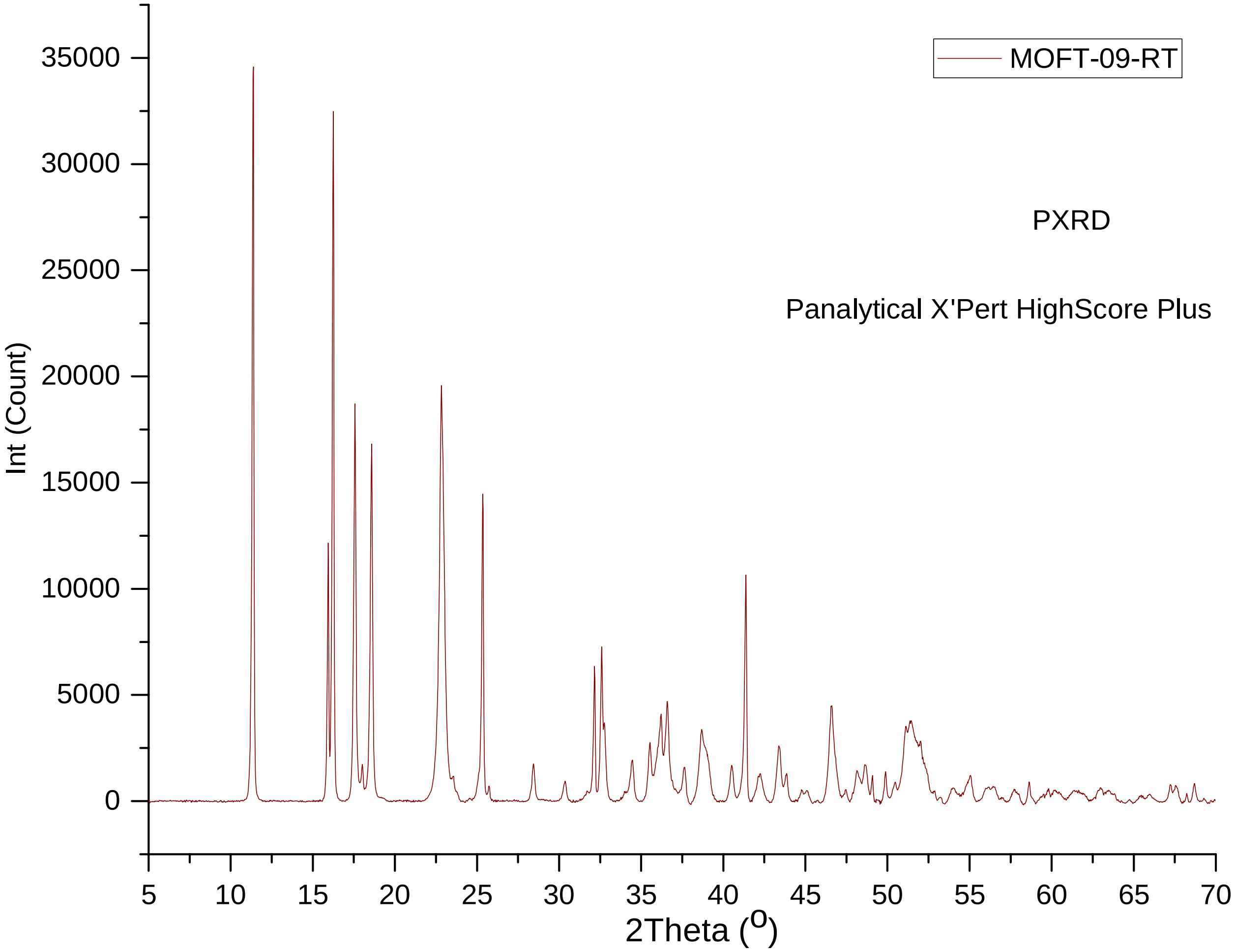

PXRD pattern of $\{[Cu_2(Ox)_2(BPY)]\cdot 0.5H_2O\}_n$

…….PXRD patterns of MOFs

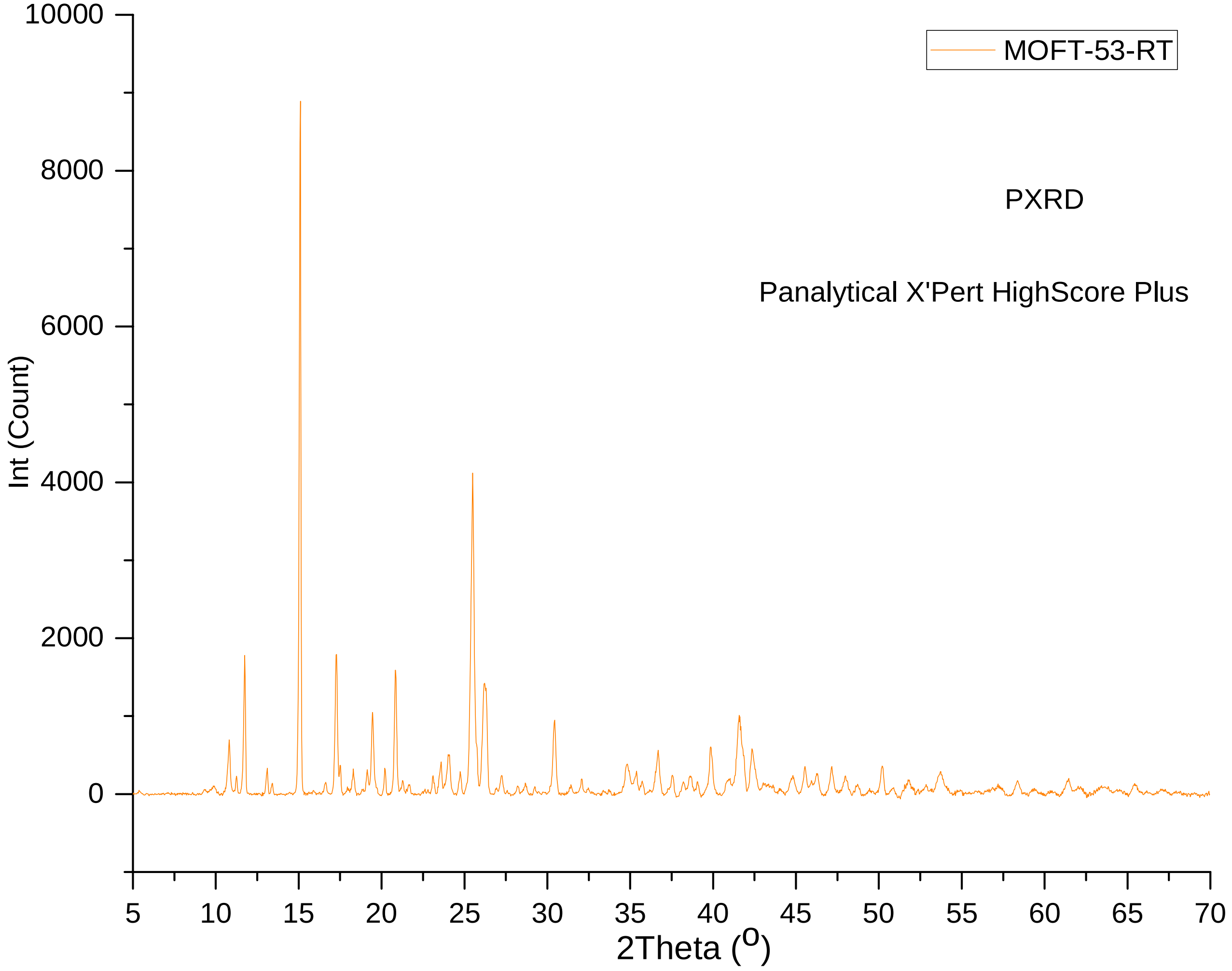

PXRD pattern of $\{[Zn_2(ATA)_2(BPY)]\cdot H_2O\}_n$

APPENDIX D: FT-IR spectra (Full size)

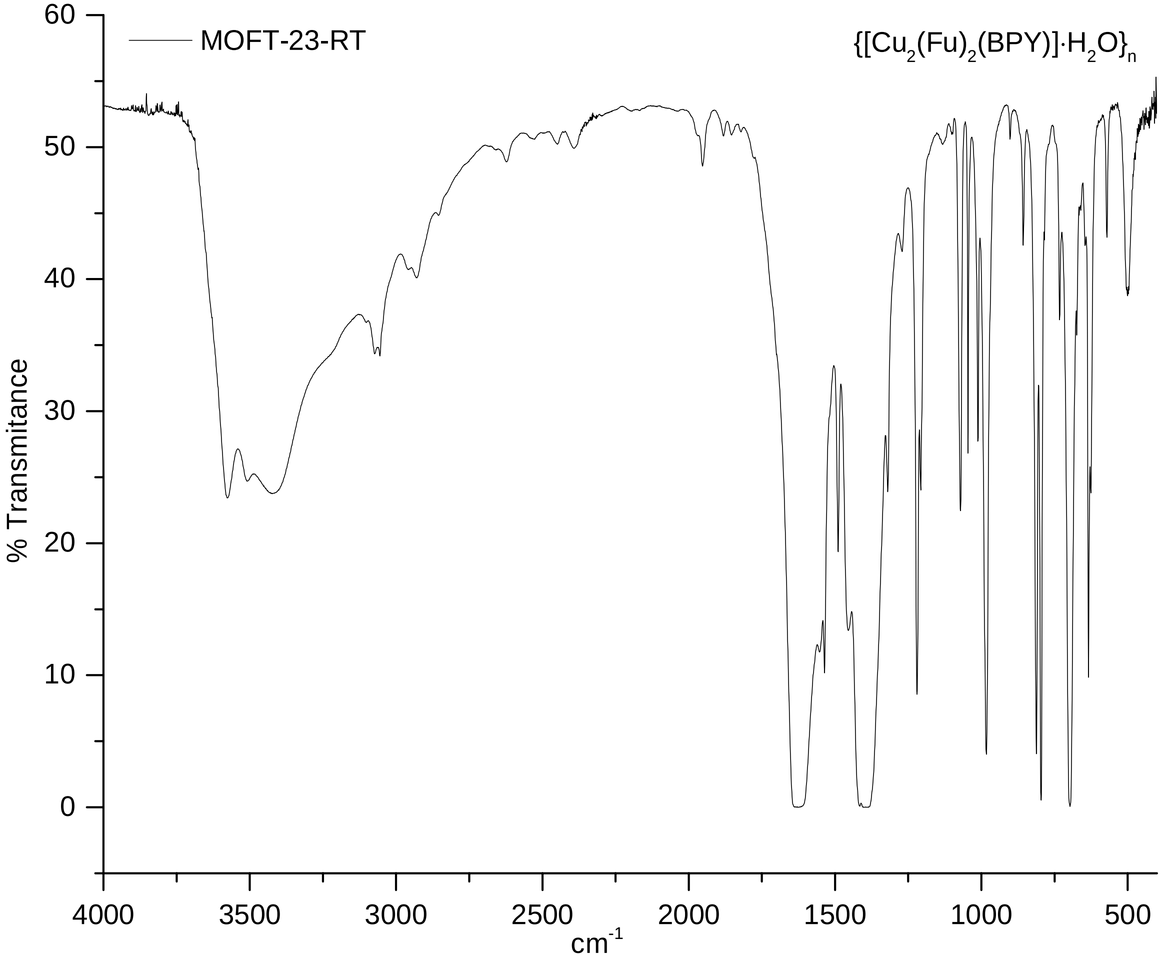

FT-IR spectrum of {[Cu$_2$(Fu)$_2$(BPY)]·H$_2$O}$_n$

….. FT-IR spectra (Full size)

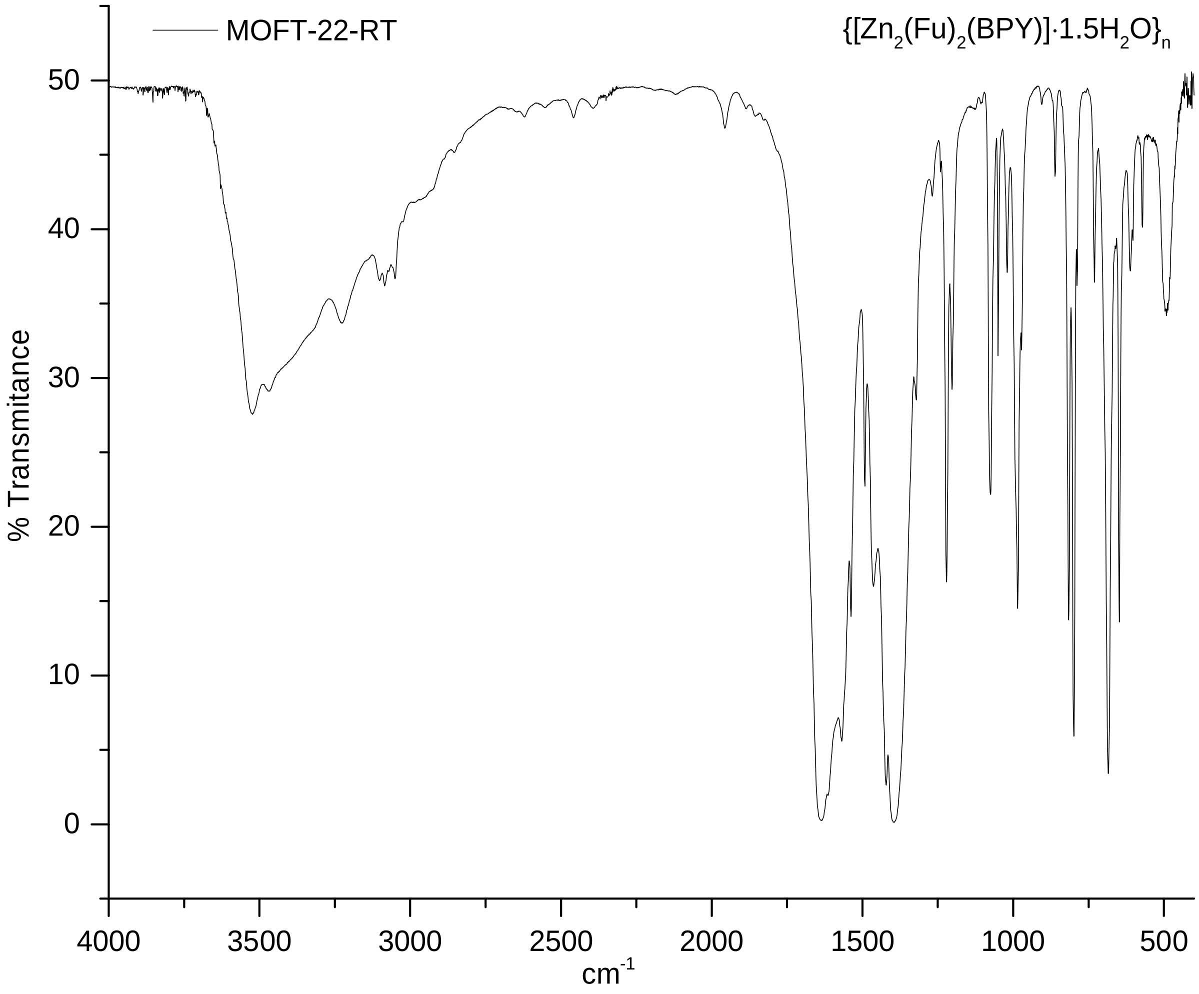

FT-IR spectrum of {[Zn$_2$(Fu)$_2$(BPY)]·1.5H$_2$O}$_n$

……. FT-IR spectra (Full size)

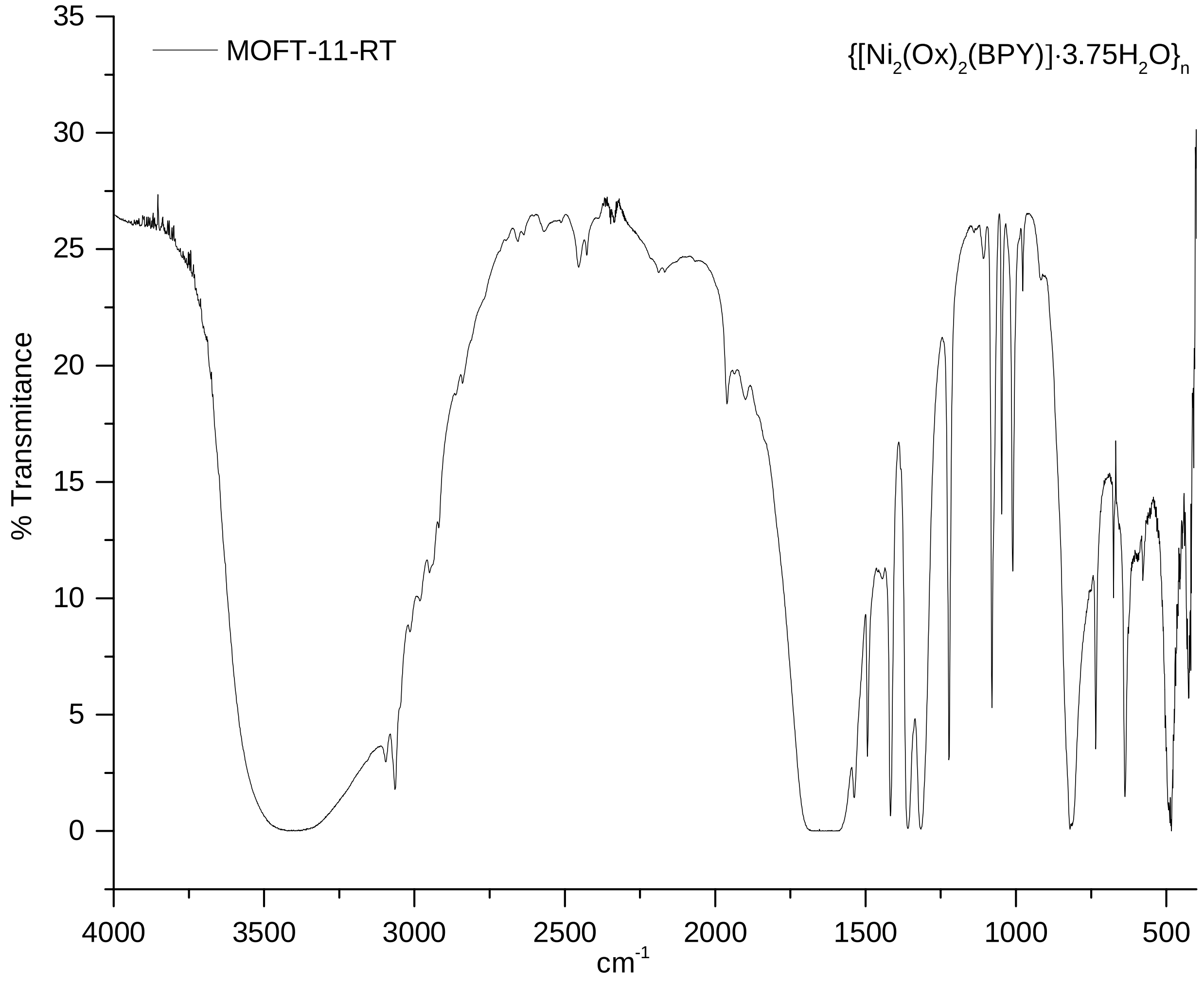

FT-IR spectrum of {[Ni$_2$(Ox)$_2$(BPY)]·3.75H$_2$O}$_n$

…… FT-IR spectra (Full size)

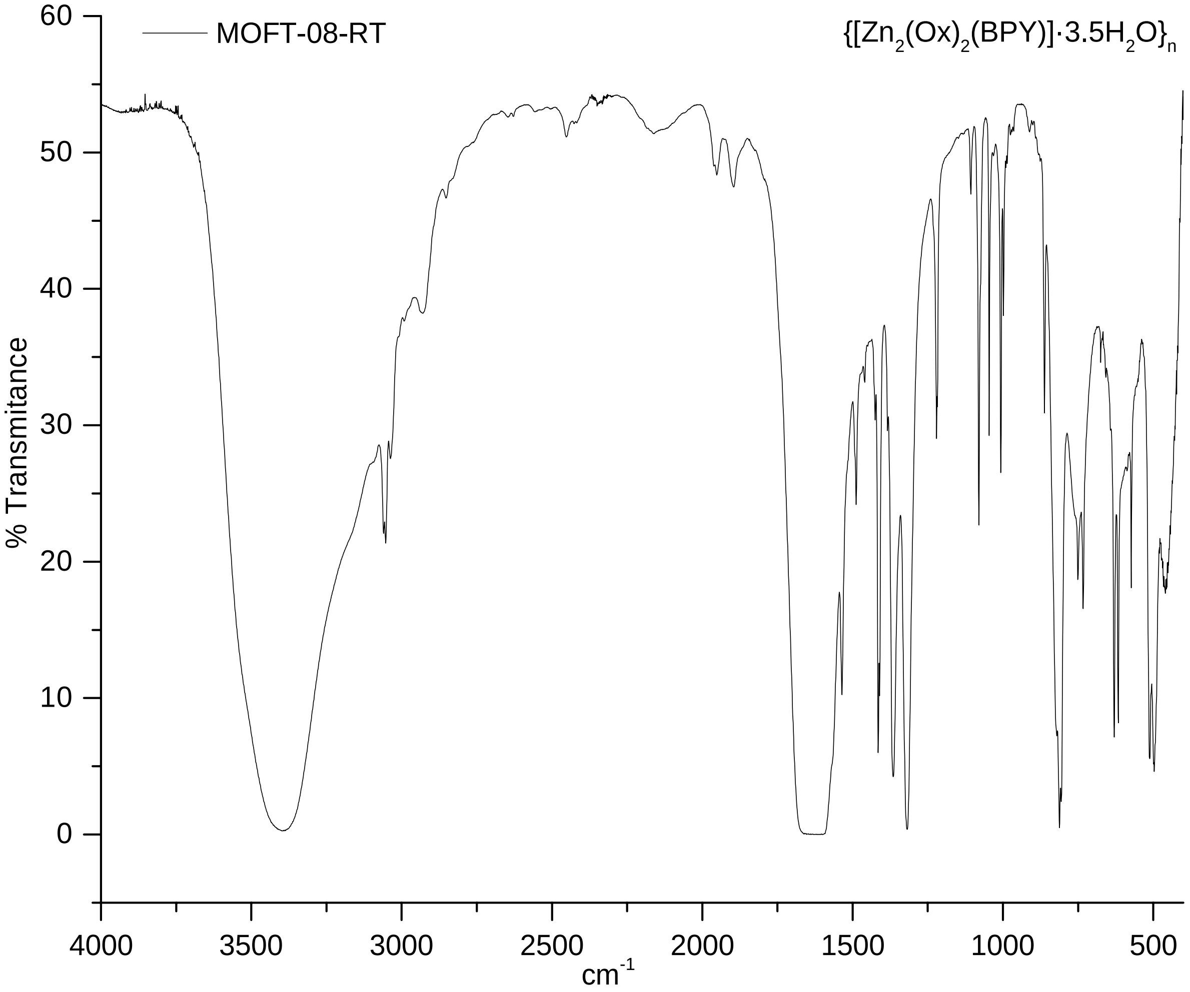

FT-IR spectrum of {[Zn$_2$(Ox)$_2$(BPY)]·3.5H$_2$O}$_n$

……. FT-IR spectra (Full size)

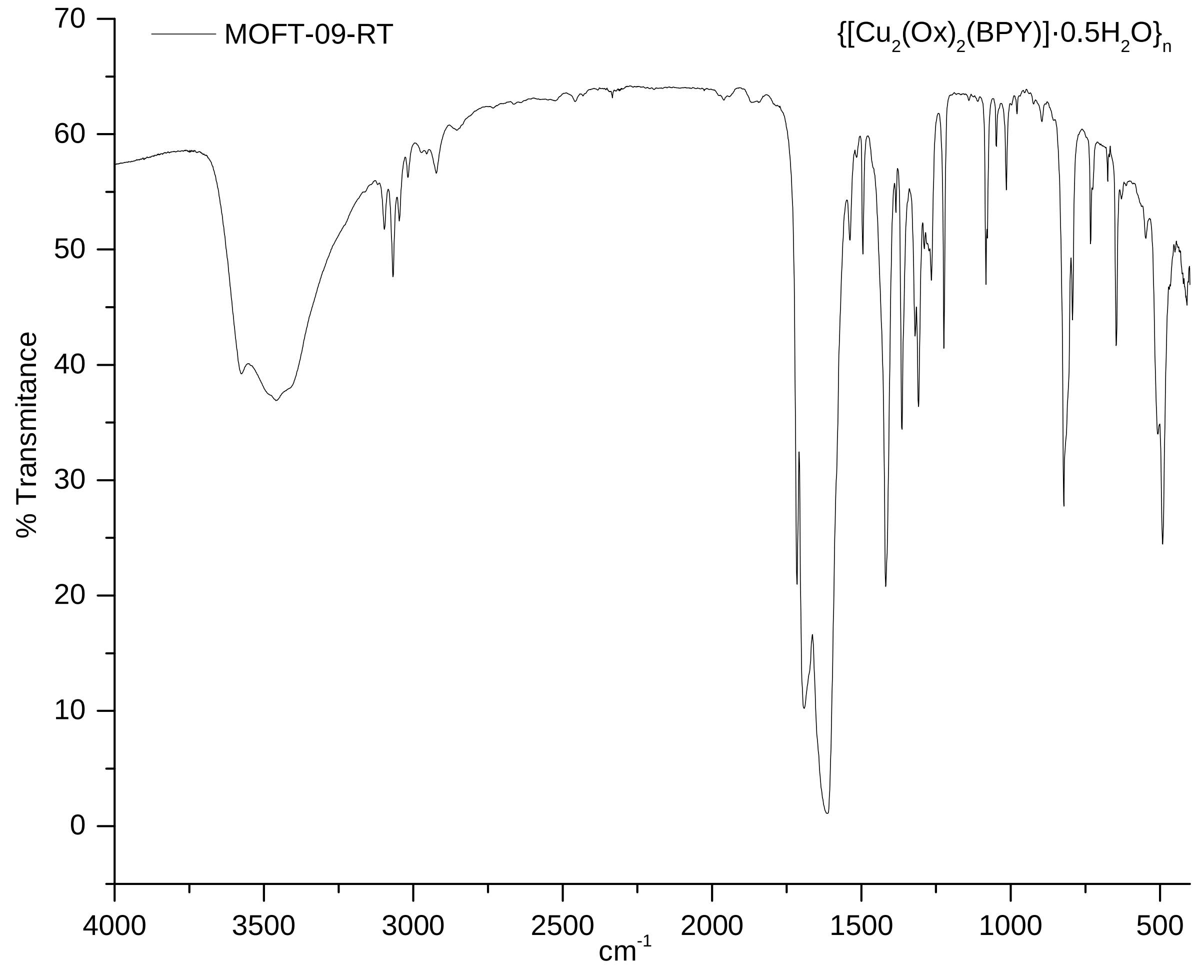

FT-IR spectrum of $\{[Cu_2(Ox)_2(BPY)]\cdot 0.5H_2O\}_n$

…………… FT-IR spectra (Full size)

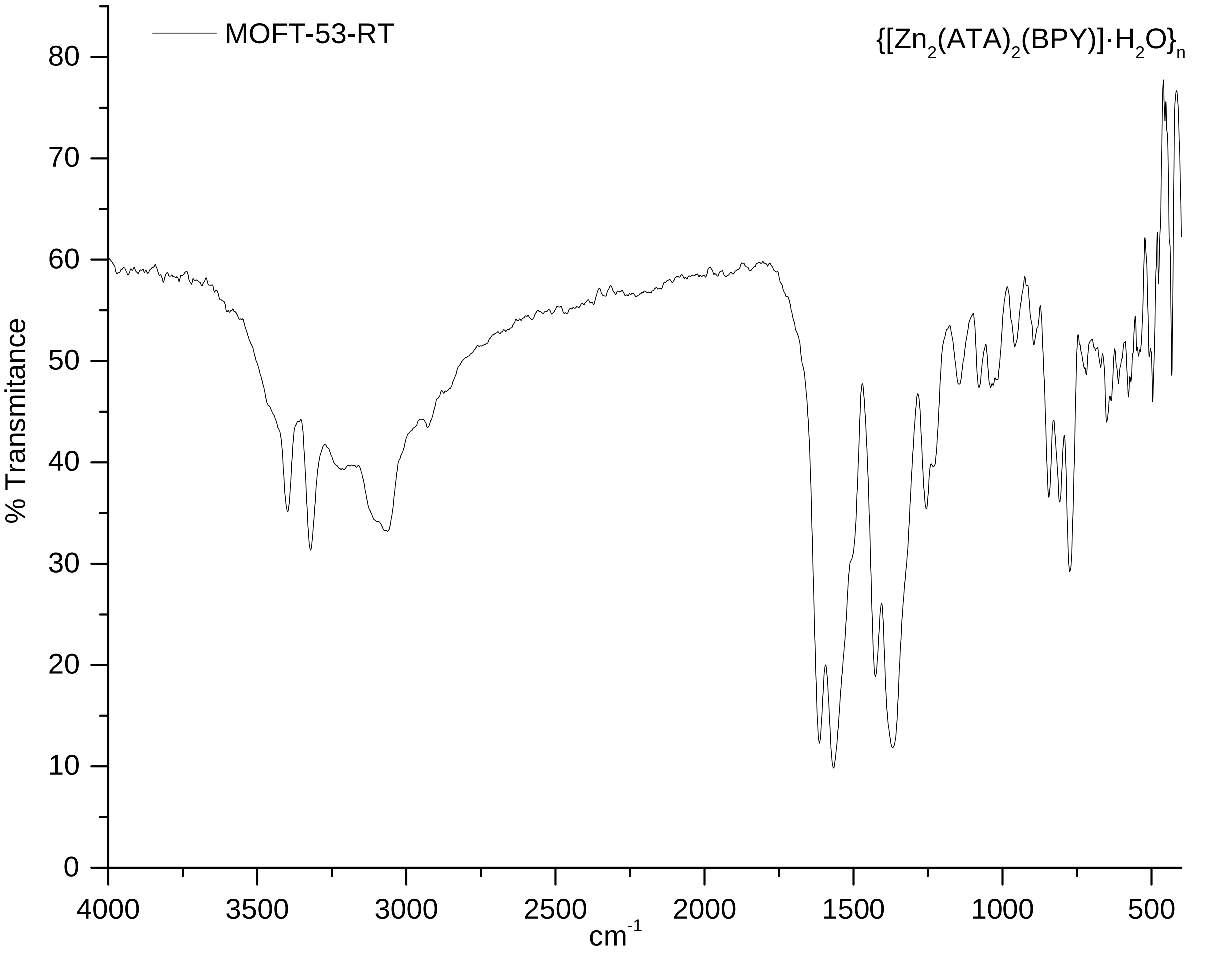

FT-IR spectrum of $\{[Zn_2(ATA)_2(BPY)]\cdot H_2O\}_n$

……. FT-IR spectra (Full size)

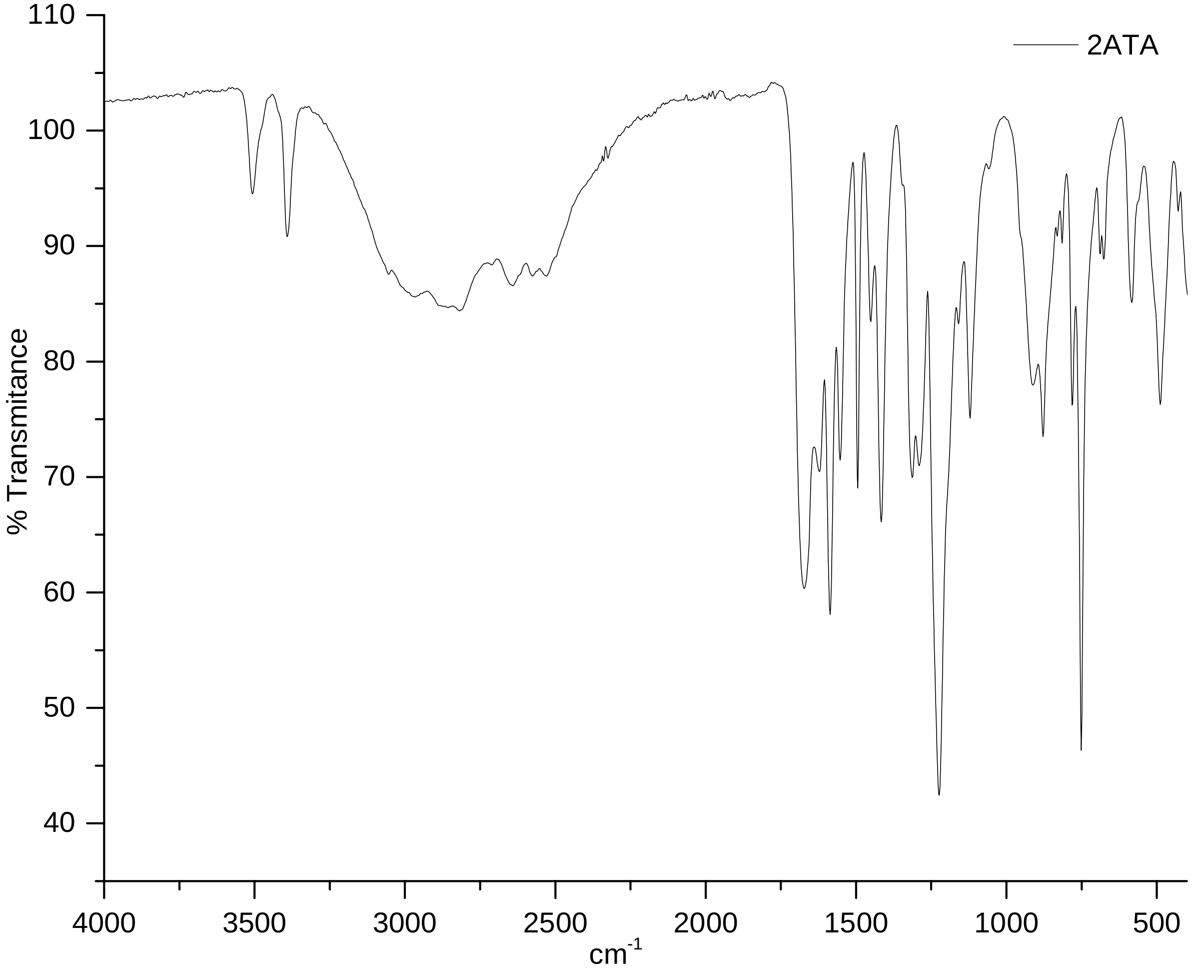

FT-IR spectrum of 2-Aminoterephtalic acid

……. FT-IR spectra (Full size)

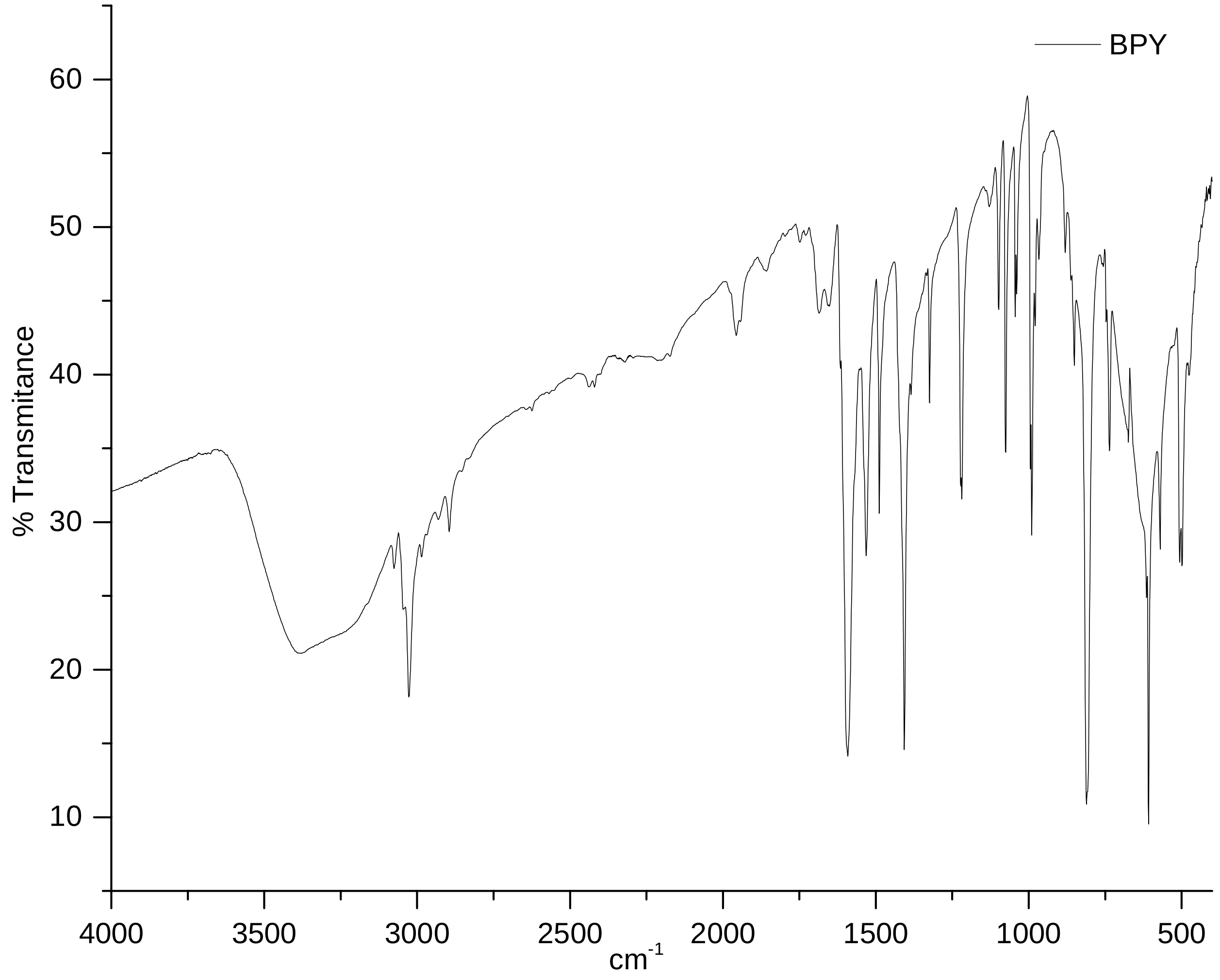

FT-IR spectrum of 4,4’-Bipyridyl hydrate

…….. FT-IR spectra (Full size)

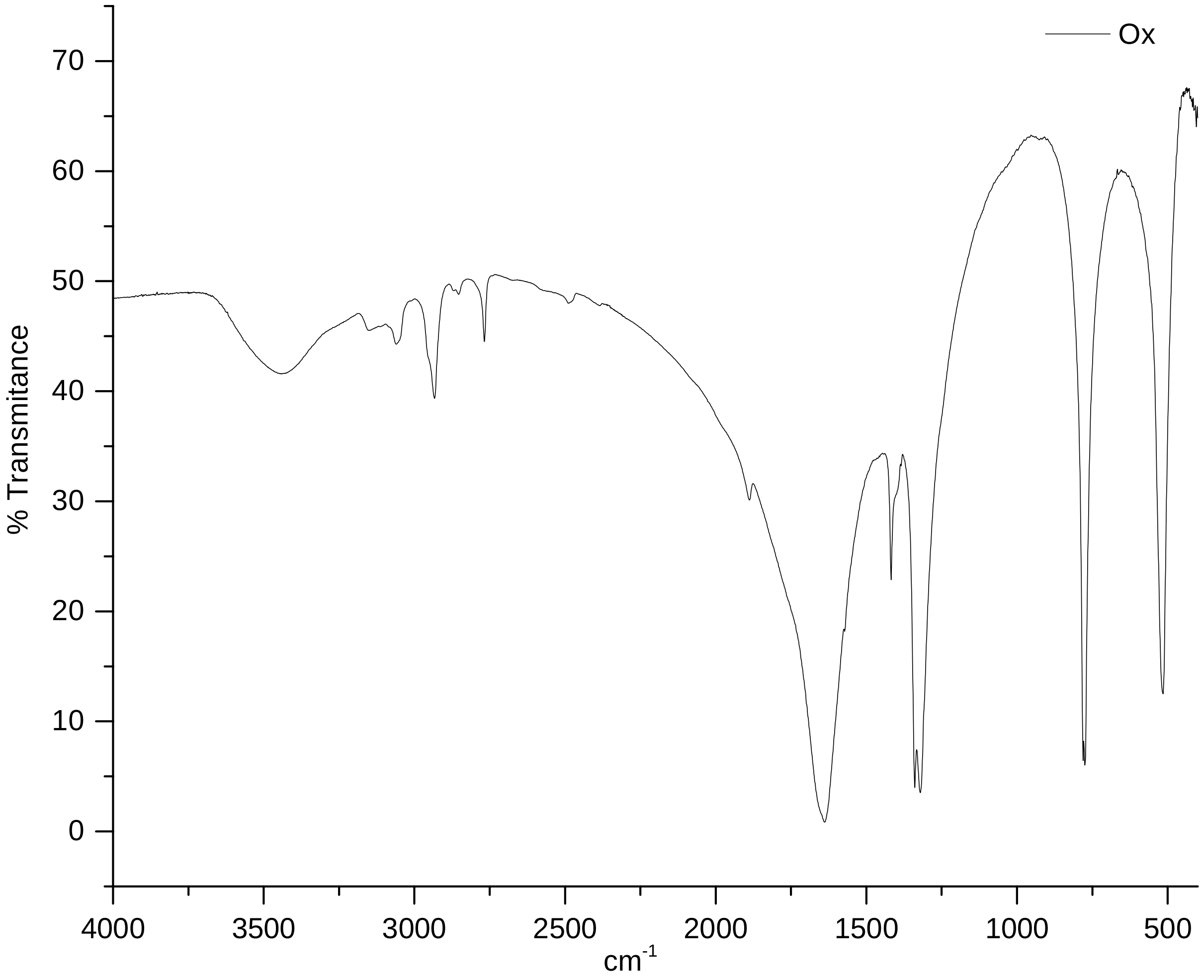

FT-IR spectrum of sodium oxalate

…… FT-IR spectra (Full size)

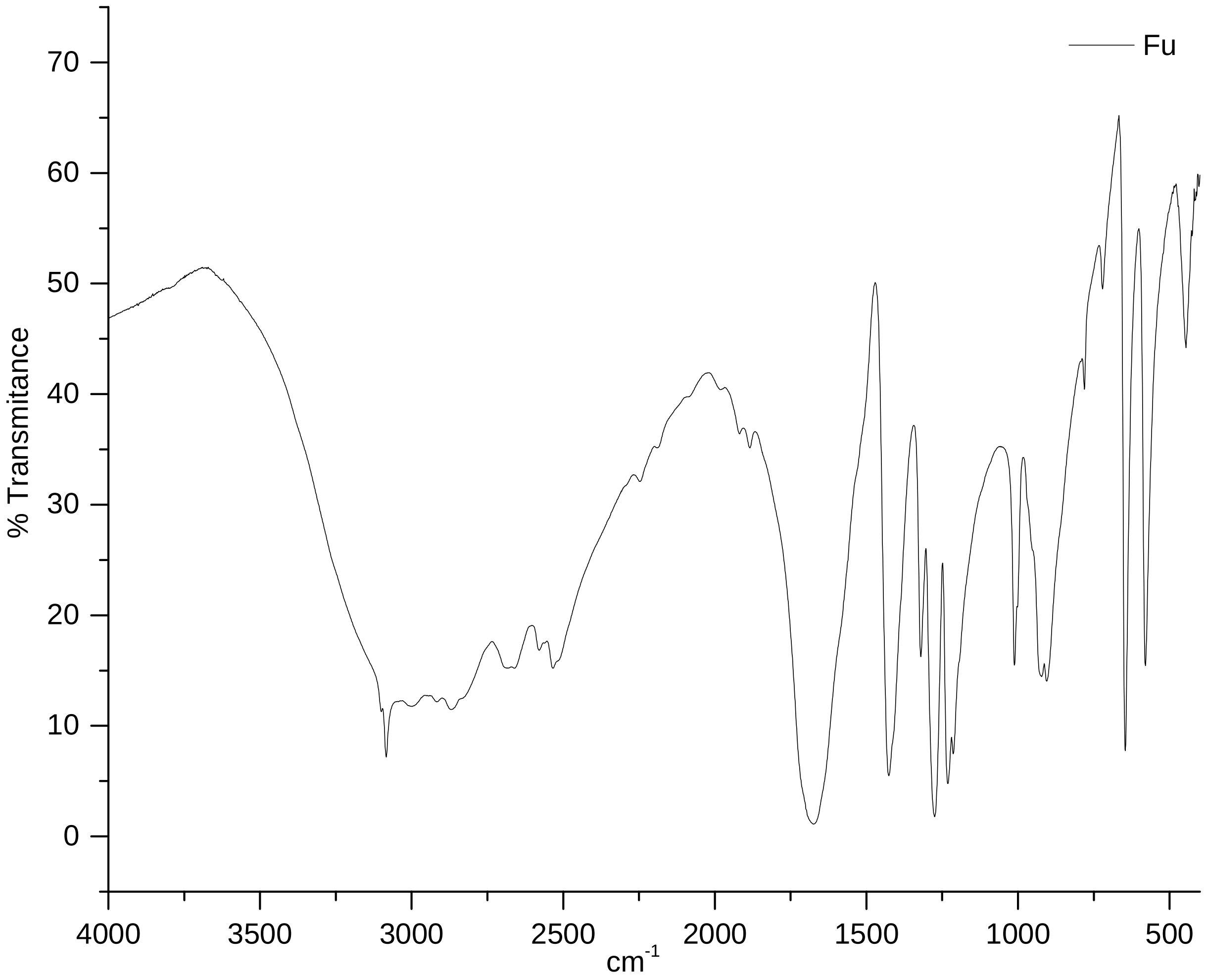

FT-IR spectrum of fumaric acid

Tabular summary of FT-IR assignments for the MOFs, linkers and pillars

			$\{[M_2(Fu)_2(BPY)]\cdot mH_2O\}_n$		$\{[M_2(Ox)_2(BPY)]\cdot mH_2O\}_n$	Assignments
Fu	BPY	Ox	Zn	Cu	Ni	
1678	-	1642	1618	1618	1630	C=O stretching
-	1405(n)	-	1405(st)	1405(st)	1405(s)	Ring breathing
-	1583	-	1618(w)	1618(w)	1630(w)	C-C + C-N
1430	-	1320	1380	1380	1333	COO- (sy + as)
-	3400		3500	3500	3450(st)	H_2O

ATA	BPY	Ox	$\{[M_2(Ox)_2(BPY)]\cdot mH_2O\}_n$		$\{[M_2(ATA)_2(BPY)]\cdot mH_2O\}_n$	Assignments
			Zn	Cu	Zn	
3507	-	-	-	-	3401	NH_2 (sym + asym),
3390	-	-	-	-	3322	
1610	-	-	-	-	-	N-H bending, NH_2 wagging, twisting
1500	-	-	-	-	-	
1678		1642	1618	1618	1564	C=O stretching
-	1583	-	1618	1618	1564	C-N
-	-	-	3400	3400	3400	H_2O(w)
-	-	-	454	407	407	M-N

* NB: Numbers are in cm^{-1} unit and n= narrow, w= wide, st= strong, sy= symmetric stretching, as= asymmetric stretching

APPENDIX E: Microelemental analysis

Elemental analysis of $\{[Cu_2(Fu)_2(BPY)]\cdot H_2O\}_n$

MOFT-23-RT Mwt = 527.93 gmol^{-1}	C (%)		H (%)		N (%)	
	Calcd.	Found	Calcd.	Found	Calcd	Found.
$C_{18}H_{14}N_2O_9Cu_2$	40.80	40.70	2.64	2.39	5.28	5.04

Elemental analysis of $\{[Zn_2(Fu)_2(BPY)]\cdot 1.5H_2O\}_n$

MOFT-22-RT Mwt = 542.08 gmol^{-1}	C (%)		H (%)		N (%)	
	Calcd.	Found	Calcd.	Found	Calcd	Found.
$C_{18}H_{15}N_2O_{9.5}Zn_2$	39.84	39.73	2.76	2.97	5.16	4.89

Elemental analysis of $\{[Ni_2(Ox)_2(BPY)]\cdot 3.75H_2O\}_n$

MOFT-11-RT Mwt = 517.17 gmol^{-1}	C (%)		H (%)		N (%)	
	Calcd.	Found	Calcd.	Found	Calcd	Found.
$C_{14}H_{15.5}N_2Ni_2O_{11.75}$	32.55	32.49	2.99	2.71	5.41	5.13

Elemental analysis of $\{[Zn_2(Ox)_2(BPY)]\cdot 3.5H_2O\}_n$

MOFT-08-RT	C (%)		H (%)		N (%)	
Mwt = 521.53 $gmol^{-1}$	Calcd.	Found	Calcd.	Found	Calcd	Found.
$C_{14}H_{14.5}N_2O_{11.25}Zn_2$	32.24	32.36	2.80	2.58	5.32	5.13

Elemental analysis of $\{[Cu_2(Ox)_2(BPY)]\cdot 0.5H_2O\}_n$

MOFT-09-RT	C (%)		H (%)		N (%)	
Mwt = 468.32 $gmol^{-1}$	Calcd.	Found	Calcd.	Found	Calcd	Found.
$C_{14}H_9N_2Cu_2O_{8.5}$	35.9	35.83	1.94	1.73	5.98	5.97

Elemental Analysis for $\{[Zn_2(ATA)_2(BPY)]\cdot H_2O\}_n$

MOFT-53-RT	C (%)		H (%)		N (%)	
Mwt = 663.22 $gmol^{-1}$	Calcd.	Found	Calcd.	Found	Calcd	Found.
$C_{26}H_{20}N_4O_9Zn_2$	47.08	47.43	3.04	2.97	8.45	8.49

APPENDIX F: PYTZ synthesis scheme

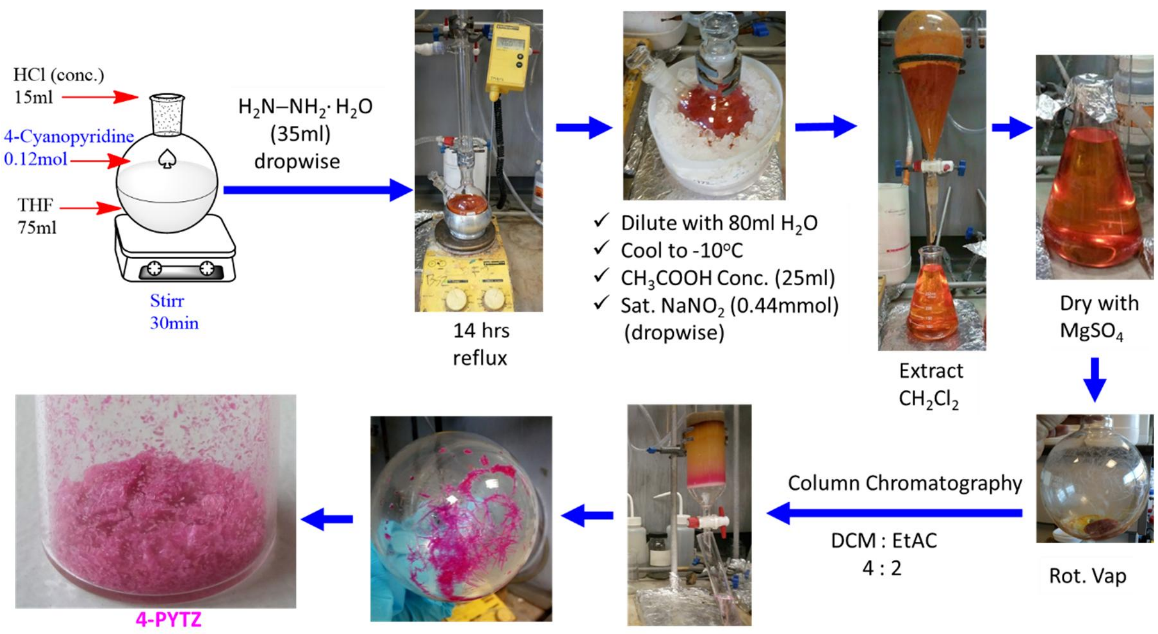

Synthetic scheme for 3,6-di(pyridin-4-yl)-1,2,4,5-tetrazine or PYTZ pillar

APPENDIX G: Proton NMR of PYTZ

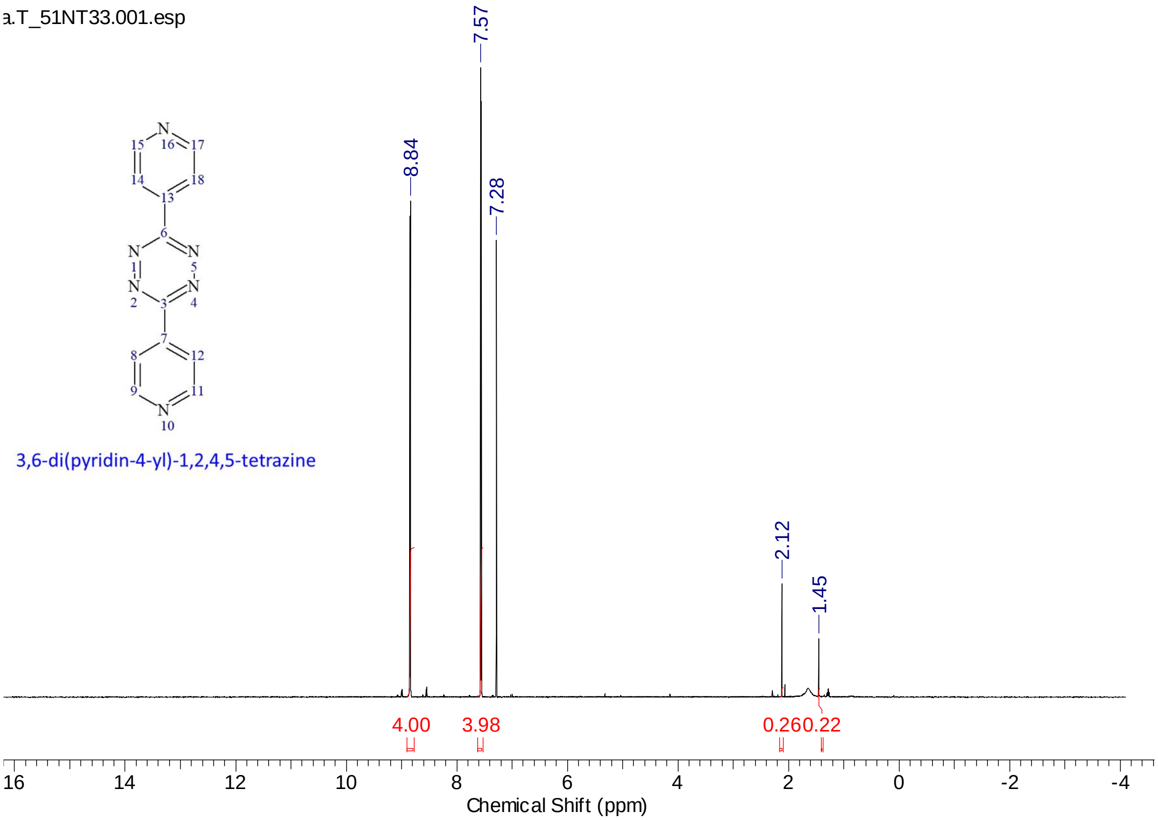

^{1}H NMR of PYTZ

APPENDIX H: Solvothermal synthesis scheme

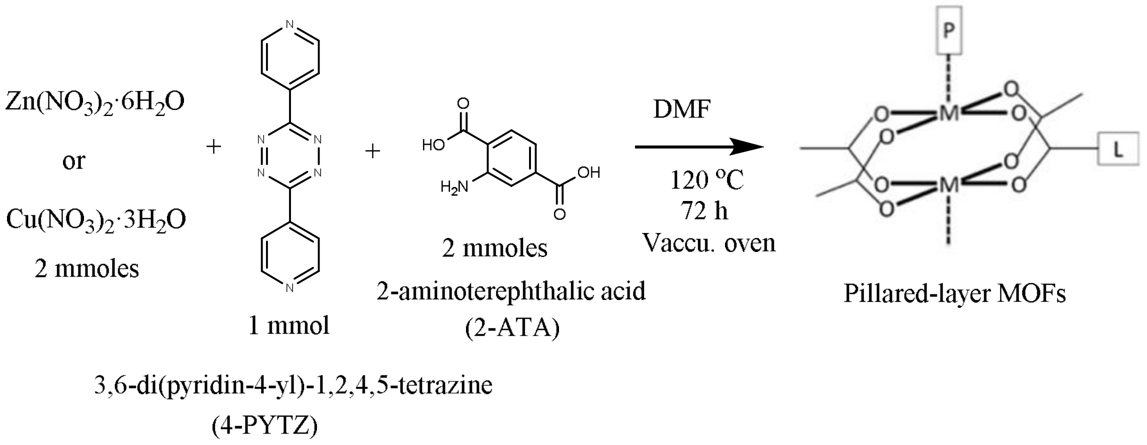

A scheme on the attempts to synthesize pillared-layer MOFs from a mixture of Cu(II) or Zn(II), ATA and PYTZ in DMF solvent in a solvothermal approach. (NB: desired Pillared-layer MOFs were not obtained as per elemental analysis result)

APPENDIX I: 1:1:1 synthetic approach

Ni(II)	Co(II)	Cu(II)	Zn(II)	Fe(III)
-11 $Ni(NO_3)_2.6H_2O$ Sodium Oxalate 44BPY hydrate m=0.239gm (T-11) 1:1:1 m=0.94gm (T-11B) 3:3:3	T-10 $Co(NO_3)_2.6H_2O$ Sodium Oxalate 44BPY hydrate m= 0.2676gm (T-10) 1:1:1 m= 0.84gm (T-10B) 3:3:3	T-09 $Cu(NO_3)_2.3H_2O$ Sodium Oxalate 44BPY hydrate m=0.3801gm 1:1:0.5	T-08 $Zn(NO_3)_2.6H_2O$ Sodium Oxalate 44BPY hydrate m=0.255gm 1:1:1	T-16 $FeCl_3$ (anhydrous) Sodium Oxalate 44BPY hydrate m=0.1243gm (T-16) 1:1:1 m=0.65gm (T-16B) 3:3:3
T-38 $Ni(NO_3)_2.6H_2O$ Sodium Oxalate Pyrazine m=0.6483gm 3:3:3	T-32 $Co(NO_3)_2.6H_2O$ Sodium Oxalate Pyrazine m=0.5483gm 3:3:3	T-37 $Cu(NO_3)_2.3H_2O$ Sodium Oxalate Pyrazine m=0.4883gm 3:3:3	T-39 $Zn(NO_3)_2.6H_2O$ Sodium Oxalate Pyrazine m=0.5483gm 3:3:3	T-40 $FeCl_3$ (anhydrous) Sodium Oxalate Pyrazine Not good
T-14 $Ni(NO_3)_2.6H_2O$ Fumaric Acid 44BPY hydrate m=0.2976gm (T-14) 2:2:2 m=0.4583gm (T-14B) 3:3:3	T-15 $Co(NO_3)_2.6H_2O$ Fumaric Acid 44BPY hydrate m=0.133gm 1:1:1	T-13 $Cu(NO_3)_2.3H_2O$ Fumaric Acid 44BPY hydrate m=0.428gm (T-13) 2:2:2 m=0.5883gm (T-13B) 3:3:3	T-12 $Zn(NO_3)_2.6H_2O$ Fumaric Acid 44BPY hydrate m=0.33gm (T-12) 1:1:1 m=0.5583gm (T-12B) 3:3:3	T-17 $FeCl_3$ (anhydrous) Fumaric Acid 44BPY hydrate m=0.25gm 1:1:1
T-21 $Ni(NO_3)_2.6H_2O$ Fumaric Acid + NaOH 44BPY hydrate m=0.95gm 3:3:3	T-24 $Co(NO_3)_2.6H_2O$ Fumaric Acid + NaOH 44BPY hydrate m=0.85gm 3:3:3	T-23 $Cu(NO_3)_2.3H_2O$ Fumaric Acid + NaOH 44BPY hydrate m=0.94gm 3:3:3	T-22 $Zn(NO_3)_2.6H_2O$ Fumaric Acid + NaOH 44BPY hydrate m=0.71gm 3:3:3	T-25 $FeCl_3$ (anhydrous) Fumaric Acid + NaOH 44BPY hydrate m=0.55gm 3:3:3
T-34 $Ni(NO_3)_2.6H_2O$ Fumaric Acid + NaOH Pyrazine Not good 3:3:3	T-31 $Co(NO_3)_2.6H_2O$ Fumaric Acid + NaOH Pyrazine m=0.0383gm 3:3:3	T-33 $Cu(NO_3)_2.3H_2O$ Fumaric Acid + NaOH Pyrazine m=0.6083gm 3:3:3	T-36 $Zn(NO_3)_2.6H_2O$ Fumaric Acid + NaOH Pyrazine m=0.0683gm 3:3:3	T-35 $FeCl_3$ (anhydrous) Fumaric Acid + NaOH Pyrazine m=0.4583gm 3:3:3
T-26 $Ni(NO_3)_2.6H_2O$ Tereptalic Acid + NaOH 44BPY hydrate m=1.12gm 3:3:3	T-28 $Co(NO_3)_2.6H_2O$ Tereptalic Acid + NaOH 44BPY hydrate m=1.08gm 3:3:3	T-27 $Cu(NO_3)_2.3H_2O$ Tereptalic Acid + NaOH 44BPY hydrate m=1.07gm 3:3:3	T-29 $Zn(NO_3)_2.6H_2O$ Tereptalic Acid + NaOH 44BPY hydrate m=1.02gm 3:3:3	T-30 $FeCl_3$ (anhydrous) Tereptalic Acid + NaOH 44BPY hydrate m=0.86gm 3:3:3

Attempts to synthesize PMOFs in 1:1:1 ratio of the L:M:P, respectively (L=linker, M=Metal salt, P= Pilar)

APPENDIX J: calibration curves

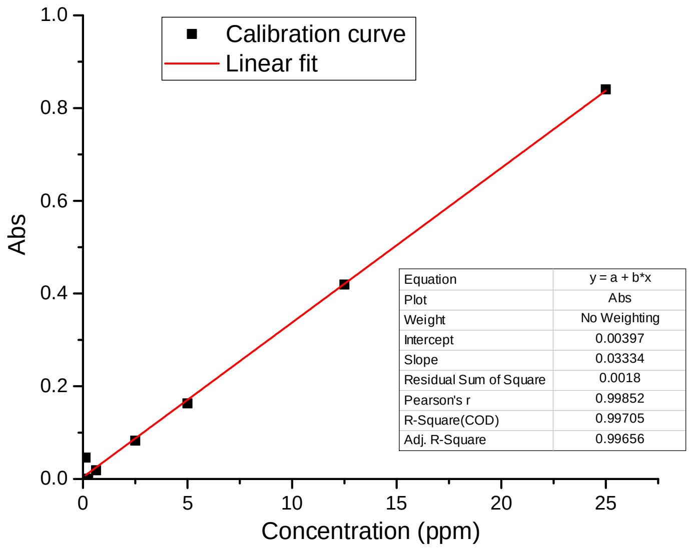

Equation	y = a + b*x
Plot	Abs
Weight	No Weighting
Intercept	0.00397
Slope	0.03334
Residual Sum of Square	0.0018
Pearson's r	0.99852
R-Square(COD)	0.99705
Adj. R-Square	0.99656

Calibration curve for effect of MOFs Loading

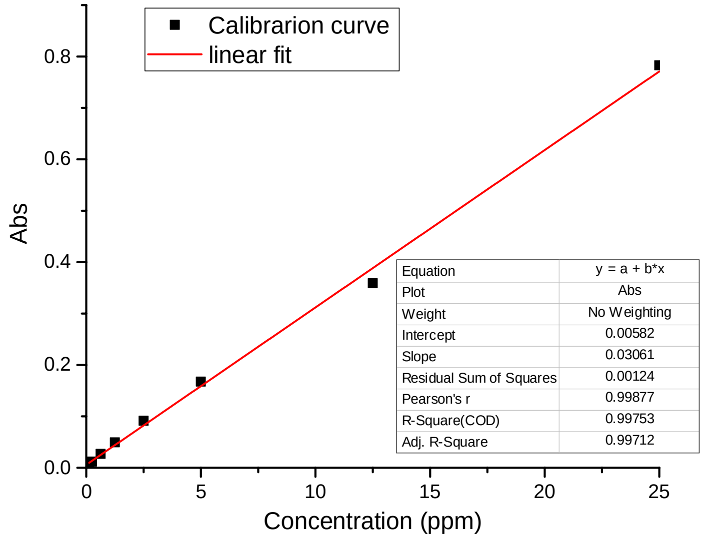

Equation	y = a + b*x
Plot	Abs
Weight	No Weighting
Intercept	0.00582
Slope	0.03061
Residual Sum of Squares	0.00124
Pearson's r	0.99877
R-Square(COD)	0.99753
Adj. R-Square	0.99712

Calibration curve for the effect of pH

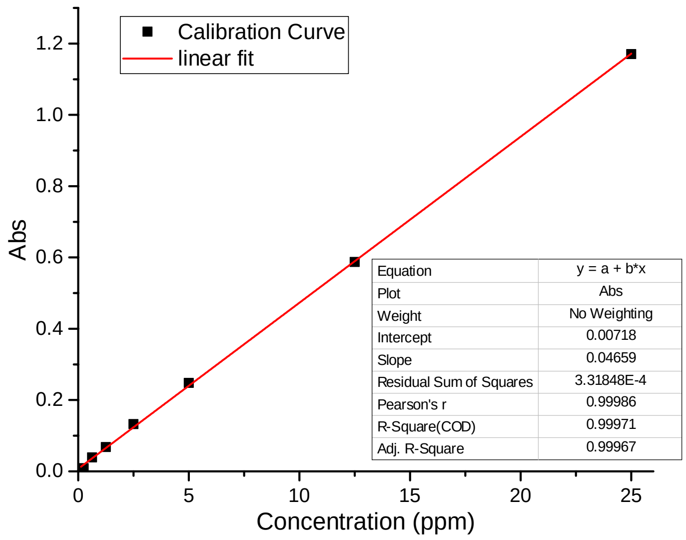

Equation	y = a + b*x
Plot	Abs
Weight	No Weighting
Intercept	0.00718
Slope	0.04659
Residual Sum of Squares	3.31848E-4
Pearson's r	0.99986
R-Square(COD)	0.99971
Adj. R-Square	0.99967

Calibration curve for the reusability test